THÈSE

Pour obtenir le grade de

DOCTEUR DE L'UNIVERSITÉ GRENOBLE ALPES

École doctorale : PHYS - Physique
Spécialité : Physique Subatomique et Astroparticules
Unité de recherche : Laboratoire de Physique Subatomique et Cosmologie

Mesures et observations en polarimétrie aux longueurs d'onde millimétriques avec des KIDs

Polarimetry measurements and observations at millimeter wavelengths with KIDs

Présentée par :

Sofia SAVORGNANO

Direction de thèse :

Andrea CATALANO DIRECTEUR DE RECHERCHE, CNRS DELEGATION ALPES	Directeur de thèse
Alessandro MONFARDINI DIRECTEUR DE RECHERCHE, CNRS DELEGATION ALPES	Co-directeur de thèse

Rapporteurs :

FRANCESCO PIACENTINI
ASSOCIATE PROFESSOR, UNIV. DEGLI STUDI DI ROMA LA SAPIENZA
SOPHIE HENROT-VERSILLE
DIRECTRICE DE RECHERCHE, CNRS DELEGATION ILE-DE-FRANCE SUD

Thèse soutenue publiquement le **5 novembre 2025**, devant le jury composé de :

JACOB LAMBLIN, PROFESSEUR DES UNIVERSITES, UNIVERSITE GRENOBLE ALPES	Président
FRANCESCO PIACENTINI, ASSOCIATE PROFESSOR, UNIV. DEGLI STUDI DI ROMA LA SAPIENZA	Rapporteur
SOPHIE HENROT-VERSILLE, DIRECTRICE DE RECHERCHE, CNRS DELEGATION ILE-DE-FRANCE SUD	Rapporteure
HERVE GEOFFRAY, INGENIEUR, CNES TOULOUSE	Examinateur

Invités :

ALICIA GOMEZ
SCIENTIST, CENTRO DE ASTROBIOLOGIA

A mia Nonna Anna
(1940 – 2023)

«An experiment is a question which science poses to Nature, and a measurement is the recording of Nature's answer.»

— Max Planck

Acknowledgments

The time of wrapping up these past three years has come. It feels strange to condense years of work, people, and moments into words, but I will try to do justice to those who shaped this PhD journey.

First of all, I sincerely thank the jury for being part of this defining moment in my career. Jacob and Hervé, you have followed my path since the beginning: I thank you for your advice and the interest you showed in my work; Sophie, Francesco, and Alicia, I recently had the pleasure of meeting you, and your feedback on my work has truly been inspiring. Thank you all for your thoughtful and stimulating questions during the defense, which pushed me to look deeper into my work and my understanding of it.

I am deeply grateful to all the colleagues I have worked with: the entire NIKA2 collaboration and its closest members at the lab; the IRAM team for their invaluable expertise on the telescope and observations; the Néel team, and Martino and Florence in particular, for your help and presence; and the COSMOCal collaboration, who welcomed me into the project and placed so much trust in me during key phases.

Merci à l'équipe W43, et en particulier à Fabien. Merci de m'avoir suivie du début à la fin, pour les nombreuses séances de questions-réponses. J'aime ton attitude toujours positive et optimiste. Tu es un collègue exceptionnel et j'espère que nous pourrons encore collaborer à l'avenir.

Un chaleureux merci au LPSC, qui a véritablement été une seconde maison pour moi : pour l'efficacité de ses services, pour la bienveillance que j'y ai toujours trouvée, et pour toutes les activités qui rendent la vie au laboratoire plus vivante — les cafés du labo, les journées du labo, et tous les événements organisés. Ceux qui me connaissent savent à quel point j'apprécie ce genre de moments.

Au troisième étage, je dois ma gratitude à beaucoup de personnes. À tout le personnel permanent de l'équipe de Cosmologie Observationnelle : merci pour votre soutien, votre présence, votre engagement enthousiaste dans les activités de team-building que j'ai proposées, et surtout pour m'avoir rappelé que la science est toujours un effort collectif. Chacun d'entre vous a contribué à façonner ma manière de faire de la recherche.

To all the PhD students and postdocs of Gros Cosmo: thank you for turning these three years into something that felt more like a long trip with friends than work — the countless briscola games, gâteaux du lundi, beers at Jardin Biergarten, late nights at Barrio Latino, the memes, and all the laughter. I know you will miss your favorite witch. The atmosphere we created is something rare, and I'm deeply grateful for it. I wish all the best to the new students for their theses (and continue to play briscola!).

Merci au service électronique, et à Olivier et Julien en particulier, de nous avoir dépannés

mille fois dans la salle de manip et avec le simulateur de ciel. Vous faites un excellent travail, merci pour cela.

Merci à l'équipe Dark Photons, notamment Daniel, Ilias et Cyprien. Travailler sur cette expérience a été un vrai plaisir. J'ai adoré nos discussions sur la manip, les données et leur interprétation. Vous m'avez permis d'explorer un domaine qui n'était pas forcement le mien, et cela a été très enrichissant. Je souhaite à Ilias une excellente continuation de thèse.

Un grazie a Silvia, per tutte le caramelle e cioccolatini che mi hai regalato in questi anni. Una bella botta glicemica ogni tanto mi ha dato lo sprint che mi serviva per continuare. Sei stata di grande supporto psicologico, con la tua energia e risata contagiosa. Grazie per i consigli sulla vita negli States, sei una persona su cui ho potuto contare.

Grazie Alessia per questi anni di lavoro insieme, in laboratorio, al telescopio, per le chiacchierate prima di dormire nella nostra stanza condivisa, e per le avventure di voli cancellati. Grazie per la fiducia che mi hai dimostrato, per la stima e l'affetto. Hai portato avanti un progetto bellissimo, anche incinta e poi con una bimba piccola, la tua splendida Emma, sempre con il sorriso. Per tutte queste ragioni, sei per me un esempio professionale e umano di altissimo livello.

Grazie Alessandro, sei stato più di un collega per me. Grazie per i consigli che mi hai dato dall'inizio alla fine della mia tesi. Sono felice di averti conosciuto, del nostro viaggio in Giappone e delle lunghe videochiamate nei momenti di crisi. Spero che ci rincontreremo e avremo ancora occasione di lavorare insieme.

Grazie Daniele, sei stato un ottimo compagno di dottorato a Grenoble. Grazie per le infinite camminate in montagna, per il supporto reciproco durante la scrittura della tesi. Ti auguro il meglio per la tua carriera e spero che le nostre strade si incroceranno ancora.

Usasi, I'm so sad you couldn't be there for my defense, because you've definitely been one of the most important people in my Grenoble chapter. I've already told you everything when you left, but I want to thank you again for all the time we spent together. Your courage and strength, despite all difficulties, truly impressed and inspired me. You're an amazing human being, and I wish you all the good you deserve in this new Finnish chapter of your life.

Merci Juan, d'avoir toujours été là pour moi, surtout pendant ma première année. Tu as été comme un encadrant supplémentaire pour moi. Merci pour ton aide à la fois pratique et humaine, pour tout ce que tu m'as appris — des bases de Python à la compréhension des champs magnétiques. Ta phrase fétiche, « on va faire un truc simple », est sans doute la plus rassurante que j'aie jamais entendue. Tu es vraiment "Juan in a million".

Merci Nicolas, toi aussi tu as été comme un encadrant supplémentaire pour moi. Ta patience et ton dévouement à l'enseignement sont rares. Tu m'as aidée à résoudre les problèmes les plus fondamentaux, depuis mes tout premiers jours jusqu'aux dernières heures avant la soutenance, quand des questions aléatoires envahissaient encore mon esprit. J'espère que tu continueras à transmettre ta passion aux futurs étudiants.

Alessandro, grazie per il tuo perfetto mix di saggezza e cinismo — un equilibrio di cui non sapevo di avere bisogno. In qualche modo avevi sempre una risposta a ogni domanda, dalla fabbricazione di KIDs in camera pulita, ai misteri della criogenia. Grazie per la tua creatività,

la tua originalità e il tuo modo di pensare profondamente indipendente — non segui mai i percorsi già tracciati, ed è proprio questo che ha reso così stimolante lavorare con te. Spero davvero che continuerai ad avere successo nel creare nuovi strumenti ancora per molti anni.

Andrea — non so nemmeno da dove cominciare. Lavorare con te in laboratorio è stato puro divertimento: aprire e chiudere il criostato, montare installazioni improbabili, trafficare con cavi, colla, Eccosorb, azoto liquido e il nostro amato KID B004. Il tuo modo appassionato di discutere di qualunque argomento è semplicemente unico: da come tenere un cacciavite, alle espressioni francesi, ai detti siciliani, alla psicologia del tennis e, di tanto in tanto, anche un po' di fisica. Mi hai dato fiducia fin dall'inizio — mi hai lasciato usare il tuo giocattolo preferito e, senza esitazioni, hai creduto che sarei arrivata fino in fondo. Sapevi quando spingermi a fare quello sforzo in più, e quando invece lasciarmi il tempo di respirare. Grazie per le dure verità sbattute in faccia, così come per le più genuine parole di incoraggiamento; grazie per le nostre conversazioni profonde e lunghissime, così come per le brevi risate di leggerezza. I colleghi in corridoio si lamentavano spesso che le nostre discussioni fossero troppo rumorose — ma se il rumore significa trasmettere passione e motivazione alla prossima generazione, allora non abbassare mai la voce. Ti auguro tutto il successo e il riconoscimento che meriti nei prossimi passi della tua carriera — e spero che continuerai a portare quella stessa combinazione di energia e curiosità a molti altri dopo di me.

Grazie Ludovico, per la nostra amicizia e il lavoro svolto insieme. Sei una persona estremamente intelligente e gentile, una combinazione sempre più rara. Grazie per i momenti insieme al telescopio, in laboratorio, per le videochiamate di confronto, per gli aperitivi (tanti) e per avermi tirata fuori dal mio guscio ai tempi della Bicocca. Grazie a te e a Matilde di essere venuti alla mia discussione di dottorato. Ti auguro un buon proseguimento di tesi, sono sicura che farai un lavoro eccellente.

Grazie Michele, sei una delle persone che più stimo al mondo. Come ti dico sempre, non so come fai a gestire tutto: la tua brillante carriera di architetto, quella da arbitro, e la tua impegnata vita sociale. Grazie per le ore di messaggi audio che ci siamo scambiati in questi anni, per la tua presenza costante seppure da lontano. Grazie di essere venuto a Grenoble per la mia discussione, nonostante i mille impegni. Significa e significhi tanto per me.

Nonna Dinca, grazie per il tuo supporto in questi anni, per essere venuta a trovarmi nella ridente Grenoble numerose volte. Questi ultimi mesi sono stati difficili per te, ma sai di poter contare sul mio affetto, anche se da lontano. Un grazie anche ai miei zii, Nicoletta e Fausto, che siete come altri due nonni per me. Grazie delle vostre telefonate, del vostro interesse e della vostra vicinanza. Un pensiero va ai miei nonni, Anna e Piero, mancati nel 2023 e nel 2020. Mi mancate molto e vi penso. So che sareste fieri di me e del mio percorso.

Gaia, quando ho iniziato il dottorato tu eri in piena crisi da liceo, e ora sei sulla strada per diventare medico. Hai mostrato una determinazione e una tenacia rare, e per questo sono infitamente orgogliosa di te. Sono certa che troverai tanta gratificazione nel tuo percorso di studi e lavorativo. Ti auguro tutto il meglio.

E infine, mamma e papà — tutto torna sempre a voi. So cosa ha significato non avermi a casa e so quanto vi sono mancata. Anche voi mi siete mancati, in un modo che le parole non possono esprimere. La distanza è stata la parte più dura del percorso che ho scelto, ma siete rimasti presenti in ogni fase. Siete la struttura portante di ciò che sono, la base stabile che rende possibile ogni mio passo. Vi ringrazio, ancora una volta, per il vostro amore caldo, incessante,

incrollabile. Tutto ciò che verrà porta la vostra impronta.

I finalize these acknowledgments sitting in my room in Como, facing the lake on a bright November morning, and I cannot help but acknowledge the transition I am living. Change is constant: we cannot stop it, but we can choose how to live with it. We can embrace it, let go of what must be left behind, and make room for what is coming. Soon I will leave for Boston, where I will begin my postdoctoral journey at Boston University. It is both daunting and thrilling, a new chapter full of unknowns, yet carrying with me everything and everyone that has shaped me so far. As I step forward, I feel ready — bolstered by all the moments, guidance, and memories that brought me here, and filled with hope for the adventures yet to come.

Contents

General introduction **15**

Introduction générale **17**

1 Polarization in astrophysics and cosmology **19**
1.1 The interest of polarization . . . 20
1.2 Polarization at galactic scales . . . 21
1.2.1 Synchrotron emission . . . 22
1.2.2 Free-free emission . . . 24
1.2.3 Thermal dust emission . . . 24
1.2.4 Spinning dust emission . . . 27
1.3 Star formation . . . 27
1.3.1 Magnetic fields and star formation dynamics . . . 28
1.3.2 Polarization as a diagnostic tool . . . 28
1.3.3 High-mass star formation and magnetic fields . . . 29
1.4 Extragalactic polarization . . . 30
1.4.1 Active Galactic Nuclei (AGN) . . . 30
1.4.2 Faraday rotation . . . 30
1.5 The ΛCDM and Hot Big Bang cosmological models . . . 31
1.5.1 The Cosmic Microwave Background . . . 32
1.5.2 The limits of the standard model . . . 35
1.5.3 The Inflation solution . . . 36
1.6 Polarization at cosmological scales . . . 36
1.6.1 CMB polarization . . . 36
1.6.2 Cosmic birefringence . . . 41
1.7 Conclusion . . . 42

2 Measuring polarization: formalism, techniques and challenges **43**
2.1 The characteristics of a polarized signal . . . 44
2.2 Formalism of polarized radiation . . . 46
2.2.1 Jones formalism . . . 46
2.2.2 Stokes formalism . . . 47
2.2.3 Mueller matrices . . . 47
2.3 Optical elements formalism . . . 48
2.3.1 Linear polarizer . . . 48
2.3.2 Half-Wave Plates (HWP) . . . 50
2.4 Modulation: concept and methods . . . 51
2.4.1 On-sky modulation . . . 52
2.4.2 Optical element modulation . . . 53
2.4.3 Boresight rotation . . . 54
2.5 Reference CMB polarization experiments . . . 55

2.6 Requirements for next-generation CMB polarization experiments . . . 58
2.6.1 Observational constraints . . . 58
2.6.2 Systematic effects and calibration requirements . . . 61
2.6.3 The particular case of the absolute orientation . . . 64
2.7 Conclusion . . . 66

3 Kinetic Inductance Detector technology for millimeter wavelength radiation 69
3.1 From photons to electrical signals . . . 70
3.2 Foundations of superconductivity . . . 71
3.2.1 Superconducting materials . . . 71
3.2.2 Transition temperature and superconducting gap . . . 71
3.2.3 Quasi-particle generation and recombination . . . 72
3.2.4 Meissner effect . . . 72
3.3 Kinetic Inductance Detectors . . . 73
3.3.1 Resonating circuits and the RLC model . . . 74
3.3.2 Working principle . . . 75
3.4 Lumped Element KIDs as photon absorbers . . . 75
3.4.1 LEKID pixel coupling and array design . . . 78
3.4.2 Readout electronics . . . 79
3.4.3 Photometry and polarimetry with LEKIDs . . . 80
3.4.4 Scientific applications and instrumentation using KIDs . . . 83
3.5 Fabrication of an aluminum LEKID array . . . 85
3.5.1 Step 1: choice of the substrate . . . 85
3.5.2 Step 2: deposition of the superconductor layer . . . 85
3.5.3 Step 3: deposition of the ground plane . . . 86
3.5.4 Step 4: photolithography (patterning through mask) . . . 86
3.5.5 Step 5: wet etching . . . 86
3.5.6 Step 6: microscopy inspection . . . 87
3.5.7 Step 7: dicing, holder installation and bonding . . . 88
3.6 Cryogenic characterization of LEKID arrays . . . 89
3.6.1 VNA scans . . . 89
3.6.2 Quality factors . . . 89
3.7 Conclusion . . . 93

4 High-precision polarization measurements with LEKIDs 95
4.1 The purpose of the project . . . 96
4.2 The experimental setup . . . 97
4.2.1 The test bench . . . 97
4.2.2 The LEKIDs receivers . . . 99
4.3 Test bench characterization . . . 101
4.3.1 Effective sky simulator's temperature estimation . . . 101
4.3.2 Optical load estimation . . . 103
4.4 Camera's performances . . . 104
4.4.1 Photometric and spectral characterization . . . 105
4.4.2 Polarimetry characterization . . . 113
4.5 Interpretation of results . . . 116
4.5.1 Polarization angle accuracy . . . 116
4.5.2 Cross-polarization contribution . . . 116
4.6 Implications for CMB B-modes observations . . . 117
4.7 Conclusions and perspectives . . . 117

5 Polarimetry observations with NIKA2 **121**
5.1 The IRAM 30m Telescope . . . 122
5.2 The NIKA2 camera . . . 123
5.2.1 Cryostat . . . 124
5.2.2 Readout electronics . . . 124
5.2.3 Optics . . . 125
5.2.4 NIKA2 as a polarimeter . . . 126
5.2.5 NIKA2's scientific targets . . . 126
5.2.6 NIKA2+: upgrade and re-commissioning preliminary results . . . 128
5.3 Polarimetry observations with NIKA2 . . . 129
5.3.1 Telescope operations . . . 130
5.3.2 Scientific data treatment: from TOI to maps . . . 132
5.4 Polarization study of W43 with NIKA2 . . . 133
5.4.1 Main goal of the observations . . . 133
5.4.2 Source description and observation strategy . . . 134
5.4.3 Data analysis methodology . . . 135
5.4.4 Results and interpretation . . . 142
5.5 Conclusions and perspectives . . . 144

6 A novel method for polarization calibration: the COSMOCal project **145**
6.1 The COSMOCal project framework . . . 146
6.1.1 Scientific purpose . . . 146
6.1.2 The spatial calibrator . . . 147
6.1.3 Project phases . . . 149
6.2 The Phase 1 adapted 260 GHz prototype . . . 149
6.2.1 Internal polarization angle calibrator . . . 149
6.2.2 Photogrammetry . . . 150
6.3 Phase 1.1: in-lab proof of concept . . . 151
6.3.1 Adapted experimental setup . . . 151
6.3.2 Coupling COSMOCal - cryostat . . . 151
6.3.3 Data model and methods . . . 152
6.3.4 Data acquisition strategy . . . 153
6.3.5 Diffraction pattern results . . . 154
6.3.6 KID results . . . 154
6.3.7 Remarks on the in-lab proof-of-concept . . . 158
6.4 Phase 1.2: IRAM 30m test campaign . . . 158
6.4.1 Optical model . . . 159
6.4.2 Signal model . . . 164
6.4.3 Preliminary detection . . . 164
6.4.4 Pipeline for data reduction: key concepts . . . 166
6.4.5 Radio alignment . . . 168
6.4.6 Photogrammetry and diffraction pattern analyses . . . 168
6.4.7 Polarization measurements . . . 170
6.4.8 Final considerations on the campaign . . . 174
6.5 Perspectives on Phases 2 and 3 . . . 175
6.6 Conclusions . . . 175

7 LEKIDs for dark matter search: the DANDELION experiment **177**
7.1 Dark photons as a dark matter candidate . . . 178
7.1.1 The dark photons physics . . . 179

7.1.2 meV dark photons as a window towards the Early Universe 179
7.1.3 State-of-the-art on dark photon detection 180
7.2 The DANDELION experiment 181
7.2.1 Experiment baseline 181
7.2.2 The instrumental setup 181
7.2.3 Background and noise mitigation 182
7.2.4 Measurement strategy 183
7.2.5 Signal modeling 184
7.2.6 Expected sensitivities 186
7.3 DANDELION first data run 187
7.3.1 Raw detected signal 188
7.3.2 Displacement of the signal on the focal plane 189
7.3.3 PCA-based background modeling and signal extraction 189
7.3.4 Exclusion curves on the χ parameter 190
7.4 Conclusions and perspectives 191

Conclusions and perspectives **193**

Conclusions et perspectives **195**

References **197**

General introduction

Over time, I came to appreciate how polarization at millimeter wavelengths is a topic that embraces a remarkable variety of astrophysical and cosmological phenomena, from the diffuse Galactic dust to the formation of stars, and even the imprint of primordial gravitational waves. This diversity is part of its scientific richness: the same observable links processes across vastly different scales, from the physics of molecular clouds to the early Universe. Working in this field meant touching many different aspects of astrophysics and instrumentation, and my thesis was conceived to be a synthesis of these. It aims to be multi-disciplinary within a single overarching theme, and follows a cyclical research path: developing detectors in the clean room, testing and characterizing them in the laboratory, deploying them in astronomical instruments, using them to extract astrophysical information from complex datasets, and finally re-adapting them to the initial scientific requirements if not fulfilled. What may appear at first sight as a collection of disconnected topics is in fact tied together by a single seamless thread: the measurement of polarization at millimeter wavelengths, approached from an experimental point of view.
This perspective reflects my preference for experimental work and direct engagement with both basic physics and fundamental phenomena. Handling real hardware, observing the response of a detector to light, and working with the data it produces has provided me with a concrete understanding of how measurements are actually made. In this way, this thesis is not only a presentation of scientific results, but wishes to tell the story of an end-to-end experimental effort, spanning from the microscopic scale of superconducting resonators to the largest maps of the sky.
Overall, this thesis aims to demonstrate how advances in detector technology, calibration strategies, and experimental methods can be translated into concrete astrophysical results. In the current era of precision cosmology, the ability to detect extremely faint polarization signals demands not only increasingly sensitive detectors, but also meticulous calibration to control every source of systematic error. Many limitations are intrinsic to ground-based observations, such as the variable emission of the atmosphere, and overcoming them requires both innovative instrument design and advanced data analysis techniques. These efforts are resource-intensive, often involving substantial financial investment, and it can be challenging to justify the importance of fundamental research in times when other, more immediate issues tend to receive priority. Nevertheless, continuing this research is essential: understanding the origin and evolution of the cosmos is one of humanity's deepest scientific questions, and each incremental improvement in our instruments and methods brings us closer to answering it. This work illustrates how polarization measurements at millimeter wavelengths can be pushed toward the precision required for cosmological studies, while simultaneously providing insights into the role of magnetic fields in star formation. In doing so, it highlights the versatility of kinetic inductance detectors as a tool for both astrophysics and fundamental physics.

The manuscript is structured to reflect this natural progression. It begins in Chapter 1 with the astrophysical and cosmological motivation: the physical mechanisms that generate polarization at millimeter wavelengths, on Galactic, extragalactic, and cosmological scales, and the observational challenges associated with detecting such faint signals. Building on this context,

Chapter 2 introduces the principles and techniques of polarimetric measurements, including modulation strategies and the control of systematic effects, setting the stage for understanding the instrumentation used throughout the thesis. Chapter 3 then focuses on Kinetic Inductance Detectors (KIDs), describing the superconducting physics that underlies their operation, their advantages for millimeter-wave polarimetry, and the implementation of Lumped Element KIDs (LEKIDs), which are at the core of the instruments used in this work.
The following chapters move from principles to concrete experimental applications. Chapter 4 presents the PolarKID project, in which two LEKID arrays are used in a specific configuration to test a polarimetric measurement method aiming for the precision required in cosmological experiments. This transition from laboratory characterization to astronomical instrumentation continues in Chapter 5, which describes the IRAM 30m telescope and the NIKA2 camera. Here, the instrumentation is put to work in an observational context, and the chapter presents polarimetric observations of the high-mass star-forming region W43. The analysis integrates observational results with physical interpretation, including the derivation of magnetic field morphology and intensity, and virial analysis to quantify the role of magnetic fields in the star formation process.
The experimental scope then extends to calibration and fundamental physics. Chapter 6 discusses the development of a device for calibrating ground-based instruments dedicated to polarization measurements, a critical step for ensuring measurement accuracy in both astrophysical and cosmological contexts. Finally, Chapter 7 explores the use of LEKID arrays in the DANDELION experiment, a novel directional probe for dark photon dark matter, illustrating how the same detector technology can be adapted to address questions much different than astrophysical polarimetry.

Introduction générale

Au fil du temps, j'ai appris à apprécier combien la polarisation aux longueurs d'onde millimétriques est un sujet qui englobe une remarquable variété de phénomènes astrophysiques, allant de la poussière diffuse de la Voie lactée à la formation stellaire, jusqu'à l'empreinte des ondes gravitationnelles primordiales. Cette diversité fait partie de sa richesse scientifique : une même observable relie des processus à des échelles extrêmement différentes, depuis la physique des nuages moléculaires jusqu'à l'Univers primordial. Travailler dans ce domaine a signifié toucher à de nombreux aspects différents de l'astrophysique et de l'instrumentation, et ma thèse est pensée pour devenir une synthèse de ceux-ci. Elle veut être multidisciplinaire tout en restant unie par un thème central, et suit un parcours de recherche cyclique : développement de détecteurs en salle blanche, tests et caractérisation en laboratoire, intégration dans des instruments astronomiques, utilisation de ceux-ci pour extraire des informations astrophysiques à partir d'ensembles de données complexes, puis réadaptation aux exigences scientifiques initiales si elles ne sont pas satisfaites. Ce qui peut sembler, à première vue, une collection de sujets disparates est en réalité relié par un fil conducteur unique : la mesure de la polarisation aux longueurs d'onde millimétriques, abordée d'un point de vue expérimental.
Cette approche reflète ma préférence pour un travail expérimental et un engagement direct avec la physique fondamentale et les phénomènes physiques. Manipuler du matériel réel, observer la réponse d'un détecteur à la lumière et exploiter les données qu'il produit m'a offert une compréhension tangible de la manière dont les mesures sont réellement effectuées. Ainsi, cette thèse n'est pas seulement une présentation de résultats scientifiques, mais vise à raconter l'histoire d'un effort expérimental complet, allant de l'échelle microscopique des résonateurs supraconducteurs aux plus grandes cartes du ciel.
Dans l'ensemble, cette thèse vise à démontrer comment les avancées en matière de technologie des détecteurs, de stratégies de calibration et de méthodes expérimentales peuvent se traduire en résultats astrophysiques concrets. À l'ère actuelle de la cosmologie de précision, la capacité à détecter des signaux de polarisation extrêmement faibles exige non seulement des détecteurs toujours plus sensibles, mais aussi une calibration minutieuse permettant de contrôler chaque source d'erreur systématique. De nombreuses limitations sont intrinsèques aux observations effectuées depuis le sol, telles que l'émission variable de l'atmosphère, et les surmonter nécessite à la fois une conception instrumentale innovante et des techniques d'analyse de données avancées. Ces efforts sont coûteux en ressources, impliquant souvent un investissement financier considérable. Il peut donc être difficile de justifier l'importance de la recherche fondamentale à une époque où d'autres enjeux plus immédiats tendent à recevoir la priorité. Néanmoins, poursuivre cette recherche est essentiel : comprendre l'origine et l'évolution du cosmos est l'une des questions scientifiques les plus profondes de l'humanité, et chaque amélioration, même marginale, de nos instruments et méthodes nous rapproche de sa résolution. Ce travail illustre comment les mesures de polarisation aux longueurs d'onde millimétriques peuvent être poussées jusqu'à la précision requise pour les études cosmologiques, tout en fournissant simultanément des informations sur le rôle du champ magnétique dans la formation stellaire. Ce faisant, il met en évidence la polyvalence des détecteurs à inductance cinétique en tant qu'outil à la fois pour l'astrophysique et la physique fondamentale.

Le manuscrit est structuré de manière à refléter cette progression naturelle. Il débute, au Chapitre 1, par la motivation astrophysique et cosmologique : les mécanismes physiques qui génèrent la polarisation aux longueurs d'onde millimétriques, aux échelles galactique, extragalactique et cosmologique, ainsi que les défis observationnels liés à la détection de signaux aussi faibles. Dans ce contexte, le Chapitre 2 présente les principes et techniques des mesures polarimétriques, incluant les stratégies de modulation et le contrôle des effets systématiques, préparant ainsi à la compréhension de l'instrumentation utilisée dans toute la thèse. Le Chapitre 3 se concentre ensuite sur les détecteurs à inductance cinétique (KIDs), en décrivant la physique supraconductrice qui sous-tend leur fonctionnement, leurs avantages pour la polarimétrie millimétrique, ainsi que la mise en œuvre des KIDs à éléments localisés (LEKIDs), qui sont au cœur des instruments utilisés dans ce travail.
Les chapitres suivants passent des principes aux applications expérimentales concrètes. Le Chapitre 4 présente le projet PolarKID, dans lequel deux matrices de LEKIDs sont utilisées dans une configuration spécifique afin de tester une méthode de mesure polarimétrique visant la précision requise pour les expériences cosmologiques. Cette transition, de la caractérisation en laboratoire à l'instrumentation astronomique, se poursuit au Chapitre 5, qui décrit le télescope de 30m de l'IRAM et la caméra NIKA2. Ici, l'instrumentation est mise en œuvre dans un contexte observationnel, et le chapitre présente des observations polarimétriques de la région de formation d'étoiles massives W43. L'analyse combine les résultats observationnels avec leur interprétation physique, incluant la détermination de la morphologie du champ magnétique et une analyse virielle pour quantifier le rôle du champ magnétique dans le processus de formation stellaire.
La portée expérimentale s'étend ensuite à la calibration et à la physique fondamentale. Le Chapitre 6 traite du développement d'un dispositif de calibration de l'orientation absolue des instruments terrestres dédiés aux mesures de polarisation, étape critique pour assurer la précision des mesures dans un contexte à la fois astrophysique et cosmologique. Enfin, le Chapitre 7 explore l'utilisation des matrices de LEKIDs dans l'expérience DANDELION : un prototype de détecteur directionnel des "Dark Photons", particules candidates pour la matière noire. Cela illustre comment une même technologie de détection peut être adaptée à des questions très différentes de la polarimétrie astrophysique.

Chapter 1

Polarization in astrophysics and cosmology

Contents

1.1 The interest of polarization **20**
1.2 Polarization at galactic scales **21**
1.2.1 Synchrotron emission 22
1.2.2 Free-free emission 24
1.2.3 Thermal dust emission 24
1.2.4 Spinning dust emission 27
1.3 Star formation **27**
1.3.1 Magnetic fields and star formation dynamics 28
1.3.2 Polarization as a diagnostic tool 28
1.3.3 High-mass star formation and magnetic fields 29
1.4 Extragalactic polarization **30**
1.4.1 Active Galactic Nuclei (AGN) 30
1.4.2 Faraday rotation 30
1.5 The ΛCDM and Hot Big Bang cosmological models **31**
1.5.1 The Cosmic Microwave Background 32
1.5.2 The limits of the standard model 35
1.5.3 The Inflation solution 36
1.6 Polarization at cosmological scales **36**
1.6.1 CMB polarization 36
1.6.2 Cosmic birefringence 41
1.7 Conclusion **42**

Abstract This chapter will mainly introduce the driving concept of this thesis: polarization at millimeter wavelengths. First, a generic introduction of the interest of studying polarization will be given; then, we will provide an overview of the main physical mechanisms responsible for generating polarization at galactic, extragalactic, and cosmological scales, always focusing on millimeter wavelengths. At galactic scales, we discuss emission processes such as synchrotron radiation, thermal and spinning dust emission and free-free emission, emphasizing their connection to magnetic fields and star formation. On extragalactic scales, we explore the role of active galactic nuclei (AGN) and Faraday rotation in shaping polarization signatures. At cosmological scales, we introduce the ΛCDM and Hot Big Bang models as a foundation for understanding the Early Universe, leading to a discussion on Inflation – a theoretical framework that, if confirmed, could explain the origin of primordial perturbations in particular. Particular attention will be given to one key observational challenge in modern cosmology: the detection of CMB B-mode polarization, a crucial signature of Inflation. The discussion in this chapter sets the stage for the following ones, where we examine the observational methods and techniques used to isolate and analyze these polarization signals.

1.1 The interest of polarization

The measurement of polarization has emerged as a transformative tool in modern astrophysics and cosmology, unlocking a deeper understanding of the Universe's most enigmatic phenomena. From the vast cosmic web that underpins the large-scale structure of the Cosmos to the intricate magnetic fields sculpting star-forming regions, polarization offers a unique lens to probe the unseen forces shaping the Universe. As illustrated in Fig. 1.1, polarization is an all-involving phenomenon, bridging scales from the galactic to the extragalactic, and extending to the cosmological realm. Beyond this, it even holds the potential to aid in the quest for life in distant stellar systems, providing an unparalleled perspective on the interplay between light and matter across the Cosmos. With its far-reaching implications, the study of polarization stands at the forefront of scientific discovery, guiding our exploration of the Universe's hidden aspects.

In cosmology, studying the polarization of the CMB is particularly compelling, as it holds the potential to unlock information about the Early Universe. The detection of primordial B-modes, a faint polarization signal thought to be produced by primordial gravitational waves during the Inflationary epoch, remains a key objective for current and future CMB experiments (Zaldarriaga et al. 2004 [301], Seljak et al. 1997 [279], Zaldarriaga et al. 1997 [302]). However, these measurements are challenging due to the presence of polarized foreground emissions from our own Galaxy. Galactic thermal dust emission, as observed by experiments like Archeops [36], WMAP [125], and Planck [241], dominates on most of the frequency range and on most of the sky. Similarly, Galactic synchrotron radiation adds another layer of complexity. These foregrounds must be carefully characterized and accounted for, as they can obscure the faint cosmological signal and limit our ability to study the Inflationary epoch [242]. By refining our understanding of these foregrounds and developing techniques to mitigate their contribution, the next generation of CMB experiments will push the boundaries of our knowledge about the origins and evolution of the Universe.

On galactic scales, polarization measurements provide invaluable insights into the physics of the ISM. High-angular-resolution experiments have been designed to study the ISM, particularly focusing on molecular clouds where star formation occurs. The Galactic magnetic field plays a key role in these environments, comprising both a regular component, characterized by its intensity and direction, and a turbulent component. While the magnetic field's intensity can be directly measured using the Zeeman effect, synchrotron polarization measurements offer additional constraints on the strength and orientation of the regular component (Beck et al.

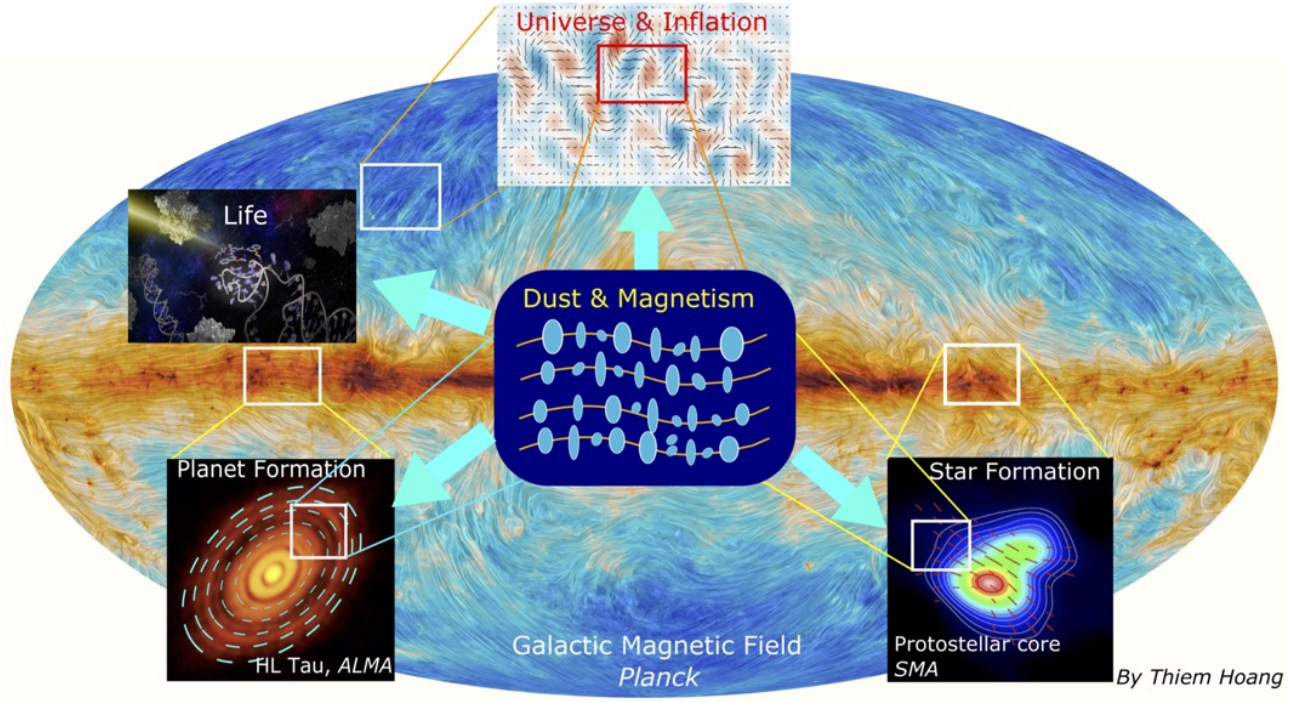

Figure 1.1: Global view of processes generating or involving polarization at galactic, extragalactic and cosmological scales. Image by Thiem Hoang: https://coma.kasi.re.kr/TAG/~thiemhoang/research.html.

2012a [33], Beck et al. 2012b [32], Beck et al. 2007 [30], Houde et al. 2013 [147]). Furthermore, dust polarization traces the direction of magnetic field lines within the Galactic thin disk, where most matter resides (Crutcher et al. 2012 [81]). Understanding the role of magnetic fields in star formation remains challenging, requiring high-resolution polarization-sensitive experiments.

1.2 Polarization at galactic scales

At galactic scales, various polarized emissions are observed at millimeter wavelengths. The polarization is primarily generated by synchrotron radiation and thermal dust emission, both tracing the interaction between interstellar matter and the Galactic magnetic field. Synchrotron emission dominates at low frequencies ($\nu \lesssim 70$ GHz) and follows a power-law spectrum, while thermal dust emission becomes prominent at higher frequencies ($\nu \gtrsim 100$ GHz) and can be modeled as a modified blackbody (see Fig. 1.3). Together, these components constitute the strongest polarized galactic foregrounds for CMB studies (Planck collaboration 2014e [238], Planck collaboration 2016 [242]). Such foregrounds contaminate the observed CMB signal and must be carefully accounted for. Fig. 1.2 illustrates the layered structure of the polarized signal reaching Earth: the primordial CMB components, then affected by cluster lensing, Galactic and extragalactic foregrounds, and finally the atmosphere.

Modeling and removing foregrounds is one of the main challenges of modern CMB polarization research. Since each component has a distinct spectral behavior, multi-frequency observations are the most effective way to separate them. Fig. 1.3 shows the brightness temperature rms as a function of frequency for temperature and polarization, highlighting the transition from synchrotron to dust domination.

A wide range of statistical techniques have been developed for component separation, including maximum likelihood approaches (Eriksen et al. 2006 [104]), blind methods such as the Internal Linear Combination (ILC) (Tegmark et al. 2003 [289]), and parametric modeling (Remazeilles

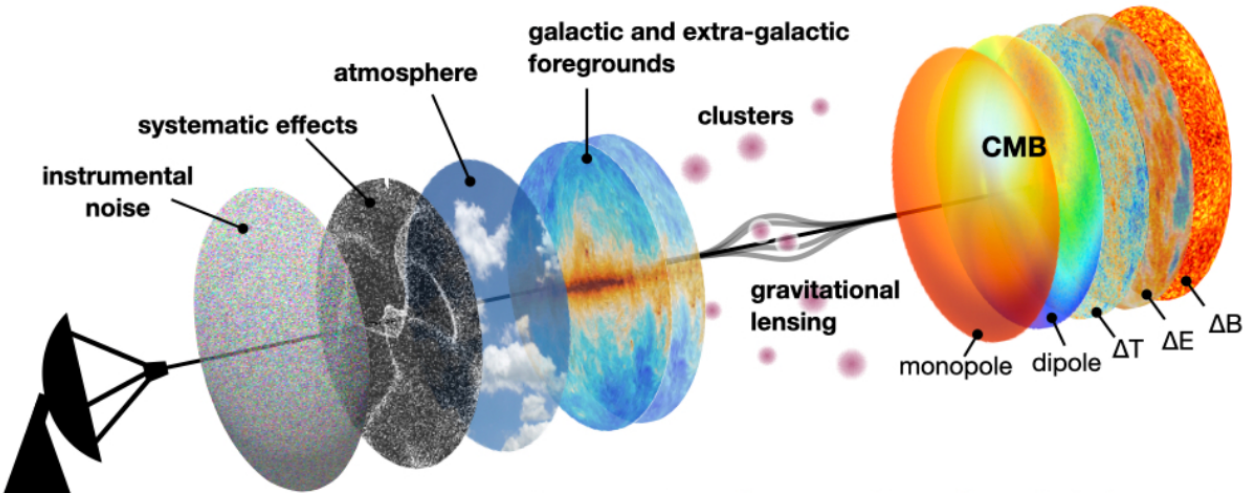

Figure 1.2: Typical layered structure of a cosmic signal seen by a ground-based observatory on Earth. Source: J. Errard (https://scipol.in2p3.fr/).

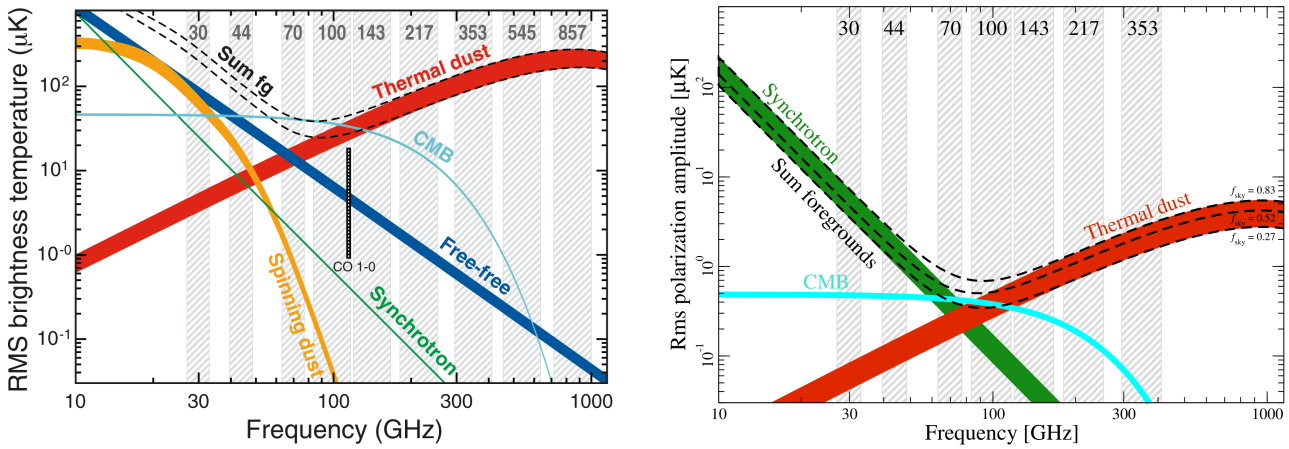

Figure 1.3: Brightness temperature rms as a function of frequency and astrophysical component for temperature (left) and polarization (right). For temperature, each component is smoothed to an angular resolution of 1° FWHM, and the lower and upper edges of each line are defined by masks covering 81 and 93% of the sky, respectively. For polarization, the corresponding smoothing scale is 40', and the sky fractions are 73 and 93%. Note that foreground rms values decrease nearly monotonically with sky fraction, whereas the CMB rms is independent of sky fraction, up to random variations. Source: Planck collaboration 2016 [242].

et al. 2011 [262]). However, the complexity of Galactic foregrounds is increased by their spatial variability: both the dust polarization fraction and its spectral index vary significantly across the sky, making global subtraction models insufficient (Planck collaboration 2018 [254]). Advanced methods incorporating spatially varying spectral parameters are thus essential (Errard et al. 2012 [105], Planck collaboration 2018 IV [248]).
In the following subsections, the physics of the main galactic foreground emissions is detailed.

1.2.1 Synchrotron emission

Synchrotron emission arises when relativistic charged particles, typically electrons, spiral around magnetic field lines. As they accelerate along curved trajectories, they emit electromagnetic radiation (Fig. 1.4) that is highly polarized and spans a broad range of frequencies.
This process is a key contributor to Galactic and extragalactic emissions at radio to millimeter

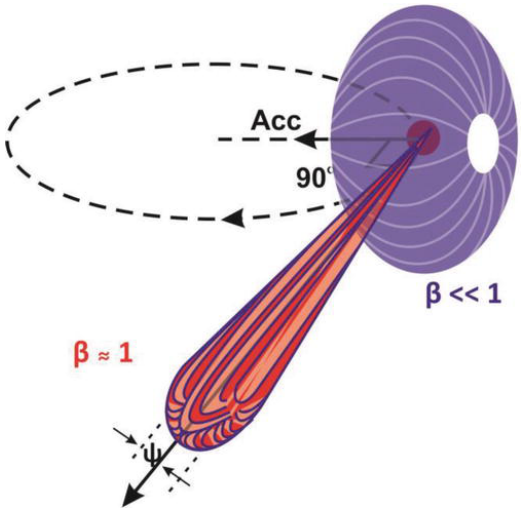

Figure 1.4: Radiation pattern of charged particles moving in a circular path: blue ($\beta \ll 1$) and red ($\beta \approx 1$). Here $\beta = v/c$ and ψ the emitted cone's solid angle (Bharti et al. 2019 [41]).

wavelengths, making it a critical foreground for cosmological studies, such as those targeting the CMB polarization.
The power radiated by a single electron undergoing synchrotron emission is given by (Rybicki et al. 1979 [271], Beck et al. 2012 [33]):

$$P = \frac{2}{3}\frac{e^4 B^2 \sin^2\alpha}{m_e^2 c^3}\gamma^2\,, \tag{1.1}$$

where e is the charge of the electron, B is the magnetic field strength, α is the pitch angle (the angle between the electron's velocity and the magnetic field), m_e is the electron mass, c is the speed of light, and γ is the Lorentz factor, defined as $\gamma = (1 - v^2/c^2)^{-1/2}$. The strong dependence on γ^2 highlights the importance of high-energy electrons in producing synchrotron radiation.
The synchrotron spectrum observed over a population of electrons with a power-law energy distribution, $N(E) \propto E^{-p}$, is characterized by a power-law frequency dependence:

$$S_\nu \propto \nu^{-\frac{p-1}{2}}\,, \tag{1.2}$$

where S_ν is the specific intensity at frequency ν, and p is the spectral index of the electron energy distribution. Typical values of p range from 2 to 3, resulting in synchrotron spectral indices β (where $S_\nu \propto \nu^\beta$) between -0.5 and -1.
The polarization fraction of synchrotron emission depends on the degree of ordering in the magnetic field. For a perfectly ordered magnetic field, the maximum polarization fraction is given by:

$$\Pi_{\max} = \frac{p+1}{p+7/3}. \tag{1.3}$$

For typical values of p, $\Pi_{\max}$ can reach up to $\sim 75\%$ (Kogut et al. 2007 [167]). However, in realistic astrophysical environments, turbulence and disordered magnetic fields reduce the observed polarization fraction.
Synchrotron emission dominates at low millimeter-wave frequencies ($\nu \lesssim 100$ GHz) and is a major foreground in studies of the CMB polarization. It also provides valuable information about the large-scale structure of the Galactic magnetic field and the energy distribution of relativistic electrons (Fig. 1.5).

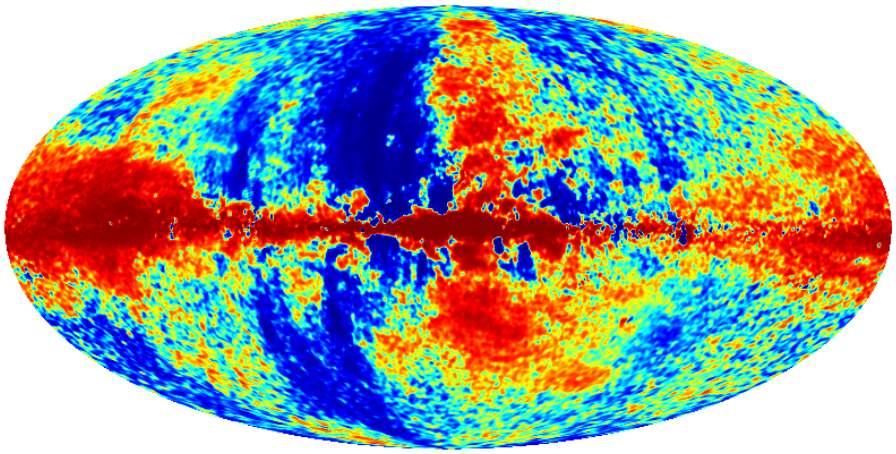

Figure 1.5: Synchrotron emission at 30 GHz from Planck 2018 results [249].

1.2.2 Free-free emission

The free-free emission, also known as thermal bremsstrahlung, occurs in HII regions, where free electrons scatter off ions without being captured. This emission process is central to regions surrounding massive stars, which form preferentially in dense cores of molecular clouds. When a star emits photons beyond the Lyman continuum limit ($\lambda < 912$ Å), it ionizes the surrounding gas. The ionized gas then re-emits the absorbed energy in the form of free-free radiation (Beckert et al. 2000 [34]). This occurs as charged particles, such as electrons, are accelerated upon encountering other charged particles. Consequently, free-free emission is expected in any environment with an ionized plasma.
The strength of this emission can be determined by the plasma's absorption coefficient k_ν, which depends on the electron density, ion density, temperature, and the Gaunt factor $h_{\rm gff}$. The absorption coefficient is related to these parameters as follows:

$$k_\nu \propto N_e N_i T_e^{-3/2}\, \nu^2 h_{\rm gff}\,, \tag{1.4}$$

where N_e is the electron density, N_i is the ion density, and T_e is the electron temperature (Nozawa et al. 1998 [220]). The emission's optical depth along the line of sight can be calculated by integrating the absorption coefficient. This optical depth is key in determining the nature of the emission. The transition from optically thick to thin behavior is governed by the frequency at which the optical depth equals unity. In the optically thick regime, the flux density increases as ν^2, while in the optically thin regime, it follows a weaker dependence, $\nu^{-0.1}$.
The emission measure (EM) of the ionized plasma, which is the integral of the electron and ion densities along the line of sight, can be used to estimate the plasma's density and, by extension, the relative age of the system. Younger systems with more massive stars typically have higher emission measures. The resulting radio spectrum from such emission thus provides valuable insight into the properties of the ionized gas surrounding young stellar objects, making it a crucial diagnostic tool in the study of high-mass star formation. The polarization of free-free emission is very weak; in fact, it is generally less than 1% when averaged over the full sky (Macellari et al. 2011 [187]).

1.2.3 Thermal dust emission

The interstellar medium (ISM) occupies the vast spaces between stars within galaxies like the Milky Way. It is composed of gas, dust, and charged particles, forming a complex and dynamic environment. The gas in the ISM is primarily hydrogen (around 70% by mass) and helium (approximately 28%), with trace amounts of heavier elements—often referred to as

"metals"—including carbon, silicon, nitrogen, and oxygen. Interstellar dust grains are micron- to sub-micron-sized solid particles, primarily composed of silicates, carbonaceous materials, and metallic compounds, often coated with icy mantles in dense regions (Wittet 2003 [297], Draine 2011 [94], Hildebrand 1988 [139]).
Dust grains are typically categorized into three primary types based on their size and composition: polycyclic aromatic hydrocarbons (PAHs), very small grains (VSGs), and big grains (BGs) (Meny et al. 2007 [197], Désert et al. 1990 [86]). PAHs, consisting of aromatic carbon molecules, have sizes of a few angstroms. VSGs are a few nanometers in size, while BGs range from tens of nanometers to micrometers. These grains play a significant role in shaping the ISM's observable properties by absorbing, scattering, and emitting electromagnetic radiation across a wide range of wavelengths.
Dust grains exhibit continuous thermal emission and tend to align in the presence of a magnetic field (Fig. 1.6). The alignment mechanism is primarily attributed to radiative torques (RATs), which align grains with their long axes perpendicular to magnetic field lines (Lazarian et al. 2007 [178], Andersson et al. 2015 [12]). This alignment results in polarized thermal emission at far-infrared (FIR) and sub-millimeter wavelengths, offering a valuable tracer of magnetic field geometry in the ISM. Observations by *Planck* have provided high-resolution maps of dust polarization, unveiling the magnetic field's structure across the Galactic plane (Fig. 1.7).

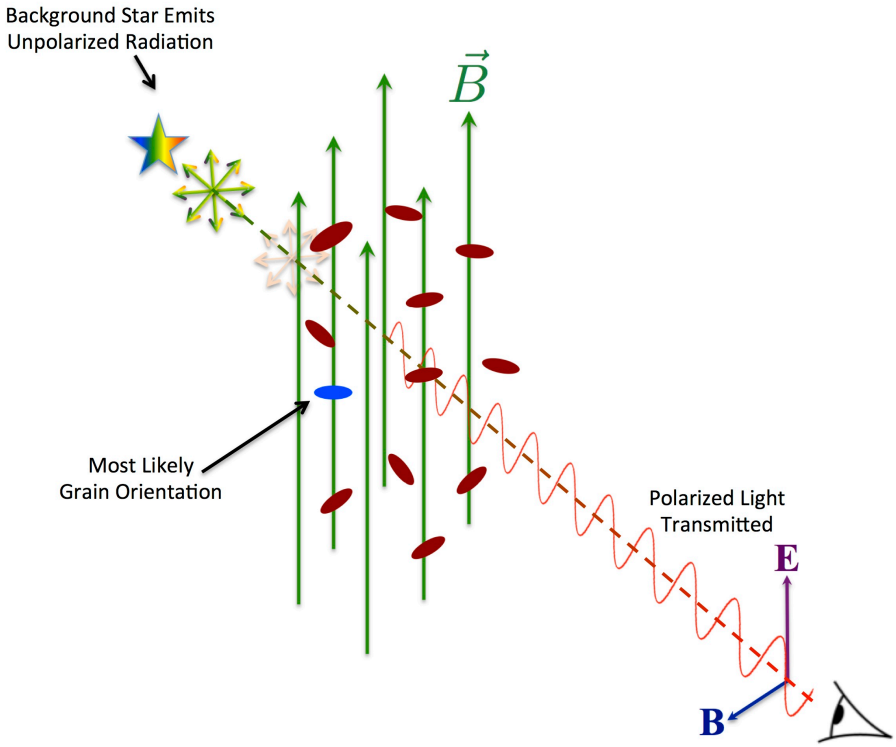

Figure 1.6: When aligned, elongated, grains intercept the light from a background star, the unpolarized light from the star acquires a polarization – typically at the level of a few percent. Drawing from B-G Andersson.

Dust grains are also responsible for interstellar extinction, which occurs as starlight is absorbed and scattered by dust along the line of sight. Extinction is wavelength-dependent, with smaller grains absorbing more effectively at shorter wavelengths, leading to a characteristic reddening of background starlight. The extinction curve, spanning from the infrared to ultraviolet, provides critical information about the grain size distribution and composition (Cardelli et al. 1989 [56], Draine 2011 [94]).
At longer wavelengths, interstellar dust re-emits absorbed energy as thermal radiation, peaking

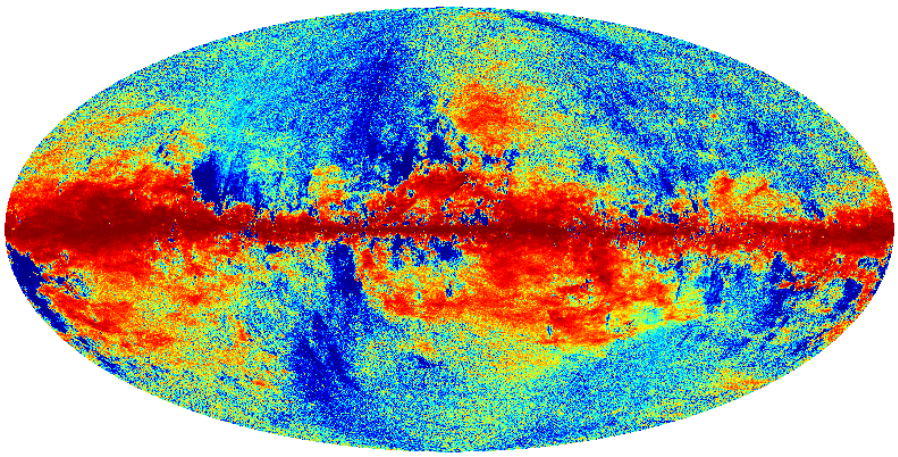

Figure 1.7: Polarized dust emission at 353 GHz from Planck 2018 results [249].

in the FIR and sub-millimeter range. This thermal dust emission dominates the diffuse Galactic emission at frequencies above 70 GHz (Fig. 1.3). The intensity of this emission is commonly modeled using a modified blackbody spectrum:

$$I_\nu = \kappa_\nu \, N_{\rm H} \, B_\nu(T_d) \,, \tag{1.5}$$

where κ_ν is the dust opacity, $N_{\rm H}$ is the hydrogen column density, T_d is the dust temperature, and $B_\nu(T_d)$ is the Planck function:

$$B_\nu(T) = \frac{2h\nu^3}{c^2} \frac{1}{e^{\frac{h\nu}{k_B T}} - 1} \,. \tag{1.6}$$

The dust opacity κ_ν scales with frequency as $\kappa_\nu \propto \nu^\beta$, where β is the spectral index, which depends on the grain composition and size distribution. Observations suggest typical values of $\beta \sim 1.5$–2.0 for diffuse interstellar dust (Planck collaboration 2014e [238]).

The ISM's gaseous component exists in various phases, ranging from cold molecular clouds to hot ionized regions. Cold molecular hydrogen clouds serve as reservoirs for star formation, collapsing under their own gravity to form stars. The presence of ionizing radiation from young, massive stars creates regions of ionized hydrogen (HII regions), where surrounding dust grains are heated and emit strongly in the IR (Kurtz et al. 1994 [174]). Additionally, the interplay between gas dynamics, magnetic fields, and turbulence influences the efficiency of star formation, making the ISM a rich laboratory for astrophysical processes.

In the microwave regime, thermal emission from interstellar dust grains, primarily composed of graphites, silicates, and PAHs, dominates the Galactic foreground at millimeter and sub-millimeter wavelengths. This emission is optically thin, with its intensity directly proportional to the column density of dust. The dust temperature T_d reflects a balance between heating by the interstellar radiation field and cooling via far-infrared emission. Observations by *Planck* and earlier missions have provided detailed maps of this emission, contributing to our understanding of Galactic foregrounds that contaminate measurements of the CMB (Planck collaboration 2014e [238], Gold et al. 2009 [125]).

The detailed study of interstellar dust, its alignment mechanisms, and its interaction with the radiation field not only enhances our understanding of Galactic processes but also helps mitigate foreground contamination in cosmological observations.

1.2.4 Spinning dust emission

Spinning dust emission originates from the rotational radiation of small dust grains, typically a few nanometers in size. These grains, often composed of polycyclic aromatic hydrocarbons (PAHs) or similar molecular structures, possess a permanent electric dipole moment μ due to the intrinsic dipole moment of molecules within the grain and uneven charge distribution. When these grains spin, interactions with the surrounding gas, radiation field, and other forces cause their angular velocity $\boldsymbol{\omega}$ to fluctuate. Assuming spherical grains for simplicity (neglecting wobbling), the power radiated by such a rotating dipole can be described by Larmor's formula:

$$P(\omega) = \frac{2}{3}\frac{\ddot{\mu}^2}{c^3} = \frac{2}{3}\frac{\omega^4 \mu_\perp^2}{c^3}, \tag{1.7}$$

where $\mu_\perp$ is the component of μ perpendicular to $\boldsymbol{\omega}$, and c is the speed of light. This power is emitted at the rotation frequency $\nu = \omega/(2\pi)$. The emissivity of spinning dust depends on the probability distribution function $f(\omega)$ for the rotation rate ω, as well as the number density of dust grains, both of which are functions of grain size. Furthermore, $f(\omega)$ is influenced by the ambient gas temperature, density, ionization fraction, and the local radiation field. Refined models (Hoang et al. 2010 [143]) account for the wobbling of non-spherical grains, where angular velocity varies even for a fixed angular momentum, resulting in radiation at multiple frequencies.

The spectral energy distribution of spinning dust emission typically peaks between 10–60 GHz, depending on the grain properties and environmental conditions. Despite being predominantly unpolarized, weak polarization arises due to partial alignment of spinning grains with the interstellar magnetic field. However, this alignment is less effective for small grains compared to larger grains responsible for thermal dust emission, leading to polarization fractions usually below 1% (Draine & Fraisse 2009 [95]). This polarization fraction depends on the magnetic field strength and orientation, as well as local variations in gas density and temperature.

Spinning dust emission represents a significant Galactic foreground in the microwave and millimeter wavelength regimes, particularly for studies of the CMB. While its low polarization fraction reduces direct interference with CMB polarization measurements, its spatial and spectral variability complicates its separation from other foregrounds, such as synchrotron and thermal dust emissions. Observations from WMAP and Planck have emphasized the need for accurate modeling of spinning dust to minimize contamination in cosmological analyses (Planck collaboration 2016 [244]).

On Galactic scales, spinning dust is most prominent in dense regions such as molecular clouds and star-forming areas, where interactions with the environment enhance rotational excitation. These regions provide valuable opportunities to study the physical mechanisms driving spinning dust emission and their dependence on local properties such as magnetic fields and radiation fields. Theoretical models (Draine & Lazarian 1998 [92] and [93]) have been instrumental in predicting the spectrum and polarization properties of spinning dust, while observations continue to refine these predictions.

1.3 Star formation

Polarization and magnetic fields play a pivotal role in understanding the processes governing star formation. Particularly in the context of high-mass star formation, these factors provide critical insights into the interplay of gravity, turbulence, and magnetic support within dense molecular clouds. The balance between these forces can be encapsulated by the mass-to-flux ratio, μ, which quantifies the relative importance of gravitational collapse and magnetic support:

$$\mu = \frac{\Sigma}{B/\sqrt{4\pi G}}, \tag{1.8}$$

where Σ is the column density of the gas, B is the magnetic field strength, and G is the gravitational constant. A supercritical cloud ($\mu > 1$) is dominated by gravity and prone to collapse, while a subcritical cloud ($\mu < 1$) is supported by magnetic fields against gravitational contraction. The concepts outlined in this section are of particular relevance for Chap. 5, where results on the role of magnetic fields in high-mass star formation will be presented.

1.3.1 Magnetic fields and star formation dynamics

Magnetic fields are key regulators in the star formation process, balancing gravitational collapse and providing structural support to molecular clouds. The interstellar magnetic field comprises two main components: an ordered field coherent in orientation and a turbulent field arising from random gas flows. Observations suggest that the ordered component dominates on large scales ($\sim 100\,\mathrm{pc}$), but gives way to turbulence at smaller scales ($\sim 1\,\mathrm{pc}$) (Heiles 2000 [134]).
Two primary theories describe the influence of magnetic fields on star formation. The first is *ambipolar diffusion*, which posits that neutral gas can condense gravitationally across magnetic field lines, reducing magnetic support in dense cores and enabling collapse (Mouschovias et al. 1999 [206]). This theory suggests that clouds evolve quasi-statically, with magnetic fields maintaining smooth morphologies. The second theory emphasizes *turbulence*, proposing that molecular clouds are transient phenomena driven by compressible turbulent flows (Elmegreen 2000 [100]). In this paradigm, turbulence dissipates rapidly, allowing cores to collapse dynamically. Observations indicate that both mechanisms may operate simultaneously, with the balance varying by region and scale (Lazarian et al. 2014 [179]).
The importance of magnetic fields is underscored by their energy density, which often rivals or exceeds gravitational and turbulent energies in the interstellar medium. This can be expressed through the Alfvén Mach number, $\mathcal{M}_A$, which quantifies the ratio of turbulent to magnetic energy:

$$\mathcal{M}_A = \frac{v_{\mathrm{turb}}}{v_A}, \tag{1.9}$$

where v_{turb} is the turbulent velocity and $v_A = B/\sqrt{4\pi\rho}$ is the Alfvén velocity, with B representing the magnetic field strength and ρ the gas density. Values of $\mathcal{M}_A \ll 1$ indicate magnetic dominance, while $\mathcal{M}_A \gg 1$ suggests turbulence-driven dynamics. Understanding the interaction between these forces remains a fundamental challenge in astrophysics (Crutcher 2010 [80]).

1.3.2 Polarization as a diagnostic tool

Polarization provides a powerful observational probe of magnetic fields in star-forming regions. Dust grains aligned by the interstellar magnetic field emit polarized light, as detailed in the previous section, which traces the field's morphology. Optical and near-infrared polarization reveal magnetic fields in low-density regions, while sub-millimeter and far-infrared observations, such as those from Planck and Herschel, probe denser environments (Planck collaboration 2016a [243], Palmeirim et al. 2013 [229]).
The alignment of dust grains, often driven by radiative torques, results in polarized emission perpendicular to the magnetic field (Cho et al. 2005 [66]). In high-density regions, the efficiency of grain alignment decreases due to reduced radiation, leading to the "polarization hole" effect (Hull et al. 2014 [152]). The degree of polarization p can be related to the grain alignment

efficiency and the strength of the magnetic field through the following equation:

$$p = \frac{I_{\rm pol}}{I_{\rm tot}} = \frac{\epsilon B}{B_{\rm tot}}\,, \tag{1.10}$$

where $I_{\rm pol}$ is the polarized intensity, $I_{\rm tot}$ is the total intensity, ϵ is the alignment efficiency of the dust grains, B is the local magnetic field strength, and $B_{\rm tot}$ is the total magnetic field strength. This equation links the observed polarization to the underlying magnetic field structure, allowing us to infer the field strength and orientation in different regions.
By mapping polarization, we can infer the strength and orientation of magnetic fields, as well as their role in shaping filamentary structures within molecular clouds (Arzoumanian et al. 2011 [16]).
Recent advancements in polarimetric observations have revealed a complex interplay between magnetic fields and turbulence, highlighting the need for multi-scale analyses to disentangle their respective contributions to star formation (Pereyra et al. 2004 [234]). This is precisely one of the main goals of the project to observe Westerhout 43 (W43) with the NIKA2 camera, presented later in Chap. 5.

1.3.3 High-mass star formation and magnetic fields

High-mass star formation (10–100 $M_\odot$) is a pivotal yet poorly understood process in astrophysics, distinguished by its profound impact on the surrounding interstellar medium and broader galactic environment. Massive stars shape their surroundings through intense radiation, powerful winds, and supernovae, driving large-scale feedback mechanisms that regulate star formation and contribute to the chemical enrichment of galaxies (Soler et al. 2013 [282], Kennicutt et al. 1998 [164]). Their formation is further linked to the evolution of molecular clouds and the generation of complex organic molecules, influencing the initial conditions for planetary system formation (Tan et al. 2014 [288]). Unlike their low-mass counterparts, massive stars face unique challenges during their formation, such as overcoming significant radiation pressure, accreting material efficiently despite strong outflows, and forming in regions of extreme densities and turbulence (Zinnecker et al. 2007 [303], Motte et al. 2018 [205]).
Magnetic fields are believed to play a crucial role in high-mass star formation, impacting the dynamics of gravitational collapse, regulating angular momentum transport, and shaping the morphology of dense cores (McKee et al. 2007 [195]). Observational studies have shown that magnetic field strength increases with gas density (Crutcher 1999 [79]), suggesting a critical influence on the fragmentation of molecular clouds and the stability of massive clumps (Pillai et al. 2015 [236]). This correlation becomes particularly significant in regions of high-mass star formation, where densities exceed 10^9 cm^{-3} and the effects of magnetic pressure are expected to counteract gravitational forces (Le Gouellec et al. 2024 [180]). The role of magnetic fields in channeling accretion flows and shaping outflows remains an open question, requiring high-resolution observations to disentangle their effects from turbulence and feedback processes (Girart et al. 2009 [124], Hull et al. 2019 [151]).
The observational project presented in Chap. 5, aims to investigate these magnetic effects in a region of active high-mass star formation, W43. Using a state-of-the-art polarization-sensitive instrument such as NIKA2, it seeks to quantify the strength and morphology of magnetic fields in extreme environments, providing critical insights into their role in shaping the formation and evolution of massive stars.

1.4 Extragalactic polarization

Polarization phenomena from extragalactic sources offer a unique perspective on the large-scale structure of the Universe and the physical processes shaping it. While these effects are not the primary focus of this thesis, they provide crucial insights and serve as important testbeds for high-precision polarization measurements and calibration techniques. These concepts directly inform the methodologies and calibration efforts discussed in subsequent chapters, particularly in the context of calibration methods (see Chap. 2, Subsec. 2.6.3).

1.4.1 Active Galactic Nuclei (AGN)

Quasars, a subset of AGNs, represent the most luminous and distant galaxies in the observable Universe (Netzer 2013 [216]). These cosmic powerhouses are characterized by Supermassive Black Holes (SMBH) at their cores, surrounded by accretion disks composed of interstellar matter. The extreme temperatures of these disks result in emission across a broad spectrum, from radio to X-ray wavelengths (Netzer 2013 [216]).
The central engines of AGNs are capable of generating highly collimated jets, where particles are accelerated to relativistic velocities, likely due to the black hole's magnetic field (Comastri et al. 2007 [70]). As these particles traverse galactic and extragalactic magnetic fields and media, they produce radiation across nearly the entire electromagnetic spectrum. A significant portion of this emission is synchrotron radiation, previously discussed. While synchrotron emission is primarily responsible for radio signals, it can also produce optical and X-ray emission in the most powerful jets (Lacki et al. 2010 [175], Hlavacek-Larrondo et al. 2012 [142]).
The observed properties of AGN and quasars are heavily influenced by the orientation of their central engine and jet relative to our line of sight. Quasars are believed to be AGNs with jets nearly aligned with our perspective, while blazars represent the extreme case where the jet is almost exactly aligned with our line of sight (Urry et al. 1995 [295]).
Short millimeter observations of radio-loud AGN provide valuable insights into the physics of their synchrotron-emitting relativistic jets, which are the primary source of radio and millimeter polarized emission (Krolik 1999 [173]). At these wavelengths, AGN jets and their emission cores experience significantly less Faraday rotation and depolarization compared to longer wavelengths (Jorstad et al. 2005 [156]). Moreover, millimeter emission originates from the compact innermost regions of the jets, which are often opaque at longer wavelengths due to synchrotron self-absorption (Omont et al. 2001 [223]).
The spectral behavior of AGNs, initially thought to follow a simple power law, is now understood to be more complex. The flux density F_ν is related to the frequency by the following relation:

$$F_\nu \propto \nu^{-\alpha}\,, \tag{1.11}$$

where α is the spectral index, typically ranging from 0.5 to 2 and increasing with frequency. At a certain transition frequency, the spectrum experiences a turnover, following a $\nu^{5/2}$ relationship (corresponding to $\alpha = -2.5$). This phenomenon occurs due to synchrotron self-absorption, where the plasma of spiraling electrons becomes opaque to its own synchrotron radiation.

1.4.2 Faraday rotation

Faraday rotation is a critical phenomenon in the study of polarization, particularly in the context of astrophysical magnetic fields. It occurs when linearly polarized electromagnetic waves propagate through a magnetized plasma, resulting in the rotation of the plane of polarization. This effect is proportional to the square of the wavelength of the radiation, making it especially

significant at long wavelengths such as those in the radio and millimeter regimes. The amount of rotation is given by the rotation measure (RM), which depends on the line-of-sight magnetic field strength, the electron density, and the path length through the plasma (Burn et al. 1966 [52], Beck 2009 [31]). Mathematically, the angle of rotation $\Delta\phi$ is expressed as:

$$\Delta\phi = \mathrm{RM} \cdot \lambda^2 \,, \tag{1.12}$$

where λ is the wavelength, and RM is the rotation measure, defined as:

$$\mathrm{RM} = 0.812 \int n_e B_{\parallel} \, dl \quad \mathrm{rad/m^2} \,. \tag{1.13}$$

Here, n_e is the electron density in cm^{-3}, $B_{\parallel}$ is the magnetic field strength along the line of sight in μG, and dl is the path length in parsecs.
Faraday rotation provides a powerful diagnostic tool for probing magnetic fields in various astrophysical environments, such as the interstellar medium (ISM), galaxy clusters, and even the large-scale structure of the Universe. By studying the rotation of polarization in radio waves emitted from distant sources, we can reconstruct the magnetic field structure along the line of sight and distinguish between different contributions, such as synchrotron emission and thermal plasma effects (Han 2006 [129]). Additionally, in the cosmological context, Faraday rotation has been proposed as a means to detect primordial magnetic fields and constrain their properties (Kosowski 1996 [171], Pogosian et al. 2018 [256]). Thus, understanding and modeling Faraday rotation is an essential step in disentangling the contributions to polarized signals across galactic, extragalactic, and cosmological scales.

1.5 The ΛCDM and Hot Big Bang cosmological models

At the foundation of cosmology lies a set of fundamental equations derived from the theory of General Relativity. One of the most significant is the Friedmann-Lemaître-Robertson-Walker (FLRW) metric, which describes a homogeneous, isotropic, and expanding Universe (Melia et al. 2022 [196]):

$$ds^2 = -c^2 dt^2 + a(t)^2 \left[dr^2 + S_k(r)^2 d\Omega^2 \right] \,, \tag{1.14}$$

where $a(t)$ is the scale factor describing the Universe's expansion, $S_k(r)$ accounts for spatial curvature, and k determines the curvature type ($k = 0$ for flat, $k = +1$ for closed, $k = -1$ for open).
The Hubble constant, H_0, which quantifies the current expansion rate of the Universe, has been measured using several independent methods. Local measurements based on type Ia supernovae (SN) yield (Riess et al. 2022 [263]):

$$H_0 \simeq 73.04 \pm 1.04 \ \mathrm{km\,s^{-1}\,Mpc^{-1}} \,, \tag{1.15}$$

while observations of the CMB by the *Planck* satellite, assuming a ΛCDM cosmology, favor a lower value (Planck collaboration 2018 VI [251]):

$$H_0 \simeq 67.4 \pm 0.5 \ \mathrm{km\,s^{-1}\,Mpc^{-1}} \,. \tag{1.16}$$

The discrepancy between these two measurements is commonly referred to as the "Hubble tension" and remains an active topic of research, with possible explanations ranging from systematic uncertainties to new physics beyond the standard cosmological model. Considering the first of the two for example, we define the Hubble distance as:

$$d_{H_0} = \frac{c}{H_0} \approx 4106 \text{ Mpc}\,. \tag{1.17}$$

The Friedmann equation, which governs the Universe's dynamics, is expressed as:

$$\frac{\ddot{a}}{a} = -\frac{4\pi G}{3}(\rho + 3p) + \frac{\Lambda}{3}\,, \tag{1.18}$$

where ρ is the mass density, p is the pressure, and Λ is the cosmological constant. It is important to note the opposite signs of the gravitational and dark energy terms, which show how they have opposite contribution to the expansion of the Universe. These equations form the backbone of the ΛCDM model, the standard framework for cosmology (Friedmann 1922 [119]; Friedmann 1924 [120]; Bernal 2019 [37]).
The ΛCDM model posits that the Universe is composed of three primary components: dark energy (associated with Λ, accounting for 70% of the entire content of the Universe), cold dark matter (CDM, the 27%), and ordinary matter (the 3%). This model successfully explains several key observations, including the characteristics of the CMB, the large-scale distribution of galaxies, the primordial abundances of light elements and the accelerating expansion of the Universe. Despite its successes, the ΛCDM model continues to be refined through ongoing observations and theoretical developments, offering insights into the fundamental nature of the cosmos.

1.5.1 The Cosmic Microwave Background

The Standard Cosmological Model is intrinsically connected to another fundamental hypothesis regarding the nature and evolution of the Universe, namely the Hot Big Bang model (Peebles 1993 [232]). This model, which is widely accepted today due to substantial experimental evidence, postulates that the Early Universe underwent a radiation-dominated era (Kolb 1990 [169]). One of the primary pieces of experimental evidence supporting this model is the presence of the diffuse Cosmic Microwave Background, which we will now introduce. A visual representation of the major milestones in the evolution of the Universe since the Big Bang, approximately 13.8 billion years ago, is shown in Fig. 1.8.

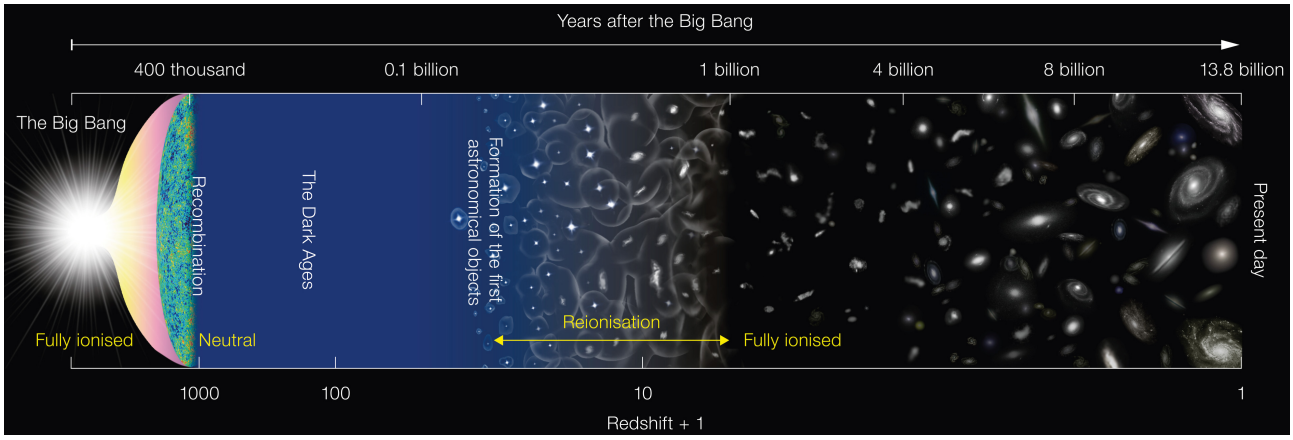

Figure 1.8: Diagram illustrating the key stages in the evolution of the Universe since the Big Bang, about 13.8 billion years ago. Note that the diagram is not to scale. Source: ESO (https://www.eso.org/public/images/eso1620a/).

Thermal properties of the CMB The CMB is a diffuse, isotropic radiation in the microwave frequency range, thought to be the remnant radiation from the Big Bang. Observations

of the most distant regions of the observable Universe reveal a nearly homogeneous Universe, with only small deviations from uniformity. These subtle inhomogeneities, which have been mapped with remarkable precision, exhibit patterns that, while nontrivial, are surprisingly simple. According to the Standard Cosmological Model, these inhomogeneities arise from primordial quantum fluctuations imprinted on the last scattering surface during the early stages of the Universe's evolution. The temperature of the CMB is $T_0 = 2.7255 \pm 0.0006$ K (Fixen 2009 [115]), and the current energy density of the CMB is given by:

$$\epsilon_{\gamma,0} = \alpha T_0^4 = 0.2606 \text{ MeV m}^{-3} . \tag{1.19}$$

This energy density represents only a small fraction (approximately one part in 19,000) of the current critical density of the Universe. However, due to the low energy of individual CMB photons (on the order of 10^{-4} eV), the number density of CMB photons is significantly high:

$$n_{\gamma,0} = 4.107 \times 10^8 \text{ m}^{-3} . \tag{1.20}$$

Following the initial detection of the CMB by Penzias and Wilson (Penzias et Wilson 1965 [233]), significant efforts were made to refine the spectrum of the CMB. At the time, proper instrumentation was still under development, and it was not yet known that dry sites were crucial for accurate detection of the CMB's wavelength. The CMB spectrum was first measured with high accuracy across a broad range of wavelengths by the Cosmic Background Explorer (COBE) satellite, launched in 1989 (Boggess 1992 [45]). Subsequent CMB measurements were made with higher angular resolution by the Wilkinson Microwave Anisotropy Probe (WMAP), launched in 2001 (Bennett et al. 2013 [35], Kogut et al. 2007 [167]), and the Planck satellite, launched in 2009 (Planck collaboration 2014 [239]). A comparison of the CMB anisotropy maps produced by these missions is shown in Fig. 1.9.

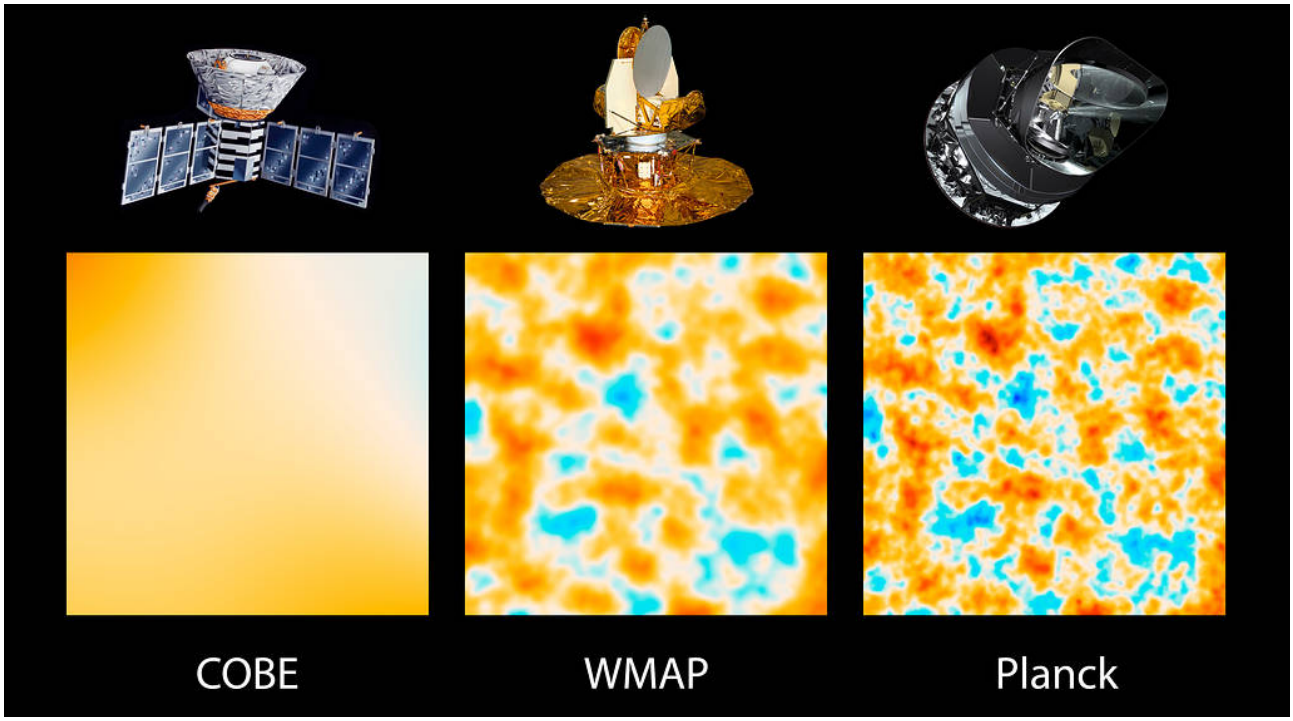

Figure 1.9: Graphic illustrating the evolution of satellites designed to measure the CMB thermal radiation. Source: NASA/JPL - Caltech/ESA (https://www.nasa.gov/image-article/universe-comes-into-sharper-focus/).

Several key conclusions can be drawn from the observations of the CMB: the first is that

the CMB spectrum follows a nearly perfect black-body distribution (Fixsen et al. 1997 [116], Mather et al. 1994 [191]). Deviations from a perfect black body model are present, but are approximately of 10^{-4}. The second key result is that the temperature anisotropies in the CMB, as observed from the Planck map, are of very small amplitude. The dimensionless temperature fluctuation, expressed as a function of the angular coordinates θ and ϕ, is:

$$\frac{\delta T}{T_0}(\theta, \phi) \equiv \frac{T(\theta, \phi) - T_0}{T_0} \,. \tag{1.21}$$

After removing the Doppler dipole due to the relative motion of the instrument with respect to a reference frame in which the CMB is isotropic, the root mean square temperature fluctuation is:

$$\left\langle \left(\frac{\delta T}{T_0} \right)^2 \right\rangle^{1/2} = 1.1 \times 10^{-5} \,. \tag{1.22}$$

This extremely small amplitude indicates that the early Universe was remarkably homogeneous and isotropic, with density fluctuations at the level of roughly one part in 100,000.
To study CMB anisotropies and constrain the cosmological model, we compute their angular power spectrum, C_ℓ, as:

$$C_\ell = \frac{1}{2\ell + 1} \sum_{m=-\ell}^{\ell} |a_{\ell m}|^2 \,, \tag{1.23}$$

with $a_{\ell m}$ being the spherical harmonic coefficients of the CMB temperature anisotropy field, defined as

$$a_{\ell m} = \int_{\mathbb{S}^2} d\hat{n}\, Y^*_{\ell m}(\hat{n})\, \frac{\delta T(\hat{n})}{T_0} \,, \tag{1.24}$$

where $\delta T(\hat{n})/T_0$ denotes the fractional temperature fluctuation in the direction $\hat{n}$, and $Y_{\ell m}(\hat{n})$ are the spherical harmonics. The power spectrum C_ℓ therefore quantifies the variance of temperature fluctuations on angular scales of order $\theta \sim \pi/\ell$.
The CMB temperature power spectrum is shown in Fig. 1.11, and this principle will be applied to polarization later on.

Recombination and decoupling To fully comprehend why the existence of the CMB serves as evidence for the Hot Big Bang model, it is necessary to qualitatively describe the conditions prevailing at the epoch when CMB photons last scattered. The presence of the CMB naturally follows from the assumption that the Early Universe was in an extremely hot, dense, and opaque state. This evolution can be understood by distinguishing three key epochs in the early Universe. The first phase, known as *recombination*, corresponds to the transition of the baryonic component from an ionized to a neutral state. This process occurred at a redshift of approximately $z_{\rm rec} \approx 1380$, when free electrons and protons combined to form neutral hydrogen. As a result, the Universe became increasingly transparent to radiation. Following this, a phase known as *photon decoupling* took place, during which the interaction rate of photons with free electrons became lower than the expansion rate of the Universe, defined by the Hubble parameter H. Mathematically, this condition can be expressed as:

$$\Gamma_{\gamma e} < H \,, \tag{1.25}$$

where $\Gamma_{\gamma e}$ represents the Compton scattering rate. This inequality implies that the probability of further photon-electron interactions decreased significantly as the Universe expanded.

Immediately after this phase, at a redshift of $z_{\rm LS} \approx 1090$, photons experienced their *last scattering* and subsequently began to propagate freely through the Universe.
The anisotropies observed in the CMB are primarily a consequence of the gravitational effects associated with density fluctuations in the distribution of non-baryonic dark matter (Peebles 1968 [231]). A CMB photon climbing out of a gravitational potential well loses energy, leading to a redshifted, and hence colder, appearance. Conversely, a photon falling into a potential well gains energy and appears blueshifted, or hotter. This effect, described by the Sachs-Wolfe relation (Sachs et Wolfe 1967 [272]), can be formulated as:

$$\frac{\Delta T}{T} \approx -\frac{\Phi}{c^2}\,, \tag{1.26}$$

where Φ represents the gravitational potential. This relation highlights the direct imprint of primordial density fluctuations on the CMB temperature anisotropies.
Despite the remarkable success of the Hot Big Bang model in explaining the presence of the CMB, several fundamental issues remain unresolved. Among them are the flatness problem, the horizon problem, and the monopole problem, each of which was a challenge that led to the development of the Inflationary paradigm.

1.5.2 The limits of the standard model

The standard cosmological model encounters several conceptual challenges, including the flatness, horizon, and monopole problems.
The flatness problem (Helbig et al. 2020 [136]) arises from the observation that the Universe is nearly spatially flat today. This implies an extraordinary fine-tuning of the initial conditions. The curvature parameter Ω must have been extraordinarily close to 1 in the early Universe. For instance, at the Planck time, deviations from flatness would have been on the order of 10^{-62}. Without a mechanism to dynamically drive Ω toward unity, such fine-tuning seems unnatural.
The horizon problem (Lakhal et al. 2019 [176]) highlights the surprising uniformity of the Universe's temperature, as observed in the CMB, across regions that were causally disconnected at the time of last scattering. According to the original Big Bang scenario, regions separated by more than 2° in the sky today were not in causal contact during recombination. Yet, these regions exhibit nearly identical physical properties, suggesting the need for a mechanism to establish such homogeneity in the early Universe.
The monopole problem (Liu 1987 [184]) stems from the lack of observed magnetic monopoles, despite theoretical predictions from Grand Unified Theories (GUTs). These theories suggest that monopoles would have formed in abundance during a phase transition around 10^{-36} seconds after the Big Bang. The expected density of monopoles today, based on these predictions, vastly exceeds observational constraints, presenting a significant discrepancy between theory and observation.
The standard cosmological model also faces the challenge of explaining the origin of the primordial density fluctuations that eventually grew into galaxies, clusters, and the large-scale structure observed today. In the Hot Big Bang framework, the early Universe is assumed to be nearly perfectly homogeneous and isotropic, which leaves no natural mechanism for generating the tiny inhomogeneities required to seed structure formation. Observations of the CMB, however, reveal temperature anisotropies at the level of $\delta T/T \sim 10^{-5}$, corresponding to initial density contrasts of similar magnitude. Without a physical process to generate these perturbations, the formation of cosmic structures remains unexplained, highlighting a crucial limitation of the standard model (Mukhanov et al. 1981 [209]).
These issues collectively point to the need for extensions or modifications to the standard Hot Big Bang model to address these foundational problems.

1.5.3 The Inflation solution

Inflation is a theoretical framework in which a scalar field, the Inflaton ϕ, drives a brief period of accelerated expansion in the early Universe (Guth 1981 [128]). While the Inflaton slowly rolls along its potential, its nearly constant vacuum energy causes the scale factor to grow exponentially:

$$a(t) \propto e^{H_i t}, \tag{1.27}$$

where H_i is the Hubble parameter during Inflation. This rapid expansion has several profound consequences. It naturally drives the density parameter Ω toward unity, resolving the flatness problem; it enlarges the horizon so that regions of the CMB that were initially causally disconnected can equilibrate, solving the horizon problem; and it dilutes hypothetical relics such as magnetic monopoles to undetectable levels, addressing the monopole problem.
A further crucial outcome of Inflation is the generation of the primordial density perturbations that seed cosmic structure. Quantum fluctuations of the Inflaton field are stretched to cosmological scales by the rapid expansion, producing small inhomogeneities in the energy density. These fluctuations later grow under gravitational instability to form galaxies, clusters, and the large-scale structure observed in the Universe today. Inflation ends when the Inflaton reaches the minimum of its potential and transitions to its true vacuum state, triggering reheating, during which the vacuum energy is converted into relativistic particles and the Universe returns to a thermal state. In this way, Inflation not only resolves the classical cosmological problems but also provides a natural mechanism for the origin of the initial density perturbations. Observational tests of Inflation primarily focus on the polarization patterns of the CMB, which carry imprints of these primordial fluctuations (Sec. 1.6).

1.6 Polarization at cosmological scales

One of the fundamental aspects of modern cosmology is the study of CMB polarization at cosmological scales, which provides crucial insights into the Early Universe and the fundamental physics governing its evolution. In this section, we will delve into the mechanisms responsible for generating CMB polarization, focusing on the role of Thomson scattering, the formalism of spherical harmonics decomposition, and the classification of polarization patterns into E and B modes. Additionally, we will discuss cosmic birefringence, a phenomenon that could introduce new physics by rotating the plane of polarization as CMB photons propagate through the Universe.

1.6.1 CMB polarization

In addition to the characteristic temperature anisotropies observed in the CMB, a small fraction of CMB photons also exhibit partial linear polarization (Zaldarriaga 1997 [300], Hu 1997 [149], Kosowsky 1996 [172]). In the case of the CMB, the observed linear polarization implies that the electric field component is confined to a single plane along the direction of propagation. The polarization pattern of the CMB is intricately linked to the temperature anisotropies, as the degree of linear polarization is directly related to the quadrupole moment of the photon distribution at the time of last scattering (Kamionkowski et al. 1997 [159], Seljak 1997 [278]). These quadrupole anisotropies arise due to the diffusion of photons at the end of the recombination epoch. During recombination, as baryons transition from an ionized to a neutral state, protons capture electrons to form neutral hydrogen atoms. However, recombination does not occur instantaneously; rather, it unfolds over a finite timescale, during which Thomson scattering remains significant. Consequently, photons undergo a residual random walk due to interactions

with free electrons (Kaiser 1983 [158]).
Although the scattering rate declines rapidly, it does not vanish instantaneously, allowing photons to travel a characteristic diffusion length before decoupling completely (Bond et al. 1984 [47]). If this diffusion length is comparable to the wavelength of the primordial perturbations, thermal mixing between hot and cold photon populations ensues, leading to a suppression of small-scale anisotropies. Since polarization is sourced by the quadrupole anisotropy in the photon temperature distribution, the polarization power spectrum exhibits a characteristic peak near the photon diffusion scale (Bond et al. 1996 [46], Dodelson et al. 2003 [88]).

Thomson scattering In the early phase of the Universe, photons and baryons were coupled in a sort of primordial plasma. Photons continue to undergo Thomson scatterings onto the electrons. Until the end of recombination, nothing significant happens, because the scattering rate is so high that whatever effect might be induced by these scatterings, soon vanishes out. However, by the end of recombination, the scattering rate is small enough to leave a net effect onto the CMB photons that free-stream away. The variation of the cross-section of Thomson scattering with respect to the solid angle is given by:

$$\frac{d\sigma_T}{d\Omega} \propto |\hat{\epsilon} \cdot \hat{\epsilon}'|\,, \tag{1.28}$$

where $\hat{\epsilon}$ and $\hat{\epsilon}'$ are the incoming and outgoing directions of light respectively. Therefore, the highest scattering probability is for an angle of 90° between the incoming and outgoing direction. The incident light sets up oscillations of the target electron in the direction of the electric field vector, so basically it induces a polarization. Of course, there is not only one photon scattering over an electron, but photons can come from many directions. If the incoming radiation is isotropic, the orthogonal polarization states from incident directions balance out and so the outgoing radiation is unpolarized. On the other hand, if the incident radiation field possesses a quadrupolar variation in intensity, we obtain a linear polarization of the outgoing radiation (Fig. 1.10 for a visual representation).

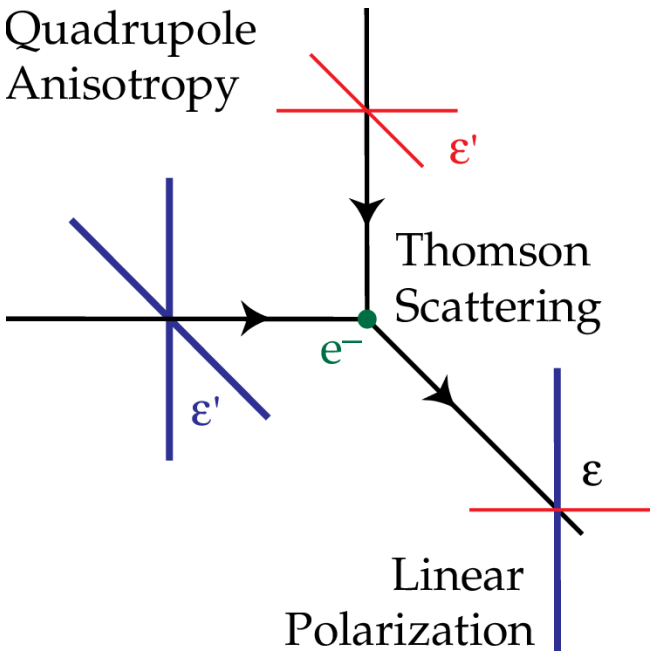

Figure 1.10: Thomson scattering of radiation with a quadrupole anisotropy that generates linear polarization. Source: Hu et al. 2002 [148].

Angular power spectra polarization In order to describe the polarization of the CMB in a formalism that is independent of the choice of reference frame, it is convenient to expand the polarization field in terms of spherical harmonics, as is done for temperature anisotropies (Subsec. 1.5.1). While the Stokes parameters are commonly used to quantify the polarization state of electromagnetic radiation, their direct usage is reference-frame dependent. A more detailed discussion on the Stokes formalism and its applications will be provided in Chap. 2.
The Stokes parameters Q and U transform under a rotation of the local reference frame by an angle ψ as

$$Q \pm iU \quad \longrightarrow \quad e^{\mp 2i\psi}\,(Q \pm iU)\,, \tag{1.29}$$

which shows that they behave as spin-± 2 quantities.
To decompose these fields into multipole moments, analogously to the temperature field, we make use of spin-weighted spherical harmonics, which generalize the usual spherical harmonics to account for the spin of the field. They form a complete orthonormal basis for each spin value s. The polarization field can thus be expanded as

$$(Q \pm iU)(\hat{n}) = \sum_{\ell m} {}_{\pm 2}a_{\ell m}\, {}_{\pm 2}Y_{\ell m}(\hat{n})\,, \tag{1.30}$$

with ${}_{\pm 2}Y_{\ell m}$ the spin-2 spherical harmonics. The expansion coefficients are obtained by projection:

$${}_{\pm 2}a_{\ell m} = \int d\hat{n}\, {}_{\pm 2}Y^{*}_{\ell m}(\hat{n})\,(Q \pm iU)(\hat{n})\,. \tag{1.31}$$

It is convenient to combine the coefficients ${}_{\pm 2}a_{\ell m}$ into two scalar (spin-0) fields, which are invariant under rotations. These are defined as

$$\begin{aligned} a^{E}_{\ell m} &\equiv -\tfrac{1}{2}\left({}_{2}a_{\ell m} + {}_{-2}a_{\ell m}\right)\,, \\ a^{B}_{\ell m} &\equiv -\tfrac{1}{2i}\left({}_{2}a_{\ell m} - {}_{-2}a_{\ell m}\right)\,. \end{aligned} \tag{1.32}$$

These combinations correspond, respectively, to the E-mode (gradient-like) and B-mode (curl-like) components of the polarization field, and play a role analogous to the temperature multipoles $a^{T}_{\ell m}$.
The statistical properties of the CMB anisotropies and polarization are then encoded in their angular power spectra, defined as

$$\langle a^{X}_{\ell m}\, a^{Y*}_{\ell' m'} \rangle = C^{XY}_{\ell}\, \delta_{\ell \ell'} \delta_{m m'}\,, \tag{1.33}$$

with $X, Y \in \{T, E, B\}$. This leads to six possible spectra: C^{TT}_{ℓ}, C^{EE}_{ℓ}, C^{BB}_{ℓ}, C^{TE}_{ℓ}, C^{TB}_{ℓ}, and C^{EB}_{ℓ}. In the standard cosmological model, statistical isotropy and parity conservation imply that only TT, EE, BB, and TE can be nonzero. Among these, the BB spectrum is expected to be much smaller than the others, arising either from gravitational lensing of E-modes or from a possible primordial contribution due to inflationary gravitational waves (Fig. 1.11).
More explicitly, the auto-spectra of E- and B-modes, which describe the variance of the polarization field at a given angular scale ℓ, are given by

$$C^{EE}_{\ell} = \frac{1}{2\ell+1} \sum_{m=-\ell}^{\ell} \left| a^{E}_{\ell m} \right|^2, \quad C^{BB}_{\ell} = \frac{1}{2\ell+1} \sum_{m=-\ell}^{\ell} \left| a^{B}_{\ell m} \right|^2, \tag{1.34}$$

where $a^{E}_{\ell m}$ and $a^{B}_{\ell m}$ are the multipole coefficients of the E- and B-modes, respectively.

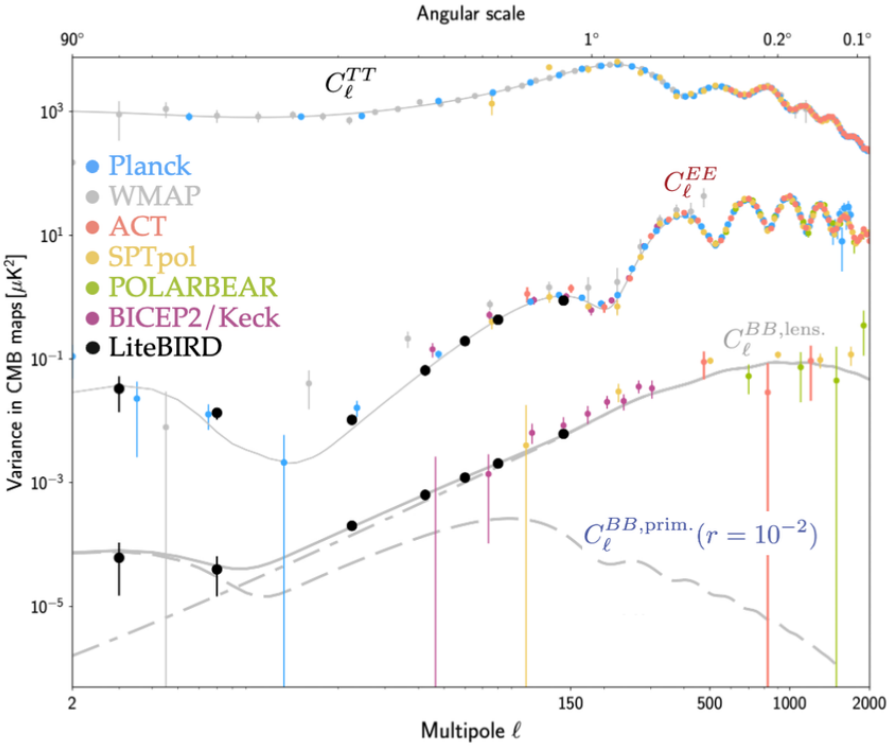

Figure 1.11: Angular power spectra of CMB anisotropies from various experiments and forecast for LiteBIRD. The top curve shows the temperature (TT) spectrum, the middle one the E-mode (EE) spectrum, and the bottom one the B-mode (BB) spectrum. The dashed gray line indicates the expected primordial B-mode contribution. (Adapted from Ghigna et al. 2024 [122], LiteBIRD Collaboration 2023 [182]).

Scalar, vector and tensor perturbations Having established the formalism for describing CMB polarization, we now examine its decomposition into E- and B-modes, which arise from different types of perturbations in the Early Universe. These polarization patterns can be directly linked to the nature of the primordial perturbations, categorized as scalar, vector or tensor perturbations.
Scalar perturbations, associated with density fluctuations in the Early Universe, are responsible for generating E-mode polarization. The expected CMB polarization from Thomson scattering in an inhomogeneous density field at recombination is purely E-mode, with spatial correlations dictated by the underlying temperature anisotropies. Essentially, E-modes are imprinted onto the CMB photons by the passage of a density wave, leading to a pattern that aligns radially around cold spots and tangentially around hot spots.
On the other hand, B-modes have a distinct origin, arising from tensor perturbations: gravitational waves propagating through the Early Universe. A plane gravitational wave perturbation induces a quadrupolar stretching of the space-time metric, affecting the wavelength of photons and creating a quadrupolar temperature anisotropy. Through Thomson scattering, this anisotropy generates a characteristic swirling polarization pattern, distinguishing B-modes from their scalar-generated counterparts (Fig. 1.12).
This decomposition into E- and B-modes provides a powerful tool for distinguishing between different physical sources of CMB polarization. Scalar perturbations dominate the formation of E-modes, whereas the detection of primordial B-modes would serve as a crucial observational signature of Early-Universe gravitational waves, offering insights into inflationary physics.

Primordial gravitational waves The passage of a density wave in the temperature field induces the E-mode polarization on CMB photons. In a similar manner, the passage of grav-

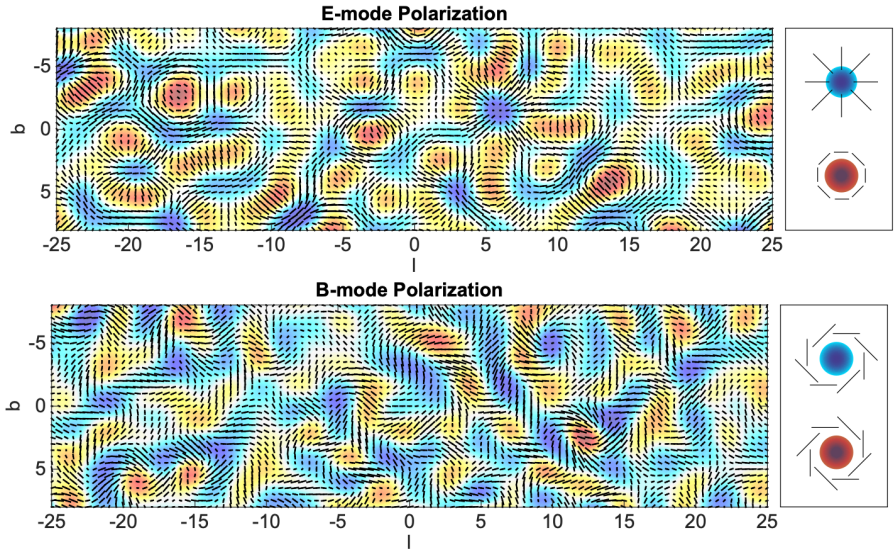

Figure 1.12: Simulated patterns of E- and B-mode polarization (Kamionkowski et al. 2016 [160]).

itational waves (GWs) imprints the B-mode polarization onto the CMB. This occurs because GWs distort the space-time metric in a quadrupolar fashion, with two possible polarization states, denoted as + and ×. These distortions stretch the photon wavelengths, generating a quadrupolar anisotropy in the temperature field, which then leads to the production of polarization through Thomson scattering (Subsec. 1.6.1). The polarization pattern that emerges is characterized by the B-mode signature.

To understand the origin of these gravitational waves, we need to look beyond single astrophysical sources such as black hole mergers. The crucial point is that we are not discussing individual GWs, but rather a diffuse background of gravitational waves (GWB) that permeates the Universe. The origin of this background is intrinsically tied to the Inflationary epoch (Subsec. 1.5.3), because Inflation is the sole proposed mechanism to generate GWs at cosmological scales.

The mechanism for the generation of this GWB is analogous to Hawking radiation from black holes, as described in Hawking 1974 [133]. In the case of a black hole, quantum relativistic effects cause the event horizon to emit radiation. Similarly, during inflation, the Universe undergoes an exponential expansion, leading to the emission of gravitational waves from the event horizon of the Universe itself. The key difference is that in the case of black holes, the radiation is observed by an observer outside the event horizon, while in the case of the Universe, all observers are inside the event horizon (i.e., within the expanding Universe). This diffuse GWB can be described as a stochastic gravitational wave background (SGWB), whose amplitude depends on the Inflationary energy scale. The SGWB power spectrum is typically parameterized by the tensor-to-scalar ratio r, which is related to the amplitude of primordial gravitational waves, and peaks around the degree angular scale. The detection of B-modes would provide strong evidence for the Inflationary model of the Early Universe, since their presence constitutes a unique signature of primordial gravitational waves. The amplitude of the signal is typically quantified through the angular power spectrum. As shown in Fig. 1.11, the temperature anisotropy spectrum is extremely well measured across all angular scales, and the E-mode spectrum is also precisely characterized, particularly at small scales. In contrast, current data are still insufficient to provide a complete characterization of the B-mode autocorrelation spectrum. The dashed gray line in Fig. 1.11 represents the expected primordial contribution, which, if detected, would serve as a smoking gun for Inflation, probing both the

energy scale and the dynamics of the very Early Universe. This diffuse gravitational wave background (GWB) is observable through its imprint on the CMB, where radiation from the Universe's "event horizon" leaves distinct polarization patterns.

The tensor-to-scalar ratio r The tensor-to-scalar ratio r is the ratio between the amplitude of the tensor and scalar perturbation in the polarization field, as expressed by:

$$r \equiv \frac{A_T}{A_S} \,. \tag{1.35}$$

The value of r is given once an Inflationary potential is specified, in particular if we normalize the energy associated to the Inflationary field at the grand unification (GUT), then we have a value of $r \sim 10^{-2}$ as derived by Challinor et al. 2013 [64]:

$$r = 8 \cdot 10^{-3} \Big(\frac{E_{inf}}{10^{16}\ GeV} \Big)^4 . \tag{1.36}$$

Therefore, assuming that Inflation occurred around the GUT scale, so $E_{inf} \sim 10^{16}\ GeV$, it yields $r \sim 10^{-2}$. This link also highlights how the measurement of the tensor-to-scalar ratio, r, constrains the Inflationary models, giving direct information on the nature of the Inflaton field. The most recent upper limit on $r < 0.032$ was published by Tristram et al. 2024 [294].

1.6.2 Cosmic birefringence

Cosmic birefringence is an effect that alters the polarization state of CMB photons as they propagate through the Universe. In optics, birefringence refers to the property of certain media that possess a refractive index dependent on the polarization and propagation direction of light. Similarly, in the cosmological context, cosmic birefringence induces a rotation of the plane of linear polarization of CMB photons due to interactions with new physics beyond the Standard Model, such as parity-violating effects or coupling to axion-like fields (Carroll et al. 1990 [58], Harari et al. 1992 [130]).
The theoretical motivation for cosmic birefringence arises from the possible interaction of CMB photons with a pseudo-scalar field, such as a cosmic axion field, which could induce a rotation angle proportional to the line integral of the axion field along the photon's trajectory (Pogosian 2001 [257]). The general form of the rotation angle α induced by such an interaction is given by:

$$\alpha = \frac{1}{2} \int d\tau \frac{d\phi}{d\tau} \,, \tag{1.37}$$

where ϕ is the axion-like field, τ is the conformal time, and $\frac{d\phi}{d\tau}$ represents the evolution of the field. This effect, if detected, would provide strong evidence for parity-violating physics in the Early Universe and could have significant implications for fundamental theories such as string theory and extensions of quantum field theory (Komatsu 2022 [170], Nakatsuka et al. 2022 [213]).
Observationally, cosmic birefringence manifests as a systematic rotation of the CMB polarization. This rotation modifies the Stokes parameters Q and U such that:

$$Q' \pm iU' = e^{\mp 2i\alpha} (Q \pm iU) \,, \tag{1.38}$$

where α is the birefringence angle. This transformation mixes the E-mode and B-mode polarization (Eq. 1.30, Eq. 1.31, Eq. 1.32), effectively converting part of the E-modes into B-modes, which could mimic or contaminate the signature of primordial GWs (Minami et al. 2020

[198], Diego-Palazuelos et al. 2022 [87]). The amplitude of this rotation is a key parameter in searches for physics beyond the Standard Model, and recent studies using Planck data have reported hints of a $(0.35 \pm 0.14)^\circ$ birefringence angle (Minami et al. 2020 [198], Eskilt et al. 2022 [107]).
A robust detection of cosmic birefringence would open a new observational window into fundamental physics and the evolution of the Universe, shedding light on the possible existence of axion-like particles and parity-violating interactions in the Early Cosmos.

1.7 Conclusion

This chapter has outlined the key physical mechanisms responsible for generating polarization across galactic, extragalactic, and cosmological scales. At galactic scales, we have discussed synchrotron emission, thermal and spinning dust emission and free-free emission, highlighting their connection to star formation and the role of magnetic fields—topics that will be explored further in Chap. 5. Moving to extragalactic scales, we examined the impact of active galactic nuclei (AGN) and Faraday rotation on polarization signals. Finally, we introduced the ΛCDM and Hot Big Bang models as a foundation for understanding Inflation, a theoretical framework that describes the evolution of the Early Universe. Inflation solves the old standard Big Bang scenario shortcomings and is now paradigmatic. Still, the exact form of the field (or fields) responsible for this phase in the early Universe are still not known. The discovery of CMB B-mode polarization would allow to constrain a large class of models. The complexity of disentangling diverse polarization sources underscores the necessity of precise observational techniques and robust data analysis methods. The next chapter will delve into the methodologies used to detect and characterize the polarization mechanisms discussed here, paving the way for a deeper understanding of the fundamental physics underlying our Universe.

Chapter 2

Measuring polarization: formalism, techniques and challenges

Contents

2.1 The characteristics of a polarized signal **44**
2.2 Formalism of polarized radiation **46**
2.2.1 Jones formalism 46
2.2.2 Stokes formalism 47
2.2.3 Mueller matrices 47
2.3 Optical elements formalism **48**
2.3.1 Linear polarizer 48
2.3.2 Half-Wave Plates (HWP) 50
2.4 Modulation: concept and methods **51**
2.4.1 On-sky modulation 52
2.4.2 Optical element modulation 53
2.4.3 Boresight rotation 54
2.5 Reference CMB polarization experiments **55**
2.6 Requirements for next-generation CMB polarization experiments **58**
2.6.1 Observational constraints 58
2.6.2 Systematic effects and calibration requirements 61
2.6.3 The particular case of the absolute orientation 64
2.7 Conclusion **66**

Abstract This chapter provides an overview of polarization measurement techniques and their scientific significance. It begins with the theoretical foundations of polarization, including the oscillatory properties of the electromagnetic field and the Stokes and Mueller formalism for characterizing polarized signals. Key optical elements such as the linear polarizer and Half-Wave Plate (HWP) are introduced, alongside essential methodologies like on-sky and optical modulation techniques for accurate measurement. The challenges posed by galactic and extragalactic foregrounds are discussed, highlighting the necessity for advanced component separation analyses in the study of CMB polarization. A timeline of major CMB polarization experiments is presented, summarizing their constraints on the tensor-to-scalar ratio r and the requirements for next-generation experiments. Calibration, a critical aspect of polarization studies, is examined in detail, including its challenges and the strategies employed to ensure measurement reliability. The chapter concludes with an analysis of systematic effects that can distort polarized signals, exploring their origins and mitigation strategies. This synthesis of theoretical, practical, and methodological insights establishes a solid foundation for the subsequent studies in this thesis.

2.1 The characteristics of a polarized signal

Polarization is a fundamental property of electromagnetic waves that describes the orientation of the electric field vector as the wave propagates through space. While unpolarized light exhibits random orientations of its electric field, polarized light exhibits a well-defined directional behavior that can provide valuable insights into the physical processes generating and modifying the radiation. This section introduces the basic physical concepts underlying polarization, including its mathematical description through field equations, and defines the different types of polarization commonly encountered in the study of electromagnetic radiation.
An electromagnetic wave can be represented as the superposition of two orthogonal components of the electric field $\mathbf{E}$, typically denoted as E_x and E_y, which oscillate perpendicular to each other and to the direction of propagation $\mathbf{k}$. Mathematically, this can be expressed as:

$$\mathbf{E}(\mathbf{r}, t) = \mathrm{Re}\left[\mathbf{E_0} e^{i(\mathbf{k}\cdot\mathbf{r}-\omega t)}\right], \tag{2.1}$$

where $\mathbf{E_0} = E_x\hat{x} + E_y\hat{y}$ is the complex amplitude of the electric field, $\mathbf{k}$ is the wave vector, ω is the angular frequency, and $\mathrm{Re}[\cdot]$ denotes the real part.
The polarization state of the wave depends on the relative amplitudes and phases of E_x and E_y. For a monochromatic wave, the electric field components can be written as:

$$E_x = A_x \cos(\mathbf{k}\cdot\mathbf{r} - \omega t), \tag{2.2}$$
$$E_y = A_y \cos(\mathbf{k}\cdot\mathbf{r} - \omega t + \delta), \tag{2.3}$$

where A_x and A_y are the amplitudes, and δ is the phase difference between the components. The state of polarization can be classified into three main types based on the trajectory traced by the tip of the electric field vector in the transverse plane (Fig. 2.1).
Linear polarization occurs when the electric field oscillates along a single direction, forming a straight line in the transverse plane. This happens when the phase difference δ between E_x and E_y is a multiple of π ($\delta = n\pi$, where $n \in \mathbb{Z}$). The electric field can then be expressed as:

$$\mathbf{E}(t) = \hat{x}A_x \cos(\omega t) + \hat{y}A_y \cos(\omega t). \tag{2.4}$$

Circular polarization occurs when the amplitudes of E_x and E_y are equal ($A_x = A_y$) and the phase difference δ is $\pm\pi/2$. The electric field traces a circle in the transverse plane, and

the wave can be right- or left-handed depending on the sign of δ:

$$\mathbf{E}(t) = A\Big[\hat{x}\cos(\omega t) \pm \hat{y}\sin(\omega t)\Big]\,, \tag{2.5}$$

where $A = A_x = A_y$.

Elliptical polarization is the most general case, occurring when the amplitudes A_x and A_y are unequal, and the phase difference δ is arbitrary. The electric field traces an ellipse in the transverse plane, described by the general equation:

$$\left(\frac{E_x}{A_x}\right)^2 + \left(\frac{E_y}{A_y}\right)^2 - 2\cos(\delta)\frac{E_x}{A_x}\frac{E_y}{A_y} = \sin^2(\delta)\,. \tag{2.6}$$

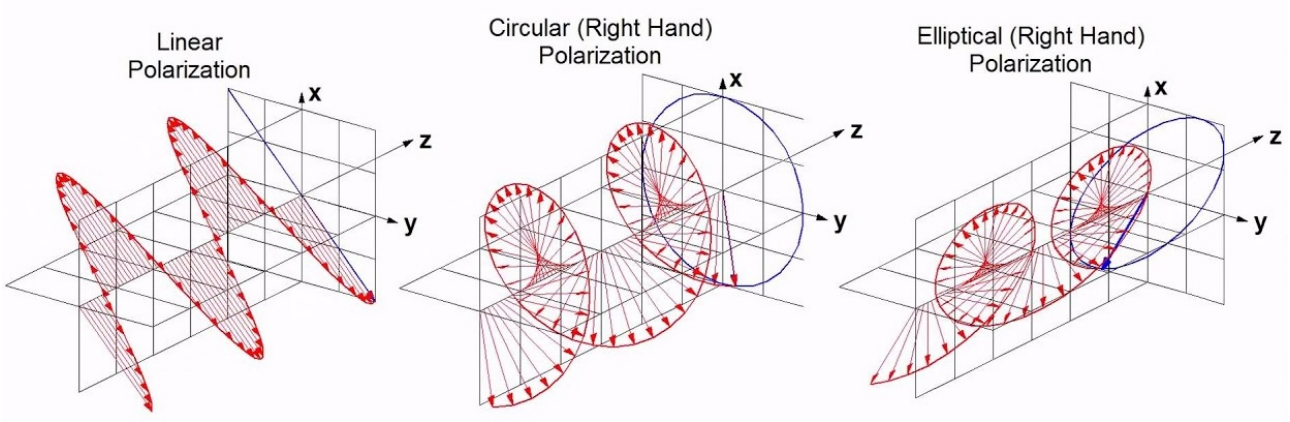

Figure 2.1: Diagram showing the three types of polarization propagation: linear (left), circular (center), elliptical (right). Source: meyavuz (https://www.youtube.com/watch?v=Q0qrU4nprB0).

Polarized signals fundamentally differ from unpolarized ones due to their ordered structure. Unlike unpolarized signals, polarized emission carries not only information about intensity but also an intrinsic oscillation direction. This dual nature makes polarization a rich source of astrophysical information. However, measuring polarized signals presents significant challenges. Firstly, polarized signals often represent only a small fraction of the total intensity, making them intrinsically weaker and more difficult to detect. Additionally, the observed polarization can be a composite of multiple contributions from different sources, necessitating sophisticated disentanglement techniques such as signal modulation. Accurate measurement is further complicated by calibration challenges, since precise characterization of the reference frame of the incoming polarization is essential to preserve the integrity of the observed data. Challenges also arise from instrumental systematics, calibration uncertainties, and foreground contamination, rather than atmospheric and thermal fluctuations, which mainly affect unpolarized measurements. Key issues include beam asymmetries, polarization leakage, and differential noise between detectors. Accurate calibration of the instrument's polarization angle and response is critical, as is mitigating polarized foregrounds like Galactic synchrotron and thermal dust emission. These factors require precise system design, multi-frequency observations, and robust data correction to accurately capture the much weaker polarization signals.
Addressing these challenges requires an integrated approach that combines meticulous instrument design, advanced data processing algorithms, and robust calibration methods. In the following sections, we will address these issues, detailing the techniques and methodologies employed to overcome them and ensure accurate measurements of polarized signals.

2.2 Formalism of polarized radiation

Having expressed the physical form of polarized light, it is useful to introduce the main formalisms employed in its analysis. Two formalisms are commonly utilized: the Jones and Stokes formalisms. The Jones formalism is particularly helpful for understanding the physical nature of a polarized signal, as it describes the properties of the electric field associated with the light wave. The Stokes formalism, on the other hand, is well-suited for practical measurement purposes, as its parameters are homogeneous to intensities. In addition to these formalisms, one often employs Mueller matrices to describe the action of optical elements on polarized light or to represent a change of reference frame. It is important to note that Mueller matrices do not constitute a separate formalism: rather, they provide a convenient matrix algebra to operate on Stokes parameters, which are the actual observables. Together, these approaches offer complementary perspectives: the Jones formalism provides insight into the wave's intrinsic properties, the Stokes formalism facilitates its quantitative measurement, and Mueller matrices describe how optical components modify the polarization state. By combining these tools, one can achieve a comprehensive understanding of how polarized light is shaped by various optical systems.

2.2.1 Jones formalism

Polarized light can be effectively described using the Jones formalism, which represents the electric field vector of the light as a complex two-dimensional vector. This vector, commonly referred to as the Jones vector, encapsulates the amplitude and phase of the electric field components along two orthogonal axes, typically denoted as x and y. Mathematically, the Jones vector is written as

$$\mathbf{E} = \begin{pmatrix} E_x \\ E_y \end{pmatrix}, \tag{2.7}$$

where E_x and E_y are the complex amplitudes of the electric field components along the x and y axes, respectively.
Optical elements, such as wave plates or other birefringent media, can modify the polarization state of light. In the Jones formalism, these elements are represented by 2×2 complex matrices called Jones matrices. The interaction between the light and the optical element is described by matrix multiplication:

$$\begin{pmatrix} E_a(t) \\ E_b(t) \end{pmatrix} = \begin{pmatrix} J_{00} & J_{01} \\ J_{11} & J_{12} \end{pmatrix} \begin{pmatrix} E_x(t) \\ E_y(t) \end{pmatrix}, \tag{2.8}$$

where we multiply the Jones matrix of the optical element and the Jones vector of the incident light.
When an optical element is rotated by an angle θ, the polarization of the emerging light changes accordingly. To account for this, it is often necessary to transform the Jones matrix of the optical element into a rotated coordinate system. The transformation is performed using a rotation matrix $\mathbf{R}_\theta$, defined as:

$$\mathbf{R}_\theta = \begin{pmatrix} \cos\theta & \sin\theta \\ -\sin\theta & \cos\theta \end{pmatrix}. \tag{2.9}$$

For a rotated optical element, the corresponding Jones matrix in the original coordinate system can be expressed as:

$$\mathbf{J}_{\text{rotated}} = \mathbf{R}_{-\theta}\mathbf{J}\mathbf{R}_\theta\,. \tag{2.10}$$

This allows the polarization state to be analyzed efficiently, regardless of the orientation of the optical element.
The Jones formalism is widely used in polarization optics due to its simplicity and direct connection to the physical properties of the light field. By combining Jones matrices with Jones vectors, one can predict the polarization state of light as it propagates through various optical systems, making the formalism an essential tool for polarization analysis.

2.2.2 Stokes formalism

The Stokes formalism is a widely adopted framework for characterizing polarized electromagnetic radiation. It offers a convenient and intuitive method for quantifying the state of polarization using four parameters, which can be derived from the electric field definition given in Eq. 2.3:

- $S_0 = I = \langle |A_x|^2 \rangle + \langle |A_y|^2 \rangle$: the total intensity
- $S_1 = Q = \langle |A_x|^2 \rangle - \langle |A_y|^2 \rangle$: the horizontal and vertical linear polarization (also referred to as "plus"/+ polarization)
- $S_2 = U = 2\langle A_x \rangle \langle A_y \rangle \cos\delta$: the 45º oriented linear polarization (also referred to as "cross"/×)
- $S_3 = V = 2\langle A_x \rangle \langle A_y \rangle \sin\delta$: the circular polarization

where $\langle \cdot \rangle$ denotes that each component is time-averaged assuming that the radiation is in a steady state at the time scale of averaging; δ is the phase difference between orthogonal components of the electric field. From these parameters, we can define some other variables that are extensively used to describe and characterize polarization:

- The polarization intensity: $I_{pol} = \sqrt{Q^2 + U^2}$
- The polarization degree: $p = \frac{I_{pol}}{I}$
- The polarization angle: $\alpha = \frac{1}{2}\arctan(U, Q)$

This last notation emphasizes that the arctangent must be defined with proper quadrant consideration, typically within $[-\pi, \pi]$, to avoid ambiguities in the polarization angle.

2.2.3 Mueller matrices

Complementing the Stokes formalism, the Mueller matrices describe how the polarization state changes when interacting with optical elements. A Mueller matrix ($\mathbf{M}$) is a 4×4 matrix that represents the transformation of the Stokes vector due to an optical system:

$$\mathbf{S}_{\text{out}} = \mathbf{M} \cdot \mathbf{S}_{\text{in}}, \tag{2.11}$$

where $\mathbf{S}_{\text{in}}$ and $\mathbf{S}_{\text{out}}$ are the input and output Stokes vectors, respectively. In Fig. 2.2, a visual representation of the four Stokes parameters and their conventions is shown.
The utility of these formalisms lies in their simplicity and flexibility. The parameters and matrices can be directly related to measurable quantities, facilitating the analysis of polarized light from various sources. These formalisms will be extensively employed throughout this work to interpret polarization data and extract its scientific meaning. In this work, we will primarily focus on linear polarization, neglecting the circular polarization component ($V \approx 0$). In fact,

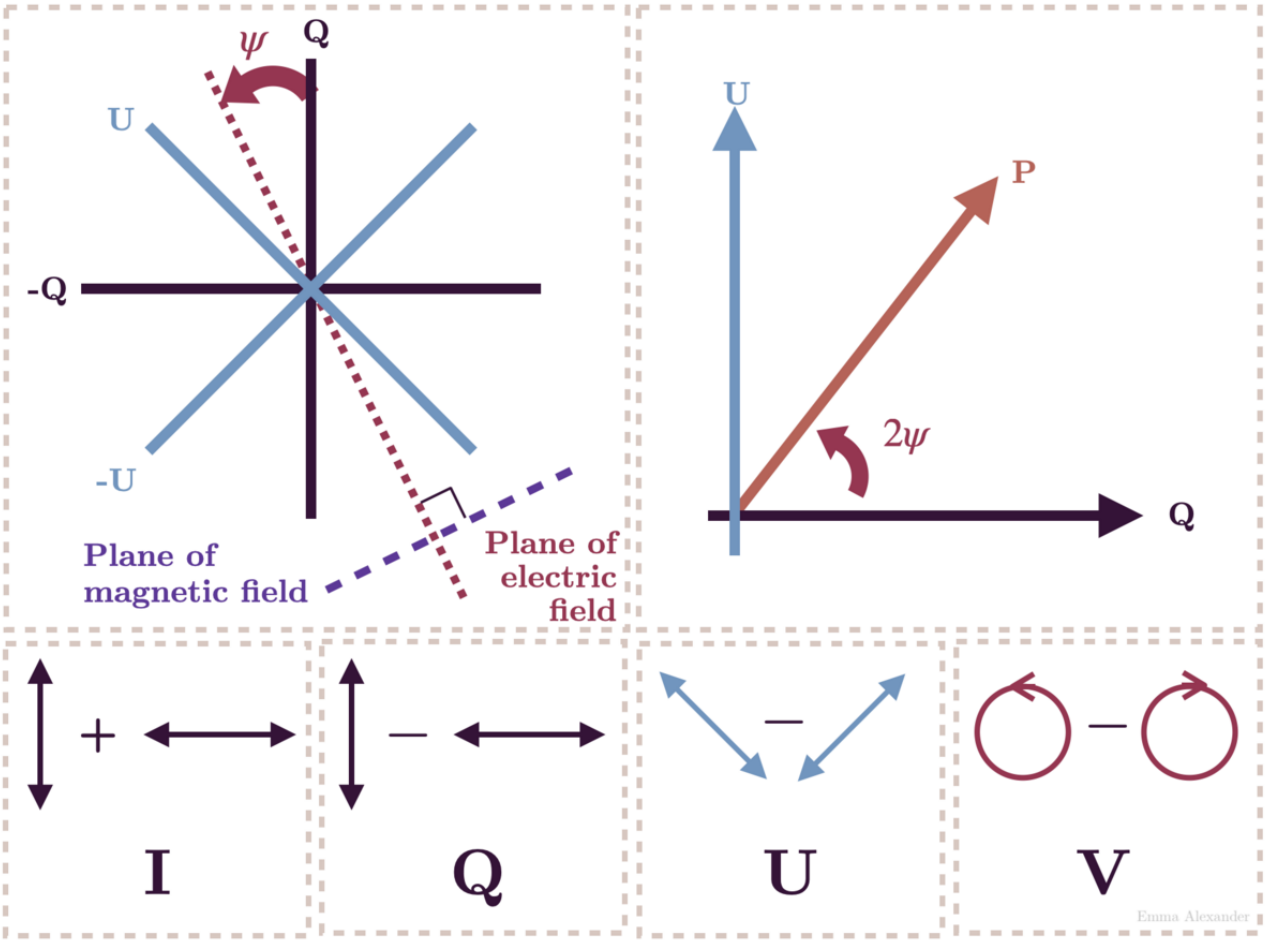

Figure 2.2: Representations of the Stokes parameters in relation to polarization angle ψ, polarization vector P, and the planes of the electric and magnetic fields. On the sky, the $\pm$Q axes correspond to reversed compass directions (i.e. clockwise from the top: North West South East), according to IAU convention. Source: E. Alexander (https://emmaalexander.github.io/index.html).

for most of the phenomena that we will analyze, there is no circular polarization expected or rather we deal with instruments insensitive to it. Some optical elements will be of particular interest in subsequent chapters, such as the linear polarizer and the half-wave plate, both ideal and non-ideal cases.

2.3 Optical elements formalism

The formalisms introduced in the previous section are crucial for describing certain optical elements that will play a significant role in the work presented later in this thesis. In particular, the Mueller matrices for linear polarizers and HWPs will be frequently utilized to formalize their effects within an optical chain.

2.3.1 Linear polarizer

A linear polarizer, also known as an analyzer, consists of a regular array of fine parallel lithographic or metallic wires placed in the path of an incident beam. Ideally, the component of the electromagnetic wave's electric field aligned parallel to the wires is completely reflected

backward along the incident direction, while the perpendicular component is fully transmitted. The Jones matrix representation of a linear polarizer is given by:

$$\mathbf{J}_{\text{pol}} = \begin{pmatrix} p_x & 0 \\ 0 & p_y \end{pmatrix}, \tag{2.12}$$

where the real values $0 \leq p_x \leq 1$ and $0 \leq p_y \leq 1$ denote the transmission factors for the x- and y-components of the electric field, respectively. The resulting transmitted electric field components are $E'_x = p_x E_x$ and $E'_y = p_y E_y$.
Starting from the Jones expression of the linear polarizer effect, we can reconstruct its equivalent Mueller matrix. The transformation from Jones to Mueller formalism involves averaging over uncorrelated phase terms of the electric field components. The Mueller matrix M of an optical system can be derived from its Jones matrix J as follows:

$$M_{kl} = \frac{1}{2}\text{Tr}\left(\sigma_k J \sigma_l J^\dagger\right), \tag{2.13}$$

where $J^\dagger$ is the Hermitian conjugate (transpose and complex conjugate) of the Jones matrix J, and σ_k are the Pauli matrices:

$$\sigma_0 = \begin{pmatrix} 1 & 0 \\ 0 & 1 \end{pmatrix}, \quad \sigma_1 = \begin{pmatrix} 1 & 0 \\ 0 & -1 \end{pmatrix}, \quad \sigma_2 = \begin{pmatrix} 0 & 1 \\ 1 & 0 \end{pmatrix}, \quad \sigma_3 = \begin{pmatrix} 0 & -i \\ i & 0 \end{pmatrix}.$$

For practical purposes, when circular polarization is neglected, the resulting Mueller matrix simplifies to a 3×3 matrix instead of the full 4×4 form. In terms of the Jones matrix components $(J_{00}, J_{01}, J_{10}, J_{11})$, the Mueller matrix can be written explicitly as:

$$M = \frac{1}{2}\begin{pmatrix} |J_{00}|^2 + |J_{01}|^2 + |J_{10}|^2 + |J_{11}|^2 & |J_{00}|^2 - |J_{01}|^2 + |J_{10}|^2 - |J_{11}|^2 & 2\text{Re}(J_{00}J_{01}^* + J_{10}J_{11}^*) \\ |J_{00}|^2 + |J_{01}|^2 - |J_{10}|^2 - |J_{11}|^2 & |J_{00}|^2 - |J_{01}|^2 - |J_{10}|^2 + |J_{11}|^2 & 2\text{Re}(J_{00}J_{01}^* - J_{10}J_{11}^*) \\ 2\text{Re}(J_{00}J_{10}^* + J_{01}J_{11}^*) & 2\text{Re}(J_{00}J_{10}^* - J_{01}J_{11}^*) & 2\text{Re}(J_{00}J_{11}^* + J_{01}J_{10}^*) \end{pmatrix}. \tag{2.14}$$

Now, using Eqs. 2.12 and 2.14, we obtain the Mueller matrix of a linear polarizer:

$$\mathbf{M}_{\text{pol}} = \begin{pmatrix} p_x^2 + p_y^2 & p_x^2 - p_y^2 & 0 \\ p_x^2 - p_y^2 & p_x^2 + p_y^2 & 0 \\ 0 & 0 & 2p_x p_y \end{pmatrix}. \tag{2.15}$$

Then, using the rotation element of Eq. 2.9, we can finally write the Mueller matrix of an ideal linear polarizer as:

$$\mathbf{M}_{\text{LP}} = \frac{1}{2}\begin{pmatrix} 1 & \cos 2\theta & \sin 2\theta \\ \cos 2\theta & \cos^2 2\theta & \sin 2\theta \cos 2\theta \\ \sin 2\theta & \sin 2\theta \cos 2\theta & \sin^2 2\theta \end{pmatrix}. \tag{2.16}$$

For a non-ideal linear polarizer, imperfections such as finite extinction ratio (E) introduce leakage between polarization states. The Mueller matrix for a non-ideal polarizer is then modified as:

$$\mathbf{M}_{\text{LP, non-ideal}} = \frac{1}{2}\begin{pmatrix} 1 & (1-2\epsilon)\cos 2\theta & (1-2\epsilon)\sin 2\theta \\ (1-2\epsilon)\cos 2\theta & (1-\epsilon)\cos^2 2\theta + \epsilon \sin^2 2\theta & (1-2\epsilon)\cos 2\theta \sin 2\theta \\ (1-2\epsilon)\sin 2\theta & (1-2\epsilon)\cos 2\theta \sin 2\theta & (1-\epsilon)\sin^2 2\theta + \epsilon \cos^2 2\theta \end{pmatrix}. \tag{2.17}$$

Here, ϵ represents the degree of imperfection, where $\epsilon = 0$ corresponds to an ideal polarizer

and $\epsilon = 0.5$ corresponds to a completely non-polarizing element. The non-ideal Mueller matrix accounts for partial polarization and attenuation effects, providing a more realistic description of the optical element.

2.3.2 Half-Wave Plates (HWP)

In a general definition, a dephaser is an optical device that introduces a relative phase shift between two orthogonal polarization components of an electromagnetic wave. The phase shift arises due to differences in the propagation speed of light along the device's principal axes, typically caused by birefringence. Birefringence is a material property where the refractive index depends on the direction of light propagation and polarization. By altering the relative phase between components, dephasers can transform the polarization state of light, such as rotating the polarization angle, converting linear to circular polarization, or producing elliptical polarization. Depending on the amount of the phase shift, we can talk about half-wave plates, quarter-wave plates or more complex devices.
To describe the action of a dephaser such as a HWP, we use the concept of birefringence. A birefringent material has two principal axes: the ordinary axis (o-axis) and the extraordinary axis (e-axis). Light components aligned along these axes experience different refractive indices, n_o and n_e, respectively. When linearly polarized light passes through a birefringent material of thickness d, the phase difference ($\Delta\phi$) introduced between the two components can be expressed as:

$$\Delta\phi = \frac{2\pi d}{\lambda}\left(n_e - n_o\right), \tag{2.18}$$

where d is the thickness of the birefringent plate, λ is the wavelength of the incident light, n_e and n_o are the refractive indices along the extraordinary and ordinary axes, respectively.
For a HWP, the phase shift is set to π, so the thickness d is chosen such that:

$$d = \frac{\lambda}{2\left(n_e - n_o\right)}. \tag{2.19}$$

The electric field of an incident wave can be expressed as:

$$\mathbf{E}_{\text{in}} = E_o\hat{\mathbf{e}}_o + E_e\hat{\mathbf{e}}_e, \tag{2.20}$$

where E_o and E_e are the components of the electric field along the ordinary and extraordinary axes, and $\hat{\mathbf{e}}_o$ and $\hat{\mathbf{e}}_e$ are the unit vectors along these axes.
After passing through the HWP, the electric field components are transformed. The extraordinary component E_e accumulates a phase shift π relative to the ordinary component E_o:

$$\mathbf{E}_{\text{out}} = E_o\hat{\mathbf{e}}_o - E_e\hat{\mathbf{e}}_e. \tag{2.21}$$

This results in a rotation of the polarization plane by an angle 2θ, where θ is the angle between the fast axis of the plate (extraordinary axis) and the initial polarization direction. The new polarization components can be expressed as:

$$E'_x = E_x\cos 2\theta + E_y\sin 2\theta, \tag{2.22}$$
$$E'_y = -E_x\sin 2\theta + E_y\cos 2\theta, \tag{2.23}$$

where E_x and E_y are the initial electric field components in the reference frame, and E'_x and E'_y are the transformed components after the plate (Fig. 2.3).

We can express the same phase shift through the Mueller formalism, obtaining the following Mueller matrix for an ideal HWP:

$$\mathbf{M}_{\mathrm{HWP}} = \begin{bmatrix} 1 & 0 & 0 \\ 0 & \cos 4\theta & \sin 4\theta \\ 0 & \sin 4\theta & -\cos 4\theta \end{bmatrix}, \tag{2.24}$$

where θ represents the angle between the fast axis of the HWP and the reference axis. A visual representation of the working principle of an HWP is shown in Fig. 2.3.

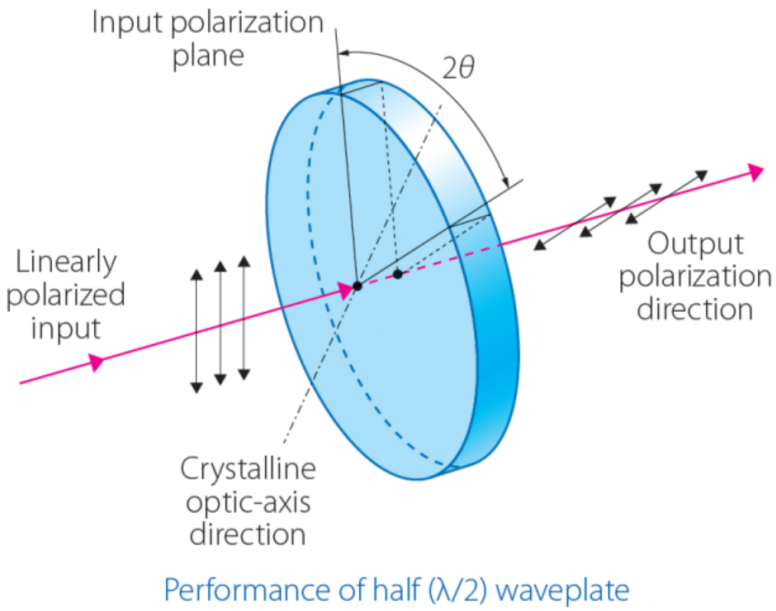

Figure 2.3: Diagram showing the optical effect of an HWP on incoming light. Source: https://instockoptics.com/crystalline-quartz-waveplates.

2.4 Modulation: concept and methods

In polarimetry, modulation is a crucial technique used to isolate the polarized signal of interest from unpolarized light and other unwanted noise. Intuitively, modulation can be thought of as a way to identify the polarized signal with a unique and predictable pattern, making it easier to detect and analyze, even in the presence of significant background noise or instrumental imperfections. In other words, modulation introduces a specific, predictable variation into the polarized signal. This allows the polarized component to stand out, even when mixed with other signals like unpolarized light or instrumental noise.
Another important reason for modulation, a fast one in particular, is to mitigate the effects of noise and systematic errors. Instruments are sensitive to various environmental factors such as temperature fluctuations, optical imperfections, and electronic noise. Modulation shifts the polarized signal into a frequency range where these low-frequency noise sources have minimal impact, thereby improving the measurement's accuracy and reliability.
Moreover, modulation enables the measurement of all components of the polarization. For instance, if the polarization state is unknown, the modulation process ensures that the instrument systematically probes different orientations of polarization, such as horizontal, vertical, and diagonal. This comprehensive sampling allows for a complete reconstruction of the polarization state.

Mathematically, modulation can be represented as a transformation of an input signal $S(t)$ by a modulation function $M(t)$:

$$S_{\rm mod}(t) = S(t) \cdot M(t)\,. \tag{2.25}$$

The choice of $M(t)$ depends on the specific modulation method employed, such as spatial scanning or the use of optical elements.

2.4.1 On-sky modulation

On-sky modulation involves changing the observed polarization signal by scanning the detectors across the sky. The scanning strategy is designed to vary the orientation of the detectors with respect to the sky polarization in a systematic way. By observing the same sky region multiple times with different orientations, the polarization signal can be disentangled from unpolarized intensity and instrumental noise. The scanning process introduces a time-dependent modulation function, $M(t)$, determined by the detector's orientation and scanning speed.
The measured signal at time t can be expressed as:

$$S(t) = I + Q\cos(2\psi(t)) + U\sin(2\psi(t))\,, \tag{2.26}$$

where I is the total intensity, Q and U are the Stokes parameters for linear polarization, and $\psi(t)$ is the angle of the detector's polarization axis and the reference axis on the sky (e.g. the local sky meridian). By fitting the time-varying signal, the polarization parameters Q and U can be reconstructed.
This method is commonly used in both small and large-scale experiments, such as the *Planck* satellite mission (Planck collaboration 2020 [247], Delabrouille et al. 2002 [85]). It is a consequence of the need to have measurements of the same pixel of the sky under different angles to separate I, Q and U, which are mixed in a single sample (Eq. 2.26).
Unlike instruments that use internal modulators such as rotating wave plates, *Planck* relied on the scanning of the sky achieved through the satellite's rotation and orbital motion, combined with polarization-sensitive bolometers (PSBs) oriented at $\pm45°$ and $\pm90°$ in the focal plane. The satellite rotated about its spin axis approximately once per minute, while the spin axis itself traced a larger circle on the sky over the course of months. This scanning strategy ensured that each point on the sky was observed at multiple angles, effectively modulating the polarization signal. However, good angular coverage per detector was only achieved near the ecliptic poles; elsewhere, the coverage was rather poor. The redundancy of PSB orientations across the focal plane was therefore crucial to fully recover the polarization signal over the whole sky. *Planck*'s detectors included polarization-sensitive bolometers (PSBs) capable of measuring orthogonal components of linear polarization, enabling the extraction of the Stokes parameters Q and U. As the satellite rotated, the polarization-sensitive detectors experienced sinusoidal variations in the signal from polarized sources, encoding the polarization information into the time-ordered data. By revisiting the same regions of the sky at different orientations, *Planck* averaged out systematic biases, ensuring robust and consistent measurements. Over the mission's lifetime, Planck achieved full-sky coverage multiple times, providing redundant data for cross-checks and minimizing the impact of noise and systematic effects. Advanced data processing techniques were used to extract the modulated polarization signals while accounting for foreground contamination, such as polarized emission from galactic dust.
However, a downside of this modulation method is the necessity to inter-calibrate the detectors. In the case of *Planck*, four detectors were required to reconstruct the polarization from the sky, arranged as two pairs observing two different directions. This configuration made an instantaneous reconstruction of the polarized signal impossible. Instead, the signals from these

detectors had to be combined post-observation, requiring precise inter-calibration because the detectors did not share the same beam. This added complexity to the data processing pipeline, as any mismatches in calibration could introduce systematic errors into the final polarization measurements.

2.4.2 Optical element modulation

In addition to on-sky modulation, polarization signals can be modulated using optical elements such as rotating HWPs or step-modulating devices. These methods provide controlled and repeatable modulation of the incoming polarization state, often operating at higher frequencies to mitigate the impact of low-frequency noise.

Step-modulation Step-modulation involves rotating an optical element, such as an HWP, in discrete steps to specific angles (e.g., 0°, 45°, 90°, etc.). At each step, the detector measures the intensity corresponding to a known polarization state. The modulation function $M(t)$ is piecewise constant and depends on the sequence of these predefined angles.

Continuous rotation In continuous rotation modulation, the HWP rotates at a constant angular velocity ω, introducing a periodic modulation of the polarization state. The HWP rotates by an angle $\theta = \omega t$, where t is time. As the HWP completes a full rotation (2π radians), the polarization state is restored to its initial configuration, leading to a complete cycle of modulation.
The modulation frequency, however, is not simply ω. Since the polarization state changes with 2θ per HWP rotation, and the detected intensity depends quadratically on the electric field, the resulting intensity modulation appears at 4ω (Eq. 2.24). The modulated signal can be expressed as:

$$S(t) = I + Q\cos(4\omega t) + U\sin(4\omega t), \tag{2.27}$$

where I, Q, and U are the Stokes parameters. A fast and continuous rotation of a HWP enables the quasi-simultaneous observation of the Stokes parameters thanks to the periodic modulation of the polarization state of the incoming light as the HWP rotates. The intensity measured by the detector varies as a function of the HWP's rotation angle, encoding the information about I, Q, and U in the time-domain signal. The modulated signal contains distinct frequency components corresponding to these parameters. The total intensity I contributes to the DC (constant) component of the signal, while the linear polarization components Q and U are encoded in the harmonic frequency 4ω. This method provides a faster and more robust approach to capturing polarization data, reducing the impact of temporal variations and noise. However, the use of continuously rotating HWPs is not without challenges. One significant issue is the systematic effects arising from the rotation of a warm optical component, which can lead to spurious signals and impact measurement precision. These systematic effects include harmonic distortions in the modulation signal and unintended flux modulation caused by temperature variations in the rotating HWP. Such distortions necessitate complex calibration procedures to correct for these artifacts. An additional concern is the mechanical and thermal demands of operating a rotating HWP in a cryogenic environment, as cooling the HWP to mitigate temperature-induced effects is technically non-trivial (Essinger-Hileman et al. 2016 [108]). Developing a device capable of operating a cryogenic rotating HWP would address these concerns, but it introduces further engineering challenges and increases the instrument's overall complexity.

Variable-delay Polarization Modulators (VPM) The Cosmology Large Angular Scale Surveyor (CLASS) employs a front-end variable-delay Polarization Modulator (VPM), a modulation approach distinct from rotating wave plates (Harrington et al. 2018 and 2021 [131], [132]). The VPM consists of a fixed wire-grid polarizer followed by a movable mirror whose displacement varies the optical path length for one polarization component. By oscillating the mirror at ∼10 Hz, CLASS modulates the phase delay between the polarization components parallel and perpendicular to the grid, producing amplitude modulation of the incoming polarization rather than rotating its angle. This phase shift alternates constructive and destructive interference, effectively converting between Stokes Q, U, and V, and allowing a lock-in style measurement that suppresses atmospheric and instrument $1/f$ noise. Mechanically, the VPM uses a flexure-guided Mirror Transport Mechanism (MTM), similar in concept to a Martin–Puplett interferometer, to ensure precise, parallel motion of the mirror over a throw of several millimeters. However, this method introduces complexity: the mirror must be physically moved and CLASS, like *Planck*, requires multiple detectors and inter-calibration when combining signals from different beams.

Overall, modulation techniques using optical elements are now standard in polarization observation experiments. Continuously rotating modulators, typically HWPs, have been widely adopted in ground-based instruments, such as NIKA2 (Pisano et al. 2022 [237], Ritacco et al. 2017 [265], Ritacco et al. 2016 [264]), and the Atacama Cosmology Telescope (ACTPol; Henderson et al. 2016 [137]), as well as balloon-borne platforms including SPIDER, which uses a cryogenic rotating sapphire HWP at the aperture to minimize systematic contamination (Filippini et al. 2011 [113], Bryan 2014 [50]), BLAST-Pol, which employs a warm achromatic HWP together with fixed analyzer grids (Fissel et al. 2010 [114], Marsden et al. 2008 [189]) and POLARBEAR-2 (Hill et al. 2016 [140]).
More recently, rotating HWPs have been proposed for missions such as the Simons Observatory small-aperture telescopes (Yamada et al. 2024 [298], Yamada et al. 2025 [299]), the space-based satellite LiteBIRD (Hoang et al. 2022 [144], Sakurai et al. 2018 [273], Columbro et al. 2020 [69]).

2.4.3 Boresight rotation

Boresight rotation is another kind of modulation technique employed in polarization experiments, particularly in studies of the CMB. This method involves physically rotating the entire telescope around its boresight axis, which alters the orientation of its polarization sensitivity relative to the sky. Unlike on-sky modulation or optical element modulation, boresight rotation offers a unique advantage: it avoids introducing systematic effects due to the rotation of a warm component or issues due to the inter-calibration of independent channels. By changing the instrument's frame of reference, this technique mitigates issues such as instrumental polarization and cross-polarization leakage, ensuring high-fidelity measurements. The BICEP series of experiments, including BICEP2 and its successors like the Keck Array, have utilized boresight rotation to achieve precise constraints on the tensor-to-scalar ratio r (Cornelison et al. 2020 [75], Cornelison et al. 2022 [76], Thomas et al. 2020 [290], Aikin et al. 2010 [8], Buder et al. 2013 [51]).
Similarly, the GroundBIRD experiment (Lee et al. 2020 [181], Oguri et al. 2016 [221]) employs boresight rotation as part of its modulation strategy. This telescope is designed with a three-axis rotation structure, enabling effective polarization modulation by rotating around its optical axis (Nagasaki et al. 2018 [212], Oguri et al. 2016b [222]). GroundBIRD also combines this with rapid azimuthal scanning to suppress low-frequency noise and enhance sky coverage. This combination ensures high sensitivity for detecting subtle B-mode polarization signals, further demonstrating the utility of boresight rotation in modern CMB experiments.

2.5 Reference CMB polarization experiments

The quest to measure the polarization of the CMB, particularly the elusive B-modes, has driven the development of advanced instruments and experimental strategies. Several ground-based, balloon-borne, and space-based experiments have contributed significantly to our understanding of CMB polarization. This section aims at reviewing and highlighting the key experiments that have targeted CMB polarization, from the 90s to current and future projects, focusing on their scientific goals, measurement strategies and major results.

WMAP The Wilkinson Microwave Anisotropy Probe (WMAP) was a space-based mission launched in 2001, designed to measure temperature and polarization anisotropies in the CMB with unprecedented precision. WMAP telescope's aperture was 1.4 m, hence delivering an angular resolution up to 13' for its highest frequency channel at 94 GHz. WMAP employed a differential microwave radiometer, targeting both temperature and large-scale polarization patterns (E-modes), with no active modulation of polarization signals. Active until 2010, WMAP's observations confirmed the standard ΛCDM model and provided precise measurements of key cosmological parameters, including the age, composition, and geometry of the Universe. While it did not achieve the sensitivity to detect B-modes directly, its measurements significantly constrained models of inflation and seeded the path for subsequent experiments, such as Planck. WMAP's legacy includes a robust determination of the reionization optical depth and detailed mapping of large-scale polarization (Kogut et al. 2007 [167], Hinshaw et al. 2013 [141]).

Planck The *Planck* satellite, launched by the European Space Agency in 2009, was a landmark mission for studying the CMB (Planck collaboration 2018 V [250]), providing full-sky observations of both temperature and polarization anisotropies with unprecedented precision (Planck collaboration 2018 I [246]). Operating in nine frequency bands from 30 to 857 GHz, *Planck* employed bolometric detectors cooled to cryogenic temperatures to minimize noise. Unlike experiments using active polarization modulators, *Planck* relied on its spin and a carefully designed scanning strategy to extract polarization information, combining data from multiple passes across the sky to reconstruct the Stokes parameters. With a telescope aperture of 1.5 m, it delivered an angular resolution from 33' at 30 GHz (10 mm) to 5' at 857 GHz (0.35 mm). One of *Planck*'s key achievements was its measurement of E-mode polarization and its cross-correlation with the temperature anisotropies (Planck collaboration 2018 VII [252]), which refined constraints on cosmological parameters such as the reionization optical depth and the scalar spectral index (Planck collaboration 2018 VI [251]). Additionally, *Planck*'s data allowed for stringent upper limits on B-mode polarization from primordial gravitational waves (Planck collaboration 2018 X [253]), setting a constraint on the tensor-to-scalar ratio of $r < 0.10$ (95% confidence level). Later combined with BICEP data, Planck data contribute to the current best upper limit on $r < 0.032$ (Tristram et al. 2021 [293]). Beyond polarization, *Planck* made significant contributions to our understanding of astrophysical foregrounds (Planck collaboration 2018 XII [255]), including galactic dust and synchrotron emission, which are crucial for isolating the primordial CMB signal (Planck collaboration 2014 [240]).

Advanced ACTPol (ACT) The Atacama Cosmology Telescope (ACT), located in the high-altitude Atacama Desert of Chile, is a premier ground-based observatory dedicated to measuring the CMB with high precision. With an aperture of 6 m, ACTPol achieved an angular resolution of approximately 1.4' at 150 GHz (2 mm) and 1' at 230 GHz (1.3 mm). Since its first light in 2007, ACT has undergone significant upgrades, including the Advanced ACTPol phase, which introduced more sensitive TES bolometer arrays optimized for polarization studies. These enhancements have enabled ACT to make detailed measurements of the CMB temperature

and polarization anisotropies across small angular scales. ACT employs a dual modulation strategy, combining on-sky scanning with a stepped HWP to disentangle polarization signals from systematic effects and atmospheric noise. The telescope operates at multiple frequency bands, ranging from 90 to 220 GHz, which are chosen to minimize foreground contamination and maximize sensitivity to both E- and B-mode polarization. Recent results from ACT have provided refined constraints on the tensor-to-scalar ratio, placing an upper limit of $r < 0.07$ (95% confidence level), thereby contributing significantly to our understanding of the primordial universe (Louis et al. 2025 [186], Naess et al. 2025 [211], Naess et al. 2020 [210]). Additionally, ACT data have been crucial in improving constraints on the standard cosmological model and characterizing astrophysical foregrounds. Its findings complement those of other observatories and provide a critical foundation for next-generation experiments targeting the faint B-mode polarization signal.

SPTpol The South Pole Telescope (SPT), located at the Amundsen-Scott South Pole Station in Antarctica, is a ground-based observatory optimized for small-scale studies of the CMB. Its unique location provides exceptional atmospheric stability, enabling high-sensitivity observations of the CMB polarization. In 2012, the telescope was upgraded with the SPTpol instrument, which is specifically designed to measure polarization anisotropies with unprecedented precision. With an aperture of 10 m, SPTPol achieved an angular resolution of approximately 1.2' at 150 GHz (2 mm) and 0.9' at 220 GHz (1.36 mm). SPTpol utilizes TES bolometers, paired with a stepped HWP for polarization modulation. This modulation strategy, combined with the telescope's fine angular resolution and multi-frequency capability, allows for effective separation of the faint CMB polarization signal from foreground emissions and instrumental systematics. Observations cover a wide frequency range, with bands centered at 95 and 150 GHz, tailored to probe E- and B-mode polarization at small angular scales. The SPTpol experiment has delivered precise measurements of the EE and BB power spectra, providing critical data for constraining cosmological parameters and testing models of Inflation. Its results complement those of other CMB observatories, such as Planck and ACT, enhancing our understanding of the Universe's early stages (Chou et al. 2022 [67], Austermann et al. 2012 [18]). SPTpol's success has paved the way for its successor, SPT-3G, which aims to further improve sensitivity and expand the scientific reach of the South Pole Telescope.

POLARBEAR POLARBEAR is a ground-based experiment located in the Atacama Desert of northern Chile, designed to measure the polarization of the CMB at small angular scales. Its primary scientific goal is to detect and characterize the elusive B-mode polarization, which encodes information about primordial gravitational waves and large-scale structure lensing. The arid and high-altitude environment of the Atacama Desert offers excellent observing conditions, minimizing atmospheric interference. With an aperture of 2.5 m, POLARBEAR achieved an angular resolution of approximately 3.5' at 150 GHz (2 mm) and 2.2' at 220 GHz (1.36 mm).The POLARBEAR instrument employs TES bolometers for its sensitive polarization measurements. A key feature of the experiment is its continuously rotating HWP, which modulates the polarization signal at higher frequencies to reduce the impact of low-frequency noise and systematic errors. This modulation strategy enhances the experiment's ability to disentangle the faint CMB polarization signal from foreground contamination and instrumental effects. Operating at a frequency of 150 GHz, POLARBEAR has delivered high-resolution measurements of the EE and BB power spectra, setting constraints on the tensor-to-scalar ratio with an upper limit of $r < 0.09$ (95% C.L.) (Arnold et al. 2012 [15], Mitchell et al. 2020 [199]). POLARBEAR's success has also laid the groundwork for the Simons Array, a next-generation experiment aimed at expanding its scientific reach.

BICEP2/Keck The BICEP/Keck Array series of ground-based experiments, located at the South Pole, are dedicated to the measurement of the B-mode polarization of the CMB at degree angular scales, targeting the faint signal from primordial gravitational waves generated during inflation. With an aperture of 0.26 m, BICEP2/Keck achieved an angular resolution of approximately 30' at 150 GHz (2 mm). The BICEP2 experiment, operational from 2010 to 2012, made headlines in 2014 with a claimed detection of B-modes, which were later determined to be significantly contaminated by galactic dust after joint analysis with Planck data (BICEP/Planck joint collaboration 2015 [42]). Building on this, the Keck Array continued observations at multiple frequencies, improving constraints on the tensor-to-scalar ratio r, with the most recent results placing $r < 0.036$ (95% confidence). The instruments use bolometric polarimeters operating at cryogenic temperatures and employ fixed optical elements rather than active modulation. These experiments have set the stage for future ground-based observations by refining techniques to separate foregrounds from primordial signals (BICEP2/Keck collaboration 2021 [3]).

Simons Observatory The Simons Observatory (SO) is a state-of-the-art ground-based initiative situated in the high-altitude Atacama Desert of Chile. Building on the legacy of experiments like ACT and POLARBEAR, SO represents a major step forward in the quest to measure the polarization of the CMB with unprecedented sensitivity. SO operates a suite of telescopes, including a 6 m Large Aperture Telescope (LAT) and initially three 0.5 m Small Aperture Telescopes (SATs), equipped with TES bolometers and continuously rotating HWPs for polarization modulation. The LAT achieves angular resolutions of approximately 1.4' at 150 GHz (2 mm) and 1' at 230 GHz (1.3 mm), while the SATs provide broader beams of 30–50' depending on frequency. This configuration enables precise measurement of both E-mode and B-mode polarization while effectively mitigating systematic errors and foregrounds. SO targets a constraint on the tensor-to-scalar ratio of $r<0.01$ (95% C.L.) and will also probe gravitational lensing, Sunyaev–Zel'dovich effects, and cluster astrophysics (SO Collaboration 2019 [4]).
As of mid-2025, two US SATs have successfully completed calibration and entered science observations in mid-2024, with the third SAT following shortly thereafter. Japan-led and UK-led SAT expansions are underway—funded by JSPS and UKRI respectively—with additional telescopes expected online around 2026. French participation, via IN2P3 and CNRS groups, aims to contribute a seventh SAT focused on enhanced galactic-dust characterization. Meanwhile, the LAT reached "first light" in February–March 2025, imaging Mars and beginning cryogenic receiver commissioning, with SMuRF readout systems meeting design requirements.
With all telescopes now operational and data pipelines underway, SO has entered a phase of early-science validation across its 60,000 detector array. Full survey operations are anticipated later this decade, with planned upgrades including new SATs and detector expansions to further enhance sensitivity.

LiteBIRD LiteBIRD (Lite satellite for the studies of B-mode polarization and Inflation from cosmic background Radiation Detection) is a groundbreaking space-based mission spearheaded by the Japan Aerospace Exploration Agency (JAXA) in collaboration with international partners. With a launch anticipated in the early 2030s, LiteBIRD is designed to measure the polarization of the CMB across the full sky with unprecedented precision. With an aperture of 0.5 m, LiteBIRD is designed to achieve an angular resolution of approximately 30' at 100 GHz (2 mm) and 69' at 40 GHz (7.5 mm). The mission will employ polarimetric bolometers and continuously rotating HWPs to achieve high sensitivity to both E-mode and B-mode polarization. This modulation strategy, combined with the stable space environment, will allow LiteBIRD to suppress systematic effects and foreground contamination effectively, ensuring the reliability of its measurements. LiteBIRD's primary scientific goal is to probe the physics of cosmic inflation

by targeting the primordial B-mode signal. By achieving constraints on the tensor-to-scalar ratio as stringent as r < 0.001 (95% C.L.), LiteBIRD will explore inflationary energy scales at unprecedented depths, potentially unveiling the physical mechanisms underlying the Universe's rapid expansion in its earliest moments. The mission also promises to deliver valuable data on reionization, large-scale structure, and other astrophysical phenomena (LiteBIRD collaboration 2023 [182]). As of the time of writing this thesis, the project is undergoing significant discussions and revisions regarding the instrument design and requirements, leaving the final configuration and specifications yet to be determined.
Overall, the data collected from all these experiments over the past 30 years contributed to sensibly improve our knowledge of the CMB power spectrum (Fig. 1.11). A summary of the presented reference CMB polarization experiments, with their main characteristics and results, is presented in Tab. 2.1.

Experiment	**Years active**	**Sky area**	**Detectors**	**Modulation**	r **constraint**
WMAP	2001–2010	Full-sky	HEMT amplifiers	Spin-based	< 0.13
Planck	2009–2013	Full-sky	Bolometers	Spin-based	< 0.10
ACT-Pol	2010–2022	Small-scale	TES bolometers	Stepped HWP	< 0.07
SPT-Pol	2012–2016	Small-scale	TES bolometers	Stepped HWP	< 0.09
POLARBEAR	2012–present	Small-scale	TES bolometers	Rotating HWP	< 0.09
BICEP2/Keck	2010–present	Small-scale	TES bolometers	None (fixed angles)	< 0.036
Simons Obs.	2027 (planned)	Multi-scale	TES bolometers	Rotating HWP	< 0.01
LiteBIRD	2030s (planned)	Full-sky	Bolometers	Rotating HWP	< 0.001

Table 2.1: Summary of major CMB polarization experiments, their characteristics and results/forecasts on the tensor-to-scalar ratio r.

2.6 Requirements for next-generation CMB polarization experiments

The next generation of experiments dedicated to observing the polarization of the CMB is already entering the installation and commissioning phase, with many more in the design stage. However, as discussed, the detection of the elusive B-mode signal remains a formidable challenge. Consequently, future instruments must be optimized to meet this demanding goal. In the following subsections, we highlight several critical aspects that these experiments must address to succeed.

2.6.1 Observational constraints

To achieve the ambitious science goals of next-generation CMB polarization experiments, the design of the instruments and the observing strategy must meet stringent requirements. These include proper scalability and sensitivity of detectors, broad frequency coverage for effective foreground removal, and specific site selection to minimize atmospheric contamination.

Instrumental sensitivity Achieving the sensitivity required to detect the faint B-mode signals demands not only ultra-sensitive detectors, such as TESs or KIDs, but also the scalability of these technologies to massive arrays with 10 - 10000 pixels. This scalability is critical for providing the large sky coverage and high resolution needed to isolate the subtle polarization

patterns. Each detector array must operate at cryogenic temperatures (below 200 mK) to suppress thermal noise, posing significant engineering challenges for cryostats and cooling systems. Moreover, the expansion to such large-scale arrays introduces complexities in the readout systems, which must handle an immense number of detector channels with high precision while minimizing noise and power consumption. Advanced multiplexing techniques, such as frequency-domain or time-domain multiplexing, are crucial to reduce the physical and thermal footprint of the readout electronics. These systems must also maintain sensitivity across the entire array and avoid introducing additional systematic errors.
As detector arrays grow in size, their physical integration with optical systems and calibration mechanisms becomes increasingly intricate, requiring robust designs to ensure uniform performance across thousands of pixels. The combination of these technical challenges underscores the need for innovative solutions in detector fabrication, readout technology, and system integration to meet the sensitivity and scale requirements of next-generation CMB polarization experiments.

Foreground mitigation through multi-frequency coverage As outlined in Sec. 1.2, galactic polarized foregrounds present a significant obstacle to the detection of primordial B-modes. The most viable technical solution lies in observing the sky across a broad range of frequencies, allowing for the disentanglement of signals from individual components. Instruments like the SAT of the Simons Observatory are purpose-built for this task, featuring detectors optimized for multiple frequency bands. However, this requirement entails significant challenges, including infrastructure to handle large datasets, the intricacies of designing and fabricating multi-frequency instruments, and the demanding task of ensuring seamless integration between different subsystems.

Atmospheric contamination and site selection A major source of contamination for ground-based millimeter-wave polarization measurements is the Earth's atmosphere. Atmospheric fluctuations arise primarily from water vapor, clouds, and turbulence, and their impact varies across observing frequencies. Importantly, to first order, the atmosphere is neither polarized nor polarizing; it contributes to additional intensity fluctuations, which effectively act as noise in the reconstructed polarization signal. Understanding and mitigating these atmospheric effects is therefore critical for maximizing the sensitivity of ground-based CMB experiments. This variability is often modeled as an additive term to the total measured signal:

$$S_{\rm obs}(t, f) = I + Q\cos 2\alpha + U\sin 2\alpha + A_{\rm atm}(t, f)\,, \tag{2.28}$$

where $S_{\rm obs}$ is the observed signal on the detector, I, Q, and U are the Stokes parameters of the true sky signal, α is the detector orientation, and $A_{\rm atm}$ represents the atmospheric contribution, which depends on both time (t) and frequency (f).
The effect of the atmosphere is particularly pronounced at low- and mid-frequency millimeter wavelengths, where atmospheric opacity τ_ν and scattering dominate. Atmospheric opacity, a function of frequency ν, can be approximated as:

$$I_{\rm trans} = I_0 e^{-\tau_\nu} \tag{2.29}$$

where $I_{\rm trans}$ is the transmitted intensity, and I_0 is the incident intensity. High levels of atmospheric water vapor increase τ_ν, particularly at frequencies near water absorption lines.
Many models have been developed to characterize the impact of the atmosphere on the detection of millimeter wavelength radiation, such as *atm* by Pardo 2019 [230] and *am* by Paine 2022 [227]. The *am* model, in particular, is widely used due to its ability to simulate atmospheric transmission by considering various atmospheric constituents, including water vapor,

oxygen, and other molecular absorbers. This model relies on input parameters such as the site altitude, temperature, and precipitable water vapor (PWV), providing a detailed estimate of the atmospheric opacity as a function of frequency. Using the *am* model, we present in Fig. 2.4 an example of the atmospheric transmission for a few sites where polarization-sensitive instruments (some for CMB in particular) are installed: Cerro Toco in the Atacama Desert in Chile (ACT), the South Pole (SPT), the Mexican Sierra Negra (LMT), Sierra Nevada in Spain (IRAM) and Sardinia (SRT). For all these sites, we used the annual estimates of PWV to characterize the atmospheric conditions. Specifically, the 95th percentile of PWV values has been adopted, representing conditions where only 5% of the time the water vapor content exceeds this threshold. This choice ensures that the simulations reflect near-optimal observing conditions at each location, aligning with the operational practices of CMB experiments aimed at minimizing atmospheric noise.

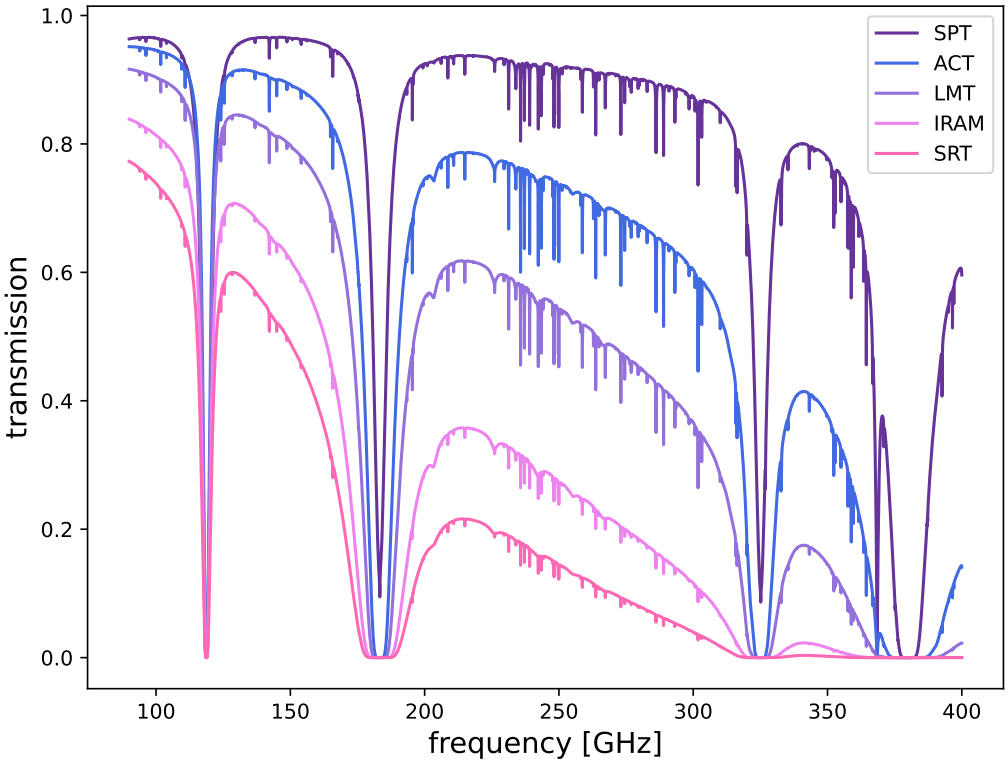

Figure 2.4: Simulation of the atmospheric transmission through *am* (Paine 2022 [227]) for 5 observational sites where SPT, ACT, LMT, IRAM and SRT are installed. The simulations have been performed considering an annual estimate of the 95th percentile PWV, a zenith angle of 0°.

As we can see in Fig. 2.4, the site plays a crucial role in the transmission of the signal depending on the frequency. The PWV being a key factor, it is essential to install CMB polarization instruments in dry and elevated sites. The atmospheric absorption is not the only limitation, as more complex turbulence and instability effects contribute to the challenge. Ground-based facilities mitigate these effects by employing atmospheric models, differential techniques, and multi-band observations. For instance, observing the same region of the sky at multiple frequencies allows for the characterization and subtraction of atmospheric contributions (Errard et al. 2015 [106]). Advanced calibration techniques, such as radiometric measurements of atmospheric emission or real-time incorporation of weather data, are crucial for reducing the impact of atmospheric noise (as done for NIKA2, detailed in Catalano et al. 2014 [61]). Sky simulations incorporating atmospheric variability, as discussed by Bussmann et al. 2005 [53] and Lay et al. 2000 [177], have shown significant improvements in recovering intrinsic polarization signals.

The development of these mitigation techniques is critical for achieving the high precision required in modern polarization experiments, such as those aimed at detecting primordial B-modes in the CMB.

2.6.2 Systematic effects and calibration requirements

In this chapter, we have frequently mentioned the concept of systematic effects in the context of polarization measurements. To provide a clearer understanding, this section aims to define systematic effects and highlight the main sources of these errors in millimeter-wavelength polarization measurements. A *systematic effect* refers to a bias or distortion introduced into the measurement process that is not due to random fluctuations, but rather arises from inherent imperfections or external factors affecting the observation. Unlike random errors, which can be mitigated through statistical averaging, systematic errors are usually consistent, predictable, and can lead to biases in the data unless properly accounted for. In the following paragraphs, we will highlight some of the most common.

Beam asymmetry and mismatch Beam distortions pose a major challenge for B-mode polarization detection, as imperfections such as asymmetries, ellipticities, and side lobes can couple intensity signals into polarization, generating spurious contributions. Minimizing these effects requires high-quality, symmetric optics, pre-deployment calibration, and continuous beam characterization during observations. Differential detectors and advanced scanning strategies help suppress common-mode distortions, while post-observation techniques such as beam deconvolution and forward modeling correct residual effects. Beam asymmetry, i.e., deviations from an ideal circular Gaussian profile, is particularly critical when patterns differ between polarization channels (Fig. 2.5).

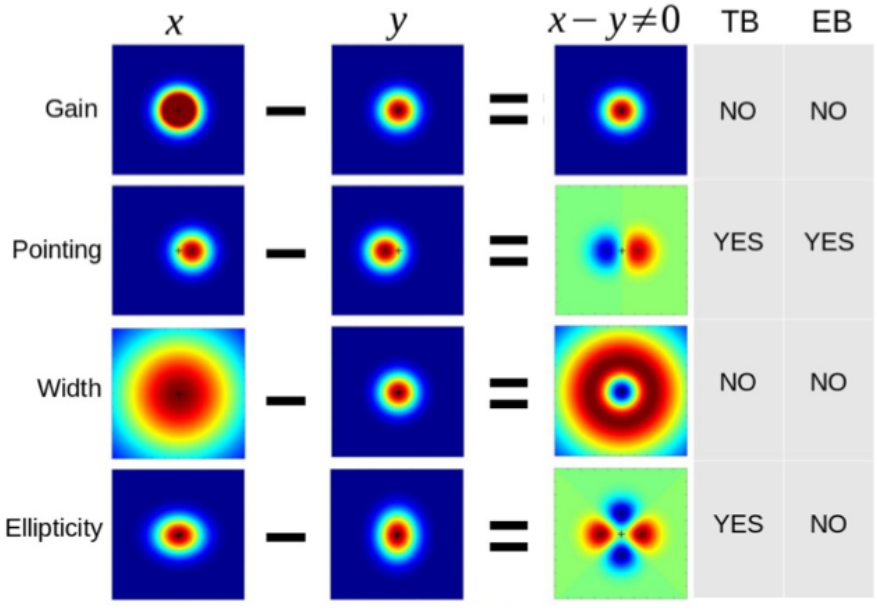

Figure 2.5: Beam distortion systematic effects: gain, pointing, width, and ellipticity. The first two columns show the beams in the X and Y directions of the focal plane; the third column shows the relative difference; the last two columns show the impact of beam mismatch on TB and EB CMB spectra. Source: F. Nati.

The effect of beam asymmetry on polarization measurements can be quantified using the beam

transfer function B_ℓ, which characterizes the response of the telescope as a function of angular scale ℓ. The effective polarization signal P_ℓ observed can be written as:

$$P_\ell^{\rm obs} = B_\ell P_\ell^{\rm true} + \Delta B_\ell T_\ell, \tag{2.30}$$

where ΔB_ℓ represents the beam mismatch and T_ℓ is the temperature anisotropy. The second term, $\Delta B_\ell T_\ell$, is referred to as temperature-to-polarization leakage, where the much stronger temperature anisotropy signal contaminates the weaker polarization signal due to imperfect beam alignment or symmetry.
Temperature-to-polarization leakage primarily affects the TB and EB cross-spectra, which are expected to vanish in the absence of parity-violating physics (Shimon et al. 2008 [280]). Any non-zero measurement in these spectra is therefore often attributed to systematic effects. For example, the leakage term for the TB spectrum can be approximated as:

$$C_\ell^{TB,\rm leak} \approx \sum_{\ell'} M_{\ell\ell'} \Delta B_{\ell'} C_{\ell'}^{TT}, \tag{2.31}$$

where $M_{\ell\ell'}$ represents the mode coupling introduced by the beam mismatch.
In addition to beam asymmetry, side lobes—regions of the beam response outside the main lobe—can pick up signals from the ground, atmosphere, or bright astrophysical sources, introducing spurious polarization contamination. Side lobe effects can be expressed as:

$$P_\ell^{\rm side} = \int d\Omega\, S(\Omega) T(\Omega), \tag{2.32}$$

where $S(\Omega)$ represents the side lobe beam response and $T(\Omega)$ is the temperature signal in the corresponding direction. Proper shielding, baffling, and modeling of the side lobe response are necessary to minimize such contamination.
Correction for beam asymmetry requires precise characterization of the beam properties, which is typically achieved through planet scans or observations of bright point sources. These measurements allow the construction of accurate beam transfer functions, B_ℓ, and their mismatches, ΔB_ℓ. Robust modeling techniques, such as those described in Huffenberger et al. 2010 [150], and iterative map-making algorithms help mitigate these effects during data analysis.
Efforts to minimize beam asymmetry also involve careful optical design, ensuring high symmetry in the telescope optics and alignment of the focal plane detectors. Additionally, scanning strategies that average out systematics over the sky and advanced deprojection techniques can significantly reduce the impact of temperature-to-polarization leakage on cosmological parameter estimation (Dou et al. 2025 [89]).

Optical elements misalignment Misalignment of optical elements, such as mirrors or lenses, can lead to a rotation of the polarization angle or a leakage of intensity into polarization. For instance, an angular misalignment $\delta\theta$ of the optical path can induce a polarization rotation error $\Delta\psi$ approximated as:

$$\Delta\psi \approx 2\delta\theta. \tag{2.33}$$

These effects can be mitigated through precise alignment procedures and frequent calibration using polarized sources.

HWP precession Imperfections in the HWP rotation, such as precession or uneven speed, can introduce spurious signals. The modulation efficiency η of the HWP depends on the accuracy of its rotation and is given by:

$$\eta = \frac{1}{2}\left(1 + \cos(4\omega t + \phi)\right) \tag{2.34}$$

where ω is the rotational frequency, t is time, and ϕ accounts for phase errors. Calibration of HWP performance using well-characterized polarized sources is critical to minimize these errors (Savini et al. 2006 [275]).

Cross-polarization and instrumental leakage Cross-polarization occurs when the instrument's polarization-sensitive elements detect signals from the orthogonal polarization state, leading to spurious polarization signals. The leakage is represented by a term L, which contributes to false polarization signals, primarily through coupling between the total intensity $T = I$ and the polarization states Q and U:

$$P_{\text{obs}} = M P_{\text{true}} + LT, \tag{2.35}$$

where M is the Mueller matrix of the optical element considered, P_{true} are the true polarization components, and P_{obs} are the observed polarization components.
To characterize and correct for cross-polarization leakage, calibration is essential. One effective method involves observing unpolarized celestial sources, such as Uranus, Neptune, or the Moon. These sources are ideal calibrators as their intrinsic polarization is negligible, allowing any detected polarization to be attributed to instrumental effects. By mapping the response of the instrument to these sources, the elements of the Mueller matrix, including the leakage term L, can be directly measured and subsequently corrected in the data processing pipeline.
For example, if Uranus is observed to have a small apparent polarization signal, this can be modeled as:

$$Q_{\text{obs}} \approx L I_{\text{true}}, \quad U_{\text{obs}} \approx 0, \tag{2.36}$$

where I_{true} is the true total intensity of Uranus. The leakage is then determined by comparing the observed Q_{obs} with the expected I_{true}.
The tolerable level of cross-polarization leakage depends on the scientific goals and the instrument's sensitivity. For next-generation CMB polarization experiments targeting the tensor-to-scalar ratio $r \sim 10^{-3}$, the leakage contribution must typically be below 0.1% ($L < 10^{-3}$) to avoid contaminating the weak B-mode polarization signal.
Mitigation of cross-polarization leakage also involves a dedicated instrument design, such as: ensuring high purity of the polarization-sensitive elements, including detectors and feedhorns; reducing non-idealities in optical elements, such as mirrors and lenses, which can introduce polarization distortions; aligning optical components to minimize differential phase shifts between orthogonal polarization states.
Finally, advanced data processing techniques, such as template fitting and iterative deprojection, can help remove residual leakage during map-making. Combined with robust calibration using unpolarized sources, these efforts ensure that cross-polarization leakage remains below the threshold required for precision polarization measurements.

Pointing inaccuracy Pointing inaccuracy can lead to errors in polarization measurements due to the misinterpretation of source position. Pointing errors $\delta\theta$ contribute to an error in the observed polarization signal:

$$P_{\text{obs}} = P_{\text{true}}(1 + \delta\theta^2/2)\,. \tag{2.37}$$

Frequent telescope pointing checks using bright, well-known sources are essential to minimize this effect (Padin et al. 2008 [225]).

2.6.3 The particular case of the absolute orientation

As detailed in Chap. 1, Subsec. 1.6.1, the tensor-to-scalar ratio, r, quantifies the relative contributions of primordial gravitational waves (tensor modes) to the scalar perturbations in the CMB. Accurate measurement of r relies on precise characterization of the B-modes in the CMB polarization. However, uncertainties in the polarization angle introduce systematic errors that propagate into the measurement of the B-modes signal. This uncertainty can be represented as an angular error, $\Delta\psi$, in the reconstructed polarization angle. This error can arise from inaccuracies in the instrument's polarization angle calibration or systematic effects during data analysis. The effect of $\Delta\psi$ propagates into increased uncertainty in r, since the tensor-to-scalar ratio is directly influenced by the amplitude and angular precision of the observed polarization patterns. Quantifying the dependence of r on $\Delta\psi$ allows us to assess the precision requirements for polarization angle measurements to robustly constrain r.
A miscalibration of the absolute polarization angle by $\Delta\psi$ introduces a coupling between the E- and B-modes of the polarization field. The C_ℓ^{EE} power spectrum, typically much larger than the C_ℓ^{BB} power spectrum, leads to the phenomenon commonly referred to as "E-to-B leakage". The effect, described in Rosset et al. 2010 [270], can be quantified, using the auto-correlation spectra defined in Eq. 1.34, as:

$$\tilde{C}_\ell^{BB} = C_\ell^{BB}\cos^2(2\Delta\psi) + C_\ell^{EE}\sin^2(2\Delta\psi)\,, \tag{2.38}$$

where $\tilde{C}_\ell^{BB}$ is the observed power spectrum in the B-modes, which includes a spurious component from the E-to-B leakage. The relative bias, $\hat{r}$, is defined as:

$$\hat{r} = \frac{\tilde{C}_\ell^{BB} - (2\Delta\psi)^2 C_\ell^{EE}}{C_\ell^{BB}(r=1)}\,, \tag{2.39}$$

where $C_\ell^{BB}(r=1)$ represents the B-mode power spectrum in the absence of E-to-B leakage. With C_ℓ^{EE} being 10 to 100 times larger than C_ℓ^{BB}, we see that a 1% error on ψ leads to a bias of 4% on r. The sensitivity of r to $\Delta\psi$ underscores the need for stringent calibration procedures in current and future CMB experiments (see Chap. 6).
Calibration can be classified as either *absolute* or *relative*, depending on the reference framework. *Absolute calibration* establishes a direct connection between the instrument's measurements and a physical standard, enabling the determination of true values for observed quantities. In contrast, *relative calibration* focuses on ensuring consistency across multiple detectors or measurements within the instrument, correcting systematic variations without necessarily linking to an external standard. Together, absolute and relative calibration form the foundation for achieving both accuracy and internal coherence in experimental data.
In the context of polarization experiments, a key aspect of calibration is the determination of the polarization angle. Miscalibration of the polarization angle introduces systematic errors, such as E-to-B leakage, which contaminates the signal being analyzed (Subsec. 2.6.2). This effect can significantly bias estimates of cosmological parameters, such as the tensor-to-scalar ratio r, making accurate angle calibration essential. Kaufman et al. 2014 [162] highlight the importance of rigorous angle calibration strategies for CMB experiments, discussing methods to quantify and mitigate these errors. Calibration of the polarization angle is an ongoing challenge for ground-based, balloon-borne, and space-based experiments alike, as even small errors can propagate into significant systematic biases. Various methods have been developed and employed for polarization calibration, tailored to the scientific objectives, instrument characteristics, and observational environment. Here follows a list of the main techniques used to calibrate the absolute polarization angle.

1. Quasars as calibrators In the context of astrophysical polarimetry observations, quasars

are commonly employed as polarization calibrators, largely because there are few alternative sources available. These extragalactic point sources can, in some cases, exhibit polarization properties that remain stable over long periods of time, making them useful references. Their relatively high flux densities and point-like appearance on the sky simplify their use as calibrators for instruments with different resolutions and sensitivities. Agudo et al. 2012 [6], for example, discuss the use of the quasar 3C286 for calibrating polarization-sensitive instruments, highlighting its suitability in certain contexts. Quasars have been used in several experiments, including *Planck*, ACTPol, and POLARBEAR, to refine polarization angle calibration and validate instrument performance. Despite these advantages, quasars also present important limitations. Their polarization fraction is often relatively low, which can reduce their effectiveness for calibrating instruments with extreme sensitivity requirements. Moreover, most quasars are not perfectly stable: their intrinsic variability must be monitored, and simultaneous observations with independent instruments (as done with NIKA2 and XPOL) are often required to ensure their reliability as calibrators. In practice, quasars remain the best available option, but their limitations must be accounted for in calibration strategies.

2. Standard polarization calibrators Another key category of calibrators includes well-studied celestial sources with nearly constant polarization properties. The Crab Nebula, also known as M1 or the Tau A supernova remnant, is one of the most widely used standard polarization calibrators (Aumont et al. 2020 [17], Ritacco et al. 2018 & 2022 [266]-[267]). Its nearly uniform and stable polarization angle across its extent has made it a reference source for many experiments targeting both astrophysical and CMB polarization. The Crab Nebula is particularly advantageous because its polarization properties are well-documented in multiple frequency bands, from radio to sub-millimeter wavelengths. This enables cross-calibration of instruments operating in different frequency regimes, ensuring consistency between observations. The use of the Crab Nebula as a calibrator offers several advantages. Its stable polarization angle makes it a reliable reference for a wide range of instruments. Additionally, its well-documented polarization properties across multiple wavelengths facilitate cross-frequency calibration, a critical requirement for modern astrophysical instruments. However, its extended nature requires careful beam modeling, particularly for instruments with high angular resolution, to account for variations in polarization across the source. Furthermore, its brightness can pose challenges for instruments operating at lower sensitivity levels, necessitating careful dynamic range management during observations.

3. Self-calibration Self-calibration is a powerful technique employed in polarimetry to mitigate systematic uncertainties by utilizing intrinsic symmetries or statistical properties of the observed sky signal. This method allows for the refinement of instrumental calibration parameters, such as the polarization angle or gain mismatch, directly from the data without relying entirely on external calibrators. Keating et al. 2013 [163] demonstrated the efficacy of self-calibration for CMB polarization experiments, leveraging the known parity properties of E- and B-modes to disentangle instrumental systematics from true sky signals. In particular, this approach exploits the absence of parity-violating cross-terms (e.g., TB and EB) in the primordial CMB signal to constrain instrumental effects. The use of self-calibration offers several advantages. It is especially beneficial for ground-based and sub-orbital experiments, where external calibrators may be sparse or inaccessible. Moreover, for high-sensitivity observations, this technique is invaluable in addressing even minor systematic biases that could otherwise significantly affect results. However, its effectiveness depends on the statistical quality and quantity of the observed data, requiring sufficient sky coverage and signal-to-noise ratio to accurately constrain instrumental parameters. Additionally, it assumes certain properties of the sky signal, such as the absence of parity-violating terms in the primordial CMB, which may not apply in all cases.

Despite these constraints, self-calibration has been successfully implemented in experiments such as POLARBEAR and BICEP2/Keck, underscoring its importance in achieving robust measurements of the faint B-mode polarization signal.

4. Artificial calibrators Due to the general lack of standard calibrators that are sufficiently well characterized in polarization, artificial calibrators are increasingly being developed for polarization calibration. These include laboratory-based sources, such as polarized emitters with well-defined polarization angles, and dedicated instruments deployed in the field to provide reference signals. Artificial calibrators are particularly useful for characterizing and calibrating instrument-specific systematics, such as instrumental polarization or polarization angle offsets. The use of artificial calibrators has become standard in pre-deployment testing for polarization-sensitive detectors, with multiple prototypes currently being developed and tested. Two complementary projects are being carried out to provide an artificial, non-astrophysical reference frame for ground-based polarization experiments: the drone-borne ERC-funded POLOCALC project (Nati et al. 2017 [214], Coppi et al. 2022 [72], Coppi et al. 2024 [73], Coppi et al. 2025 [74]) and COSMOCal (Ritacco et al. 2024 [268]). The POLOCALC project primarily targets small ground-based telescopes, such as the SATs of the Simons Observatory, while COSMOCal focuses on delivering a high-precision reference for polarization angles for large ground-based and potentially space-based telescopes. Its innovative strategies and potential impact on future experiments will be detailed in Chap. 6. The development and use of artificial calibrators offer several advantages. They provide controlled and reproducible reference signals, enabling precise characterization of instrument-specific systematics under well-defined conditions. Additionally, they can be tailored to specific experimental needs, such as calibration at particular frequencies or for specific instrument configurations. However, artificial calibrators are not without limitations. Their deployment often requires significant logistical and technical effort, especially for field-based systems like drone-borne calibrators. Moreover, their ability to mimic real astrophysical signals may be limited, potentially introducing discrepancies when transitioning from artificial to natural calibrators. Despite these challenges, artificial calibrators remain indispensable for achieving high-precision polarization measurements, especially in the absence of well-characterized natural calibrators.

2.7 Conclusion

In this chapter, we have examined the measurement of polarization with an emphasis on the techniques and strategies that enable precise observations of the CMB. We began by introducing the fundamental formalisms used to describe polarization, namely the Stokes and Jones vectors and the Mueller matrix framework, which together provide the tools to characterize and manipulate polarized radiation. The main optical elements employed in CMB polarimetry, such as linear polarizers and HWPs, were presented, along with modulation techniques that are crucial for extracting faint polarization signals from dominant intensity fluctuations. A historical overview of major CMB polarization experiments, including *WMAP*, *Planck*, ACTPol, SPTpol, POLARBEAR, as well as the upcoming Simons Observatory, and possibly LiteBIRD, highlighted the progress in constraining the tensor-to-scalar ratio r and in advancing instrumental capabilities. The lessons learned from these instruments directly inform the requirements of next-generation experiments. We discussed these requirements in terms of three main fronts. *(i) Observational constraints:* the need for ever-larger detector arrays (scaling to thousands of pixels), operated at cryogenic temperatures below 200 mK, with exquisite sensitivity to reach the targeted noise levels; mitigation of polarized foregrounds through broad multi-frequency coverage; and control of atmospheric contamination, favoring high-altitude, arid sites such as the Atacama Desert and the South Pole. The latter, however, is becoming increasingly dif-

ficult to access and operate logistically, making site selection a technical, but also political, challenge. *(ii) Systematic effects:* beam distortions, optical misalignment, HWP precession, cross-polarization leakage, and pointing inaccuracies represent the most critical sources of spurious B-mode contamination. Their mitigation requires a combination of careful optical design, stringent pre-deployment calibration, and advanced analysis techniques. *(iii) Calibration:* accurate calibration underpins the reliability of all measurements, with a particular emphasis on the absolute determination of the polarization angle. Achieving an error below 0.1° is a strict requirement for unbiased recovery of B-modes. Several calibration methods, including astrophysical sources, ground-based polarized calibrators, self-calibration techniques, and artificial calibrators, have been developed, each with its own advantages and limitations. The theoretical, observational, and methodological elements outlined here form the basis for the experimental studies presented in the rest of this thesis.

Chapter 3

Kinetic Inductance Detector technology for millimeter wavelength radiation

Contents

3.1 From photons to electrical signals **70**
3.2 Foundations of superconductivity **71**
3.2.1 Superconducting materials 71
3.2.2 Transition temperature and superconducting gap 71
3.2.3 Quasi-particle generation and recombination 72
3.2.4 Meissner effect 72
3.3 Kinetic Inductance Detectors **73**
3.3.1 Resonating circuits and the RLC model 74
3.3.2 Working principle 75
3.4 Lumped Element KIDs as photon absorbers **75**
3.4.1 LEKID pixel coupling and array design 78
3.4.2 Readout electronics 79
3.4.3 Photometry and polarimetry with LEKIDs 80
3.4.4 Scientific applications and instrumentation using KIDs 83
3.5 Fabrication of an aluminum LEKID array **85**
3.5.1 Step 1: choice of the substrate 85
3.5.2 Step 2: deposition of the superconductor layer 85
3.5.3 Step 3: deposition of the ground plane 86
3.5.4 Step 4: photolithography (patterning through mask) 86
3.5.5 Step 5: wet etching 86
3.5.6 Step 6: microscopy inspection 87
3.5.7 Step 7: dicing, holder installation and bonding 88
3.6 Cryogenic characterization of LEKID arrays **89**
3.6.1 VNA scans 89
3.6.2 Quality factors 89
3.7 Conclusion **93**

Abstract The GIS-KID (Groupement d'Interet Scientifique KIDs) collaboration of Grenoble has been actively involved in the development of Kinetic Inductance Detector (KID) technology for several decades, covering a wide range of applications: from millimeter-wave astronomy to visible-light instrumentation and dark matter searches.
In this chapter, we start by providing an overview of the working principle of KIDs, from the fundamental concepts of superconductivity, followed by the design of superconducting resonators, and the mechanisms of radiation absorption in the specific case of Lumped Element KIDs (LEKIDs). The discussion then proceeds to the assembly of detectors into large-scale arrays, the architecture of readout electronics for multiplexed operation, and finally, the complete fabrication process of an aluminum LEKID array for laboratory use. A typical cryogenic characterization of these arrays is also detailed, emphasizing their advantages over competing detector technologies and their versatility for both photometric and polarimetric applications.
My contribution to this work focused on fabricating two functional LEKID arrays in a cleanroom environment. Subsequently, I tested these arrays in the cryogenic laboratory at LPSC. In this context, I performed a complete electrical characterization, including Vector Network Analyzer (VNA) scans, detection of resonances, and fitting procedures to extract key parameters such as the internal and coupling quality factors.

3.1 From photons to electrical signals

In the previous chapter, we examined the methods and techniques used to extract polarization from an unpolarized background, with a particular focus on CMB polarization. This discussion took us through the fundamental challenges of E-to-B mode leakage, contamination by extragalactic and galactic foregrounds, atmospheric interference, and instrumental systematic effects. These factors underscore the complexity of extracting and analyzing polarized radiation, emphasizing the necessity of robust and precise measurement techniques. To complete this chain of measurement, we must address the critical role of detectors. Detectors can be seen as the final "eyes" of observational astronomy, converting incoming electromagnetic radiation captured by the instruments into data that can be analyzed. The performance of these detectors directly impacts the quality of the data collected and, consequently, the reliability of the scientific conclusions drawn.
The detection of polarized radiation is particularly challenging, due to its typically faint intensity, easily distorted by noise, instrumental systematics, or inadequate sensitivity. As such, advanced detector technologies are required to achieve the precision necessary for modern astronomical studies. From bolometers and Transition Edge Sensors (TES) (Irwin 2005 [153]) to Kinetic Inductance Detectors (KIDs) (Zmuidzinas et al. 2002 [305], Zmuidzinas et al. 2004 [304], Baselmans et al. 2007 [23]), each type of detector has unique attributes and specific advantages for measuring polarization. These devices have been developed to ensure high sensitivity, minimal noise, and robustness against systematic errors. Superconducting detectors, in particular, have revolutionized the field of millimeter and sub-millimeter astronomy (Day et al. 2003 [84]). Their ability to operate at cryogenic temperatures, combined with their unparalleled sensitivity to faint signals, makes them indispensable for polarization studies. Technologies like bolometers, which measure radiation by detecting minute temperature changes, and TESs, which exploit the sharp resistance change at the superconducting transition, have been widely used in CMB experiments so far.
Since all the measurements and observations conducted for this thesis relied on KIDs, and Lumped Element KIDs (LEKIDs) in particular, this entire chapter is dedicated to these superconducting detectors.

3.2 Foundations of superconductivity

Superconductivity is a quantum mechanical phenomenon observed in certain materials when cooled below a critical temperature T_c. A full detailed review on superconductivity can be found in Bardeen 1957 [22], while in this section we only provide the main concepts and physical variables involved. The phenomenon of superconductivity is characterized by two properties: the complete absence of electrical resistance and the expulsion of magnetic fields, which is known as the Meissner effect (Bardeen 1955 [21]). These effects result from the collective behavior of electrons forming Cooper pairs—bound pairs of electrons with opposite momenta and spin—that move without scattering through the material.

3.2.1 Superconducting materials

Superconductivity is a phenomenon that only occurs in certain materials, and the precise conditions that enable it remain not fully understood. Broadly, superconducting materials can be categorized into elemental superconductors, inter-metallic compounds, high-temperature superconductors, and engineered hetero-structures. Among elemental superconductors, materials such as aluminum, lead, and niobium are well-known examples that transition to a superconducting state below their respective critical temperatures (e.g., 1.2 K for aluminum, 7.2 K for lead, and 9.3 K for niobium). These elements typically have relatively low electron-phonon scattering and suitable conduction electron densities. In contrast, noble metals like gold, silver, and copper do not exhibit superconductivity under any known conditions, likely due to their high density of conduction electrons and weak electron-phonon coupling.
Remarkably, superconductivity has also been observed in certain semiconductors and insulators when doped or structured appropriately. For instance, doped silicon and diamond can exhibit superconducting behavior at low temperatures. Even more exotic are the high-temperature superconductors, such as the cuprates and iron-based superconductors, which can remain superconducting at temperatures well above the boiling point of liquid nitrogen. These materials, however, are typically not used in applications like KIDs due to fabrication complexity and challenges in achieving uniform film properties.
In recent years, bi-layer and multilayer hetero-structures have emerged as powerful tools to engineer superconducting properties. These structures typically consist of a superconducting layer (e.g., aluminum or niobium) deposited on a normal metal or dielectric substrate. Bi-layers can be designed to tailor the transition temperature, quasi-particle dynamics, or kinetic inductance, making them highly relevant for detector applications. For instance, in the context of LEKIDs, aluminum bi-layers or tri-layers can be used to optimize sensitivity and improve impedance matching with the readout circuitry. Such composite films can also help mitigate material-related losses and enable greater flexibility in device design.

3.2.2 Transition temperature and superconducting gap

In the specific case described before, the transition to the superconducting state occurs when a material is cooled below its critical temperature T_c. At this temperature, the thermal energy becomes insufficient to disrupt the Cooper pairs, leading to the emergence of superconductivity. The Bardeen-Cooper-Schrieffer (BCS) theory provides the theoretical framework to describe this transition and the associated energy gap Δ, which separates the superconducting ground state from the normal electronic states.
The superconducting gap is temperature-dependent and follows the approximate relation at temperatures close to absolute zero:

$$\Delta(T) \approx 1.76\ k_B\ T_c\,, \tag{3.1}$$

where k_B is Boltzmann's constant. As the temperature approaches T_c, the gap closes, vanishing at the critical temperature. The energy gap is directly related to the binding energy of Cooper pairs and serves as a key indicator of the strength of the superconducting state. The temperature dependence of $\Delta(T)$ can be further described by the BCS relation:

$$\Delta(T) = \Delta_0 \tanh\left(\frac{\pi T_c}{\Delta_0}\sqrt{\alpha\left(\frac{T_c}{T}-1\right)}\right), \tag{3.2}$$

where $\Delta(0)$ is the superconducting gap at absolute zero and α is parameter dependent upon the particular pairing state.

3.2.3 Quasi-particle generation and recombination

In the superconducting state ($T \ll T_c$), photons with energies higher than twice the superconducting gap (2Δ) break Cooper pairs into quasi-particles. These quasi-particles are unstable and recombine into Cooper pairs through phonon emission. In thermal equilibrium, the balance between generation and recombination maintains a constant quasi-particle density.
The density of thermally excited quasi-particles, n_{qp}, is proportional to the density of states N_0 and the Fermi distribution function $f(E)$:

$$n_{\mathrm{qp}}(T) \propto \int_{\Delta}^{\infty} E\sqrt{E^2-\Delta^2} f(E)\,\mathrm{d}E\,, \tag{3.3}$$

where N_0 is the single-spin density of states at the Fermi surface, and Δ is the energy gap. For $k_B T \ll \Delta$, the quasi-particle density approximately follows an exponential dependence:

$$n_{\mathrm{qp}} \approx 2N_0\sqrt{2\pi k_B T\Delta}\exp\left(-\frac{\Delta}{k_B T}\right). \tag{3.4}$$

The quasi-particle lifetime τ_{qp} measures the average time a quasi-particle remains above the gap energy before recombining. At low temperatures ($T \ll T_c$), the lifetime can be expressed as:

$$\frac{1}{\tau_{\mathrm{qp}}} \propto T^{1/2}\exp\left(-\frac{\Delta}{k_B T}\right). \tag{3.5}$$

Under continuous photon absorption, the equilibrium number of excess quasi-particles, n_{excess}, is given by:

$$n_{\mathrm{excess}} = \frac{\eta P \tau_{\mathrm{qp}}}{\Delta}, \tag{3.6}$$

where P is the optical power and η is the quasi-particle creation efficiency. These fluctuations in quasi-particles form the fundamental signal in pair-breaking detectors, where incident power is detected through changes in the quasi-particle population.

3.2.4 Meissner effect

As mentioned in the introduction, the Meissner effect is a fundamental property of superconductors, characterized by the expulsion of magnetic flux from the interior of a superconducting material when it transitions below its critical temperature (T_c) in the presence of an external magnetic field (Bardeen 1955 [21], Tinkham et al. 1996 [291]). This phenomenon demonstrates the perfect diamagnetism of superconductors, as the magnetic field inside the material is reduced to zero.

Mathematically, the Meissner effect is described by the London equations, which relate the super-current density to the magnetic field. The characteristic length scale over which the magnetic field is expelled is known as the London penetration depth, λ_L. This effect is a key distinction between superconductors and perfect conductors, as the latter would allow magnetic flux to remain trapped rather than being expelled. See Fig. 3.1 for a visual representation of the Meissner effect.

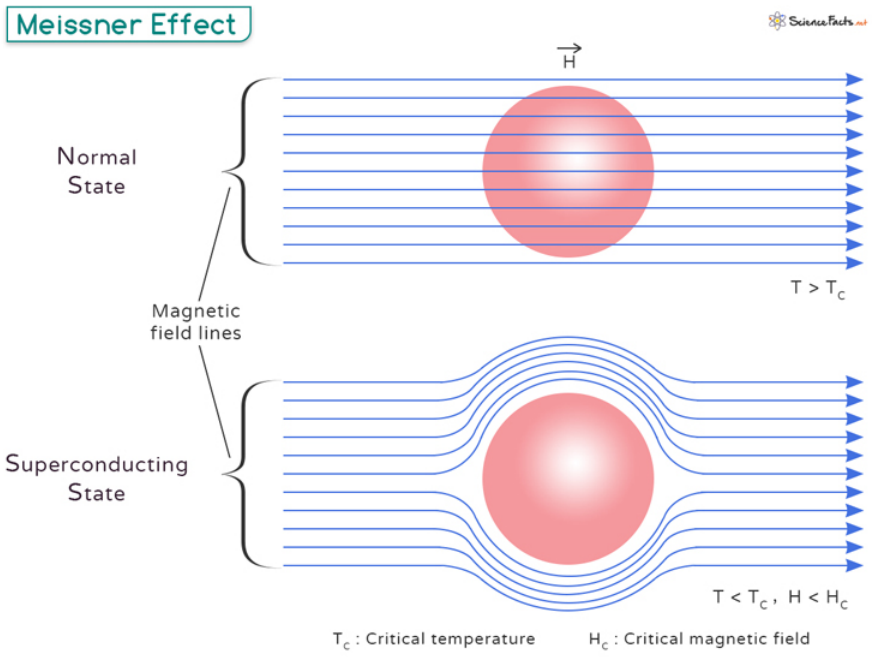

Figure 3.1: Below the critical temperature (Tc), superconductors exhibit perfect diamagnetism by expelling internal magnetic fields through surface currents, resulting in a magnetic susceptibility (χ) of -1. Source: https://www.sciencefacts.net/meissner-effect.html.

3.3 Kinetic Inductance Detectors

Kinetic Inductance Detectors (KIDs) were first developed by P. Day and his team at the California Institute of Technology and the Jet Propulsion Lab in 2003 (Day et al. 2003 [84]). They exploit the intrinsic properties of superconducting materials to detect incoming radiation. In particular, they leverage the kinetic inductance effect, a phenomenon that arises from the inertia of Cooper pairs. When an alternating current flows through a superconducting film, energy is stored not only in the magnetic field (geometric inductance) but also in the kinetic motion of the Cooper pairs. This latter contribution is known as the kinetic inductance.
In a simplified model, the total inductance L in a superconducting circuit is the sum of the geometric inductance L_m and the kinetic inductance L_k:

$$L = L_m + L_k \,. \tag{3.7}$$

The magnetic energy stored due to this total inductance is:

$$W = \frac{1}{2} L I^2 \,, \tag{3.8}$$

where I is the current in the circuit.

The kinetic inductance arises due to the inertia of charge carriers and can be expressed as:

$$L_k = \frac{m}{ne^2}\frac{l}{a}\,, \tag{3.9}$$

where m is the effective mass of the carriers, n their number density, e the elementary charge, l the length of the conductor, and a its cross-sectional area. This contribution is typically negligible in normal metals because of frequent electron scattering, but becomes significant in superconductors where dissipation is strongly suppressed and scattering is minimal.
In thin superconducting films where the film thickness $d \ll \lambda_L$ (the London penetration depth), the kinetic inductance can dominate the total inductance. The surface inductance L_s in such cases is related to the imaginary part of the complex conductivity σ_2 as:

$$L_s = \frac{1}{\omega\sigma_2 d}\,, \tag{3.10}$$

with ω the angular frequency of the signal. The fraction of total inductance due to kinetic effects is described by the kinetic inductance fraction:

$$\alpha = \frac{L_k}{L_m + L_k}\,. \tag{3.11}$$

The temperature dependence of the superconducting film enters through the effective penetration depth:

$$\lambda(T) = \frac{\lambda_L(T)}{d}\,, \tag{3.12}$$

which increases with temperature as fewer Cooper pairs are available to carry the current. At very low temperatures ($T \ll T_c$), the response of the superconductor becomes purely reactive and its impedance is given by:

$$Z(\omega) = i\omega L_k\,, \tag{3.13}$$

enabling highly sensitive resonant circuits that respond to small variations in absorbed radiation.

3.3.1 Resonating circuits and the RLC model

The working principle of KIDs relies on embedding the superconducting inductor in a resonating circuit. The simplest example is an RLC circuit, composed of a resistor R, an inductor L, and a capacitor C. Its impedance is given by:

$$Z(\omega) = R + i\omega L - \frac{i}{\omega C}\,. \tag{3.14}$$

At resonance, the inductive and capacitive reactances cancel each other:

$$\omega_0 L = \frac{1}{\omega_0 C}\,, \tag{3.15}$$

yielding the resonance frequency:

$$\omega_0 = \frac{1}{\sqrt{LC}} \quad \text{or} \quad f_0 = \frac{1}{2\pi\sqrt{LC}}\,. \tag{3.16}$$

The sharpness of the resonance is quantified by the quality factor:

$$Q = \frac{\omega_0}{\Delta\omega} = \frac{1}{R}\sqrt{\frac{L}{C}}, \tag{3.17}$$

where $\Delta\omega$ is the bandwidth around the resonance.
In KIDs, the inductance L includes the temperature- and radiation-dependent kinetic inductance L_k, making the resonance frequency f_0 sensitive to changes in the absorbed optical power. As photons are absorbed by the superconducting film, they break Cooper pairs into quasi-particles, modifying L_k and hence shifting the resonance frequency. This shift is the core observable in KID-based detection.
Therefore, KIDs function as high-Q resonators whose frequency encodes the incoming optical signal. Their operation depends intricately on the properties of the superconducting material, the geometry of the resonator, and the readout electronics, which together define their sensitivity and bandwidth.

3.3.2 Working principle

When a photon with sufficient energy strikes the detector array, it breaks Cooper pairs, creating quasi-particles. This process changes the kinetic inductance of the system, which in turn affects the resonance characteristics of the circuit (Mazin et al. 2020 [194]). As the kinetic inductance L_k increases due to the generation of quasi-particles, the resonance frequency f_0 shifts to a lower value, as demonstrated by Eq. 3.16. This shift Δf is proportional to the energy deposited by the incoming photon, enabling precise measurement of the radiation's intensity. Mathematically, the shift in resonance frequency can be expressed as:

$$\Delta f \propto -\Delta L_k,$$

where ΔL_k represents the change in kinetic inductance induced by the absorption of a photon. The negative sign indicates that an increase in L_k leads to a decrease in f_0.
In practice, every KID in an array is tuned to a distinct frequency, serving both as an identifier of their position on the array and a practical solution to the multiplexing problem. The resonance frequency is controlled geometrically by changing the capacitance of the inter-digitated capacitors of each detector. The schematic representation of the described working principle is shown in Fig. 3.2.
KIDs operate based on the principles of superconductivity, which are inherently sensitive to external magnetic fields. Below their critical temperature, superconductors exhibit the Meissner effect, expelling magnetic fields from their interior, as mentioned earlier in this chapter. However, if the external magnetic field exceeds a critical threshold, it can disrupt the superconducting state or interfere with the surface currents and kinetic inductance that KIDs rely on for their precise operation. This sensitivity necessitates robust magnetic shielding of the cryostat housing the KIDs. Shielding protects the detectors from stray magnetic fields, including Earth's magnetism and interference from nearby equipment, ensuring stable superconducting conditions and accurate measurements.

3.4 Lumped Element KIDs as photon absorbers

The absorption of millimeter and sub-millimeter radiation is a fundamental challenge for detectors in astrophysical and cosmological applications. To efficiently absorb incident radiation from free space, a detector must match the impedance of free space ($Z_0 \simeq 377\ \Omega$). In KIDs,

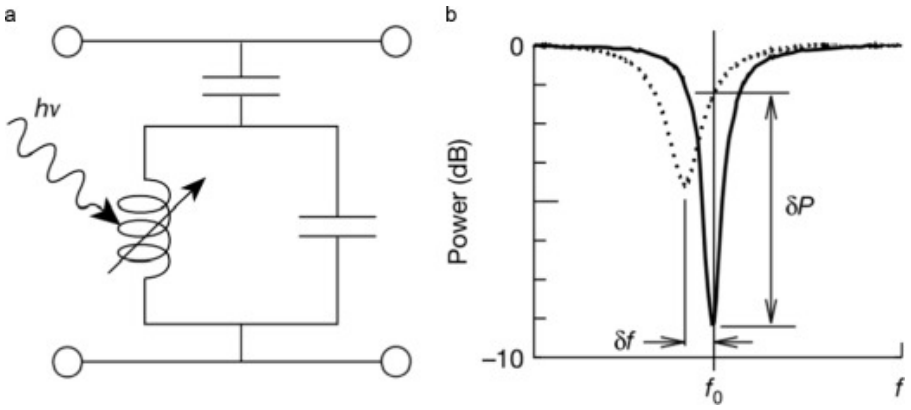

Figure 3.2: KIDs working principle: when a photon with sufficient energy ($\sim$ superconductor gap) to break the Cooper pairs of the material hits the detector (*left*), a shift in the resonance frequency of the circuit is observed (*right*). Source: https://cmb.physics.wisc.edu/kinetic-inductance-detectors/.

this can be achieved in two ways: either by coupling the resonator to free space through an antenna and lens system (antenna-coupled KIDs), or by designing the resonator itself as a direct absorber of radiation, as in the case of Lumped Element KIDs (LEKIDs) (Doyle et al. 2008 [90]).
In the LEKID architecture, the inductive section of the resonator is shaped as a meandered line that directly absorbs incoming radiation. This inductive meander is fabricated from a superconducting thin film, typically aluminum or a titanium-aluminum bi-layer, and is designed with a pitch much smaller than the incident wavelength ($p \ll \lambda$), so that the structure appears homogeneous to the incoming wave. The overall pixel dimensions are instead matched to the wavelength to enable efficient coupling. When back-illuminated through a silicon wafer of optimized thickness, the absorber forms a resonant cavity that maximizes absorption through constructive interference. The thickness of the silicon wafer is usually chosen to satisfy the criterion:

$$d = \frac{\lambda_{\mathrm{Si}}}{4n}\,, \tag{3.18}$$

where λ_{Si} is the wavelength of the targeted radiation in silicon and n is the refractive index of silicon at the observing frequency. At millimeter wavelengths, $n_{\mathrm{Si}} \approx 3.4$. This relation assumes that no backshort cavity or vacuum layer is present behind the silicon substrate. In this configuration, the silicon itself acts as a dielectric spacer in a Fabry-Pérot-like resonant structure.
In some KID designs, a reflective surface known as a backshort is placed at a precise distance behind the detector to enhance absorption efficiency. This configuration forms a resonant optical cavity, where the backshort reflects the incoming radiation back toward the absorber. By tuning the spacing between the absorbing film and the backshort, constructive interference at the location of the absorber can be achieved, thereby maximizing the power absorbed. The optimal backshort distance corresponds to an odd multiple of one-quarter of the free-space wavelength:

$$d_{\mathrm{backshort}} = \left(m + \frac{1}{2}\right)\frac{\lambda_0}{2}, \quad m \in \mathbb{Z}\,, \tag{3.19}$$

where λ_0 is the free-space wavelength of the incident radiation. In practice, the simplest configuration with $m = 0$ is typically used, corresponding to $d_{\mathrm{backshort}} = \lambda_0/4$. When a silicon substrate of finite thickness is present between the absorber and the backshort, the total optical

path must be accounted for. In this case, the spacing should be chosen such that the phase accumulated in both silicon and vacuum yields constructive interference at the absorbing film. This is often optimized using full-wave simulations or by solving the optical cavity conditions numerically, taking into account the refractive index and the specific layer geometry of the detector stack.

At a microscopic level, the absorption mechanism relies on the breaking of Cooper pairs. A photon of frequency ν is absorbed when its energy exceeds twice the superconducting energy gap, meaning $h\nu > 2\Delta$, where Δ depends on the material. This interaction produces two quasi-particles, increasing the population of mobile excitations in the superconductor. Since the kinetic inductance is directly related to the Cooper pair density, the resulting change in quasi-particle population alters both the resonance frequency and the quality factor of the resonator. These changes are detected via a shift in the complex transmission S_{21} of the resonator, thus encoding the incoming photon signal, as explained in the working principle section.

The choice of superconducting material governs the spectral range over which the detector can absorb. For example, aluminum, with a critical temperature $T_c \sim 1.2$ K, yields a spectral cutoff around 90 GHz. To detect lower frequency photons (or longer wavelengths), materials with lower energy gaps must be used. This is commonly achieved with bi-layer structures, such as titanium-aluminum, which reduce the effective Δ and allow sensitivity down to 70 GHz or even lower. Consequently, LEKIDs can be designed to cover a wide frequency range — from $\sim$50 GHz up to several THz — by adjusting both material composition and pixel geometry.

From an electrical perspective, the LEKID is modeled as a lumped-element resonator, composed of an inter-digitated capacitor and the absorbing meandered inductor. The inductor contributes both geometric and kinetic inductance, the latter being sensitive to changes in the quasi-particle population. Importantly, this circuit must also be impedance-matched to free space in order to act as an efficient absorber. This is achieved by tailoring the sheet impedance of the superconducting film (via thickness, width, and material properties) so that the effective impedance of the absorbing structure approaches 377 Ω.

The architecture of LEKIDs offers several key advantages, which emerge naturally from their physical principles. Because the meander acts as both absorber and inductor, the optical design is simplified: there is no need for antennas, lenses, or dielectric matching layers, which reduces complexity and fabrication effort. Moreover, the time constant of LEKIDs (but KIDs in general), determined primarily by the quasi-particle recombination time, is naturally short, typically in the range of 20 to 70 μs depending on the optical background and material. This enables rapid response to changes in optical power, which is especially advantageous for fast scanning ground-based experiments or for time-domain astronomy.

The multiplexing capabilities of KIDs are another direct outcome of their resonant design. By assigning a unique resonance frequency to each pixel, hundreds of LEKIDs can be read out simultaneously over a single transmission line using frequency-domain multiplexing. This drastically reduces the wiring complexity and thermal load on the cryogenic system. In typical arrays, multiplexing factors of $\sim$400 are already standard.

Additionally, LEKIDs exhibit remarkable immunity to environmental disturbances. Since the readout relies on narrow-band changes around a GHz-scale resonance, the detectors are inherently less sensitive to broadband electromagnetic interference (EMI). Their response is also weakly dependent on small fluctuations in the base temperature of the cryostat, thanks to the exponential suppression of thermal quasi-particles at low temperature. In space applications, LEKIDs have shown to be about an order of magnitude less affected by cosmic ray hits compared to thermal detectors, due to the rapid recovery and localized response of the superconducting film (Monfardini et al. 2016 [204]).

Finally, the fabrication of LEKIDs is relatively straightforward and well-suited to batch processing. Arrays are fabricated using standard microfabrication techniques such as optical lithogra-

phy and thin-film deposition, without the need for multilayer alignments or complex sacrificial steps. This makes it possible to produce complete arrays in less than a day, significantly accelerating development cycles.
For all these reasons — fast response, broad spectral tunability, and scalability — LEKIDs have become a leading technology for millimeter and sub-millimeter photon detection.

3.4.1 LEKID pixel coupling and array design

The geometry of the meandered absorber in a LEKID pixel is tailored to the scientific objectives of the instrument. In particular, the absorber design determines the polarization sensitivity of the pixel. Two main geometries have been developed by the Grenoble group: the first is sensitive to a single linear polarization and consists of a linear meander aligned in one direction; the second adopts a fractal design based on a Hilbert curve, which enables sensitivity to two orthogonal polarization states simultaneously Roesch et al. 2012 [269]. The Hilbert geometry ensures a dense, space-filling meander that maintains symmetry and uniform absorption in both polarizations. A visual comparison between these two types of pixels is shown in Fig. 3.3.

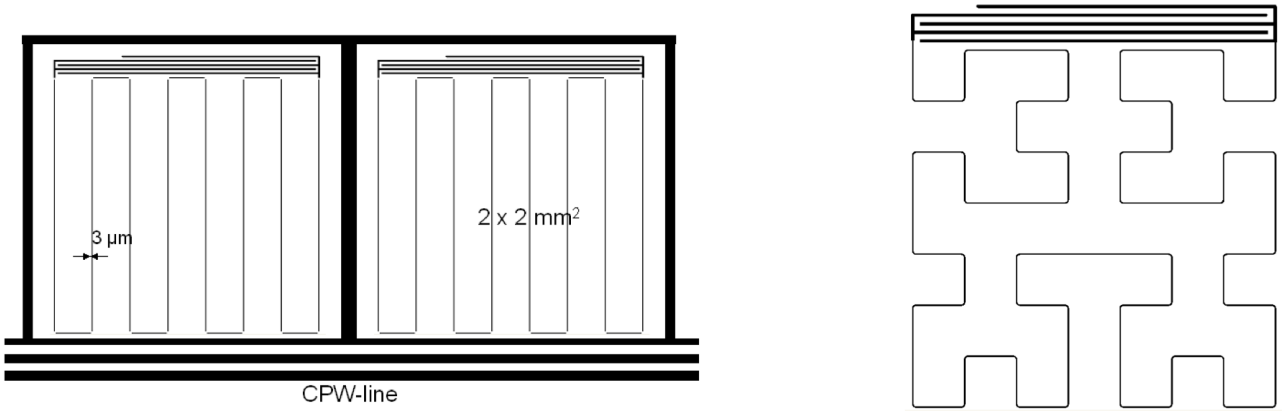

Figure 3.3: *Left:* schematic of two LEKID pixels. The resonators are coupled to a Co-Planar Waveguide (CPW) transmission line; the line width is 3 μm and the pixel size is approximately 2×2 mm^2. *Right:* LEKID pixel designed for dual-polarization sensitivity, using a third-order Hilbert curve. Figures adapted from Roesch et al. 2012 [269].

To couple a large number of LEKIDs to the readout electronics, resonators are placed along a common feedline that transmits the probing signal. Each resonator is tuned to a different frequency within the readout bandwidth, enabling frequency-domain multiplexing. Two principal feedline architectures are commonly used: the Co-Planar Waveguide (CPW) and the microstrip.
In the CPW configuration, the feedline consists of a central conductor flanked by ground planes on the same plane, with a small gap separating them. This planar geometry simplifies fabrication and provides low-loss transmission at cryogenic temperatures. However, the CPW mode is susceptible to the propagation of parasitic slotline modes, which can lead to impedance mismatch and resonance distortion. To suppress these unwanted modes, metallic wire bonds or air bridges are used periodically to connect the two ground planes, enforcing symmetry and preventing differential-mode propagation.
The microstrip alternative consists of a central conducting strip on one side of the substrate and a continuous ground plane on the opposite side. This configuration provides better control over the transmission mode and is less prone to parasitic coupling, but it is more complex to fabricate due to the need for backside ground plane deposition. In both approaches, the ground plane plays a crucial role in stabilizing the electromagnetic environment and ensuring

reproducible coupling to the resonators.
Each resonator in the array can be characterized by its quality factors, which describe how energy is stored and dissipated. The internal quality factor, Q_i, quantifies the intrinsic energy losses within the resonator due to material imperfections, quasi-particle generation, or two-level systems in the dielectric. The coupling quality factor, Q_c, describes the strength of the interaction between the resonator and the transmission line, or in other words how efficiently energy is transferred in and out of the resonator. The total quality factor is given by the harmonic sum:

$$\frac{1}{Q_{\text{tot}}} = \frac{1}{Q_i} + \frac{1}{Q_c}\,, \tag{3.20}$$

and determines the width of the resonance and the detector response time. The balance between Q_i and Q_c can be adjusted during design to optimize readout sensitivity and signal-to-noise ratio.

3.4.2 Readout electronics

Once the resonators are arranged and coupled along a feedline, the next step is to interface the LEKID array with a readout system capable of monitoring the response of each resonator in real time and in parallel. The standard KID readout scheme is based on the excitation of each resonator using a dedicated tone at its unique resonance frequency. By analyzing how each tone is modified after passing through the feedline, due to changes in the resonance conditions of the detectors, it is possible to reconstruct the optical signal absorbed by each pixel.
Each tone is a continuous wave (CW) excitation at a fixed frequency, typically in the range of 100 MHz to several GHz, depending on the design of the resonator. These tones are injected simultaneously into the feedline, forming a so-called frequency comb. After propagating through the resonators, the transmitted signal is compared to a reference copy of the original excitation to extract its in-phase (I) and quadrature (Q) components. Variations in the resonance due to photon absorption produce characteristic trajectories in the complex IQ plane, which are tracked to infer changes in absorbed power.
One of the major advantages of KID technology lies in the simplicity of the cold electronics. Two single coaxial lines are sufficient to inject the excitation comb and extract the transmitted signal from an entire block of resonators. This dramatically reduces the wiring complexity compared to other detector technologies, especially for large arrays.
The excitation line consists of a stainless-steel coaxial cable, routed from room temperature down to the sub-Kelvin stage of the cryostat. To minimize the transmission of thermal noise from higher temperature stages, the line is thermally anchored at each cryogenic stage and includes fixed attenuators at 4 K that filter thermal noise. The excitation power per resonator is typically on the order of 10 pW, sufficient to probe the resonator without causing unwanted heating or saturation. Note that this power is not dissipated at 100 mK, as everything is in a superconducting regime.
At the base temperature stage, the excitation line is wire-bonded with aluminum micro-bonds to the silicon wafer holding the detectors. On the readout side, a symmetric set of micro-bonds extracts the transmitted signal, which is then routed through a superconducting niobium coaxial cable to a cryogenic low-noise amplifier (LNA) placed at the 4 K stage. The LNA boosts the signal power while preserving its phase and amplitude information. The amplified signal is then passed through the upper cryostat stages and routed out to room temperature electronics. Outside the cryostat, the signal is processed by a dedicated warm electronics system. Within the Grenoble GIS-KID, the readout platform known as NIKEL (New IRAM KID ELectronics) has been developed for this purpose by Bourrion et al. 2016 [48]. The NIKEL readout is capable of generating and acquiring up to 400 tones over a 1 GHz bandwidth, and is used in

several large-format KID instruments, such as CONCERTO.
Tone generation is performed using field-programmable gate arrays (FPGAs), each controlling a subset of the frequency range via high-speed digital-to-analog converters (DACs). The generated sub-bands are digitally combined, shifted, and filtered to form the full excitation comb. This composite signal is upconverted to the desired readout band and injected into the detector feedline. After passing through the array and cryogenic amplification stage, the signal is downconverted, digitized by analog-to-digital converters (ADCs), and separated back into sub-bands.
Each FPGA processes its assigned sub-band independently, extracting I and Q for each tone with high time resolution. The modular design enables real-time tracking of resonance shifts and efficient data acquisition for hundreds of detectors per board. The boards are implemented in Advanced Mezzanine Card (AMC) format and hosted in a Micro-Telecommunication Computing Architecture (MicroTCA or MTCA) crate (Fig. 3.4). A central control and clocking board (CCSB) ensures synchronization between modules. Depending on the total number of pixels and bandwidth requirements, multiple boards or crates can be deployed for a single instrument.

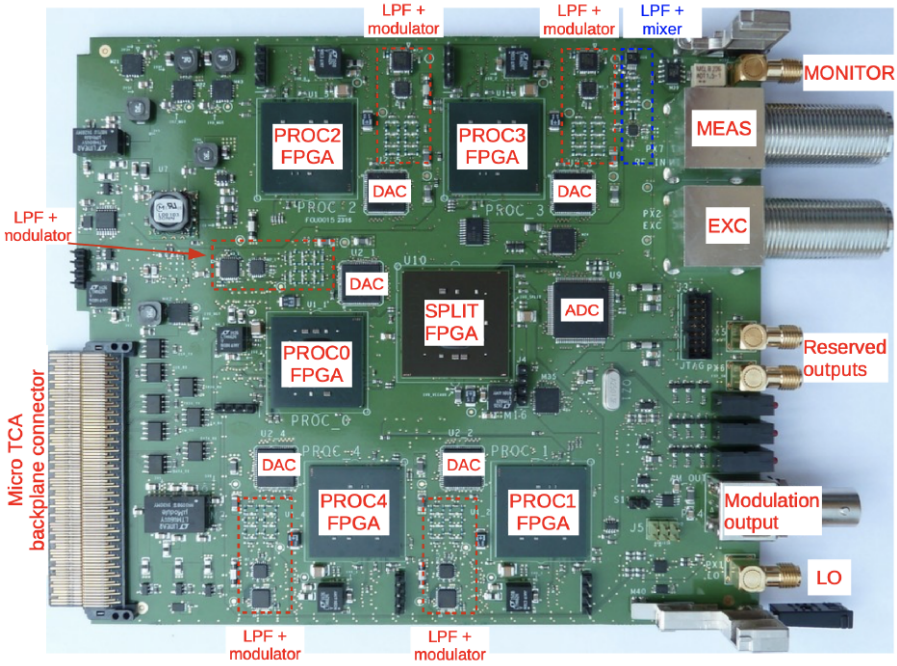

Figure 3.4: Readout Board designed and fabricated within the Grenoble Collaboration. Picture from Bourrion et al. 2016 [48].

The number of detectors that can be read out per feedline, the multiplexing factor, is a key performance parameter of KID systems. In the latest version of the NIKEL system, the multiplexing factor reaches up to 500 detectors per feedline, limited mainly by the total bandwidth, tone spacing (to avoid overlap), and achievable signal-to-noise ratio. This high multiplexing capability is critical to scaling up KID arrays to the kilo-pixel or even mega-pixel regime without a corresponding explosion in readout complexity or thermal load on the cryostat.

3.4.3 Photometry and polarimetry with LEKIDs

Now that we have completed the entire logical process of designing a single pixel, coupling multiple pixels into an array, and reading out their signal through a dedicated electronic system, we can discuss how LEKIDs are practically used for photometric and polarimetric observations.

In a typical observation, each LEKID pixel acts as a resonant absorber tuned to a specific optical frequency. When the telescope points to an astronomical target, the incoming radiation is focused onto the array and selectively absorbed by each resonator. Since each pixel is actively and continuously monitored via its resonance, every variation in absorbed power, whether due to the source brightness, background fluctuations, or instrumental effects, is encoded in the measured phase and amplitude response. This makes LEKIDs ideal tools for photometry: the detection chain is both direct and fast, with no need for intermediate thermalization stages or bolometric coupling, and the resonator responds to changes in optical power with a time constant of tens of μs. At frequencies around 300 GHz, LEKIDs based on appropriate low-gap materials (e.g., bilayers) still operate efficiently, though absorption efficiency and quasi-particle yield become more sensitive to material and design parameters.
When designed appropriately, LEKIDs can also measure the polarization of incoming radiation. For polarized millimeter-wave photons, a properly oriented absorber can preferentially couple to a specific polarization component. Standard linear meander designs, with the absorber oriented along a single axis, are intrinsically sensitive to one linear polarization only. This means that each pixel selectively absorbs photons whose electric field oscillates along the meander direction. To measure the full polarization state, a combination of two orthogonal pixels is needed.
The choice between single-polarization and dual-polarization pixels depends on the scientific goals and instrument architecture, but both configurations benefit from the same resonator physics and readout strategy. In both cases, a study on the cross-polarization contribution must be taken into account, meaning the leakage of signal from one polarization state into the orthogonal one, which can introduce systematic errors in the reconstruction of the true sky polarization. Accurate characterization of this effect, both through simulations and on-sky calibration, is essential to ensure the reliability of polarimetric measurements.
The transmission coefficient of a KID resonator is characterized by the scattering parameter S_{21}. This is a complex quantity that can be expressed in terms of its in-phase ($\mathcal{I}$) and quadrature ($\mathcal{Q}$) components as $S_{21} = I + jQ$, where j is the imaginary unit. The magnitude and phase of S_{21} are given by $|S_{21}| = \sqrt{I^2 + Q^2}$ and $\phi = \arctan(Q/I)$, respectively. By plotting I vs Q, a semi-circle is obtained, as shown in Fig. 3.5.

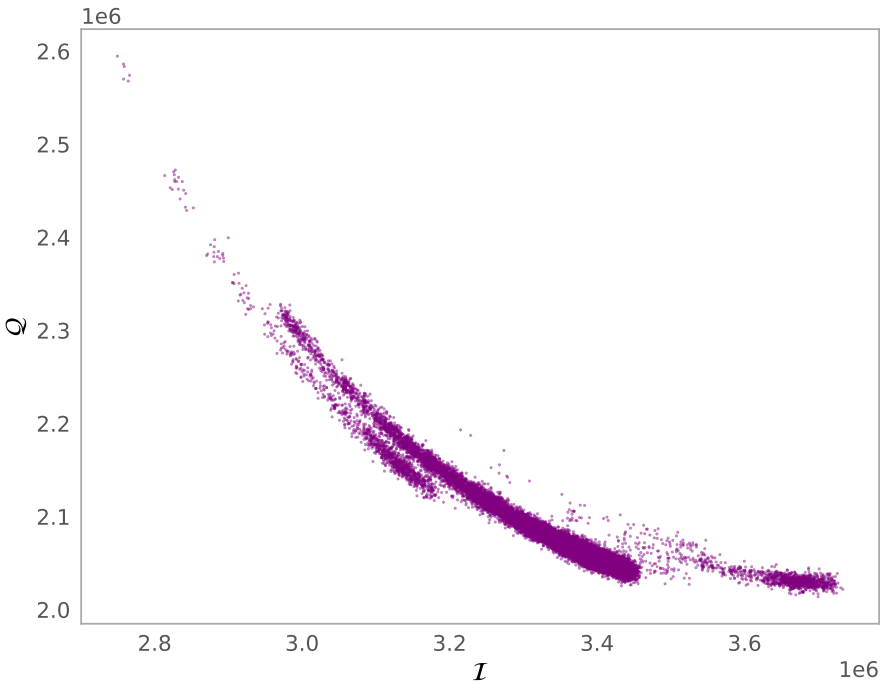

Figure 3.5: Example of $\mathcal{I}$ vs $\mathcal{Q}$ semi-circle.

2-point modulation A key feature in the readout scheme of LEKIDs is the modulation strategy, first developed for the NIKA prototype and later adopted for the final NIKA2 instrument (Catalano et al. 2014 [61], Calvo et al. 2013 [54]). The principle is to replace the standard excitation of the detectors, which relies on a single fixed tone, with an excitation using two tones generated around the resonant frequency. This is achieved by modulating the local oscillator by a few kHz, synchronously with the FPGA, to produce one tone just above and one just below the resonance. The FPGA then averages over ~ 50 points, providing a clean, low-noise signal. The advantage of this strategy is twofold: (i) by constructing differential measurements, $(dI/d\omega,\, dQ/d\omega)$, from the two tones, the system directly estimates the gradient of the resonance circle, and (ii) the frequency shift of the detector, $\Delta\hat{\omega}_0(t)$, can then be obtained by projecting the variations $(\Delta I(t),\, \Delta Q(t))$ onto this gradient:

$$\Delta\hat{\omega}_0(t) = \frac{(\Delta I(t),\, \Delta Q(t)) \cdot (dI/d\omega(t),\, dQ/d\omega(t))}{(dI/d\omega(t),\, dQ/d\omega(t))^2}\, \delta\omega_{\mathrm{LO}}. \tag{3.21}$$

As a result, each data point sent to the acquisition software contains both the raw values $(I(t), Q(t))$ and their differential counterparts, allowing for an accurate reconstruction of the resonance frequency evolution. Since this approach reduces the original sampling rate by a factor of ~ 50, it is particularly well suited for LEKID-based photometric instruments, where the required data rate is typically in the range of 10 - 100 Hz, depending only on the telescope scanning speed. The frequency shifts in Hz are then converted into flux densities (Jy/beam) through a calibration procedure (Perotto et al. 2020 [235]).

3-point modulation For interferometric instruments such as KISS and CONCERTO, the requirements on the acquisition sampling rate are much more stringent than for photometers like NIKA2. In order to follow the fast mirror motion of the FTS and preserve the spectral information, the readout must operate at several kHz. Under these conditions, the two-point modulation strategy adopted for NIKA2 cannot be applied, since it would require modulating the local oscillator at each sampling point, a rate beyond the capabilities of the FPGA. Instead, an alternative method is employed: the 3-point modulation is performed once per interferogram block, during short dead times when the mirrors are not moving, allowing us to monitor the optical background variations without exceeding the hardware limits.
The principle of 3-point modulation consists of modulating the readout tone of each KID around its central frequency: first with a positive offset, then with a negative offset, followed by acquisition with no modulation. This sequence enables both the extraction of the detector response and the rejection of common-mode noise. In practice, a typical data block is composed of 1024 samples: the first 64 samples are acquired with a positive frequency shift $(f_{\mathrm{tone}} + \Delta f_{\mathrm{LO}})$, the next 64 with a negative shift $(f_{\mathrm{tone}} - \Delta f_{\mathrm{LO}})$, and the remaining 896 samples are acquired without any modulation, as shown in Fig. 3.6. This configuration results in 87.5% of the data being dedicated to pure science observations, while 12.5% is used for calibration purposes.
The amplitude of the frequency modulation Δf_{LO} is chosen to be large enough to be easily detected in the presence of noise, yet small enough to preserve the linear regime of the detector response. Typical modulation values are 2-3 times larger than the expected signal, so for our purposes on the order of 5 to 10 kHz. Given the typical spacing between adjacent KID resonances (about 1.3 MHz), such modulation does not introduce interference between pixels. This technique is broadly applicable across a wide range of scientific targets and observing strategies, and is especially useful when signal stability and accurate calibration are required.

Calibration One of the challenges of working with KIDs is the conversion of the observed $\mathcal{I}$ and $\mathcal{Q}$ signal to absorbed optical power. One of the latest developed solutions consists in determining the center of the resonance circle and then extrapolating the calibration factor

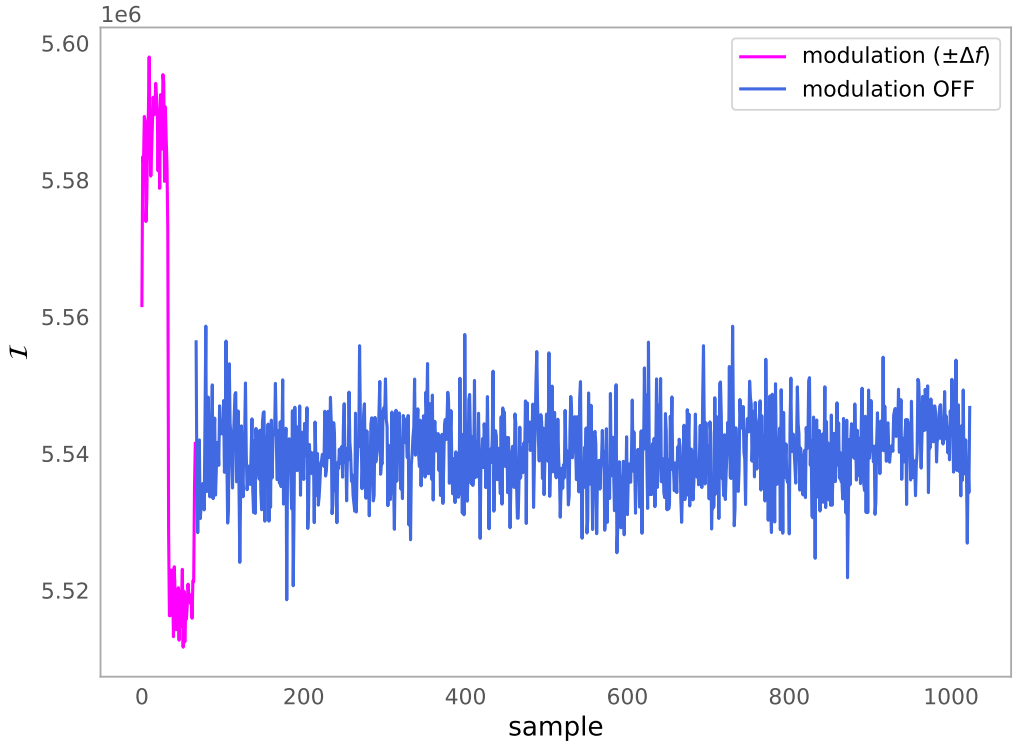

Figure 3.6: One sample data bloc for one KID. We plot $\mathcal{I}$ as a function of the sample number. In magenta we show the modulation points, in blue the "science" points.

C [Hz/rad] through a circular fit on the modulation points (x1, y1) and (x2, y2), as shown in Fig. 3.7.
By fitting these points, one can extrapolate the coordinates of the circle's center (Ic, Qc) and hence derive the angles ϕ_1 and ϕ_2 shown in the figure as:

$$\phi_1 = \arctan\left(\frac{I_c - x_1}{Q_c - y_1}\right), \tag{3.22}$$

$$\phi_2 = \arctan\left(\frac{I_c - x_2}{Q_c - y_2}\right). \tag{3.23}$$

From these results, the modulation factor is obtained as:

$$\Delta\phi = \phi_2 - \phi_1 \qquad \rightarrow \qquad C = \frac{\Delta\phi}{\Delta\omega}. \tag{3.24}$$

where $\Delta\omega$ is the modulation in Hertz set by the injecting tone.

3.4.4 Scientific applications and instrumentation using KIDs

A variety of KID-based instruments have been developed to address a wide range of scientific objectives, from continuum and polarization imaging to spectroscopic line-intensity mapping and cosmological studies. Instruments like NIKA and its successor NIKA2, operating at the IRAM 30-meter telescope, use dual-band arrays at 150 and 260 GHz for high-resolution continuum and polarization imaging of galactic and extragalactic sources (Catalano et al. 2016 [62]). Similarly, TolTEC at the Large Millimeter Telescope (LMT) extends this capability across three frequency bands (150, 214, and 260 GHz) (Austermann et al. 2018 [19]), while

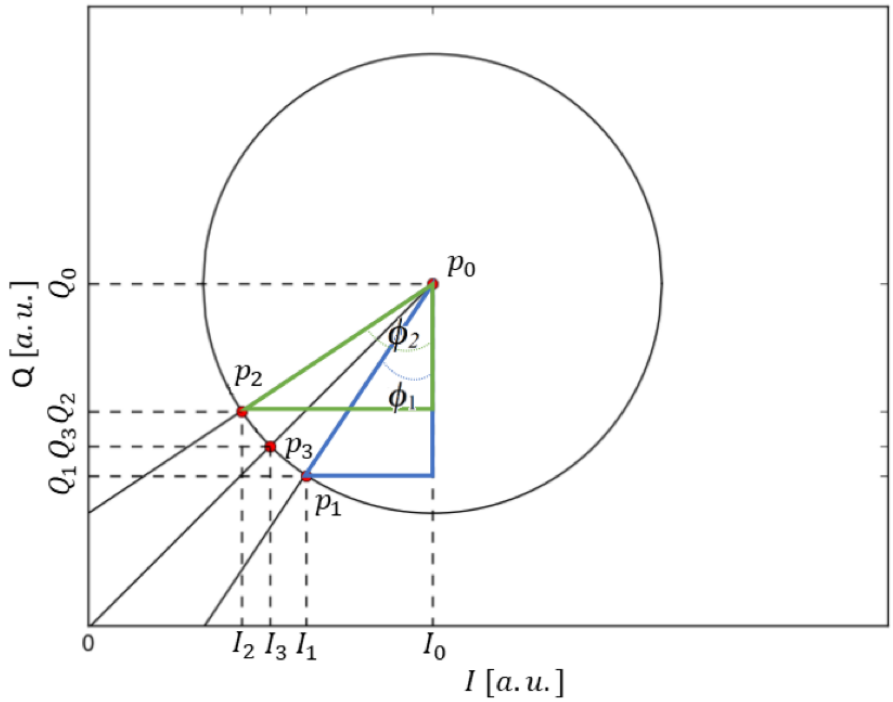

Figure 3.7: Resonance circle in the (I, Q) plane in [au]; $p_1 = (I_1, Q_1)$ and $p_2 = (I_2, Q_2)$ are the modulation points, while $p_3 = (I_3, Q_3)$ is the measurement point; p0 = (I_0, Q_0) is the circle center. From Fasano et al. 2021 [112].

MUSIC demonstrated multi-band imaging at 150, 220, 280, and 350 GHz from the Caltech Submillimeter Observatory (CSO) (Duan and Golwala 2020 [96]). Balloon-borne experiments such as OLIMPO and BLAST-TNG leverage the reduced atmospheric opacity at stratospheric altitudes to operate in the submillimeter range (150–460 GHz for OLIMPO and 600-1200 GHz for BLAST-TNG) (Paiella et al. 2019 [226]).
For spectroscopic and line-intensity mapping applications, on-chip filterbank spectrometers like DESHIMA, SuperSpec, A-MKID and SPT-SLIM have been developed. DESHIMA operates in the 220–440 GHz range and has been deployed on ASTE for on-sky demonstrations (Endo et al. 2012a/b [102], [103]). SuperSpec targets a narrower band (190–310 GHz) and has been tested at APEX (Wheeler et al. 2018 [296]). More recently, SuperSpec has been installed for a test campaign at LMT and preliminary data are under treatment right now. A-MKID, covering 300–360 GHz, remains a laboratory prototype (Baselmans 2018 [25]), while new perspectives at THz frequencies are being developed (Baselmans et al. 2022 [24]). CONCERTO, installed at APEX, is a wide-band imaging spectrometer (130–310 GHz) designed for intensity mapping of the [CII] line during the Epoch of Reionization and the Cosmic Dawn (CONCERTO Collaboration 2020 [71]. The SPT-SLIM project aims to use similar techniques at the South Pole Telescope, targeting frequencies between 220 and 400 GHz (Karkare et al. 2022 [161]).
In the domain of cosmology and CMB polarization, KID-based instruments are increasingly considered for ground-based and space-borne missions. GroundBIRD, operating at the Teide Observatory of Tenerife, uses KIDs at 145 and 220 GHz to detect B-mode polarization from the ground (Honda et al. 2020 [145]). On a larger scale, LiteBIRD, a planned space mission led by JAXA, might includes KID-based focal plane modules covering a wide frequency range (40–400 GHz) to measure the primordial CMB polarization signal with unprecedented sensitivity.

3.5 Fabrication of an aluminum LEKID array

As we said in Sec. 3.4, one of the main advantages on KIDs with respect to other cryogenic detectors is the relatively quick fabrication process. In fact, one complete LEKID array, for example, can be fabricated within 1-3 days, depending on the materials used and the layers deposited. Moreover, the success rate of one fully functional array is quite high, at least for in-lab measurements. For what concerns arrays destined to be used for on-sky observations, the performances must be extremely optimized. However, in both cases, every step in the fabrication process is delicate and must be handled with care to ensure the best performances. In the context of this thesis, one kind of LEKID array has been fabricated, and then tested, to be used for the in-lab measurements presented in Chap. 4. In this section, an outline of the fabrication steps is presented, with a description of the main materials, machines and techniques used. Steps from 1 to 6 were conducted in the PTA clean room facility in the CEA unit of Grenoble, while step 7 was conducted in the mechanical lab of Institut Néel.

3.5.1 Step 1: choice of the substrate

The fabrication process begins with the selection of an appropriate substrate, which serves as the base for the LEKID array. The substrate material must exhibit low dielectric losses and excellent thermal conductivity at cryogenic temperatures. Commonly used materials include high-resistivity silicon or sapphire, as they ensure minimal energy dissipation and optimal signal transmission. For the purpose of this fabrication, a silicon substrate has been chosen. The thickness of the substrate is chosen considering the target radiation frequency (Sec. 3.4). Following this criterion, the required thickness in this case was d = 350 μm. The 100 mm circular substrate is thoroughly cleaned to remove any impurities or residues, ensuring a pristine surface for subsequent deposition steps. Just before continuing to the following steps, the wafer is sprayed with $N2$ to remove dust and particle residues.

3.5.2 Step 2: deposition of the superconductor layer

The silicon substrate is then installed in the ion beam evaporator system (Plassys MEB550) to deposit the superconducting layer: aluminum, in our case. The Plassys MEB550 is a physical vapor deposition (PVD) unit that employs electron-beam thermal evaporation and offers additional functionalities, such as ion-beam etching and oxidation.
Prior to deposition, the substrate undergoes a 2'30" etching process using argon ions (Ar^+) to remove the native oxide layer (SiO_2). The etching rate depends on both the ion beam voltage and the angular orientation of the sample. In our setup, operating with a beam voltage of 300 V, a beam current of 14 mA, and an accelerating voltage of -60 V at a pressure of 10^{-4} mbar, the typical etch rate for SiO_2 is approximately 1.5 nm/min.
Following this, aluminum is deposited onto the substrate at a controlled rate of 0.25 nm/s until a final thickness of 20 nm is reached. Throughout the deposition, the sample holder is rotated at 5 rpm to ensure uniform coverage. The process is carried out in high vacuum, with a working pressure maintained below 10^{-7} mbar, to minimize contamination and enhance the quality of the deposited film.
In this method, electrons are accelerated toward an aluminum reservoir, transferring their kinetic energy upon impact. This energy causes aluminum atoms to be ejected from the target's surface in vapor form, which then condense onto the substrate, forming a uniform thin film. The electron beam evaporator is equipped with precise control systems to regulate the deposition rate and ensure homogeneity across the wafer.
The thickness of the aluminum layer is monitored in real time using a quartz crystal microbalance, which measures both the instantaneous deposition rate and the total film thickness with

nanometer precision. This technique ensures the production of a high-quality superconducting layer with excellent uniformity and adhesion, which is critical for the performance of LEKID detectors.

3.5.3 Step 3: deposition of the ground plane

The next step in the fabrication process involves depositing the ground plane on the opposite side of the silicon wafer. For this design, a multilayered ground plane consisting of aluminum (Al), titanium (Ti), and gold (Au) is used, with relative thicknesses of 100 nm, 50 nm, and 100 nm, respectively. The deposition of the ground plane is performed using the same ion beam evaporator machine as for the superconductor layer. The process involves selecting a predefined "recipe" in the machine's control system, which automates the sequential deposition of the three materials. Each layer is deposited at a controlled rate of 0.25 nm/s to achieve the desired thicknesses. The aluminum provides good conductivity and compatibility with the superconducting layer, titanium acts as an adhesive layer to improve bonding between the aluminum and gold, and gold ensures excellent conductivity and resistance to oxidation.

3.5.4 Step 4: photolithography (patterning through mask)

The wafer with the deposited superconductor layer is first coated with a positive photoresist, such as AZ1512HS, using a spin-coating process to achieve a uniform layer. After spin-coating, the wafer undergoes a soft-baking step at 100 °C for 2 minutes to fix the photoresist and prepare it for UV exposure. A UV mask aligner, the MJB4 in this case, is used for the photolithography process. Before exposure, the alignment between the mask and the substrate is optimized to ensure precise pattern placement. This involves carefully adjusting the substrate position relative to the mask, considering its shape and the intricacies of the mask design. Proper alignment is critical to maintaining the integrity of the LEKIDs pattern. During exposure, the photoresist layer is brought into soft contact with the mask, and UV light is directed through the transparent regions of the mask for 22 seconds. The UV radiation chemically alters the exposed photoresist, making it soluble in the developer solution while leaving the unexposed areas intact to serve as a protective layer. Following exposure, the wafer is developed using an AZ developer diluted with deionized (DI) water in a 1:1 ratio for 40 seconds. This process removes the exposed photoresist, leaving the desired LEKID pattern in the remaining photoresist. The wafer is then thoroughly rinsed with DI water and dried using nitrogen gas. A post-baking step at 120 °C for 2 minutes is performed to harden the remaining photoresist, ensuring it withstands subsequent processing steps.

3.5.5 Step 5: wet etching

After the photolithography process defines the LEKID pattern in the photoresist, the wafer undergoes wet etching to transfer this pattern into the underlying superconductor layer. Wet etching is a chemical process that selectively removes material from the wafer, exposing the areas not protected by the hardened photoresist. For aluminum, a common etchant is a solution composed of phosphoric acid (H_3PO_4), acetic acid (CH_3COOH), nitric acid (HNO_3), and deionized (DI) water in carefully controlled proportions. The wafer is immersed in the etchant, which reacts with the exposed aluminum, dissolving it away while leaving the photoresist-covered regions intact. The etching process is highly dependent on time and temperature, requiring precise control to avoid over-etching or under-etching the pattern. During this step, the wafer is constantly monitored to ensure that the etching progresses uniformly and that the desired pattern is fully transferred. After etching is complete, the wafer is removed from

the solution, thoroughly rinsed with DI water to stop the chemical reaction, and dried using nitrogen gas (N_2). The result of the wet etching process is a patterned superconductor layer that matches the LEKID design defined in the photolithography step. This step is critical as it shapes the resonators and other features essential for the functionality of the LEKID array. Fig. 3.8 visually summarizes the steps described to this point, from the silicon substrate to the final device after the clean room procedure.

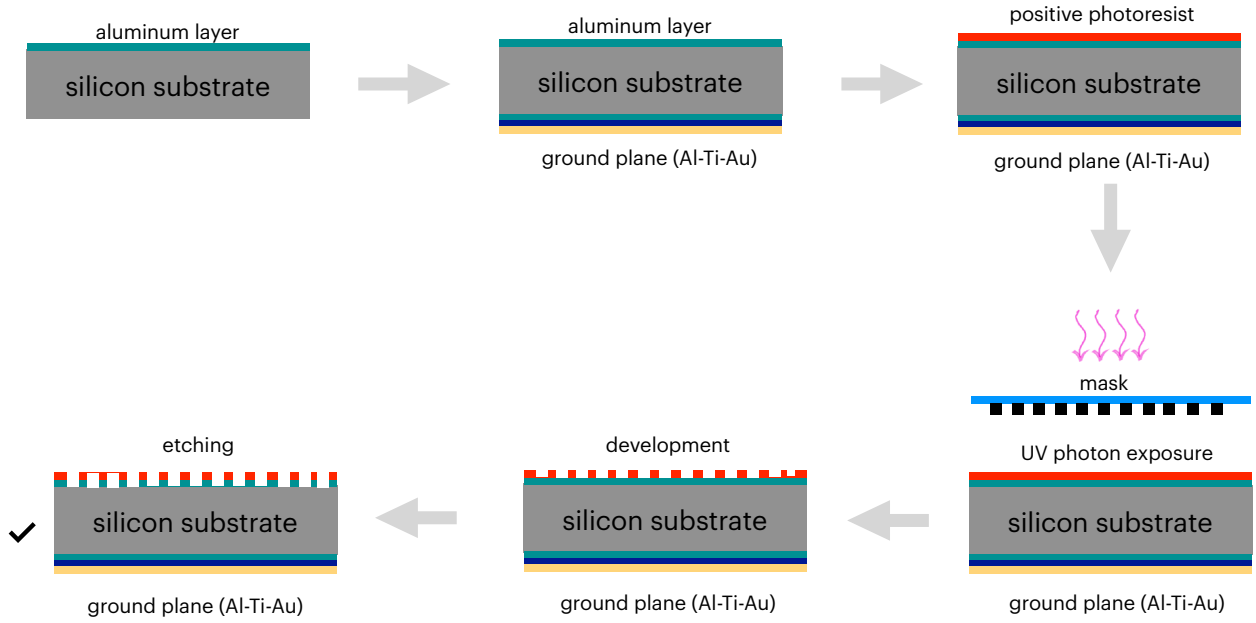

Figure 3.8: Steps conducted in the clean room to fabricate an aluminum LEKIDs array from a silicon substrate. Thickness proportions are not to scale.

3.5.6 Step 6: microscopy inspection

Once the previous steps have been successfully completed, the wafer undergoes microscopy inspection to verify the integrity of the obtained LEKIDs pattern. This step is essential to identify any fabrication flaws that could negatively impact the performance of the array or disrupt subsequent measurements. Common issues detected during this inspection include incomplete etching, which may leave residual material in the regions meant to be clear; over-etching, where the superconductor layer is excessively removed, potentially damaging the resonator structures; and alignment errors, where the mask pattern does not perfectly match the intended position on the substrate. Additional defects such as irregularities in the photoresist layer, scratches on the wafer surface, or particle contamination may also be observed. Microscopy tools, such as optical microscopes or scanning electron microscopes (SEM), are employed to examine the wafer at high magnification, ensuring detailed visualization of the pattern. Any imperfections identified during this step are documented and analyzed to determine their impact on the array's performance and to refine the fabrication process for future iterations. For example, Fig. 3.9 highlights three common fabrication defects. These imperfections are likely caused by residual impurities introduced during the fabrication process. The most critical defect is one that affects the feedline. While damage to a single pixel results in the loss of just one pixel out of ∼400, an interruption in the feedline compromises the entire array, rendering it unusable.

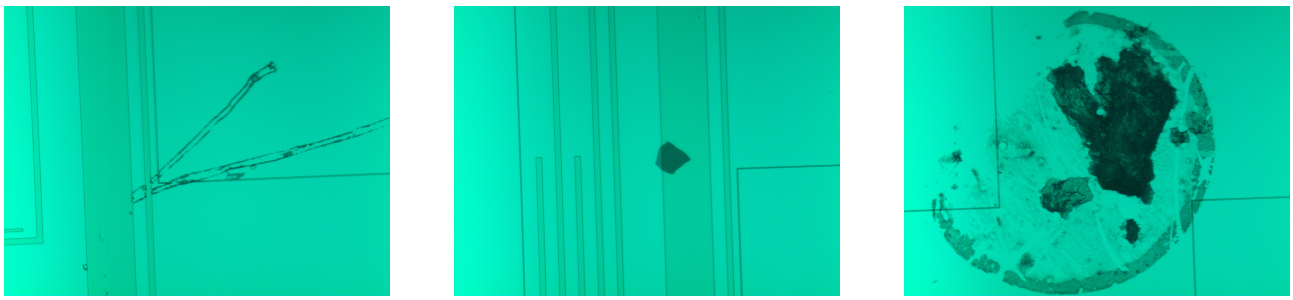

Figure 3.9: Three examples of fabrication defaults that can potentially impact the functioning of the array, detected using a microscope in the clean room.

3.5.7 Step 7: dicing, holder installation and bonding

The final step in the fabrication process involves preparing the wafer for practical use through dicing, mounting the array onto a dedicated holder, and wire bonding. Dicing is performed to cut the wafer into the required 66 mm square array using a high-precision diamond saw. This operation is carried out outside the clean room, specifically in the mechanical lab at Institut Néel, ensuring minimal mechanical stress on the structure while achieving precise dimensions. Once diced, the array is installed onto a custom-designed holder, typically made of aluminum or copper to ensure thermal and mechanical stability. The holder features specific alignment pins and clamps to securely fix the array in place, ensuring proper positioning for subsequent connections and cryogenic operation.
The final step involves wire bonding, which is performed to establish electrical connections between the LEKIDs array and the external readout electronics. Gold or aluminum wires are used for bonding due to their excellent conductivity and compatibility with cryogenic environments. This process requires extreme precision to avoid damaging the delicate structures of the array while ensuring robust and reliable connections.
The final outcome of all the fabrication processes described so far is shown in Fig. 3.10.

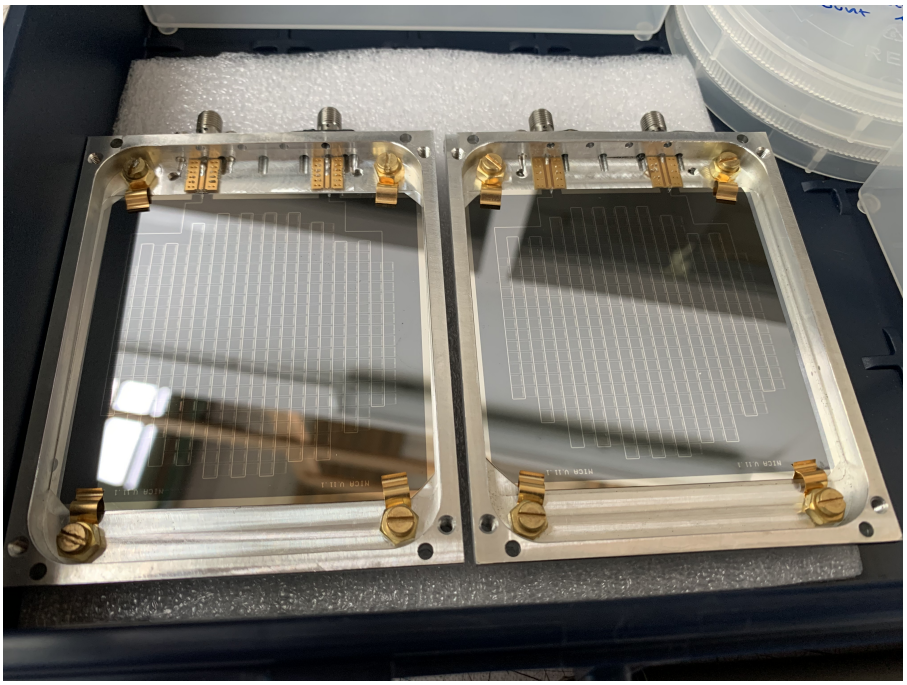

Figure 3.10: Picture of two LEKID aluminum arrays fabricated by myself, mounted on dedicated aluminum holders and ready to be installed in the cryostat for testing.

3.6 Cryogenic characterization of LEKID arrays

Following fabrication in the clean room, arrays are subject to performance evaluation in the cryogenic facility of LPSC. I have characterized two pairs of LEKID arrays: the pair displayed in Fig. 3.10 and the pair used for polarization measurements presented in Chap. 4 and in Savorgnano et al. 2025a [276]. These two pairs differ in their targeted optical wavelength: the first is designed to absorb photons at 1 mm, the second at 2 mm. The specifics of the testing platform and methodology will be elaborated in Chap. 4. The primary objective of these tests is to verify the proper functioning, efficiency, cosmetics and overall performance of the newly fabricated arrays. To qualify for scientific use, an array must meet a stringent set of performance criteria. Arrays that fail to meet these standards are deemed unsuitable, requiring their erasure and the re-initiation of the fabrication process from the beginning. This happened for arrays at 1 mm, so the final presented outcome is the result of several attempts.

3.6.1 VNA scans

A Vector Network Analyzer (VNA) is an instrument used to measure the response of a device under test across a range of frequencies. By transmitting a signal and analyzing the reflected and transmitted waves, the VNA provides information about the device's scattering parameters (S-parameters), which describe how the device responds to electromagnetic waves. In the context of this work, a VNA scan is employed to detect the resonances of the fabricated LEKID array. These resonances correspond to specific frequencies at which the detectors exhibit a distinct dip in transmission due to their unique resonant structures. Using this method, we can isolate and identify a number of resonances within the array, depending on the quality of the fabrication, ensuring that each resonator operates at its designated frequency for optimal performance.
Since the cryostat used for this characterization can host two arrays at the same time, we always work in pairs, both for fabrication and testing. To be coherent with the nomenclature used in Chap. 4, we refer to AT to indicate the transmission array, and to AR to indicate the reflection array. The meaning of such configuration will be clear in the following chapter. For the moment, we only focus on testing these arrays regardless of their future utilization.
In Figs. 3.11 and 3.12, we show the feedlines obtained by VNA scans of the two pairs of tested arrays, at 1 and 2 mm respectively.

3.6.2 Quality factors

The transmission coefficient $S_{21}(f)$, measured from the VNA scan around a resonance, exhibits a characteristic dip due to energy being stored and dissipated in the resonator. In the vicinity of the resonance frequency, f_r, the complex response can be modeled as a Lorentzian function, possibly with an asymmetric background due to experimental imperfections (cable delay, impedance mismatch, standing waves). Near a resonance, the transmission function $S_{21}(f)$ can be approximated by a Lorentzian dip:

$$S_{21}(f) \approx \frac{1}{1 + 2iQ_r \frac{f-f_r}{f_r}}, \tag{3.25}$$

where f is the frequency, f_r is the resonance frequency, and Q_r is the quality factor of the resonator. This arises from the response of a damped harmonic oscillator or an RLC circuit, where the denominator represents the de-tuning from resonance scaled by the quality factor. Taking the modulus squared of Eq. 3.25 gives the power transmission:

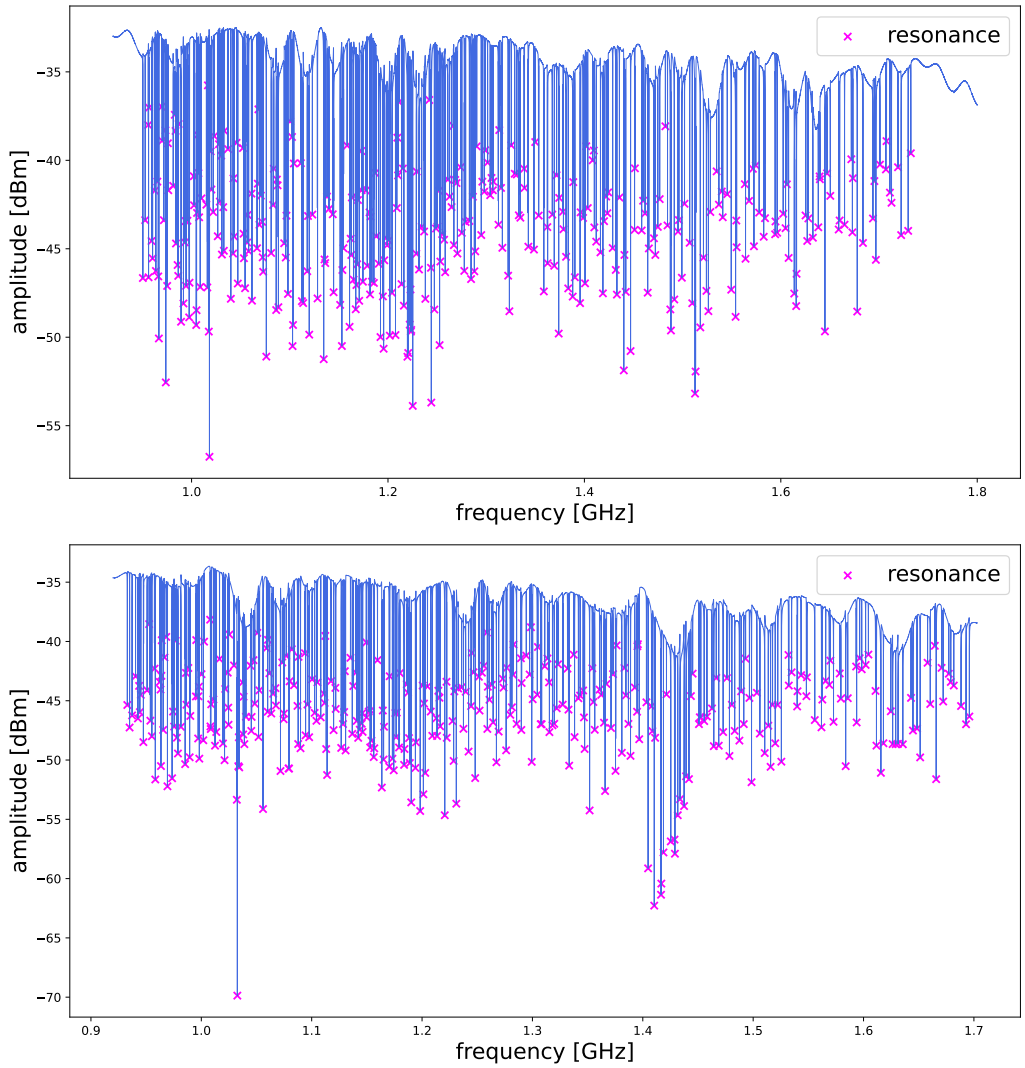

Figure 3.11: VNA feedlines of AT (top) and AR (bottom) arrays at 1 mm. We detect 361/418 and 355/418 resonances respectively.

$$|S_{21}(f)|^2 = \frac{1}{1 + 4Q_r^2 \left(\frac{f-f_r}{f_r}\right)^2}\,, \tag{3.26}$$

which is a symmetric Lorentzian function centered at f_r with a full width at half maximum (FWHM) of $\Delta f = f_r/Q_r$.
However, in practice, the resonance is superimposed on a slowly varying complex background. To account for this, we expand the complex baseline as a linear function around f_r:

$$S_{\mathrm{bg}}(f) = A_1 + A_2(f - f_r)\,, \tag{3.27}$$

where A_1, A_2 are complex coefficients that account for the baseline level and slope. The Lorentzian component itself may also exhibit asymmetry due to coupling or measurement artifacts. Therefore, we model its numerator as another linear function:

$$S_{\mathrm{res}}(f) = \frac{A_3 + A_4(f - f_r)}{1 + 4Q_r^2 \left(\frac{f-f_r}{f_r}\right)^2}\,, \tag{3.28}$$

where A_3, A_4 are complex coefficients accounting for the amplitude and asymmetry of the resonance.

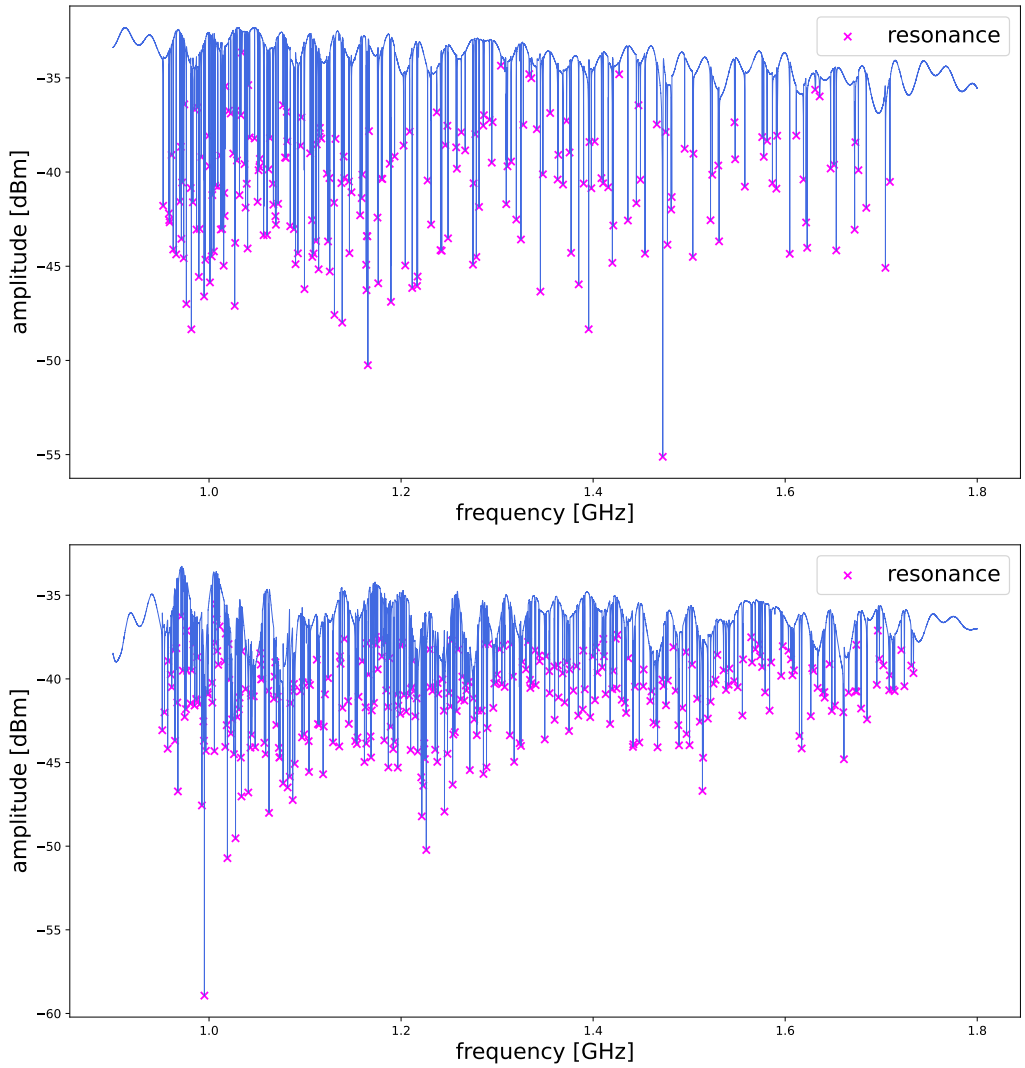

Figure 3.12: VNA feedlines of AT (top) and AR (bottom) arrays at 2 mm. We detect 348/418 and 359/418 resonances respectively.

The final model is the sum of background and resonance contributions:

$$S_{21}(f) = S_{\text{bg}}(f) + S_{\text{res}}(f)\,, \tag{3.29}$$

leading to the final fitting expression:

$$S_{21}(f) = A_1 + A_2(f - f_r) + \frac{A_3 + A_4(f - f_r)}{1 + 4Q_r^2\left(\frac{f-f_r}{f_r}\right)^2}\,. \tag{3.30}$$

This model is flexible and fits both the magnitude and the complex behavior of the transmission curve. The coefficients A_i are generally complex-valued and determined via nonlinear least-squares fitting to the measured $S_{21}(f)$. The quality factor Q_r extracted from this fit characterizes the sharpness of the resonance and is a key performance parameter of the resonator. The quality factor Q_r is an important metric characterizing the sharpness of the resonance. It is defined as the ratio between the central resonance frequency, f_r and the FWHM of the resonance curve, Δf:

$$Q_r = \frac{f_r}{\Delta f}\,. \tag{3.31}$$

By fitting the measured resonance curve using the specified function, we can extract the resonance frequency f_r, the total quality factor Q_r, and, using Eq. 3.20, an estimate for the internal and coupling quality factors, all crucial parameters to evaluate the performance of an array. The fitted quality factors of the 1 mm arrays are shown in Fig. 3.13, while those for the 2 mm arrays are shown in Fig. 3.14.

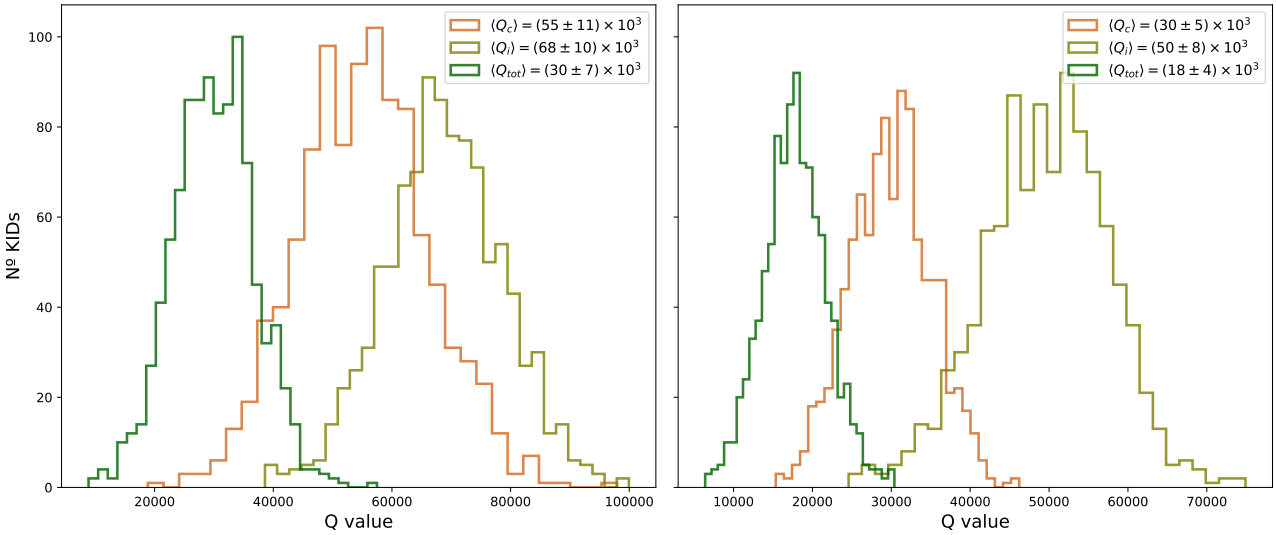

Figure 3.13: Histograms of internal, coupling, and total quality factors for both tested arrays at 1 mm, *AT* on the left and *AR* on the right.

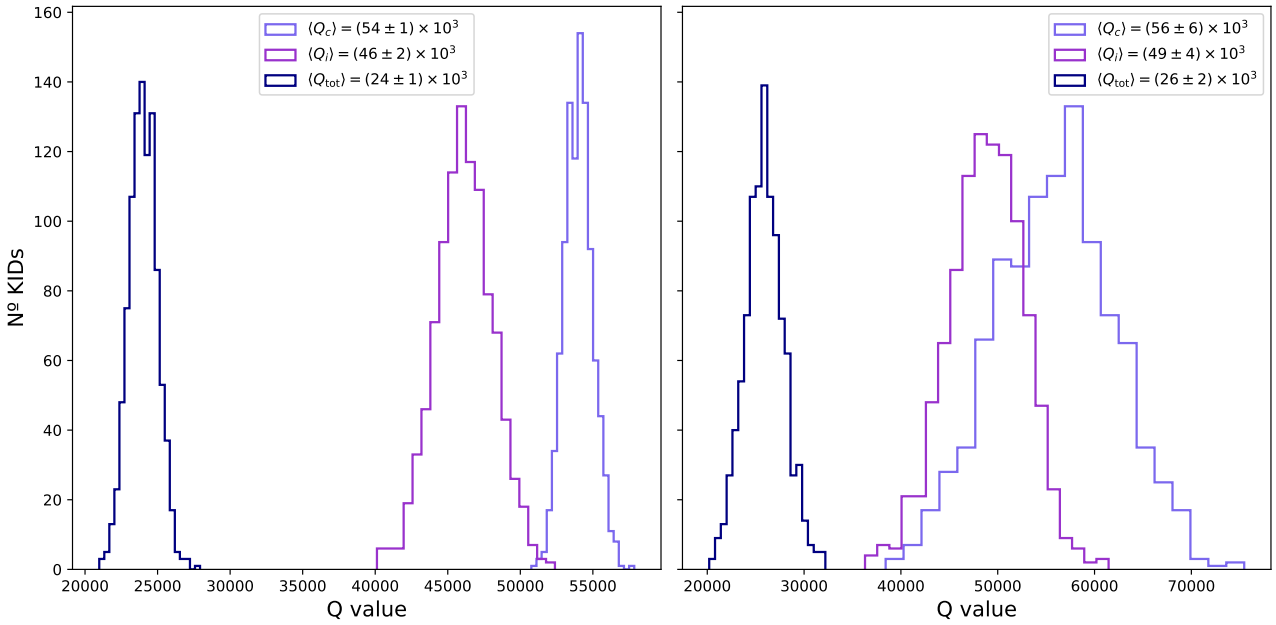

Figure 3.14: Histograms of internal, coupling, and total quality factors for both tested arrays at 2 mm, *AT* on the left and *AR* on the right.

The measured quality factors align well with predictions, confirming the design's performance. Such predictions derive from previous experiments with similar optical load and pixel designs, such as NIKA and NIKA2 (Monfardini et al. 2011 [203], Monfardini et al. 2016 [204]).

3.7 Conclusion

A central component of my work on LEKIDs has been the complete fabrication and cryogenic characterization of two LEKID arrays optimized for 1 mm wavelength detection. Starting from bare high-resistivity silicon wafers, I followed the full microfabrication process to produce fully functional arrays. These arrays were then installed and tested in a dilution refrigerator. Using a VNA, I performed resonance scans to identify the frequency response of each pixel, and analyzed the data to extract key performance parameters such as the internal, coupling, and total quality factors. The successful detection of the majority of resonances and the extraction of realistic quality factors confirmed the functionality of the fabricated devices and their responsiveness to changes in optical load.

This chapter has therefore combined an overview of LEKID physics and technology with a hands-on implementation that reflects the growing maturity of the field. Through this work, the main advantages of LEKIDs have clearly emerged: their relatively simple and scalable fabrication process, fast time response, and high multiplexing capability make them highly attractive for large-format, cryogenic detector arrays. Their design flexibility — including sensitivity to linear polarization through tailored absorber geometries — further enhances their applicability in both photometric and polarimetric observations. However, the analysis has also highlighted key challenges: the efficiency of photon absorption strongly depends on the energy relative to the superconducting gap, and high-frequency photons (e.g., above 300 GHz) may not convert fully into detectable quasi-particles. In addition, achieving high pixel yield requires precise control of the microfabrication process, and resonance overlap (frequency collisions) can limit effective multiplexing. These factors must be carefully managed in future developments.

Chapter 4

High-precision polarization measurements with LEKIDs

Contents

4.1 The purpose of the project **96**
4.2 The experimental setup **97**
4.2.1 The test bench 97
4.2.2 The LEKIDs receivers 99
4.3 Test bench characterization **101**
4.3.1 Effective sky simulator's temperature estimation 101
4.3.2 Optical load estimation 103
4.4 Camera's performances **104**
4.4.1 Photometric and spectral characterization 105
4.4.2 Polarimetry characterization 113
4.5 Interpretation of results **116**
4.5.1 Polarization angle accuracy 116
4.5.2 Cross-polarization contribution 116
4.6 Implications for CMB B-modes observations **117**
4.7 Conclusions and perspectives **117**

Abstract As introduced in the first and second chapters of this thesis, the measurement of polarized signals in the millimeter range plays a central role in modern cosmology, particularly in the study of the CMB polarization. Different instrumental and detector configurations have been implemented to maximize the precision on the reconstruction of the polarization angle.
While NIKA2 has already demonstrated the capability of measuring polarization with high sensitivity, achieving higher precision and tighter control over systematic effects remains a critical challenge for next-generation experiments. In this context, the work presented in this chapter contributes to advancing the application of LEKIDs for high-precision polarimetry, exploring their potential in a filled-array configuration.
This study is centered on the in-lab characterization of a dedicated experimental setup designed to simulate observational conditions with unprecedented control. The test bench, installed in the cryogenic laboratory at LPSC, is composed of a sky simulator coupled to a polarized source, enabling controlled testing of the camera's performance in conditions closely resembling those encountered in astrophysical observations.
Within this framework, I conducted a comprehensive characterization campaign, encompassing the electrical, photometric, spectroscopic, and polarization response of the LEKID arrays. My work included the estimation of the optical responsivity using VNA scans and point-like sources, the evaluation of detector performance via key metrics such as Noise Equivalent Power (NEP) per pixel, spectral bandpass, beam size distribution, and array geometry, and the precise measurement of polarization angles. The results confirm that this configuration meets the stringent requirements imposed by CMB polarization studies, with a level of precision of $\sim 0.1^{o}$ and fine systematic control.
Overall, this chapter presents the core experimental contribution of this thesis and demonstrates the potential of this methodology for future cosmological applications. This work is published in Savorgnano et al. 2025a [276].

4.1 The purpose of the project

In millimeter-wave instrumentation, the design of the focal plane is a critical factor that influences key performance characteristics such as optical coupling efficiency, field of view and scalability of the instrument. One prominent focal plane architecture is the horn-coupled design, which utilizes feedhorns to guide incoming radiation toward the detectors. This configuration provides excellent beam control and minimizes crosstalk between pixels (Posada et al. 2015 [258]), ensuring high precision in measurements. However, it comes with significant trade-offs: increased complexity, bulk, reduced packing density hence a smaller filling factor and space loss, anomalous refraction (particularly problematic for ground-based experiments), reduced quantum efficiency. These can be substantial limitations for large-scale surveys or high-resolution imaging, where maximizing the focal plane occupation and minimizing instrument size are crucial goals.
Other solutions, such as a filled-array focal plane, also show some disadvantages. For instance, it is trickier to implement on-chip polarization or multichroic techniques to measure both polarization direction at the same time. On the other hand, a filled-array focal plane directly couples radiation to the detectors without the need for intermediate optical elements (Monfardini et al. 2010 [202], Doyle et al. 2009 [91]). This architecture enables a higher detector filling factor, which increases the number of detectors per unit area, making it particularly advantageous for large-format arrays. As a result, filled-array focal planes offer higher overall quantum efficiency (lower photons loss), and benefit from a simplified fabrication process that reduces the complexity and cost of production.
In this work, we used a specific configuration, already used in the NIKA2 instrument: two LEKID arrays oriented at 90° with respect to each other, separated by a linear polarizer at 45°

that splits the beam on the two. This way, we only have to deal with optical element systematics, such as those related to the cold polarizer, rather than on individual pixels'. This study aims to demonstrate a refined measurement technique for linear polarization using LEKIDs in a filled-array configuration. The results presented here were obtained in a band centered at 150 GHz, a frequency range that is especially relevant for CMB polarization studies.

4.2 The experimental setup

Describing the experimental setup is crucial to understand the kind of measurements we have conducted, so a significant part of this chapter will be dedicated to introducing it and its components. The experimental setup is composed of two main parts: the test bench and the LEKIDs camera. These two parts are described separately, respectively in Subsec. 4.2.1 and Subsec. 4.2.2.

4.2.1 The test bench

The test bench is composed of a closed-circuit ^{3}He - ^{4}He dilution cryostat designed as a camera for optical measurements. The cryostat is optically coupled to a sky simulator, which is a tool that allows us to mimic the emission from the atmosphere in on-sky observations. The sky simulator can be coupled to the main cryostat using a Martin-Puplett interferometer (as shown in the right panel of Fig. 4.1) for spectroscopic characterization, or using a 45º-oriented flat mirror for photometric and polarimetric characterization (as shown in the left panel of Fig. 4.1). The entire system is optimized to operate under an optical background typical of a ground-based instrument at 150 GHz. An estimate of this optical load will be given later, in Sec. 4.3. This optical background is achieved by coupling the camera to the sky simulator and can be adjusted by regulating the cold stop aperture within the camera (Catalano et al. 2020 [63]). The sky simulator is capable of performing both total intensity and polarization measurements, thanks to interchangeable optical sources positioned in front of the cold black body. Each subsystem is detailed in the following paragraphs.

Optical coupling with the sky simulator The coupling between the camera and the sky simulator is achieved using two HDPE lenses and two possible optical configurations, depending on the type of measurement to be performed (see Fig. 4.1). For spectral measurements, a Martin-Puplett interferometer is used (Fasano et al. [111], Macías-Perez et al. 2024 [188]), capable of performing interferograms with a path length up to 80 mm, providing a spectral resolution of about 1 GHz. For total intensity measurements, the camera is directly coupled to the sky simulator via a 45° flat mirror. The reduction in optical path length compared to the spectral configuration is compensated by replacing one of the two HDPE lenses.

Sky simulator The sky simulator is composed of two entities: the cold uniform background, simulating the atmospheric signal from the ground; and the warm (300 K) astrophysical sources scanned in front of it. The cold background is basically black body created by cooling a large black disk (270 mm in diameter) to approximately 16 K inside a dedicated pulse tube cryostat. The cryostat includes a 50 K screen equipped with an IR filter made of ZITEX G110. The window is made of HDPE and has a diameter of 300 mm. The optical sources are mounted on a Kapton membrane with a diameter of 400 mm and a thickness of 50 μm. These sources are placed at 300 K, in front of the cold black body. Three sources were fabricated, even though only the first and second were used for photometric and polarization characterization:

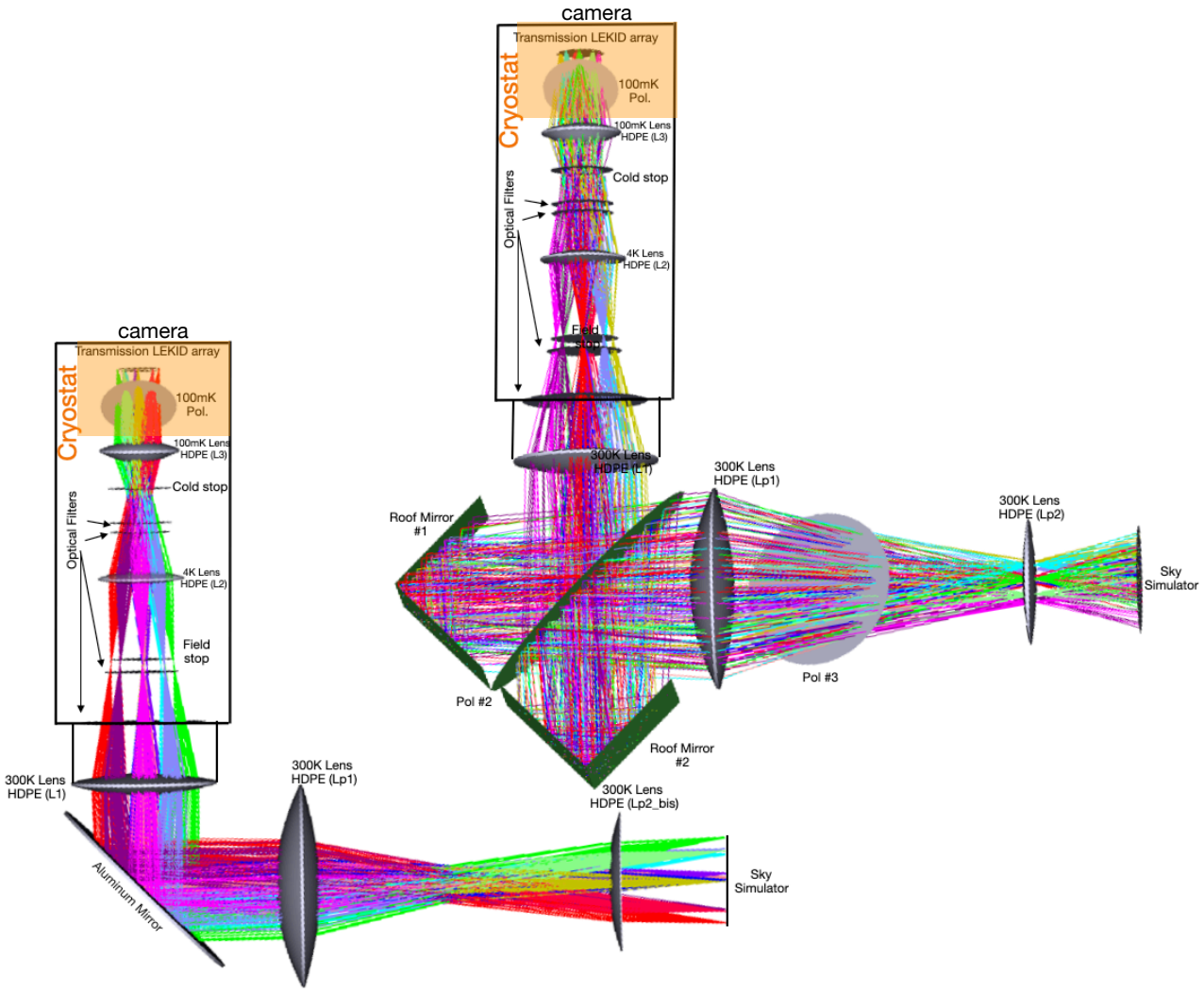

Figure 4.1: Zemax representation of the experimental setup in the two implemented configurations: left - photometric and polarimetric configuration; right - spectrometric configuration employing the Martin-Puplett interferometer. All the elements composing the setup are individually labeled in the figure. The orange shaded regions highlight the camera within the cryostat.

- Photometric point source: a high-emissivity disk with a diameter of 3 mm, attached to the Kapton membrane (left panel of Fig. 4.2). With a beam of the instrument of ∼14 mm, the source is not resolved and hence is seen as point-like. It produces a contrast with respect to the background of ∼15 K.

- Extended polarized source: a 30 mm diameter polarizer fixed to the Kapton membrane, acting as a fully polarized extended source. It generates a temperature contrast of approximately 150 K, simulating a polarized nebula from an observational perspective (right panel of Fig. 4.2).

- Point-line polarized source or dipole: a 3 mm long metallic wire, also fixed to a Kapton membrane. This source is designed to simulate a perfectly polarized, point-like emitter, such as a quasar. We do not show the relative picture as it would be invisible to the naked eye.

The optical sources can be moved vertically and horizontally within a range of ±150 mm around the optical axis using two DC remote controlled motors and linear tables, which provide a

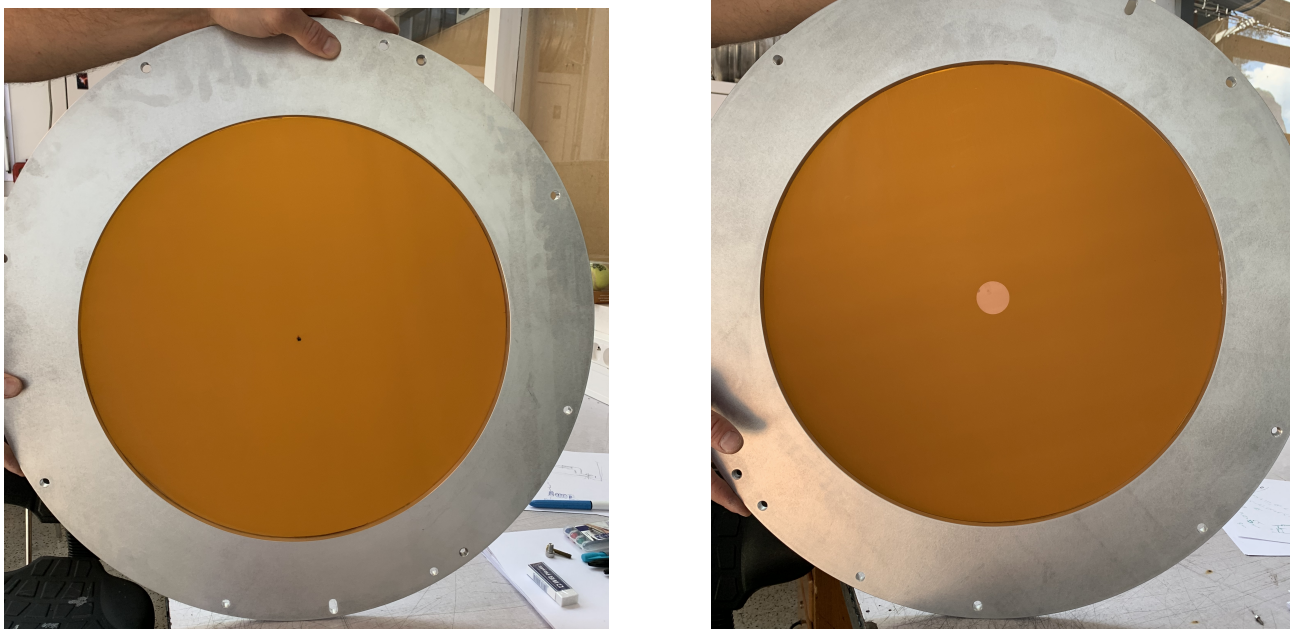

Figure 4.2: Pictures of the two experimental sources used for measurements. *Left:* photometric source simulating a point-like unpolarized source, such as a planet; *Right:* polarimetric source simulating an extended fully polarized source.

resolution of 0.1 mm. A third motor enables rotational motion at speeds of up to 1 Hz with an accuracy of 0.1°. Position control is managed via controllers and encoders, ensuring precise alignment. A GPS clock operating at 10 MHz ensures precise synchronization between the data streams of the KIDs and the pointing system. Additionally, a pulse-per-second (PPS) signal establishes a unified starting point for data acquisition.
The fully assembled experimental setup is illustrated in Fig. 4.3, while Tab. 4.1 summarizes the main characteristics and requirements for this study.

4.2.2 The LEKIDs receivers

On the other end of the experimental setup with respect to the sky simulator, the receivers are installed. The receivers are a pair of LEKIDs arrays, arranged in a specific configuration. The camera itself, the arrays' configuration and the coupling with a VNA are detailed in the following subsections.

The camera The two LEKIDs arrays are mounted in the coldest stage of the cryostat, which maintains a base temperature of approximately 130 mK with a 0.1 mK stability over the typical length of one measurement campaign. The cryostat is designed to support two independent RF channels, each equipped with a cryogenic low-noise amplifier. Since LEKIDs are sensitive to magnetic fields, three magnetic shields have been implemented to mitigate this noise source: a μ-metal enclosure at 300 K, a superconducting lead screen at the 1 K stage, and an aluminum screen at the 100 mK stage.
Within the camera, a cold stop is created at the 100 mK stage, while a field stop is positioned at the 4 K stage. These optical components are assured by three High-Density Poly Ethylene (HDPE) lenses, located at the 100 mK (L3), 4 K (L2) and 300 K (L1) cryogenic stages.
To limit the radiative load from the optical access, a sequence of filters are placed at various cryogenic stages. These include IR-blocking thermal filters at the warmest stages, as well as

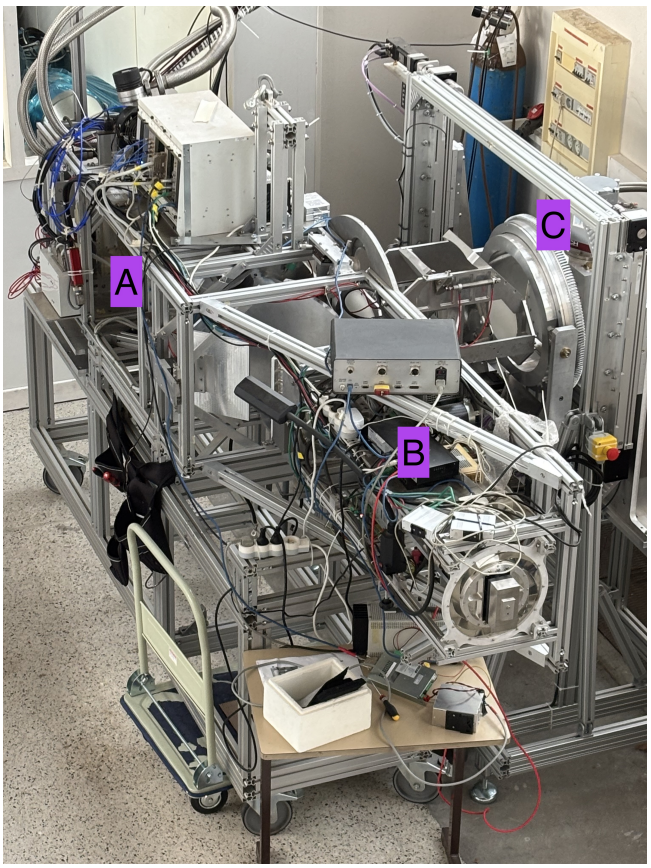

Figure 4.3: Picture of the experimental setup in the cryogenic lab of the LPSC of Grenoble: *A* marks the 100 mK cryostat, *B* marks the Martin-Puplett interferometer and *C* marks the sky simulator.

metallic multi-mesh low-pass filters at lower temperatures (Catalano et al. 2016 [62], Monfardini et al. 2009 [201]). A blackened baffle is installed at the 4 K stage, immediately after the field stop, to minimize stray-light contamination.

LEKID array configuration The focal plane comprises two single-polarization sensitive LEKIDs arrays positioned perpendicularly to each other, named *AT* for transmission array and *AR* for reflection array. Each array is designed to contain 400 pixels, but due to the typical sub-band layout of the electronic readout system, only 317 pixels per array are actually read, reducing the number of available pixels below the design specification. A linear polarizer (P2), oriented at 45°, is placed to split the incoming beam between the two arrays (see Fig. 4.4). The action of this polarizer is effectively to introduce a phase difference of 90° between the two detected polarization components.
The arrays used in this study are the 2 mm arrays presented in Chap. 3, Sec. 3.6. To maximize photon absorption, we employ a back-short cavity located at an optimized distance, which is calculated individually for each array to account for the wafer thickness variations.
To set the high-frequency cut-off, metal-mesh based Low Pass Edge filters are used, while the low-frequency cutoff is achieved through the superconducting cutoff of the thin aluminum film. The polarizer is a wire grid made of copper wires with a pitch of 50 μm, realized on a 30 μm thick Kapton membrane.

Coupling with the VNA Each array is connected to the VNA one at a time via coaxial cables, which run directly from the coldest stage of the cryostat, where the arrays are housed, to the input and output channels of the VNA. This ensures a reliable electrical connection

Test bench characteristics	
Component	Description
Sky simulator's black body	270 mm diameter black disk cooled to 16 K
Cryostat	Custom pulse tube cryostat cooled to 130 mK
Window	HDPE, 300 mm diameter
Optical sources	Mounted on 50 μm Kapton membrane (400 mm diameter): • High-emissivity disk (3 mm diameter) for photometric point source • 30 mm polarizer for extended polarized source
Source movement range	$\pm$150 mm horizontally and vertically
Motor control	DC geared motors with 0.1 mm resolution and rotation up to 1 Hz
Position synchronization	Rubidium 10 MHz clock
Lenses	Two HDPE lenses for coupling camera and sky simulator
Stray-light reduction	Blackened baffle at 4 K stage
Camera characteristics	
Component	Description
Temperature stability	0.1 mK
Arrays	CPW LEKIDs
Illumination	back illuminated
Configuration	filled-array

Table 4.1: Main characteristics and requirements of the experimental setup, divided into test bench and camera specifications.

for precise testing. The optical configuration remains the same as that used for photometric characterization; however, in this case, the readout system exclusively relies on the VNA for measurements.

NIKEL readout system When the arrays are not coupled to VNA, they are read out by the NIKEL electronic readout system. This custom-made readout system was presented in Chap. 3, Subsec. 3.4.2.

4.3 Test bench characterization

The test bench characterization focuses on the precise estimation of the effective temperature of the sky simulator and the associated optical load on the detectors. These parameters are critical for assessing the sensitivity of the setup, optimizing the detector's performance, and ensuring that the noise contributions are well understood and minimized.

4.3.1 Effective sky simulator's temperature estimation

The temperature of the sky simulator is a critical parameter in the characterization of our test bench. Many of the models and measurements presented rely on an accurate estimation of this temperature to derive meaningful physical results. The sky simulator's temperature is monitored using a carbon resistance thermometer installed on the cold Stycast plate, a structure made of a mixture of Stycast epoxy, silicon grains and lampblack. These materials are chosen to create in principle a perfect black body, with an emissivity $\epsilon \approx 1$. Moreover, they allow the

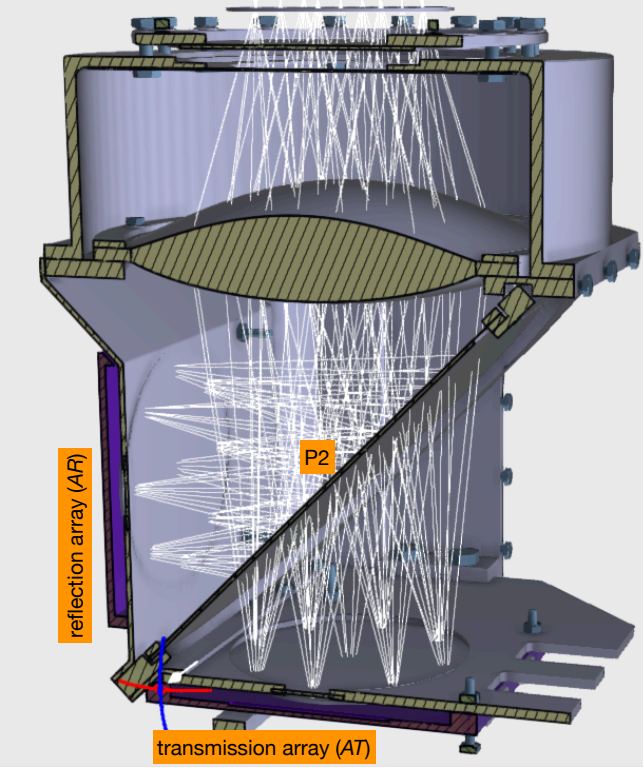

Figure 4.4: CAD design of the 100 mK stage, where the linear polarizer (P2) and the two perpendicular arrays are located.

plate to maintain a stable and controlled temperature that simulates the cold background of the sky. The measured value of ∼16 K, however, does not correspond to the effective background temperature perceived by the detectors. This discrepancy arises from the additional off-axis emission from 300 K stray-light and the sky simulator HDPE windows.
To estimate the equivalent sky simulator temperature, we analyze three VNA scans performed under different optical loads, using only the transmission array *AT* for simplicity. The optical loads correspond to:

- T_1: the nominal sky simulator temperature (T_{sky}),
- T_2: the nominal sky simulator temperature plus a variation ($T_{\mathrm{var}} = 20$ K),
- T_3: 300 K, corresponding to an Eccosorb layer placed in front of the sky simulator.

It is important to stress that all KIDs receive the same power, despite of their location on the focal plane, as we are conducting a completely unfocused measurement. Therefore, all KIDs are used for this estimate.
The responsivity of the array, R, is derived from the resonance frequency variation Δf between T_2 and T_1 as:

$$\mathrm{R} = \frac{\Delta f}{T_{\mathrm{var}}} = \frac{(6 \pm 0.3)\ \mathrm{kHz}}{20\ \mathrm{K}} = (0.31 \pm 0.03)\ \mathrm{kHz/K}. \tag{4.1}$$

The effective sky simulator temperature, T_{sky}, is computed using:

$$T_{\mathrm{sky}} = T_3 - \frac{f_3 - f_1}{\mathrm{R}}, \tag{4.2}$$

where $f_3 - f_1 = (83 \pm 1)$ kHz is the resonance frequency shift between T_3 and T_1. Substituting the values we obtain:

$$T_{\text{sky}} = 300 \text{ K} - \frac{(83 \pm 1) \text{ kHz}}{(0.31 \pm 0.03) \text{ kHz/K}} = (22.3 \pm 0.8) \text{ K}. \tag{4.3}$$

This value reflects the combined contributions from the sky simulator and the entrance HDPE lens. The uncertainty in the temperature is derived from the statistical distribution of the KID data. Specifically, the resonance frequency shifts, which are used to calculate the temperature, are averaged across the pixels in the array. The associated uncertainty is then determined as the standard deviation of this average. It is important to note that the reference temperatures provided by thermometers are treated as absolute values without associated uncertainties, as it was not possible to reliably quantify their uncertainty.

4.3.2 Optical load estimation

In order to compare the sensitivity of the detectors to their equivalent photon noise, an optical simulation was performed to estimate the incident power on each KID. The optical load on a detector, W_{pixel}, is the sum of the optical power generated by the sky simulator and all self-emission contributions, as shown in Eq. 4.4:

$$\begin{aligned} W_{\text{pixel}} &= W_{\text{sky sim}} + W_{\text{self emission}} \\ &= \int_0^\infty \eta(\nu) A\Omega(\nu) S(\nu) BB(T_{\text{sky sim}}, \nu)\, d\nu \quad + \int_0^\infty \eta(\nu) A\Omega(\nu) S(\nu) BB(T_{\text{self emission}}, \nu)\, d\nu\,, \end{aligned} \tag{4.4}$$

where:

- $\eta(\nu)$ is the overall transmission, mostly defined by the transmission of the 5 HDPE lenses. The transmission of each single lens is calculated as

$$\eta_{\text{lens}}(\nu) = \mathscr{T}\, e^{-2\pi\nu B p \frac{n_{\text{HDPE}}}{c}}\,, \tag{4.5}$$

  where p is the thickness of the lens, B is an empirically measured absorption parameter, and n_{HDPE} is the refractive index of HDPE. The transmission term is given by

$$\mathscr{T} = (1 - 2\mathscr{R}), \qquad \mathscr{R} = \left(\frac{n_{\text{HDPE}} - n_{\text{vac}}}{n_{\text{HDPE}} + n_{\text{vac}}}\right)^2, \tag{4.6}$$

  with $n_{\text{vac}} = 1$. For $n_{\text{HDPE}} \simeq 1.56$, one obtains $\mathscr{R} \simeq 0.048$ (i.e. 4.8% per surface), and hence $\mathscr{T} \simeq 0.91$, meaning that about 91% of the incident power is transmitted after the two vacuum–HDPE interfaces of a single lens. The exponential term accounts for absorption losses inside the bulk material. The overall transmission over the selected bandwidth is estimated to be $\eta = 0.8$.

- $A\Omega(\nu)$ is the throughput of each pixel, and it is a geometric property of the optical system. For a diffraction-limited system, it depends on the effective collecting area, A, and the solid angle, Ω, subtended by the diffraction-limited beam, and it can also be expressed as

$$A\Omega(\nu) = 0.54 \text{ mm}^2/\text{sr}\,, \tag{4.7}$$

  considering a pixel of 2.7 mm.

- $D(\nu)$ is the bandpass normalized to one (Fig. 4.7).

- $BB(T, \nu)$ is the black body brightness as a function of the working temperature, T, and frequency, ν.

By performing this calculation using the actual parameters of our setup, we find that at the working temperature of the sky simulator of 22.3 K (derived in Subsec. 4.3.1), the total incident power per pixel is (20±5) pW. The 30% uncertainty reflects the absorption factor of the optical components, which is based on experimental estimates due to the lack of precise measurement tools.
From this estimate, we can compute the photon Noise Equivalent Power ($\mathrm{NEP_{phot}}$) at the central frequency of the bandpass (150 GHz) using the same relation as in A. Catalano's HDR manuscript:

$$\mathrm{NEP_{phot}} = \sqrt{2h\nu_{\mathrm{central}} W_{\mathrm{pixel}}} = (6.6 \pm 1.5) \times 10^{-17}\,\mathrm{W}/\sqrt{\mathrm{Hz}}\,. \tag{4.8}$$

The photon NEP can be directly compared to the total NEP, which is composed of multiple noise sources. In order to refer to photon-noise-dominated detectors, we want the following expression to be satisfied:

$$\mathrm{NEP_{goal}} \lesssim \sqrt{2}\,\mathrm{NEP_{phot}}\,. \tag{4.9}$$

If our configuration assures such condition, it would mean that the biggest contribution to the system noise is the photon noise itself.

4.4 Camera's performances

We conducted extensive measurements to evaluate both the total intensity and polarization performances of the LEKID arrays and of our test bench in general. The primary goals of these measurements were:

1. Photometric and spectral characterization: estimation of the working bandpass using the Martin-Puplett interferometer, assessment of noise properties and optical responsivity, and characterization of the photometric response to a point source, including beam properties (Subsec. 4.4.1);

2. Polarimetric characterization: determination of the polarization angle along with its associated uncertainty (Subsec. 4.4.2).

This workflow, summarized in Tab. 4.2, was designed to demonstrate that our test bench can achieve the accuracy required by current cosmological experiments. The primary objective of the polarized measurements is to ensure that the error associated with the estimated polarization angle is $\leq 0.1°$. The photometric and polarimetric analyses were performed using 30% of the best-performing pixels, selected based on their low noise levels, expected beam shapes and high responsivity. The rationale for the choice of this subset of pixels lies in the focus of the study: to validate an experimental method rather than to assess the uniformity of results across the entire array. Achieving the required performance with this selected group of KIDs is sufficient to demonstrate the method's feasibility.

Characteristic	Mode	Configuration
Bandpass	polarizer	Martin-Puplett
Noise	mirror	photom. source
Optical responsivity	mirror	photom. source/VNA
Beam properties	mirror	photom. source
Polarization angle	mirror	ext. polar. source

Table 4.2: Characteristics of the camera and its coupling configurations.

4.4.1 Photometric and spectral characterization

The data acquisition method involves performing on-the-fly (OTF) maps by raster scanning the photometric point source in front of the sky simulator, mimicking the mapping procedure used in telescopes. A raster scan covers a selected area with defined dimensions, subscan steps and scanning speed. Typically, the source is scanned over a range of ± 50 mm in both x and y directions, with a scanning speed of 4 mm/s and a subscan step size of 3 mm. This approach ensures uniform coverage of the mapped area while achieving diffraction-limited resolution for data analysis. With an expected beam FWHM of 14 mm and a subscan step size of 3 mm, the sampling factor is approximately 5, comfortably exceeding the Nyquist criterion of 2.5.
In measurements involving KIDs and sky simulator data as ours, precise alignment between the pointing system and the time-ordered information (TOI) from the detectors is critical for accurate data analysis. An interpolation function is employed to synchronize these two data streams by interpolating the pointing coordinates X and Y from the pointing system to match the time stamps of the KIDs data. This process ensures that the data from the detectors is correctly aligned with the pointing information, which is essential for mapping the sky with high precision. The synchronization begins by identifying the overlapping time interval between the pointing system and the KIDs data. The function determines the maximum start time and minimum end time of the two time ranges to find the common interval. Once the shared interval is established, the corresponding indices for both datasets are extracted. The pointing coordinates are then interpolated over this common time range using a linear interpolation function. This interpolation maps the pointing coordinates, which are sampled at the time stamps of the pointing system, onto the time stamps of the KIDs data. Simultaneously, the TOI data from the KIDs array is sliced to include only the samples within the synchronized time range. The function returns the interpolated pointing coordinates, the synchronized TOI, and the new, shared time vector.
A typical time stream of the signal detected by every KID is shown in Fig. 4.5, together with a typical raster scan in the top-left corner. In this plot, we distinguish the timeline before (green) and after (blue) subtracting a common mode of all KIDs and decorrelating.
The objective of decorrelation is to isolate the physical signal by removing correlated noise patterns that originate from instrumental or environmental factors, such as thermal fluctuations, background variations due to the sky simulator's displacement or electronic artifacts. The process begins with the identification of reliable detectors, achieved by analyzing the statistical properties of the TOI. For each detector, the root mean square (RMS) of its signal is calculated and compared to the median RMS across all detectors. Detectors whose RMS deviates significantly, defined by a threshold based on the Median Absolute Deviation (MAD), are excluded from further analysis. This step ensures that only detectors with stable and consistent behavior are considered.
Following this, the correlation coefficients between the signals of all selected detectors are computed to identify those with the most similar noise patterns. For each detector, the signals from the most correlated detectors are used as templates to model and subtract the correlated noise.

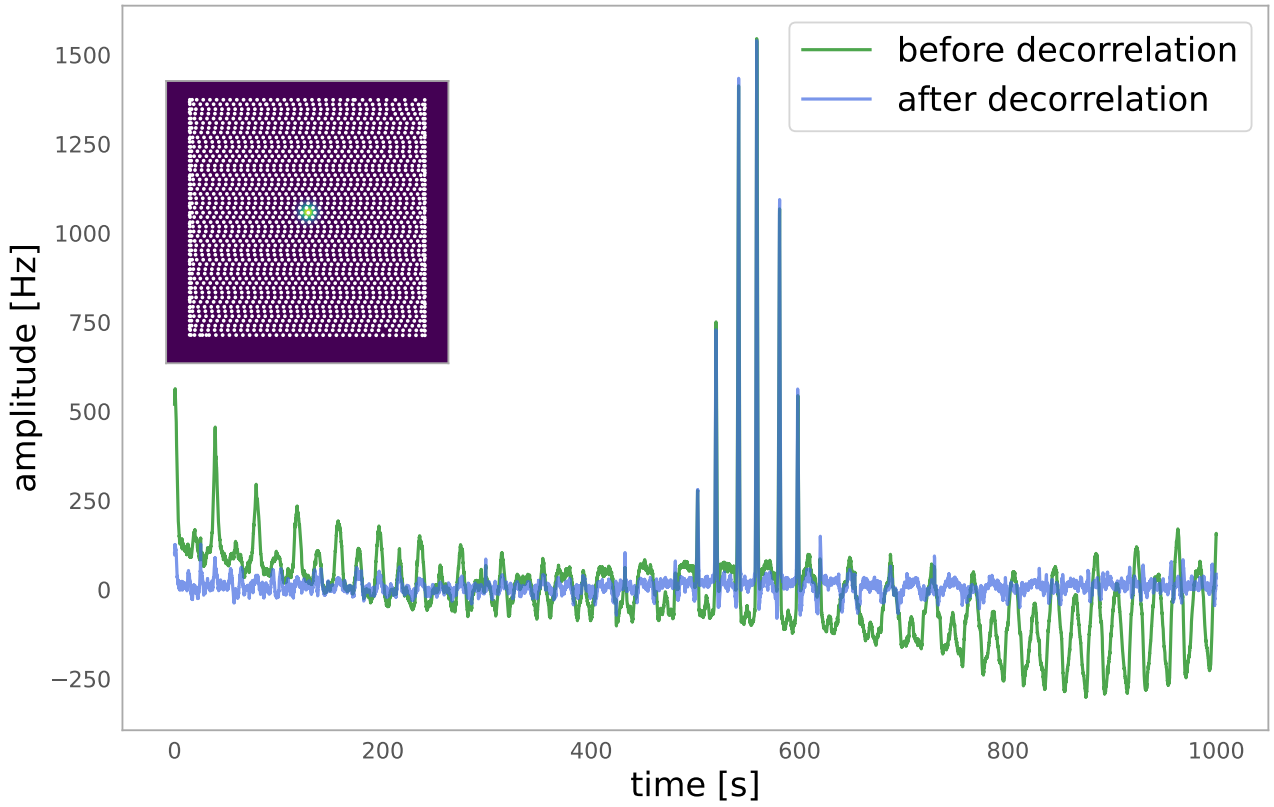

Figure 4.5: Typical timeline of the signal detected by one KID while the photometric source is being scanned, as shown in the top-left corner, in green before decorrelation and in blue after decorrelation. The intensity peaks correspond to successive passages of the photometric source through the line of sight of the selected KID, while the off-source oscillations in green result from small optical background variations following the scanning strategy.

Two approaches are employed for this decorrelation. The first, called the common mode (CM) method, calculates a common noise signal by averaging or taking the median of the selected templates. This common mode represents the shared noise across detectors, and a scaled version of it is subtracted from each detector's signal to decorrelate it. The second approach, known as all detectors as templates (ADT), performs a linear regression for each detector's signal using the most correlated detectors as independent templates. The regression coefficients quantify the contribution of each template to the noise in the target detector, and these contributions are subtracted to yield the decorrelated signal. Both methods rely on a threshold applied to the correlation coefficients to ensure that only sufficiently correlated templates are used for the decorrelation. The choice between the CM and ADT approaches depends on the nature of the correlated noise and the specific requirements of the analysis. By employing this decorrelation procedure, we significantly reduce noise contributions, enabling the extraction of cleaner signals from the KIDs data.
Another important step in the preliminary data treatment is the de-glitching procedure. Glitches are sharp, transient anomalies in the data, typically caused by high-energy particles interacting with the detector substrate. In ground-based experiments such as ours, these events are primarily due to relativistic secondary cosmic rays, and in particular to atmospheric muons. These muons are the most penetrating component of the cosmic-ray shower at sea level and deposit energy as they pass through the silicon substrate of the detectors. A typical muon flux at ground level is about 1 muon/cm^2/s. Given that our LEKID array has an active area of approximately 6 cm $\times$ 6 cm, we expect around 36 muons/s traversing the substrate. However, due to the geometry and layout of the resonator matrix, only a fraction of these events effec-

tively couple to the KID pixels and produce observable glitches. In practice, we observe about 0.5 glitches/s per pixel. The energy deposited by each muon is approximately constant and depends primarily on the path length in the substrate (about 300 μm thick in our case) and the angle of incidence. Since these LEKID arrays are not optimized to minimize glitch impact, these events introduce significant and non-negligible distortions into the timelines.
The glitch problem is particularly critical in the context of space-based instruments, where the particle flux is higher and more variable, and extensive efforts have been devoted to developing de-glitching techniques, as described in Catalano et al. 2014 [60] and Stever et al. 2021 [285]. To address this issue in our case, we implemented a dedicated de-glitching function to clean two-dimensional arrays of time-ordered data. The algorithm operates row by row, identifying and correcting anomalous values based on their deviation from a smoothed baseline. For each row, a median filter is applied using a specified kernel size to generate a smoothed version of the data. This smoothed signal serves as a baseline reference. The absolute difference between the raw data and the median-filtered version is computed to quantify deviations. A threshold is then applied to these deviations, defined as a multiple of their standard deviation. Data points exceeding this threshold are flagged as glitches. Once identified, glitches are corrected by replacing them with interpolated values based on the nearest non-flagged points, thereby preserving the overall continuity and structure of the signal. The function is fully parameterized, allowing flexibility in its application through user-defined kernel sizes and threshold multipliers to tune the detection sensitivity. This approach effectively suppresses spurious particle-induced signals while maintaining the integrity of the underlying astrophysical signal, and prepares the data for further processing and analysis. An example of the effect of the implemented de-glitch function is shown in Fig. 4.6, where the original timeline and the cleaned one are compared.

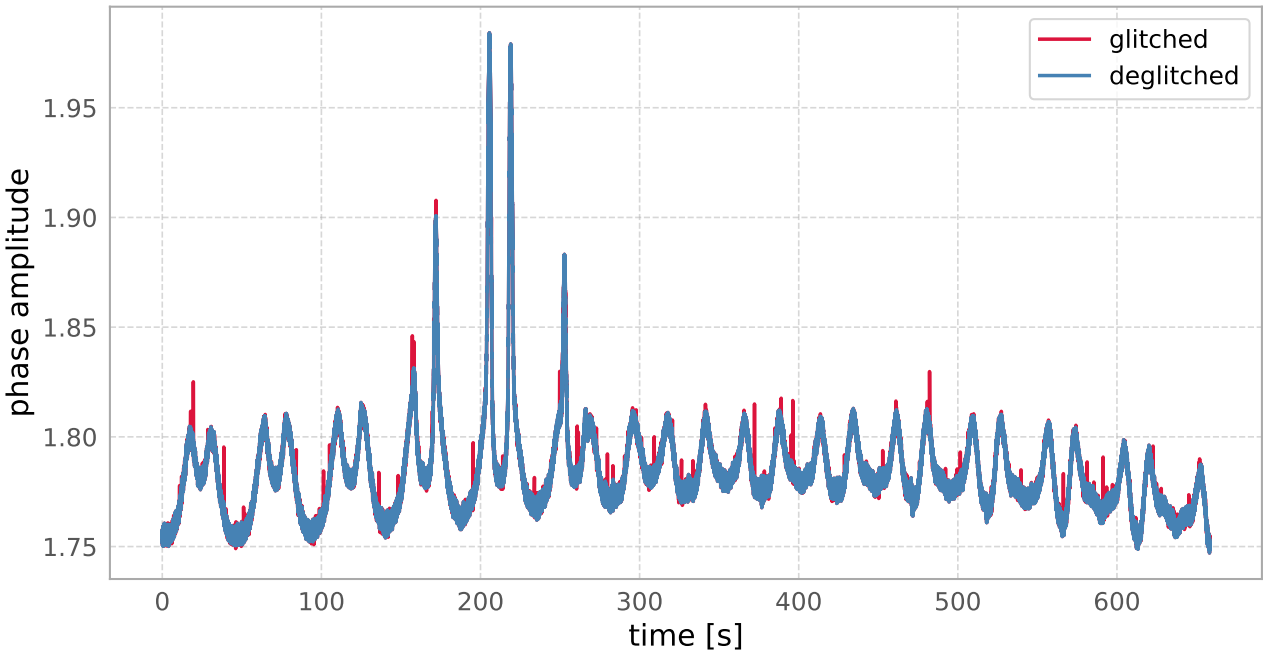

Figure 4.6: Example of the effect of the implemented de-glitch function: the original, glitch-affected timeline is shown in *red*, while the cleaned version obtained after applying the de-glitch filter is shown in *blue*.

By investigating the bandwidth, Noise Equivalent Power (NEP) and beam profile, we aimed to validate the system's design while assessing its sensitivity and efficiency under realistic operating conditions.

Bandwidth The bandwidth was determined from the absorption spectrum obtained using the Martin-Puplett interferometer configuration. This type of interferometer is a Fourier-transform spectrometer specifically designed for millimeter and sub-millimeter wavelengths, which operates based on the interference of two orthogonally polarized beams. The detector array is illuminated with a modulated broadband source whose spectrum is encoded by varying the optical path difference between the two arms of the interferometer. As the movable mirror in one arm translates, it produces an interferogram, which is a record of the detector signal as a function of optical path difference. A Fourier transform is then applied to the interferogram to retrieve the spectral response of the system. The resulting absorption spectrum reflects the frequency-dependent optical efficiency of the detector and associated components. The bandwidth is defined as FWHM of this spectrum, or alternatively, as the frequency range over which the response exceeds a given threshold (e.g., 50% of the peak). This approach allows precise determination of the spectral sensitivity of the array and is essential for characterizing its performance within the target observing band. We show in Fig. 4.7 the estimated bandwidth centered at 150 GHz in pink, and the experimental one in purple. The low-frequency cutoff is due to the aluminum typical transition temperature, while the high-frequency cutoff is given by an optical filter.

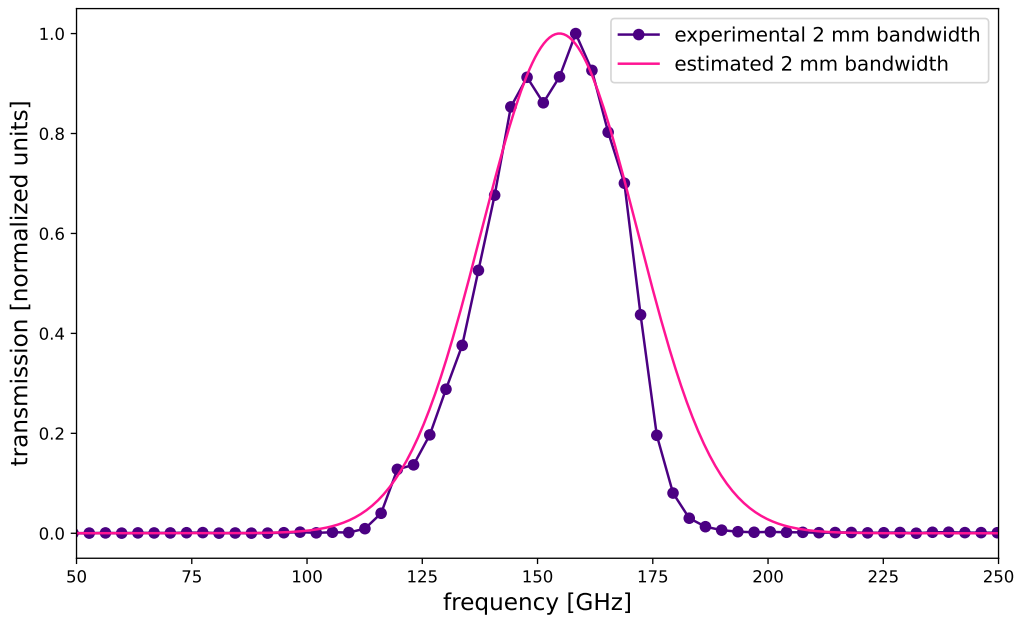

Figure 4.7: Normalized bandwidth for measurements at 2 mm: in purple the experimental bandwidth and in pink the estimated bandwidth, centered at 150 GHz and with a 30% width as the experimental one.

For the optical estimations presented earlier (Sec. 4.3), the bandwidth was characterized by its fractional value, defined as $\Delta\nu/\nu_0$, where $\Delta\nu$ represents the width of the spectrum and ν_0 is the central frequency. The measured bandwidth of approximately 30% is consistent with typical photometric bandpasses, representing the 2 mm atmosphere window and confirming the suitability of the system for precision optical measurements.

Sensitivity To estimate the single-pixel sensitivity averaged over the most responsive pixels in the array, we measured the optical responsivity. This was done using an extended source composed of an Eccosorb layer at 300 K and the sky background, with the resulting signal variation measured through VNA scans. The responsivity was computed as the ratio between

the resonance frequency shift and the temperature difference of the optical load. This measurement yielded (0.35 ± 0.02) kHz/K for the *AT* array and (0.31 ± 0.02) kHz/K for the *AR* array (Fig. 4.8).

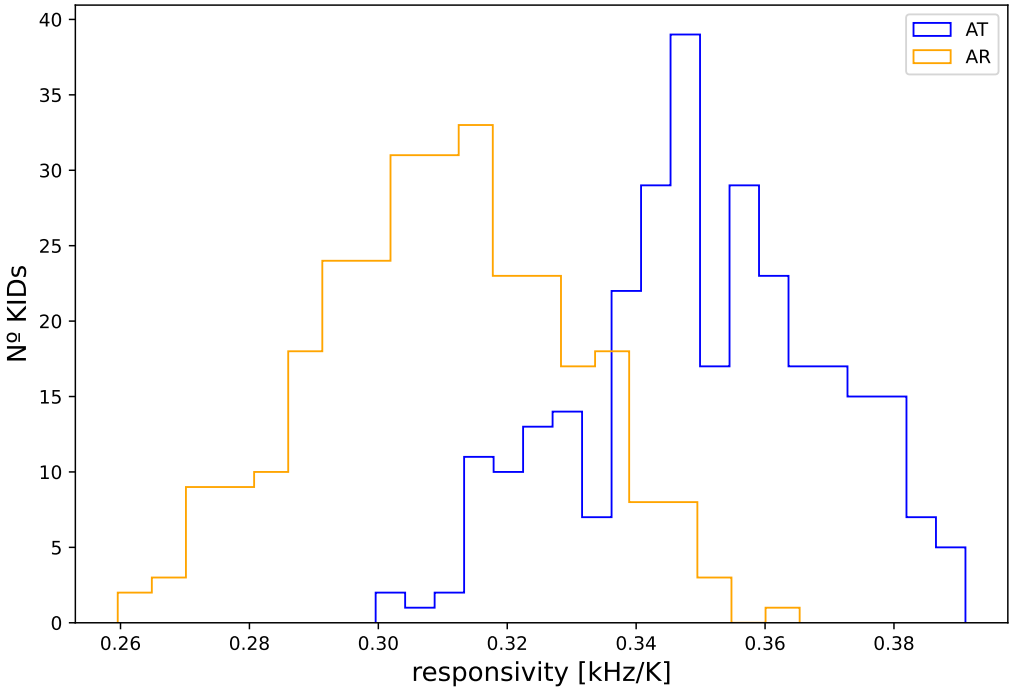

Figure 4.8: Histograms of the responsivity of *AT* and *AR*.

Using the optical model illustrated in Sec. 4.3, the corresponding average power responsivity per pixel is found to be:

$$\mathcal{R}_{\text{pixel}} = (12.5 \pm 0.4) \text{ kHz/pW} . \tag{4.10}$$

Noise The spectral noise density $S_n(f)$ in Hz/$\sqrt{\text{Hz}}$ is calculated at a fixed sky simulator temperature of 22.3 K, using the custom-made NIKEL electronic system, with a multiplexing factor of 400 and a sampling frequency of 1 kHz (Bourrion et al. 2016 [48]). In Fig. 4.9 we compare the spectral noise densities obtained while an OTF map is running (in blue) and with the system stopped (in magenta), with no decorrelation applied to the timeline in neither case. The faint gray curves are the spectra of each KID of the 30% selected KIDs, while the colored curves are the relative averaged values.
The $1/f$ noise detectable in the blue curve of Fig. 4.9 is caused by optical spatial fluctuations during a typical subscan, clearly visible in the green line of Fig. 4.5. These fluctuations are due to the displacement of the optical source support, leading to micro-variations of the background temperature. The noise spectrum acquired without running the OTF map does not exhibit a perfect $1/f$ behavior due to the presence of multiple fluctuation sources: optical, electronic and cryogenic. In particular, fluctuations in the optical background, essentially related to the temperature stability of the sky simulator, dominate the noise. These fluctuations are partially correlated across the KIDs array, as they observe similar behaviors; however, some noise components remain complex and difficult to disentangle. While the discrepancy in noise levels at low frequencies can be directly attributed to sub-scan movements and associated fluctuations, only present while the OTF map is running, the higher noise level observed without the OTF map running, compared to with it running, can likely be explained by differences in acquisition conditions. Specifically, the data were not collected simultaneously, and external

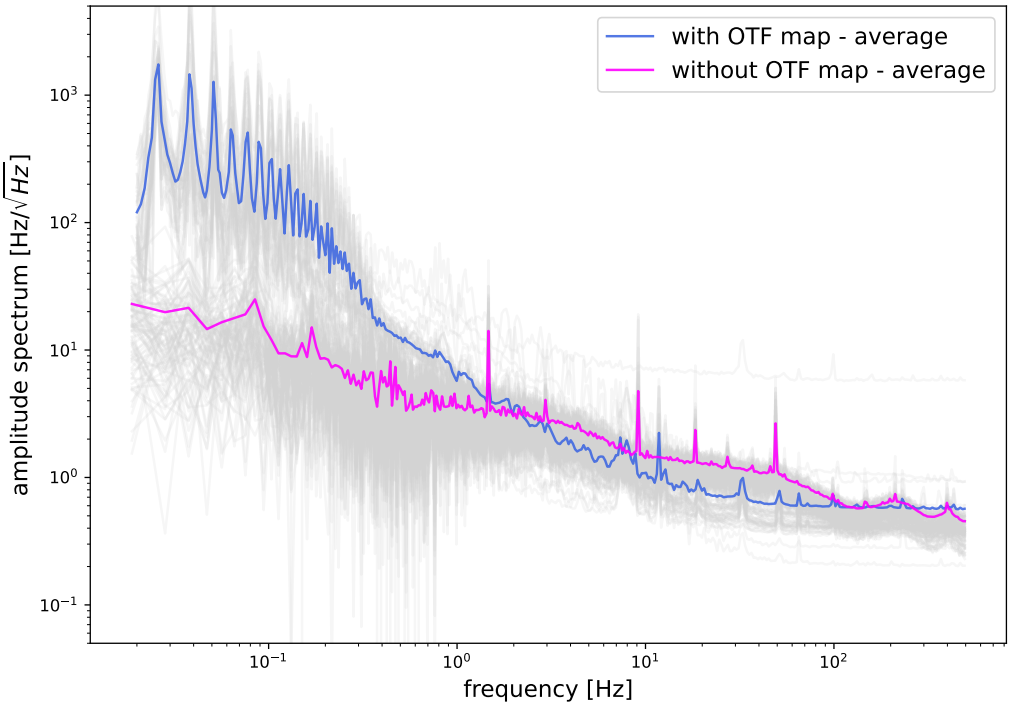

Figure 4.9: Comparison of spectra derived in two different conditions: in blue, we show the spectrum computed over data when the photometric source is being scanned, while in magenta we show the pure instrumental noise. In gray the curves for each KID in the selection are shown.

noise sources may have varied between measurements. Nevertheless, the primary objective of this noise analysis was to confirm that the system operates within a realistic noise regime. Then, we selected the 1–10 Hz frequency range of OTF-free spectrum to compute the mean noise value, $< S_n(f) >$, equal to (1.7 ± 0.5) Hz/$\sqrt{\text{Hz}}$, because it corresponds to the typical timescale of the source passage through the beam, thus encompassing the relevant scientific signal. Although our setup currently does not include a rotating HWP, this frequency range remains appropriate when considering possible future project developments involving polarization modulation, as such modulation frequencies typically lie within this band.
Thanks to this noise analysis, we can now compute the NEP for a pixel in the selected range 1-10 Hz as:

$$\text{NEP}_{\text{pixel}} = \frac{< S_n(f) >}{\mathcal{R}_{\text{pixel}}} = (1.5 \pm 0.5) \times 10^{-16}\,\text{W}/\sqrt{\text{Hz}}\,. \tag{4.11}$$

This result satisfies Eq. 4.9: in fact, the relative discrepancy between $\text{NEP}_{\text{pixel}}(= \text{NEP}_{\text{goal}})$ and NEP_{phot} is 1.1. This indicates that the difference between the values is comparable to their combined uncertainties, supporting the conclusion that we are actually dominated by the photon noise component.

Beam Another result derived from the projected maps of the photometric source onto the focal plane is the estimate of the average beam. The beam is derived by projecting the time stream signal, as the one shown in Fig. 4.5, onto a 2D map using the synchronous pointing data.
The geometry provides a means to precisely identify the position of each pixel on the focal plane. Due to their multiplexed feature, KIDs do not have a direct electrical or optical readout mechanism that correlates their physical position to their response. As a result, mapping

their spatial configuration using projected optical measurements is the only reliable method to determine their positions on the focal plane. The geometries of the two arrays in the focal plane are shown in Fig. 4.10.

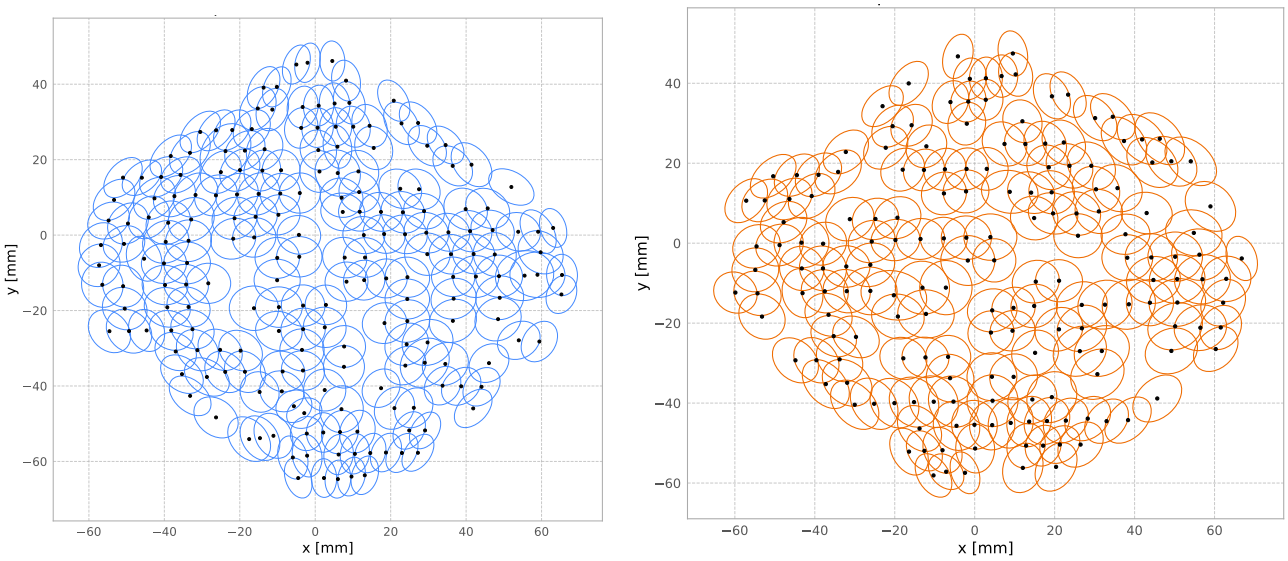

Figure 4.10: Focal plane geometries of filtered pixels of *AT* (*left*) and *AR* (*right*). Every black dot corresponds to the center of a pixel on the focal plane, while the colored ellipses around them represent the FWHM of the beam.

We observe overlapping beams in the focal plane geometry, which is expected due to the oversampling of the focal plane. This overlap arises from the combination of angular resolution and pixel size. Oversampling ensures better coverage and enhanced precision in photometric measurements. The distribution of beam sizes across the central region of the focal plane is uniform, with an average of FWHM $= 13.9 \pm 1.2$ mm. By averaging the beams of a selection of central KIDs, we can see (in Fig. 4.11) how closely the expected Zemax simulated FWHM approximates the experimental average FWHM, both in terms of mean value and ellipticity e.

With the knowledge of the beam, we can estimate the responsivity of the detectors to a point source, to be compared to the responsivity to an extended source that we have estimated previously, through VNA measurements. The responsivity is always derived through the same relation between the intensity variation and the temperature difference:

$$\mathbb{R}_{\text{pixel}} = \frac{\Delta I}{\Delta T}[\text{Hz/K}]\,, \tag{4.12}$$

where ΔI is the difference between the background signal level and the peak signal of the photometric source, and ΔT is the temperature contrast of the point source diluted into the beam and the background (Fig. 4.12).

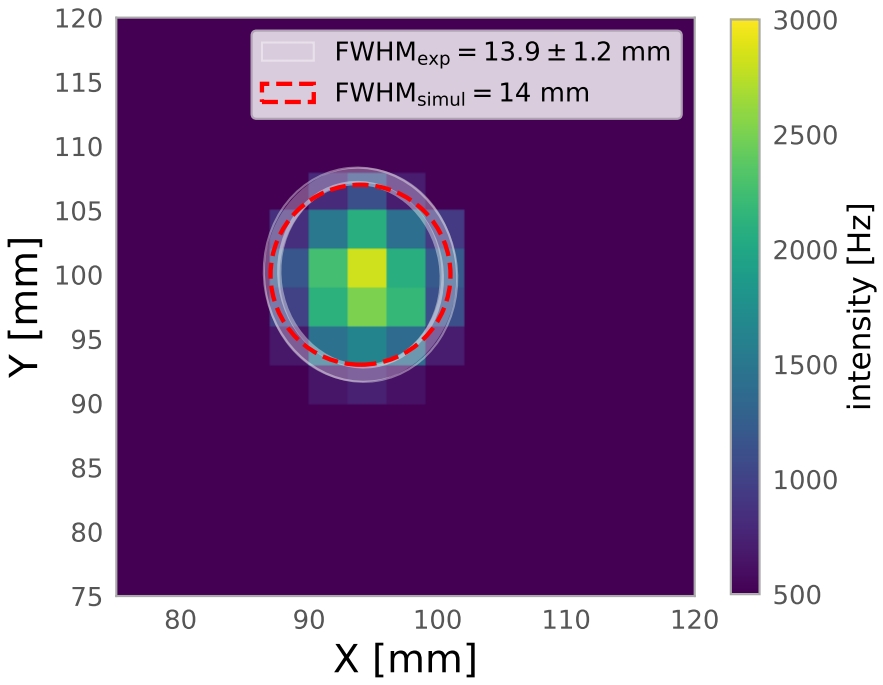

Figure 4.11: Projected image of the photometric source as seen by one sample KID. The white halo is the average FWHM over a selection of central KIDs of the focal plane (FWHM = 13.9 ± 1.2 mm, $e = 0.15 \pm 0.01$); the dashed red circle is the simulated FWHM = 14 mm, $e = 0$.

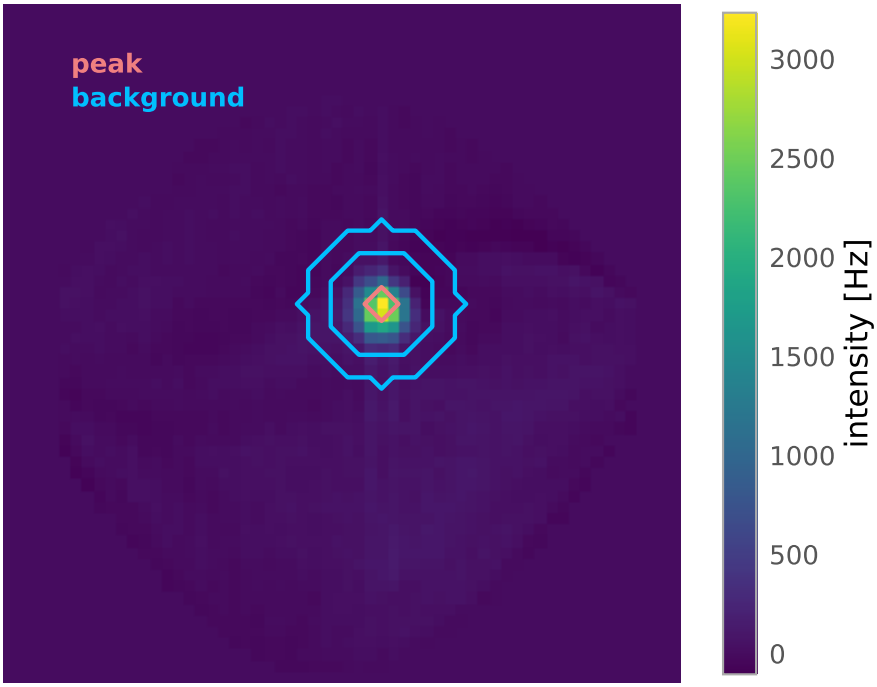

Figure 4.12: Method applied to estimate the response to an extended source using the photometric maps.

This analysis has been done for the selected best pixels of both arrays, obtaining:

$$\mathbb{R}\,[\mathrm{kHz/K}] = \frac{\Delta I\,(T_{\mathrm{source}}/\mathrm{dilution} - T_{\mathrm{sky}})}{\Delta T} = \frac{(1250 \pm 50)\ \mathrm{Hz}}{5\,\mathrm{K}} = (0.25 \pm 0.2)\ \mathrm{kHz/K}\,. \quad (4.13)$$

Here, *dilution* refers to the dilution factor of the photometric source (3 mm) relative to the beam size (13.9 mm). The resulting value of responsivity is approximately 30% lower compared to the one obtained from VNA scans. This discrepancy is expected, as the extended source created with Eccosorb ensures that every KID observes the same signal consistently. In contrast, the photometric point-like source may introduce edge effects, which can impact the response efficiency. A similar characterization was done for the NIKA2 instrument and provided similar results (Perotto et al. 2020 [235]). In that case, however, the power loss was due to the intrinsic imperfect shape of the primary dish. Anyway, this comparison is to highlight that we work under realistic single-dish-like conditions.

4.4.2 Polarimetry characterization

The last and most original aspect of this work is the characterization of the polarization angle absolute value and associated uncertainty. For this purpose, we carried out polarization measurements using the extended polarized source already described in Subsec. 4.2.1. A precise reference for the source's polarization angle was established empirically to serve as a baseline for comparison with the angle estimated by the detectors. The method involved aligning a polarizer's wire with the wheel's orientation, using a microscope to ensure precision given the wire's small size (50 μm). A representation of such method is shown in Fig. 4.13. By propagating the uncertainty over the entire length of the wheel, the initial orientation was determined with an accuracy of up to 0.1°. This preliminary calibration ensures a precision of 0.1° for the orientation of the source polarizer (P1) relative to the optical line of sight.

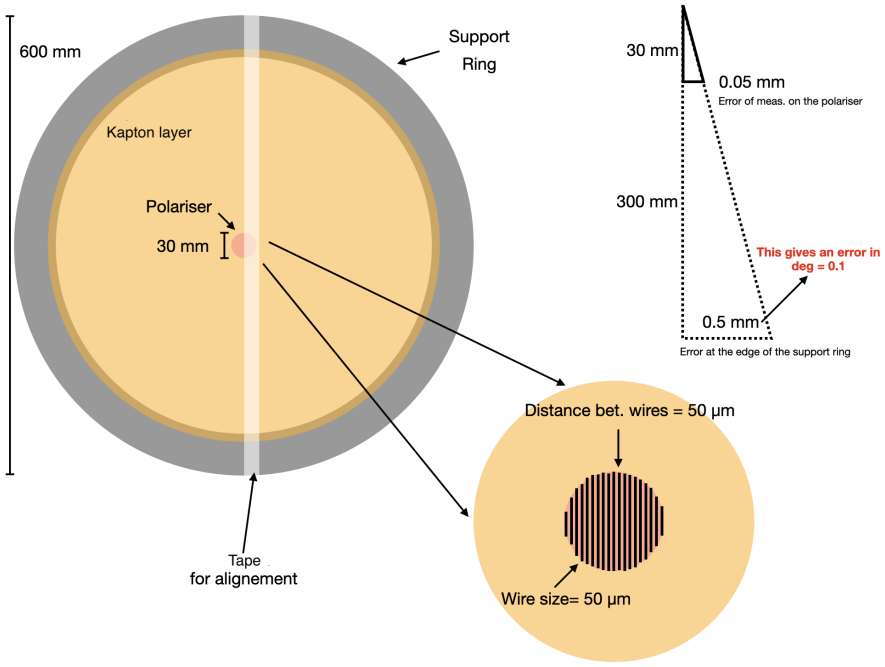

Figure 4.13: Visual representation of the adopted pre-calibration strategy for determining the 0-level reference frame of P1.

Moreover, the polarizer at the 100 mK stage (P2) has been positioned with a given orientation of $\beta = 0° \pm 1º$, empirically leveled with respect to the line of sight. The parameter β is a central element in these measurements and in the subsequent analysis. In previous experiments using the same camera configuration, such as NIKA2, achieving extremely high precision in the characterization of this angle and its associated uncertainty was not a primary concern. Indeed,

for typical astrophysical polarimetry observations, a precision better than 1° is generally not required, unlike in the case of CMB polarization measurements, where such accuracy becomes critical. However, in the context of this work, calibrating β with high precision proves to be essential, as it cannot be corrected or re-calibrated during or after sky observations. It represents our only absolute reference for the orientation of the polarization. Therefore, an accurate determination of this parameter is crucial to ensure the global precision of the reconstructed polarization angle of the incoming radiation.
Polarimetric characterization involves the production of OTF maps in which for each map, the source polarizer (P1) is rotated by 15° relative to its previous orientation. This rotation is controlled via an angular encoder, enabling an angular precision of 0.01º (0.6 arcmin). By producing polarization maps for each KID analogous to those previously generated for a photometric point source, we applied an aperture photometry technique to extract the flux within a defined region of interest, as shown in Fig. 4.14. Aperture photometry is a widely used technique for estimating the flux of sources in maps, regardless of their specific morphology. This method requires defining two critical parameters: the center of the aperture and the cut-off radius. In this analysis, the center was selected as the location of the signal's maximum intensity, ensuring the aperture is well-centered on the source of interest. The cut-off radius was determined to enclose 90% of the total flux, providing a balance between capturing the majority of the signal and minimizing contamination from surrounding noise.

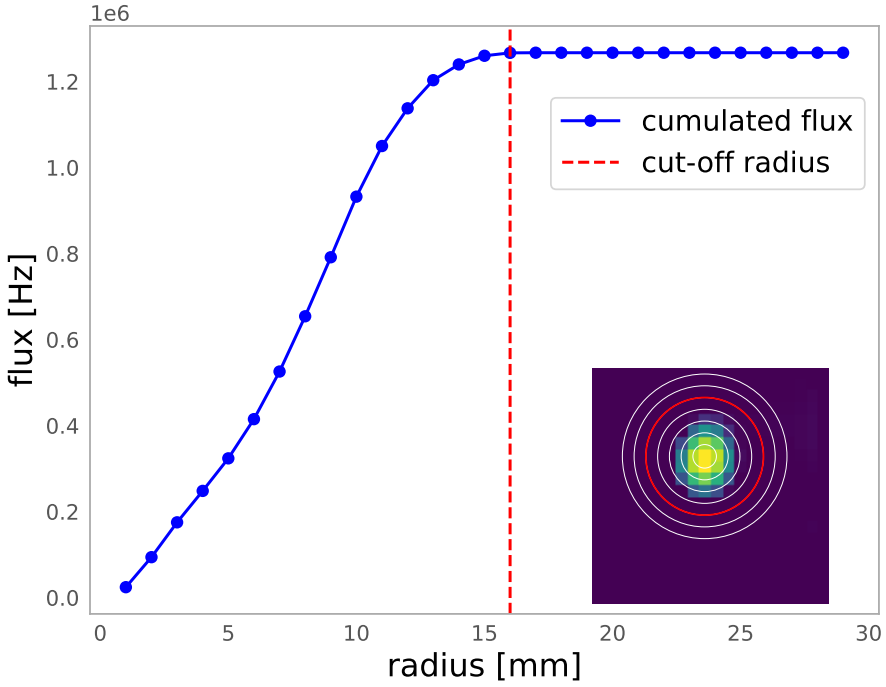

Figure 4.14: Aperture photometry technique used to estimate the cumulative flux within a defined radius. The red dashed line in the flux plot and the corresponding circle on the map represent the selected cut-off radius, indicating the boundary considered for analysis.

Using these flux measurements, we derived polarization curves averaged over the usual selection of best-performing pixels.
The top panel of Fig. 4.15 shows the images of the polarized source (P1) in the focal plane as a function of its relative orientation with respect to P2, for the transmission (T on the left) and for the reflection (R on the left) arrays. As expected, when the transmission array records a maximum signal (the middle map at 90º), the reflection array observes a minimum, and vice versa. This behavior arises directly from the action of the cold linear polarizer, which splits the signal into two orthogonal polarizations, separated by a phase difference of 90°.

In the bottom panel of Fig. 4.15, we show the intensity curves obtained as explained before, again for both arrays. We can fit the measured data to an analytical model, in order to determine the orientation of P2 (angle β). The model function, V, shown in Eq. 4.14, was derived from the Stokes vector of unpolarized light, emitted by the sky simulator, and applying the Mueller matrices corresponding to the polarized source orientation (P1, angle α) and the cold polarizer (P2, angle β):

$$V = 1 + \sin 2\alpha \cos 2\beta + \cos 2\alpha \sin 2\beta \,. \tag{4.14}$$

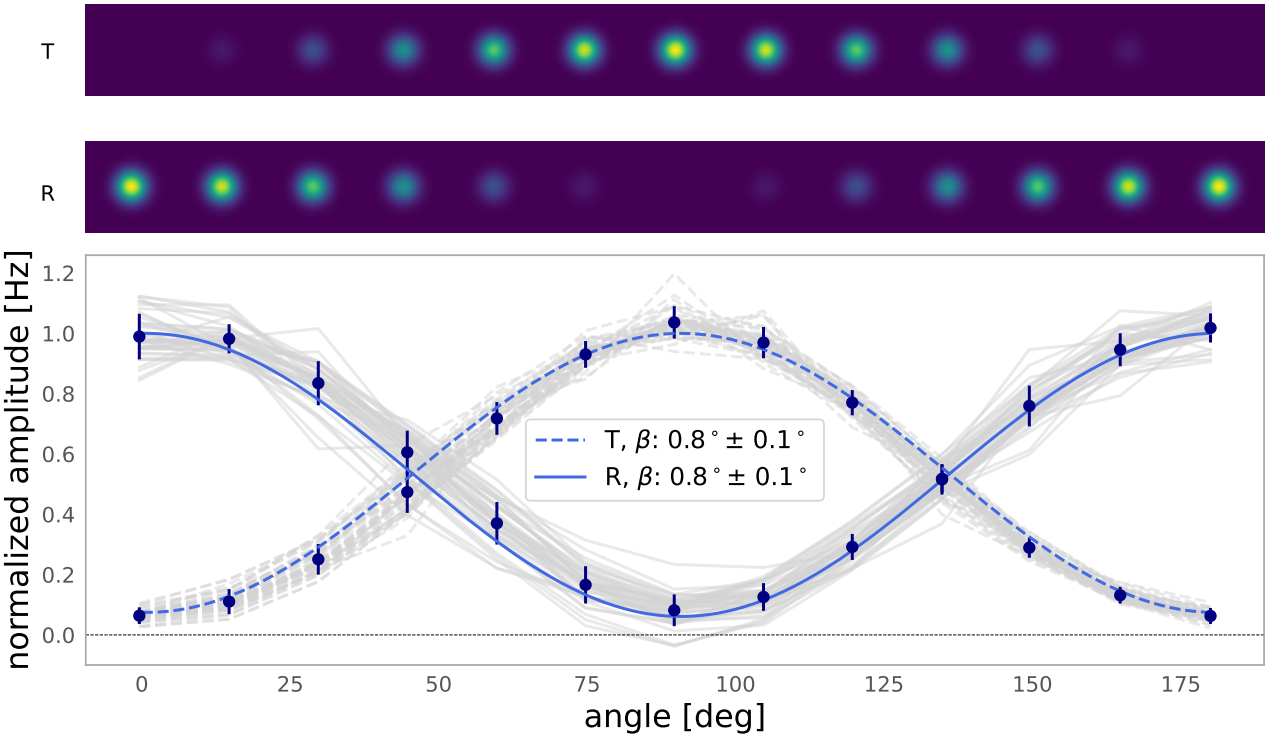

Figure 4.15: Top panels: projected maps of the polarized source (P1) oriented at different angles as seen by the transmission (T) and reflection (R) arrays; Bottom panel: intensity of P1's maps as a function of the orientation angle for the transmission (T, dashed curves) and reflection (R, solid curves) arrays, obtained using an aperture photometry technique and fitted to derive $\beta = 0.8° \pm 0.1°$. The superposed gray lines represent individual results for the selection of best KIDs.

The experimental data points in the bottom panel of Fig. 4.15 have been fitted jointly using a Monte Carlo Markov Chain (MCMC) algorithm implemented via the `emcee` Python library to ensure robust estimation of parameters (Foreman-Mackey 2013 [118]). The fit results, obtained for the usual selection of best pixels, provide a final estimate of $\beta = 0.8° \pm 0.1°$. In the final error estimate for β, we have accounted for the intrinsic error on α, 0.6 arcmin, the angular encoder's uncertainty. This contribution is not shown in the plot as it is a minor and non-limiting source of error. The dispersion among the gray curves, each corresponding to a selected KID, arises from variations in their intrinsic response properties, differences in their positions on the focal plane, hence carrying optical distortions, and potential beam distortions. These factors may result in varying flux contributions when performing aperture photometry.

4.5 Interpretation of results

The results of polarimetry measurements show some interesting features: in particular, we want to focus on the interpretation of the polarization angle accuracy and its limiting factors, along with the offset of all curves, which do not reach a zero level at any moment.

4.5.1 Polarization angle accuracy

The fitted estimate of β can be interpreted by distinguishing between systematic and statistical uncertainties. The central value, $\beta = 0.8°$, is consistent with the expected pre-calibrated value of $\beta = 0° \pm 1°$. This relatively high uncertainty is expected, as the angle could not be calibrated with a precision better than 1°. It reflects a good control over systematic effects, particularly considering the pre-calibration uncertainty on the orientations of P1 and P2, which is limited to 1°.
On the other hand, the associated statistical uncertainty of $\pm 0.1°$ reflects both the reproducibility of the measurement and the intrinsic dispersion observed among the KIDs within the same array, as illustrated by the superposed gray lines in Fig. 4.15. The reproducibility is particularly important: in principle, this measurement procedure could have been repeated multiple times, retrieving a value of the polarization angle β for each KID at each iteration, and thereby quantifying the stability of the measurement across repetitions. This component of the uncertainty is essential for establishing the reliability of the measurement method itself. In contrast, the dispersion between KIDs is not critical from a purely precision-focused standpoint. One could, in fact, characterize a single KID and assign an individual uncertainty to it. However, since the analysis aims to ensure consistency across all detectors in the array, we adopt a statistical uncertainty that encompasses inter-KID variability. This choice serves more to assess array uniformity and robustness than to enhance the absolute precision of the result.

4.5.2 Cross-polarization contribution

Furthermore, it is important to note that the curves do not reach a zero level, which implies that the polarization is not entirely pure and there is an observable degree of cross-polarization. This effect probably results from observing two signal sources simultaneously: one from the sky simulator and another from the reflected ambient signal. The source polarizer (P1) does not emit any signal, but either reflects or transmits incoming signals based on its orientation. Positioned at a 10º downward tilt, P1 reflects the 300 K ambient signal while allowing the cold signal from the sky simulator to pass through. As a result, the 300 K signal dominates, but mixes with the cold sky simulator signal, preventing a complete nullification, even with the 90º phase difference between P1 and P2. This behavior is modeled by:

$$V_{dual} = V_{refl} + k(T) \cdot V_{trans}\,, \tag{4.15}$$

where V_{refl} is the reflection component, V_{trans} is the transmission component, and $k(T) = T/300$ is a factor depending on the temperature. The model is represented in Fig. 4.16, where we simulate curves for AT and AR, following the same behavior of Fig. 4.15, but changing the relative optical load.
It is clear that for higher background temperatures, the cross-polarization effect is increasingly dominating, shifting the minima of curves to higher intensities. By fitting the curves of the bottom panel of Fig. 4.15 to the model of Eq. 4.15, we estimate that the parasitic component accounts for approximately 1% of the signal, which corresponds to a cross-polarization of 1% or parasitic temperature of (17 ±9) K. We observe a large dispersion from one KID to another, which can explain the discrepancy between this result and the temperature of the sky simulator

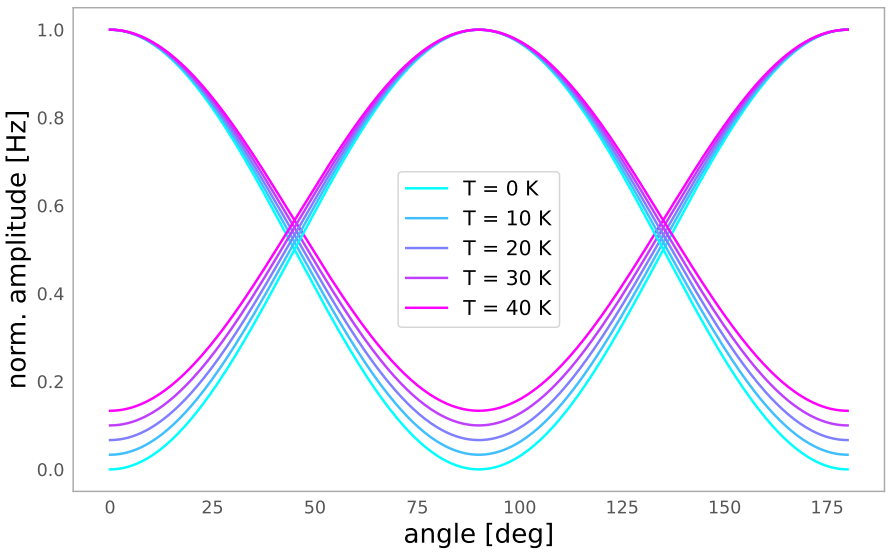

Figure 4.16: Simulated response of the curves as a function of the temperature of the reflected component, for both transmission and reflection arrays.

derived in Subsec. 4.3.1. It is important to emphasize that the effect we refer to as cross-polarization is not a systematic error in the strict sense and does not compromise the validity of our polarimetric characterization. On the contrary, this effect can be modeled, as we did, and properly accounted for in the subsequent data analysis.

4.6 Implications for CMB B-modes observations

The high-precision results presented for polarization measurements carry substantial implications for the future application of this technology in instruments designed to observe the polarization of the CMB. In particular, the ability to detect B-modes or accurately characterize galactic foregrounds, key challenges in CMB studies, could be significantly enhanced by advances in this field, as discussed in detail in Chap. 1. These findings underscore the importance of this work in demonstrating technologies capable of meeting the stringent requirements for such observations.
For a better understanding of the impact of $\Delta\psi$ on r, we can plot Δr as a function of $\Delta\psi$, as shown in Fig. 4.17. The relation between these two quantities has been explained in Chap. 2, Sec. 2.6. In this plot, we show the model curve compared to a set of experimental or simulated results. In particular, we show upper limits from Planck intermediate results (Planck collaboration 2016 [245]), obtained considering the nulling effect from E to B modes. The forecast limit on Δr for SO is also shown, following the simulated value presented in Giardiello et al. 2024 [123], combining estimates from the SO for both the Small Aperture Telescopes and the Large Aperture Telescope (SO collaboration 2019 [4]). As we can see, our experimental uncertainty on the polarization angle lies well below all available and forecasted current constraints.

4.7 Conclusions and perspectives

This work has successfully established a fully equipped facility for rigorously testing the polarization capabilities of LEKIDs arrays with elevated precision. Using this setup, we demonstrated that two orthogonal LEKIDs arrays, configured with a 45° linear polarizer between them, achieved polarization angle reconstruction with a precision of 0.1°, meeting the strin-

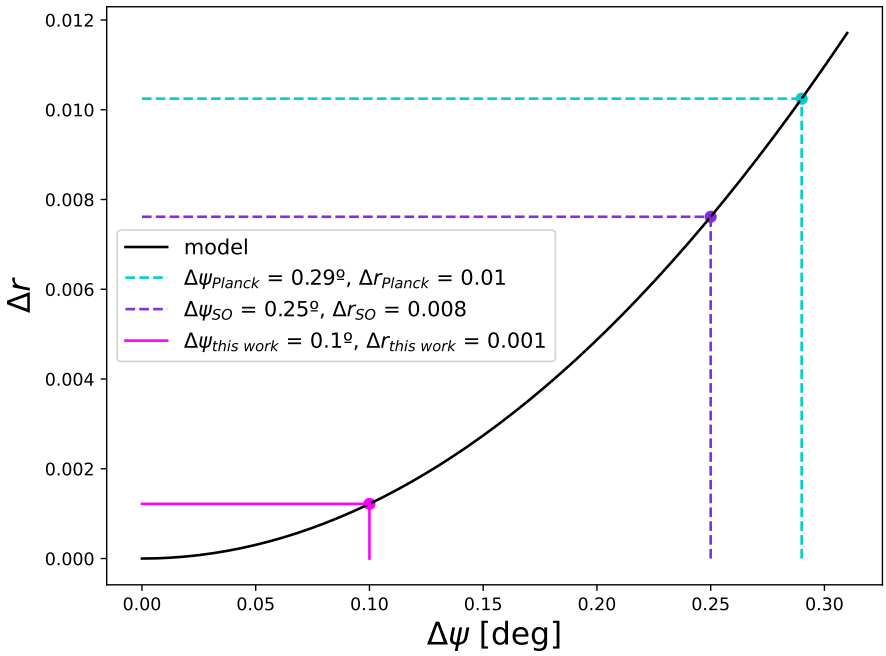

Figure 4.17: Forecast for Δr values as a function of error on the polarization angle. The light blue line represents values from Planck constraint, the purple one for SO simulations and the magenta one shows results for this work.

gent performance requirements of next-generation CMB experiments. Additionally, the Noise Equivalent Power (NEP) of the arrays was measured to be $(1.5 \pm 0.5) \times 10^{-16}$ W/$\sqrt{\text{Hz}}$, comparable to the photon noise limit (NEP_{phot}), underscoring their competitiveness in millimeter-wave instrumentation.

The cryogenic system exhibited stable operation, maintaining temperature fluctuations of the 100 mK stage within 1 mK during typical measurement sessions. Optical components, including the cold polarizer, displayed high reliability. The readout electronics ensured the required multiplexing factor, and the sky simulator demonstrated precise angle and position encoding, with accuracies of 0.6 arcmin and 0.01 mm, respectively. These achievements confirm the robustness and reliability of the experimental setup across all components.

A critical lesson learned from this study is the importance of rigorous calibration, particularly concerning the zero-level reference of the polarized source (P1) and the precise orientation of the cold polarizer (P2). Ensuring accurate pre-calibration of P1 and maintaining precise alignment of P2 are essential to minimizing systematic uncertainties and enhancing measurement precision. These insights will guide future refinements to experimental setups, significantly improving polarization angle reconstruction accuracy.

Looking ahead, several key directions have been identified to further advance the development and application of LEKID technology for CMB research. A major priority is extending the validation of polarization performance from 150 GHz (2 mm) to higher frequencies, particularly up to 260 GHz (1 mm). Observations in this frequency range are crucial for separating foreground contamination, especially thermal dust emission, and for providing complementary data to refine our understanding of the cosmological signal. This effort is already underway, as presented in Chap. 3, Sec. 3.6, where we describe the fabrication and initial characterization of detector arrays optimized for operation at 1 mm. Photometric and spectral measurements at this wavelength have already begun, along with preliminary polarization tests. However, in-lab measurements at 1 mm present additional challenges compared to those at 2 mm. These include a more demanding optical setup, due to the smaller beam sizes and increased sensitivity to optical misalignments and imperfections in the polarizing elements. At these higher frequen-

cies, the detectors are also subject to a greater photon background from laboratory blackbody sources, and the narrower spectral features require finer resolution and more precise calibration. Furthermore, resonator design and fabrication become more complex due to the need for smaller geometries and tighter frequency spacing. While this work is already well advanced, further studies are necessary to fully characterize the system and reach the level of precision required for high-frequency CMB polarimetry.

Another promising direction involves the testing of the dipole, complementing the point-like unpolarized and extended polarized sources already used. Preliminary measurements with the dipole source have been carried out, but the results remain inconclusive. Although the source was detected, its SNR was too low to draw firm conclusions, and the data analysis proved particularly challenging. Nonetheless, this remains a scientifically valuable avenue for further exploration. By improving the optical alignment and exercising tighter control over the noise environment, it may be possible to enhance the detectability of the dipole signal and fully exploit this source for precise in-lab polarimetric validation.

This work also emphasizes the need for further study of beam distortions and their orientation-dependent effects. Beam distortions significantly influence the estimation of cosmological parameters, particularly in the detection and characterization of CMB B-modes. Understanding the relationship between beam distortions and the orientation of the instrument will enable more precise modeling and correction of systematic effects, ensuring the technology's readiness for future CMB experiments.

In summary, this study has laid a strong foundation for LEKIDs-based polarization measurements, provided valuable lessons for improving calibration and alignment, and outlined clear paths for future advancements. Extending measurements to higher frequencies, refining calibration techniques, testing new optical sources, and addressing beam distortions will collectively strengthen the capabilities of LEKIDs technology, paving the way for its integration into advanced millimeter-wave instrumentation for cosmology.

Chapter 5

Polarimetry observations with NIKA2

Contents

5.1 The IRAM 30m Telescope **122**
5.2 The NIKA2 camera **123**
5.2.1 Cryostat 124
5.2.2 Readout electronics 124
5.2.3 Optics 125
5.2.4 NIKA2 as a polarimeter 126
5.2.5 NIKA2's scientific targets 126
5.2.6 NIKA2+: upgrade and re-commissioning preliminary results 128
5.3 Polarimetry observations with NIKA2 . . . . . **129**
5.3.1 Telescope operations 130
5.3.2 Scientific data treatment: from TOI to maps 132
5.4 Polarization study of W43 with NIKA2 . . . . . **133**
5.4.1 Main goal of the observations 133
5.4.2 Source description and observation strategy 134
5.4.3 Data analysis methodology 135
5.4.4 Results and interpretation 142
5.5 Conclusions and perspectives **144**

Abstract A significant part of this thesis is dedicated to polarization observations carried out with the New IRAM KID Array 2 (NIKA2) camera. In this chapter, we present the IRAM 30m telescope and the NIKA2 camera, with a focus on its polarimetric capabilities. A description of the recent instrumental upgrade (NIKA2+) is also provided, along with the preliminary results of the re-commissioning campaign, including updates on the focal plane geometry and sensitivity performance.
We then describe how typical NIKA2 polarimetric observations are conducted, based on an open-time project targeting a star-forming region in our Galaxy, which I led. This project was awarded 19 hours of telescope time with NIKA2, aimed at investigating the role of magnetic fields in high-mass star formation. Of these, 6.5 hours have already been observed, while the remaining time has been allocated for the Summer Semester 2025. Thanks to the high quality of the data, we were already able to obtain results, producing both a map of the magnetic field morphology and an estimate of its intensity.
This work offers a novel perspective on a well-studied region by providing polarization data at intermediate angular scales—those of NIKA2 at 12″—bridging the gap between the coarse resolution of *Planck* (5′) and the fine-scale observations of ALMA (0.5″).

5.1 The IRAM 30m Telescope

The IRAM (*Institut de Radio Astronomie Millimetrique*) 30m telescope, located at an altitude of 2850 m on Pico Veleta in the Sierra Nevada mountains of Spain (coordinates 03:23:33.7 W / 37:03:58.3 N), is one of the most advanced facilities for millimeter-wavelength astronomy. It was designed and built between 1980 and 1984 by IRAM, in a consortium shared between Spain, France and Germany.



Figure 5.1: Picture of the IRAM 30m telescope before (left) and after (right) the re-painting. Shot by M. Castillo.

The telescope features a 30-meter parabolic dish, constructed from 420 precisely aligned aluminum panels with a surface accuracy of 55 μm RMS. These panels are covered with an infrared reflector that reduces the deformations due to temperature gradients, especially at critical times such as sunrise and sunset. The dish has been completely re-painted in 2024 to enhance this

stabilization feature (Fig. 5.1), now featuring a surface roughness of 50 ± 8 μm. The telescope shows two main collecting mirrors: M1, the primary mirror, and M2, the secondary mirror. The primary mirror also has a temperature stabilization system, mostly useful for the de-icing procedure. The primary mirror is supported by a steel backup structure that ensures stability and maintains the surface's precision under varying environmental conditions. A sub-reflector, 2.7 m in diameter, is mounted on a Nasmyth platform and provides beam correction and re-imaging. This Cassegrain design minimizes optical aberrations and allows for efficient coupling of the incoming radiation to the receivers. The secondary mirror, 2 m wide, is located at the focal length of the 30m telescope, which is 10.5 m away from the primary (Baars et al. 1987 [20]). The large aperture of the primary mirror provides a high angular resolution, following Eq. 5.1:

$$\theta = 1.22\frac{\lambda}{D}\,, \tag{5.1}$$

where λ is the observed wavelength of radiation and D is the mirror's diameter. For a perfectly monochromatic wave at 150 and 260 GHz, the angular resolution would be 8.2" and 14.1" respectively. However, the light reaching the telescope is rather polychromatic, hence the effective beam for an instrument installed at the IRAM 30m telescope operating at such frequencies is 11.5" and 17" at 150 and 260 GHz respectively (Adam et al. 2018 [2]).
The site benefits of its high-altitude and low-humidity conditions, which help stabilizing the atmosphere, and enhance its transmission. However, the atmospheric contamination remains one of the key factors when dealing with data taken at this site. In particular, the instrument benefits of a τ-meter, constantly operating at the site. This tool allows to calculate in real time the opacity of the atmosphere at the Zenith, providing indication on whether to perform observations or not. Usually, observations can be performed when $\tau < 0.2$, depending on the season and general weather conditions.
Inside the telescope's Nasmyth cabin, multiple instruments can be housed and over the years many have been installed, always delivering fresh data to the scientific community. Typically, two kinds of instruments are installed at the same time: one heterodyne receiver, with high spectral resolution, mono-pixel and fitted for molecular observations (EMIR currently); and one bolometric receiver, characterized by a large bandwidth without spectral resolution, fitted for continuum observation, currently NIKA2. The NIKA2 instrument is coupled to the telescope via several off-axis mirrors.

5.2 The NIKA2 camera

NIKA2 is a dual-band continuum camera successfully installed at the telescope in October 2015. It is equipped with three frequency-multiplexed kilo-pixels arrays of LEKIDs cooled at 150 mK. NIKA2 observes simultaneously in two bands centered at 1.2 and 2.0 mm, and has polarimetry capabilities in the 1.2 mm band. With a field of view of 6.5' and a resolution of 11.5" at 1.15 mm, it is well-suited for mapping extended regions like molecular clouds and star-forming regions. In Tab. 5.1, we summarize the main technical characteristics of NIKA2. The Noise Equivalent Flux Density (NEFD) quantifies the sensitivity of a detector to incoming astronomical signals. It is defined as the flux density that produces a signal equal to the noise level in one second of integration, expressed in units of mJy $\sqrt{\text{s}}$. Lower NEFD values indicate higher sensitivity, as fainter sources can be detected in shorter observing times.

Parameter	150 GHz (2.05 mm)	260 GHz (1.15 mm)
Field of View (FoV) [arcmin]	6.5'	6.5'
Number of detectors	1020	1140
Valid detectors	90%	84%
Main beam FWHM [arcsec]	17.6" ± 0.1"	11.1" ± 0.2"
Bandpass [GHz]	125–170	240–280
RMS pointing error	< 3"	< 3"
NEFD [mJy · $s^{1/2}$] (tot. intensity)	9 ± 1 (I)	30 ± 3 (I)
NEFD [mJy · $s^{1/2}$] (polar. mode)	9.5 ± 2 (I)	33 ± 4 (I); 20 ± 3 (Q, U)

Table 5.1: NIKA2 technical characteristics, as presented in Perotto et al. 2020 [235] and in the NIKA2pol commissioning report, IRAM internal document, 2024.

5.2.1 Cryostat

The focal plane arrays and the final segment of the optical system are cooled to a base temperature of approximately 150 mK using a ^{3}He–^{4}He dilution refrigerator. The NIKA2 cryostat follows the pathfinder NIKA instrument, converted to the KISS instrument after being decommissioned, and now used for in-lab measurements at LPSC (see Chap. 4). The NIKA2 cryostat is composed of multiple cryogenic stages, as shown in Fig. 5.2, from 300 K to the coldest mixing chamber at 150 mK. The dilution refrigerator, and the rest of the cryostat, has been entirely designed and realized by CNRS Grenoble. NIKA2 employs two Cryomech PT415 pulses-tubes, each delivering a cooling power of 1.35 W at the reference temperature of 4.2 K (second stage) and several tens of Watts at 3070 K (first stage).

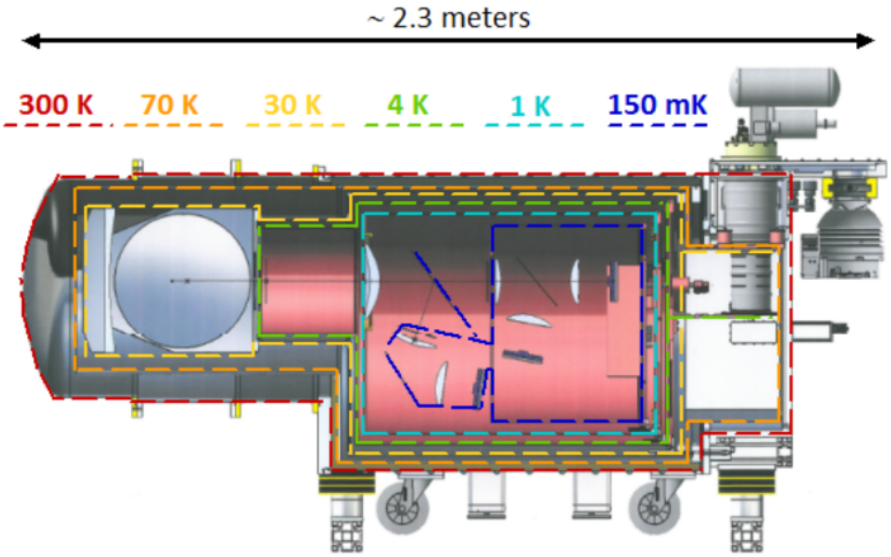

Figure 5.2: Schematics of the NIKA2 cryostat, highlighting the 6 cryogenics stages: 300 K, 70 K, 30 K, 4 K, 1 K and the coldest at 150 mK. From Adam et al. 2018 [2].

5.2.2 Readout electronics

To efficiently manage the large-scale arrays of the NIKA2 camera, a custom-designed readout system has been implemented: *NIKEL_AMC* (as in Chap. 3, Subsec. 3.4.2, Bourrion et al. 2016 [48], Fig. 5.3). This readout system consists of 20 advanced readout boards, housed within three microTCA crates. Each board is capable of multiplexing up to 400 detectors,

enabling precise signal processing with consistent performance across all boards, even under real observing conditions. The system achieves a threefold reduction in physical volume compared to previous generations, while providing enhanced functionality and reliability. This innovative design ensures seamless integration with the KID arrays and supports reliable data acquisition for NIKA2's advanced astronomical observations.

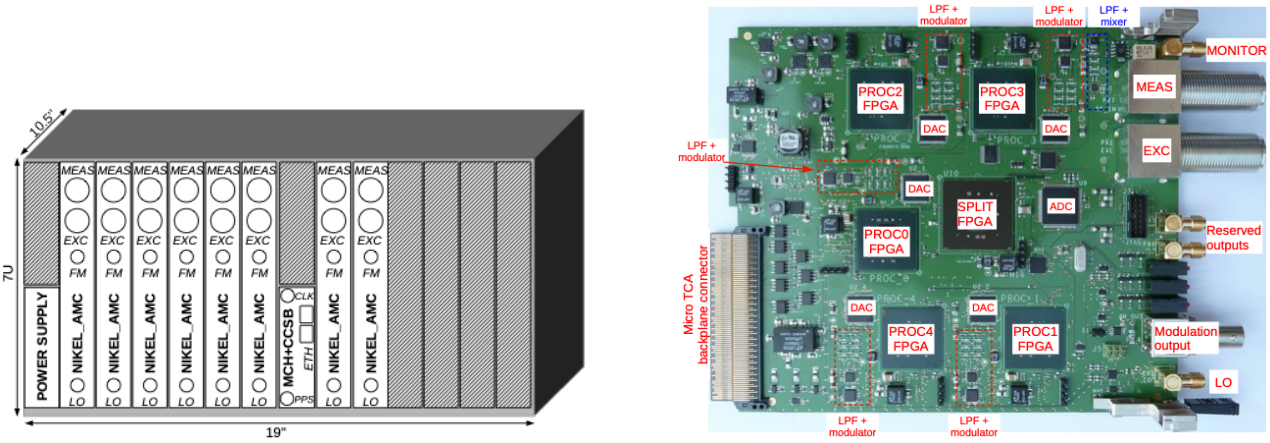

Figure 5.3: *Left:* Overview of one array readout electronics crate. *Right:* NIKEL_AMC board picture, with dimensions of 18 × 15 × cm^3. From Bourrion et al. 2016 [48].

5.2.3 Optics

The design of the NIKA2 optics employs a set of mirrors coupled to the antenna to focus radiation from the secondary mirror into the Nasmyth cabin and eventually into the cryostat. A set of 6 mirrors, from the main dish, M1, to M6 is designed and realized to direct the beam towards the NIKA2 detectors, as shown in Fig. 5.4.

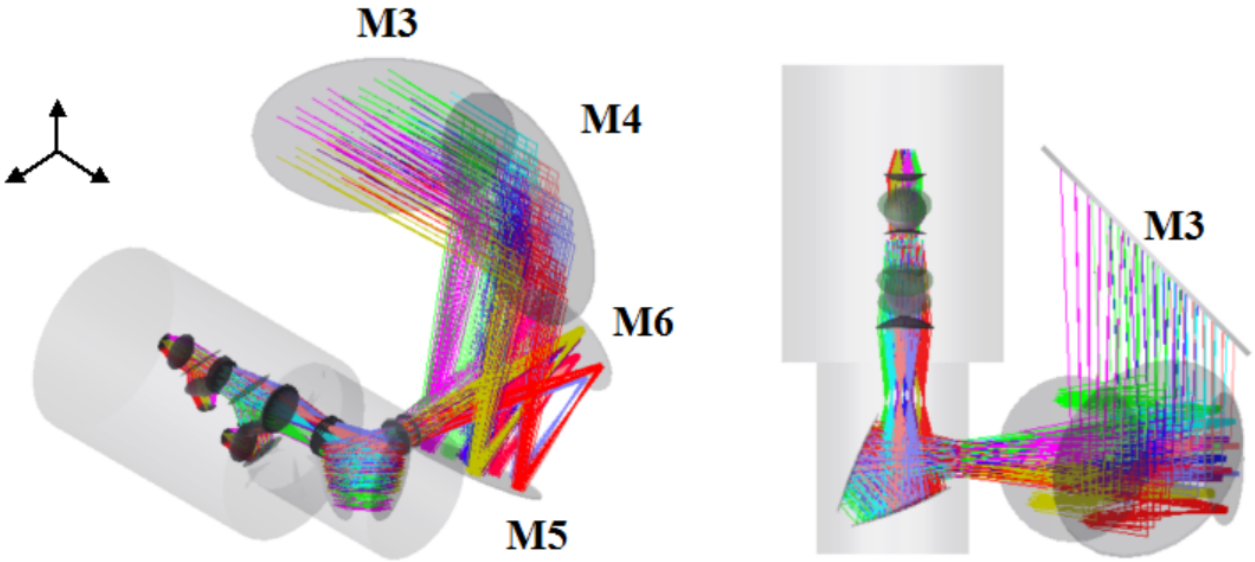

Figure 5.4: *Left:* Isometric view of the cabin optics scheme, illustrating the mirrors M3, M4, M5 and M6. The ideal case in which the elevation angle is zero degrees is shown. *Right:* top view of the cabin optics feeding NIKA2. From Adam et al. 2018 [2].

After M6, the beam enters the cryostat through a flat HDPE window and is again reflected by two mirrors. Subsequently, a dichroic filter separates incoming light into two channels at 150 GHz (2.05 mm) and 260 GHz (1.15 mm). Multiple lenses are present to ensure beam focusing. The configuration of the polarization-sensitive channel is exactly the same as described in Chap. 4, Subsec. 4.2.2. In contrast, the 150 GHz channel in NIKA2 remains unpolarized, optimized instead for total intensity measurements. A cross-section representation of the interior of the NIKA2 cryostat is shown in Fig. 5.5.

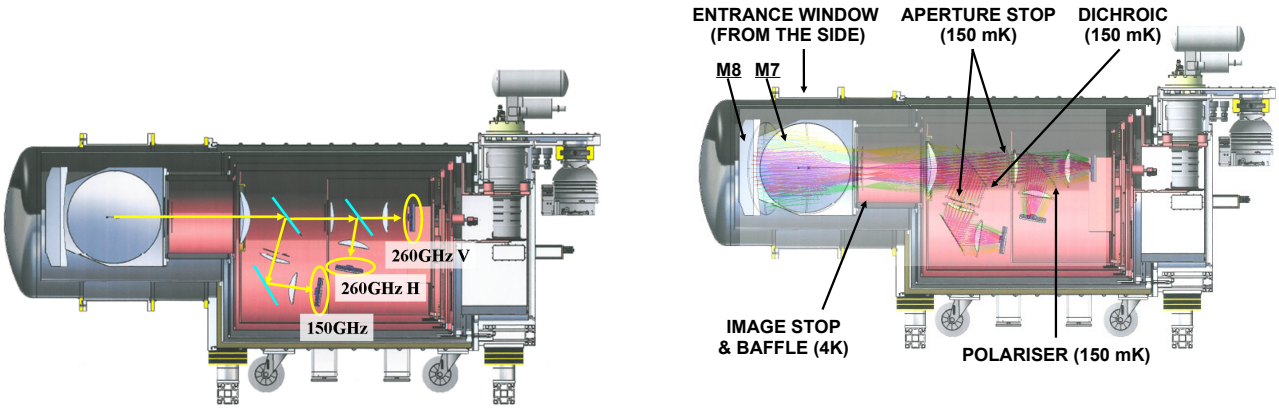

Figure 5.5: *Left:* Cross-section of the NIKA2 instrument illustrating the position of the three detector arrays (150 GHz, 260 GHz vertical and 260 GHz horizontal); the optical axis and the photon direction of propagation are shown as well. *Right:* Cross-section of the NIKA2 instrument illustrating the cold optics and the main elements and surfaces. From Adam et al. 2018 [2].

5.2.4 NIKA2 as a polarimeter

One of the key advantages of the NIKA2 instrument is its dual capability to operate both as a photometer and a polarimeter, with practical switching between configurations. The polarimetric mode is achieved by integrating a specific optical component, a HWP, into the optical setup. This HWP is positioned in front of the cryostat window, following M6. The HWP plays a crucial role in modulating the polarized signal, enabling the extraction of the Stokes parameters, as detailed in Chap. 1, Subsec. 2.3.2 and Subsec. 2.4.2. After passing through the HWP, the signal is directed toward a cold polarizer, which separates the two orthogonal polarization states. The resulting modulated polarized signal is then detected by the KID arrays. This setup allows NIKA2 to reconstruct the polarization of the incoming radiation with a precision of $\sim 1^{\circ}$. Furthermore, the polarization measurements benefit from the precise calibration of the HWP and the cold polarizer, ensuring minimal instrumental polarization and systematic effects. A schematic view of the polarization detection process is shown in Fig. 5.6.

5.2.5 NIKA2's scientific targets

The NIKA2 collaboration was granted 1300 hours of telescope time by the IRAM consortium, distributed across five large programs (LPs), each targeting a major astrophysical objective.

Clusters of galaxies via the Sunyaev-Zel'dovich (SZ) effect The thermal Sunyaev–Zel'dovich (tSZ) effect (Sunyaev & Zel'dovich 1970 [287]; Sunyaev & Zel'dovich 1980 [286]) enables the detection of high-redshift galaxy clusters, providing a cosmology-independent probe

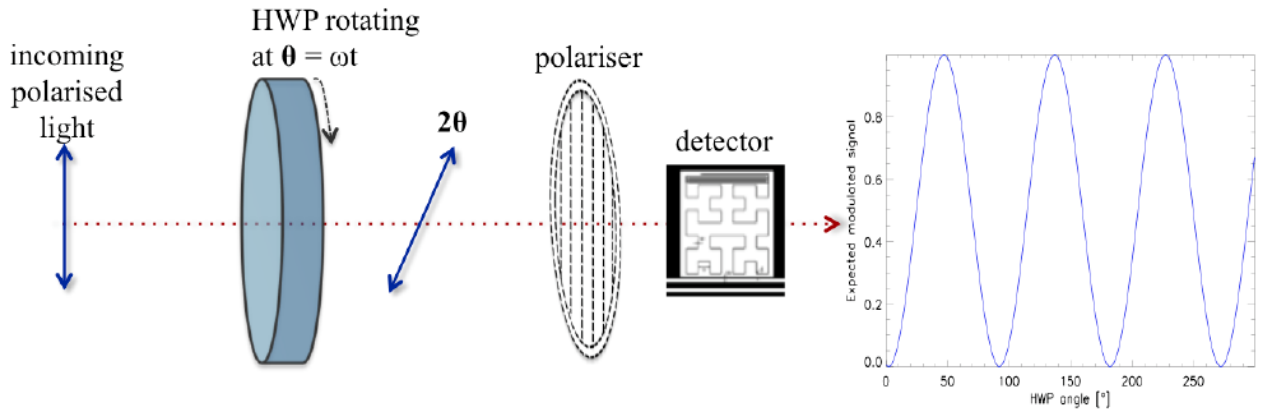

Figure 5.6: Schematic view of the NIKA2 polarization detection strategy: from left to right, the incoming light passes through a rotating HWP and a cold polarizer, which is used to select the orientation of the linear polarization. From A. Ritacco's PhD manuscript.

of the intra-cluster medium (ICM). NIKA2 offers high-resolution (12–20″) and high-sensitivity (approximately 4×10^{-5} per beam per hour) tSZ imaging. From 2017 to 2021, 38 clusters were observed and characterized in the redshift range $0.5 < z < 1.5$, with scientific goals including calibration of the tSZ signal as a mass proxy, investigations of cluster dynamics, and constraints on cosmological parameters—building upon the prototype NIKA, which achieved the first tSZ observations using a KID-based instrument (Adam et al. 2013 [1]). In particular, the NIKA2 Sunyaev–Zel'dovich Large Program (LPSZ) has completed high-resolution tSZ mapping of 38 clusters in the intermediate-to-high redshift range ($0.5 < z < 0.9$), combining SZ measurements with X-ray data to refine hydrostatic mass estimates, characterize ICM pressure profiles, and establish robust scaling relations for cluster cosmology (Moyer-Anin et al. 2025 [207]). Recent work using "THE THREE HUNDRED" simulations in concert with LPSZ data has quantified biases in mass reconstruction caused by assumptions of spherical symmetry and projection effects—finding that projection introduces uncertainties of order 10–16% in mass estimates, with an additional scatter of up to 9% between clusters (Muñoz-Echeverría et al. 2024 [208]). Moreover, case studies such as ACT-CL J0240.0+0116 demonstrate the power of LPSZ's high-resolution imaging: combining tSZ, X-ray, and optical data to derive pressure and mass profiles, assess dynamical state and morphological disturbances, and contend with contaminating central point sources—ultimately yielding precise hydrostatic mass estimates and insights into cluster substructure (Paliwal et al. 2025 [228]).

Deep surveys Thanks to its dual-band mapping capabilities, NIKA2 probes the early Universe by detecting dusty, optically faint galaxies during peak star formation epochs, in the context of the N2CLS (NIKA2 Cosmology Legacy Survey). Observations near the confusion limit, benefiting from the negative K-correction, enable efficient detection of high-redshift galaxies ($z > 1.5$). These deep field surveys aim to refine the cosmic star formation history by targeting obscured populations not captured in rest-frame UV surveys and investigating galaxy clustering to connect star formation with dark matter halo mass (Béthermin et al. 2025 [39], Ponthieu et al. 2025 accepted by A&A, Bing et al. 2023 [44]).

Mapping the interstellar medium The millimeter capabilities of NIKA2 allow detailed studies of dust emissivity variations and the stellar initial mass function (IMF) extremes, including brown dwarfs and massive stars. By mapping nearby and Galactic plane star-forming regions at 1 and 2 mm, NIKA2 addresses questions about dust grain growth, core and cloud-

fed star formation, and the origin of brown dwarfs. These observations aim to constrain the physical processes regulating star formation across a range of environments (Nguyen-Luong et al. 2024 [219]).

Nearby galaxies NIKA2 observations of approximately 100 galaxies from the Herschel Reference Survey (HRS) offer a unique window into millimeter-wave emission from dust, free-free, and synchrotron processes. With resolution comparable to Herschel PACS 160 μm, NIKA2 enables kpc-scale studies within 40 Mpc (Ejlali et al. 2024 [99]). These data are used to model spectral energy distributions, investigate gas-to-dust ratios, assess metal distribution, and calibrate star formation rate tracers, serving as a pathfinder for future radio surveys such as those planned with the SKA.

Polarization measurements of Galactic regions Magnetic fields are fundamental to star formation, yet their observational signatures remain elusive (Crutcher et al. 2010 [80]; Mouschovias et al. 1999 [206]). The 1 mm polarization channel of NIKA2 targets magnetic field morphology in filamentary clouds identified by *Herschel* (André et al. 2010 [13]; Molinari et al. 2010 [200]; Arzoumanian et al. 2011 [16]), where accretion may occur along field lines (Palmeirim et al. 2013 [229]; Hennemann et al. 2012 [138]). NIKA2 offers high-resolution (10″–60″) polarization mapping of nearby clouds and face-on galaxies, complementing large-scale *Planck* maps and radio synchrotron polarization studies (Matthews et al. 2001 [192]; Crutcher et al. 2004 [82]; Fletcher et al. 2011 [117]). These observations aim to constrain the role of magnetic fields in core formation and star formation regulation.

5.2.6 NIKA2+: upgrade and re-commissioning preliminary results

In March 2025, a major upgrade on NIKA2 has been carried out by the responsible NIKA2 team: the 260 GHz channel arrays were replaced, along with the dichroic filter splitting the beam between the two channels.

The new dichroic filter As discussed in previous sections, the NIKA2 camera employs a dichroic filter to separate its operational frequency bands, a critical component in its design. The development of this filter underwent extensive iterations, with multiple prototypes fabricated in Cardiff and tested in a dedicated cryostat at IRAM. Following evaluations, the third prototype (D3) filter was selected for integration into the pre-upgraded NIKA2 camera. This dichroic filter is constructed from vacuum-separated membranes and is supplemented by six tensioned thermal filters. Initial operational challenges, such as deformation under cryogenic conditions, were resolved through improved manufacturing techniques. The earlier dichroic filter introduced an undesired gradient effect on the focal plane of the 260 GHz channel, particularly affecting the A1 detector (260 GHz-V in Fig. 5.5). This issue stemmed from the non-uniform transmission and reflection of the polarized signal across the focal plane. The new dichroic filter (Fig. 5.7) is supposed to limit this effect due to reduced thermal and geometrical distortions.

New 260 GHz arrays A significant modification in the upgraded design of NIKA2 involves the arrays of the 260 GHz channel, the sole channel sensitive to polarization. Initially, Hilbert arrays were utilized in NIKA2, representing early prototypes of micro-strip technology, a novel approach at the time (see Chap. 3). Over time, advancements in technology led to the development of new wafer designs in 2019. These wafers, with a reduced thickness of 90 μm (compared to the previous 260 μm), introduced single-polarization capabilities and featured an optimized design. The improved arrays provide a broader operational bandwidth spanning

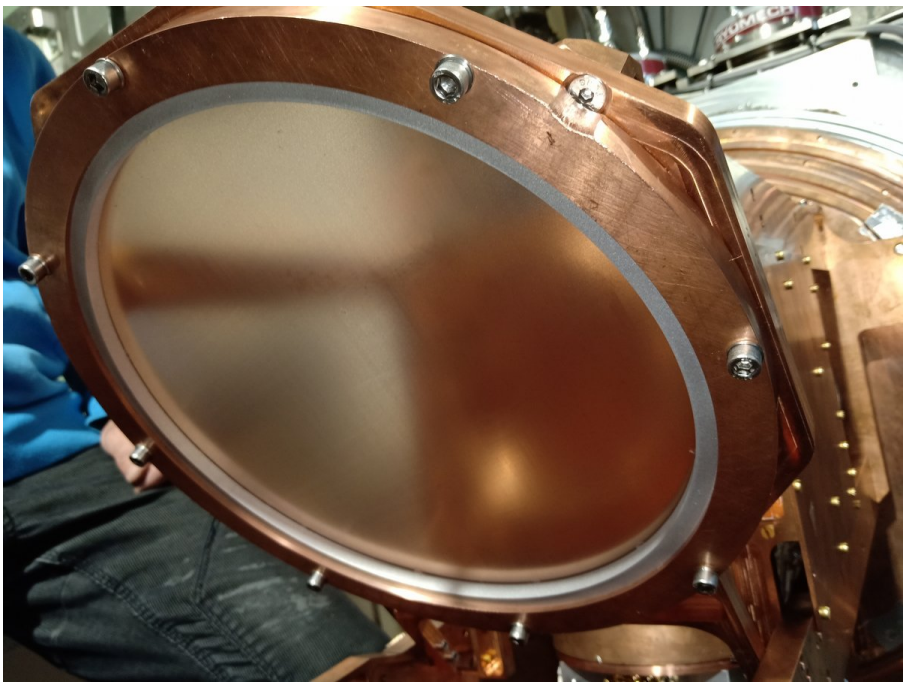

Figure 5.7: Picture of the new dichroic filter installed in NIKA2. Shot by the NIKA2+ team during installation.

200 to 300 GHz. The newer arrays also exhibit enhanced cosmetic quality and a different frequency resonance distribution, eliminating the doublets and triplets that were prevalent in earlier designs. The number of LEKIDs per array remains unchanged, with 1140 detectors per array. Additionally, the orientation of arrays A1 and A3 has been configured so that the incoming polarization direction matches the LEKID pattern of each (see Chap. 3), while they were previously oriented in the same direction.

Main improvements The newly developed dichroic filter, incorporating additional layers and an optimized design, seems to mitigate the gradient effect, leading to a more homogeneous performance across the detector array. Although the final re-commissioning analysis of the upgraded NIKA2+ instrument is still in progress, preliminary results already show a marked improvement in total intensity sensitivity. In particular, the noise equivalent flux density for at least one array of the 260 GHz focal plane has been reduced by a factor of two. This gain in sensitivity translates into a fourfold reduction in the observing time required to reach the same RMS noise level. Such an improvement will be especially valuable for deep surveys and wide-area sky mapping, enabling more efficient and detailed investigations of astrophysical phenomena.

5.3 Polarimetry observations with NIKA2

The process from telescope operations to the production of final astrophysical maps is complex and involves multiple stages. In this section, we provide a concise overview of the NIKA2 polarimetry observation procedure. A detailed description of the raw data analysis techniques leading to the final maps is not presented here, as these steps are handled by the official NIKA2 data reduction pipelines (Perotto et al. 2020 [235], Ritacco et al. 2017 [265] polarization-specific). A schematic workflow of such procedure is shown in Fig. 5.8.

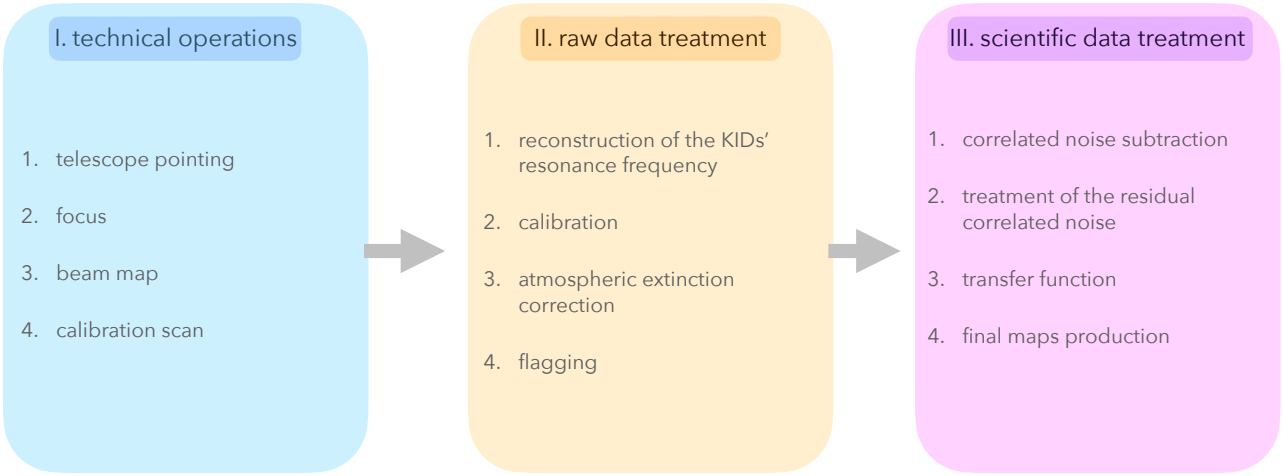

Figure 5.8: NIKA2 typical workflow: from the telescope operations to acquire data, to the raw data treatment to obtain TOI from KID data, to the scientific data treatment to obtain maps from TOI.

5.3.1 Telescope operations

Before observing the scientific targets, several preparatory operations are carried out at the telescope to ensure optimal data quality and to acquire the necessary information for calibration.

Pointing The first step is to verify the alignment of the telescope optics with target source. This is achieved through regular pointing scans on bright, compact sources. These scans are performed in a cross pattern, with two passes in azimuth followed by two in elevation. A 1D Gaussian is fitted to the signal in each direction, and the peak position is compared to the known sky coordinates of the source. The resulting offsets provide corrections in azimuth and elevation, which are applied to refine the telescope pointing. While a more complex pointing model, under IRAM responsibility, accounts for seasonal and temperature variations, the pointing scans correct the residual random deviations on a time scale of a few hours.

Focus The telescope focus is periodically adjusted by moving the secondary mirror relative to the primary. An incorrect focus results in beam broadening, reduced angular resolution, and distorted source shapes. Focus scans consist of five raster scans of a bright source, each performed at a different secondary–primary separation. For each scan, a map of the source is produced and the beam size and source flux are measured. The optimal focus is determined by maximizing the flux of the calibration source, which in nominal conditions also corresponds to minimizing the beam effective FWHM.

`Beammaps`: focal plane reconstruction The NIKA2 readout electronics measure the resonance frequencies of the detectors, but do not directly indicate their physical locations on the focal plane. Prior to science observations, the geometry of the focal plane is reconstructed using `beammaps`: observations of bright, well-known sources, typically planets such as Uranus, Neptune, or Jupiter, with fine sampling of the map that allows a fully sampled image per KID. High signal-to-noise maps are obtained for each detector, allowing the association of each resonance frequency with a specific position on the sky. This process also identifies false resonances, out-of-resonance KIDs, and detectors affected by crosstalk. Relative calibration is obtained from the frequency shift of each detector compared to the known flux of the source. Beam properties are characterized for each KID, and detectors with excessively large beams are excluded. Absolute surface brightness calibration is derived from the combined `beammaps` of

all valid detectors, using the known brightness of the planet. `Beammaps` are performed multiple times during each observation campaign to ensure stability.

Calibration scans In addition to beam maps, calibration scans are carried out throughout the observing period to monitor the absolute flux calibration. As described in Perotto et al. 2020 [235], two types of calibration sources are used. Primary calibrators are well-characterized sources that define the absolute calibration; for NIKA2 these are usually planets such as Uranus and Neptune. The calibration factors obtained from primary sources are then verified using secondary calibrators, including MWC349 (a stellar binary), CRL2688 (an AGB star), and NGC7027 (a compact planetary nebula).

Scientific scans Once the focus and pointing are corrected, the telescope performs raster scans over the target field, while continuously tracking the sky position of a reference KID. Each detector measures the optical power variation at a sampling rate of 24 Hz for total intensity, and at 47 Hz for polarimetry, producing the Time Ordered Information (TOI). A pointing matrix, combining the telescope pointing and the relative position of each KID on the focal plane, allows the TOI to be projected into sky coordinates.

Instrumental polarization correction In general, NIKA2 polarimetry observations should be conducted under stable atmospheric conditions and low wind speeds to minimize tracking errors. Half-power beam widths (HPBWs) should be regularly monitored. Beam stability during daytime observations has significantly improved following the primary mirror repaint in summer 2024. To avoid beam smearing, scanning speeds should not exceed 35-40 arcsec/s. These speeds are consistent with Nyquist sampling of the 1 mm beam at each HWP phase. Instrumental polarization (IP) is a leakage from total intensity into Stokes Q and U and it can be up to 3% for compact sources. For extended sources, the IP tends to average out and is less critical. The characterization of IP depends on the availability of suitable calibration sources, which should ideally be observed at similar elevation and focus settings as the science targets. Recommended IP calibration sources include:

- **Uranus:** Compact, unpolarized, and stable; primary choice when available.
- **Neptune:** Rises a few hours before Uranus; suitable alternative.
- **Mars:** At opposition, Mars can nearly fill the beam, making IP pattern measurements more challenging.
- **Bright QSOs:** Sources such as 3C286, 3C454, or 3C84 may be used. However, their variability and intrinsic polarization complicate calibration, and the method is still under testing.

An alternative IP correction method is the transit method, in which the science source is observed over a range of parallactic angles. This separates the fixed IP pattern in Nasmyth coordinates from the source polarization fixed in RA/Dec. This method requires stable weather conditions and is currently being evaluated in the B-FUN project. In the future, a database of Uranus scans may be used for IP characterization.

`Skydip` Atmospheric extinction must also be corrected, since millimeter observations are strongly affected by atmospheric water vapor, as said in Chap. 2, Subsec. 2.6.1. The transmission at frequency ν can be expressed as

$$T_\nu = \exp\left(-\frac{\tau_\nu}{\sin\delta}\right) , \tag{5.2}$$

where τ_ν is the atmospheric opacity and δ the telescope elevation. The air mass factor $1/\sin(\delta)$ accounts for the larger atmospheric column crossed at low elevations. The sky opacity quantifies the ratio between the flux density measured by a ground-based telescope and the flux density above the atmosphere.
Opacity is continuously monitored at the telescope using two complementary methods. A `taumeter` provides fast, real-time measurements of the line-of-sight opacity at a reference frequency. In parallel, `skydip` procedures, consisting in measuring the sky signal at different elevations and at different azimuths as well, help determine two coefficients per KID, namely c_0 and c_1, that in turn, allow us to compute opacity at any time during observations. While `taumeters` are essential for continuous monitoring during observations, `skydips` provide calibrations specific to the pointing coordinates and target source (Catalano et al. 2014 [61], Perotto et al. 2020 [235]).
The derived corresponding transmission losses, integrated over the NIKA2 bandpasses, are corrected by applying multiplicative factors to the time-ordered information (TOI). Not only poor atmospheric conditions reduce the absolute transmission by lowering the measured brightness, but also increase detector noise. Finally, noisy or saturated detectors, as well as unstable regions of the TOI (e.g. between subscans or during rapid telescope accelerations), are flagged and discarded (Catalano et al. 2014 [61]). The resulting cleaned TOI are then suitable for further processing and map-making.

5.3.2 Scientific data treatment: from TOI to maps

At this point, raw KID data are calibrated as described in Chap. 3, Subsec. 3.4.3, to finally obtain TOI in Hz. Then, `beammaps` are used to measure the beam size of each detector and calibrate its flux response against well-known sources at 150 and 260 GHz, providing the relative calibration between KIDs. Then, combining all beam maps with calibration scans refines the absolute calibration, ensuring a consistent conversion of frequency shifts into physical flux densities. At this stage, the geometry of the focal plane is also reconstructed, enabling the construction of the pointing matrix $P_k(t, x, y)$, which maps the sky coordinates (x, y) of each detector k at any time t.
Once science-ready TOI are obtained, the astrophysical signal must be separated from dominant noise sources such as atmospheric emission, electronic noise, and cryogenic vibrations. The TOI for each detector k can be expressed schematically as:

$$\mathrm{TOI}_k(t,\nu) = P_k(t,x,y)S(x,y,\nu) + \alpha_k A(t,\nu) + \beta_k E(t,\nu) + C_k(t) + N_k(t) , \tag{5.3}$$

where $S(x, y, \nu)$ is the sky signal, A and E are the atmospheric and electronic noise contributions, C_k is cryogenic noise, and N_k the detector white noise. Atmospheric emission, typically orders of magnitude stronger than the astrophysical signal, is largely common to all detectors and can be estimated as a common mode. Electronic noise is similarly correlated within readout groups, while cryogenic contributions can be identified in Fourier space. In practice, decorrelation is performed by estimating common modes from groups of correlated detectors, masking the regions containing the astrophysical source to reduce signal loss. This process is iterated, refining the mask (or subtracting the estimated signal) to minimize filtering effects. Two pipelines are commonly used:

- **IMCM** (Iterative Multi Common Modes) estimates common modes from the most correlated detectors, masking the source and iteratively refining the mask based on signal-to-noise maps.

- **PIIC** follows a similar iterative approach but subtracts an estimate of the source signal from the TOI in each iteration, recalculating common modes on cleaner noise-dominated data.

Both methods project cleaned TOI into maps using a pointing matrix. Differences in projection kernels and signal treatment lead to small variations in the recovered fluxes and morphologies, but cross-comparison shows robust and consistent results. For detailed implementations, see Perotto et al. 2020 [235].

5.4 Polarization study of W43 with NIKA2

In the context of NIKA2 open-time projects for the Winter Semester 2024, we proposed a research study to investigate the role of magnetic field strength in the process of massive star formation. This proposal, of which I was P.I., was conducted in collaboration with F. Louvet, N. Ponthieu, F. Motte, and M. Valeille-Manet from IPAG, as well as other members of the NIKA2 core team, including A. Catalano, J.F. Macías-Pérez, F.X. Désert, S. Berta, and C. Kramer.
The selected probe for such study was W43, a bright star forming region in our Galaxy. We already introduced the scientific context of star formation in Chap. 1, Sec. 1.3. In this section, we present the polarimetry observations conducted with NIKA2, the data analysis strategy and preliminary results on how the intensity of magnetic field regulates the collapse that leads to star formation. This work will be presented in Savorgnano et al. 2025b (in preparation) once finalized.

5.4.1 Main goal of the observations

Observationally, the orientation of magnetic fields (ϕ) in star-forming regions can be derived from polarization measurements, and in particular from Stokes Q and U maps as follows:

$$\phi = 0.5 \arctan(U, Q) + \frac{\pi}{2}\,. \tag{5.4}$$

On the other hand, to estimate the strength of the plane-of-sky magnetic field ($B_{\rm POS}$) more components are required. One common method used for this purpose (as in Cortes et al. 2019 [78]) is the Davis-Chandrasekhar-Fermi (DCF) relation (Chandrasekhar and Fermi 1953 [65], Davis 1951 [83]):

$$B_{\rm POS} = \mathcal{F} \frac{\sqrt{4\pi\rho}\,\sigma_v}{\sigma_\theta}, \tag{5.5}$$

where $\mathcal{F}$ is an efficiency factor, ρ is the gas mass density, σ_v is the velocity dispersion, and σ_θ is the dispersion of polarization angles. We derived these quantities from a combination of continuum maps to estimate ρ, molecular line observations to measure σ_v, and polarization data for σ_θ. The methodology used to derive such maps is detailed in Subsec. 5.4.3. Obtaining this magnetic field map was the main goal of the study, as it represents an innovative result: the first complete map of the magnetic field intensity in this region. W43 had previously been the subject of polarization studies with Planck, at an angular resolution of $5'$, and with ALMA, at $0.5''$. In this context, Planck could only provide a broad estimate of the magnetic field structure across the large W43 complex, while ALMA can resolve individual clumps but not the global structure. This study therefore bridges the gap between these angular scales.

5.4.2 Source description and observation strategy

The target source for this study is W43, one of the most massive and active star-forming regions in the Milky Way, with a star formation rate of approximately 0.1 $M_\odot$ yr^{-1} (Nguyen-Luong et al. 2011 [217]). Located at a distance of $\sim$ 5.5 kpc in the Eagle constellation, W43's proximity, combined with the 11" angular resolution of the NIKA2 instrument at 260 GHz permits to reach a physical scale of $\sim$20 pc on target, which allows us to trace the magnetic field structure across the entire region and resolve the internal structure of individual one parsec-scale clumps. W43 spans $12' \times 10'$, exhibits high brightness (175 to 1000 mJy beam^{-1} at 1 mm), and shows significant polarization levels, between 1 and 8% (values derived from this work). The region contains an extensive reservoir of molecular gas, totaling approximately 7×10^6 $M_\odot$, and features regions of extremely high density. These properties make W43 an ideal target for studying the role of magnetic fields in massive star formation. The galactic coordinates of W43 (J2000.0) are $l = 30.76°$, $b = -0.01°$, corresponding to RA = $18^h47^m32^s$, DEC = $-01°56'31''$.
A considerable amount of preparatory work was carried out prior to the W43 polarimetric campaign in order to optimize the observational strategy. The adopted scanning strategy employs classic On-The-Fly (OTF) raster scans, performed twice at distinct orientations of 35° and 125°. These orientations were chosen with respect to both the source geometry and the requirements of the data analysis. The target region contains two extended horizontal filaments and one vertical filament; if scans were performed strictly along Right Ascension or Declination, the telescope motion would align with these structures, reducing the efficiency of the decorrelation process, since many detectors would remain on-source throughout the scans. By scanning diagonally, part of the focal plane continuously samples emission-free regions, allowing comparisons between KIDs exposed to the source and those observing the background, which improves atmospheric decorrelation.
From an atmospheric perspective, scans in telescope coordinates (Azimuth - Elevation) at constant elevation are generally optimal because they maintain a stable air mass, making the atmospheric contribution easier to model and subtract, while scans along elevation are less favorable due to rapid air-mass variations. In the present case, however, the limiting factor is not the atmosphere but the orthogonal morphology of the region in celestial coordinates. The adoption of two perpendicular diagonal scan orientations thus mitigates these geometrical complications, ensures robust decorrelation, and enhances the overall quality of the polarization measurements. Therefore, we decided to scan the source with two patterns rotated by 90° with respect to each other.
The preparatory work prior to the observations was not limited to the scanning strategy, but also included optimization of the scan size, the length of the subscans, the scanning speed, and the inter-subscan spacing. These parameters were tuned to maximize the signal-to-noise ratio (SNR) in the regions of interest, while maintaining sufficient margin outside the cloud for reliable data processing. The observations exploited the polarization capabilities of the NIKA2 instrument to map the magnetic field structure within W43. By running simulations based on MAMBO data, the region's minimum intensity was estimated to be $I_{\rm least} = 175$ mJy beam^{-1}, and a signal-to-noise ratio of 7 was targeted. Assuming a polarization fraction of $f_{\rm pol} = 0.03$, the required root mean square (RMS) noise was $\sigma_{\rm pol} = 1.2$ mJy beam^{-1}. This SNR takes into account uncertainties in instrumental polarization correction as well as noise debiasing in the estimation of the degree of polarization.
Instrumental polarization, which can reach levels of up to 3% for compact sources, must be corrected by observing a bright, unpolarized calibrator such as Uranus. Unfortunately, during the Winter campaign when W43 was observed, no strong unpolarized source was available within the same visibility window. Uranus was already too low on the horizon, and Mars was too extended to be considered point-like. We therefore relied on quasars, such as NGC7027, whose polarization degree is in principle well known. However, as discussed in Chap. 2, Subsec. 2.6.3,

quasars are not always ideal calibrators due to their intrinsic variability. As a result, a more elaborate post-observation analysis is required to correct for IP when using quasars. At the present stage, the data presented here have not yet been corrected for instrumental polarization, as this work is still in progress. Nevertheless, the effect of IP is partially mitigated by the natural rotation of the sky during the observations: while the leakage pattern remains approximately constant in the Nasmyth reference frame, it rotates in equatorial coordinates (RA, Dec.), thus providing a partial compensation even without an explicit correction.
Although our simulations provided us with all the required scan parameters, the exact final requested observation time was derived with the official IRAM time estimator (version 2024.FEB.26). Assuming a mapping speed of 13.9 arcmin^{-2} hour^{-1} mJy^{-2}, a PWV of 4.0 mm, an elevation of 46°, a filter factor of 2.0, and an overhead factor of 2.0, the time required to map a 360.0 arcmin^2 region with an RMS of 1.2 mJy beam^{-1} was estimated to be 19.4 hours. Of this, 6 hours of observations were completed during Winter Semester 2024 under the project 132-24, leaving a complementary required time of 13 hours. This time has been approved for the follow-up project 039-25 for Summer Semester 2025. This work relies on data from project 132-24 only.

5.4.3 Data analysis methodology

The data reduction for this project was articulated in multiple phases: first, we derived the Stokes maps I, Q and U from raw data; then from Stokes Q and U maps we derived the map of the magnetic field morphology; then we analyzed separately data from different surveys, such as the polarization data from NIKA2 in order to derive the polarization angles' dispersion map, the velocity dispersion map from ^{13}CO transition lines and the density map from *Herschel* data. Finally, we combine these maps to obtain one final map of the magnetic field on the plane of the sky (B_{POS}) using the Davis-Chandrasekhar-Fermi method, already introduced in Subsec. 5.4.1.

From raw data to the magnetic field morphology map The data obtained during the first 6.5 hours of the allocated time were of very high quality, thanks to a very good τ value during most of the observing time, rarely above 0.1. Maps of the I, Q and U Stokes parameters could be produced through the NIKA2 official pipeline, obtaining the results shown in Fig. 5.9.

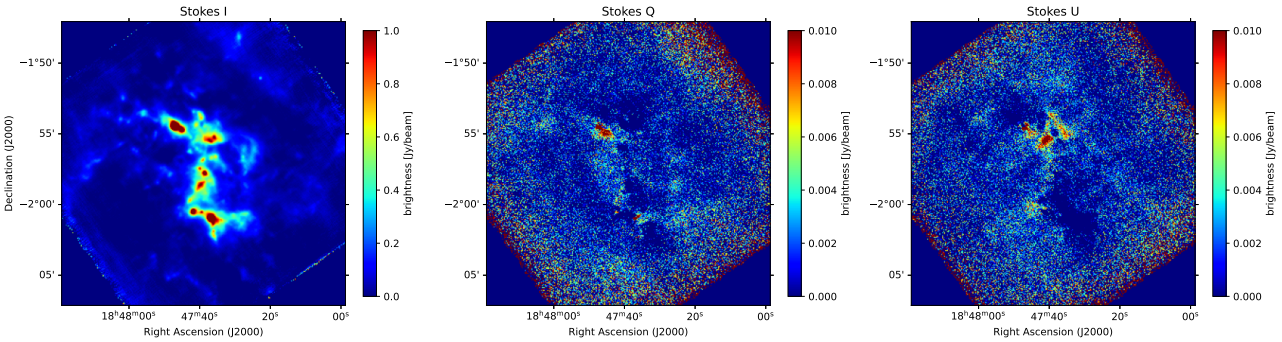

Figure 5.9: Stokes I, Q and U maps at 260 GHz of W43 from NIKA2 data.

We combined data from Q and U Stokes maps and obtained the polarized intensity map (left of Fig. 5.10), expressed as a function of the Stokes parameters Q and U:

$$I_{pol} = \sqrt{Q^2 + U^2}\,. \tag{5.6}$$

In Fig. 5.11, we show a map of the magnetic field morphology of W43, where the color scale shows the total intensity (Stokes I), while the white segments are oriented as the polarization

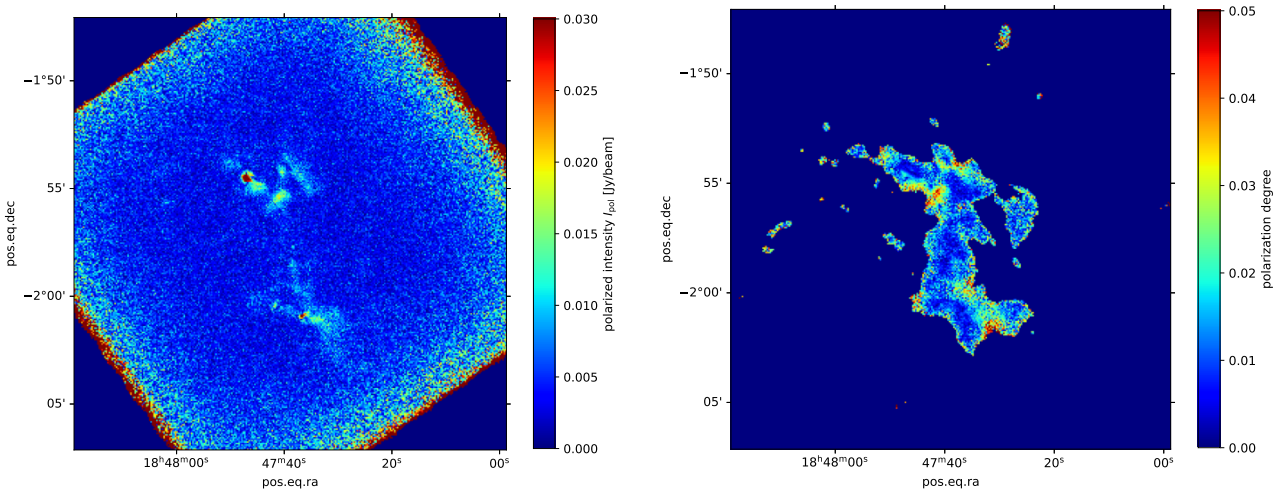

Figure 5.10: *Left:* map of the polarized intensity I_{pol} from NIKA2 polarimetry data. *Right:* map of the polarization degree in a masked region of W43. The mask is not applied to I_{pol} to show comparison with the background.

angle, but tilted by $\pi/2$ (Eq. 5.4) and are proportional in size to the polarization degree. The polarization degree is defined as I_{pol}/I, and its map is shown in the right panel of Fig. 5.10. From this plot, we observe a polarization degree spanning from 0 to 8%.

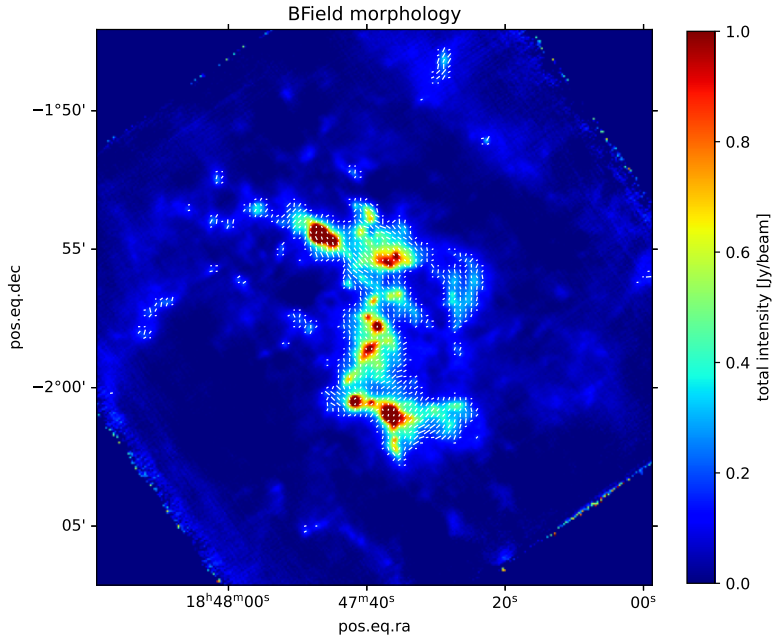

Figure 5.11: Map of W43: the color scale shows the total intensity (Stokes I), while the white segments are oriented following the magnetic field morphology, being proportional in size to the polarization degree.

The magnetic field morphology is shown only within a masked region corresponding to the main W43 complex. This mask selects the pixels where the standard deviation associated with Stokes I, denoted as σ_I, is less than 3% of the Stokes I signal, in order to enhance visualization quality. The same mask is applied to the polarization degree map. In the magnetic field morphology map, which is displayed over the total intensity background, the polarization segments appear shorter (indicating a lower polarization degree) in the densest regions of W43, and longer in more diffuse areas. In terms of orientation, some regions appear to exhibit a higher degree of

magnetic field turbulence compared to others.

Polarization angle dispersion map Considering the original Q and U NIKA2 maps, we computed the mean values of Q and U within a square kernel of size $N \times N$ pixels, with $N = 10$:

$$\langle Q \rangle = \frac{1}{N^2} \sum_{i,j} Q_{i,j}, \quad \langle U \rangle = \frac{1}{N^2} \sum_{i,j} U_{i,j}\,, \tag{5.7}$$

where the sums extend over all pixels within the kernel. The kernel size is not a computational arbitrary variable, but it is key to a robust estimation of the polarization angle dispersion: since one pixel corresponds to 4", 10 pixels correspond to 40", meaning almost 4 times the NIKA2 beam at 1 mm. This beam coverage ensures a consistent and unbiased estimation of the polarization angle dispersion.
Using $\langle Q \rangle$ and $\langle U \rangle$, the local deviation in the polarization angle was then computed using the same method presented in Planck collaboration 2015 [241]:

$$\Delta\theta_{i,j} = 0.5 \arctan(Q_{i,j}\langle U \rangle - U_{i,j}\langle Q \rangle, Q_{i,j}\langle Q \rangle + U_{i,j}\langle U \rangle)\,, \tag{5.8}$$

defined in [-π,π].
Finally, the dispersion σ_θ at each pixel was estimated as the root mean square of $\Delta\theta_{i,j}$ values within the kernel:

$$\sigma_\theta = \sqrt{\frac{1}{N^2} \sum_{i,j} \Delta\theta_{i,j}^2}\,. \tag{5.9}$$

The resulting dispersion map (Fig. 5.12) provides a measure of the variability of the polarization angles within the selected kernel size.

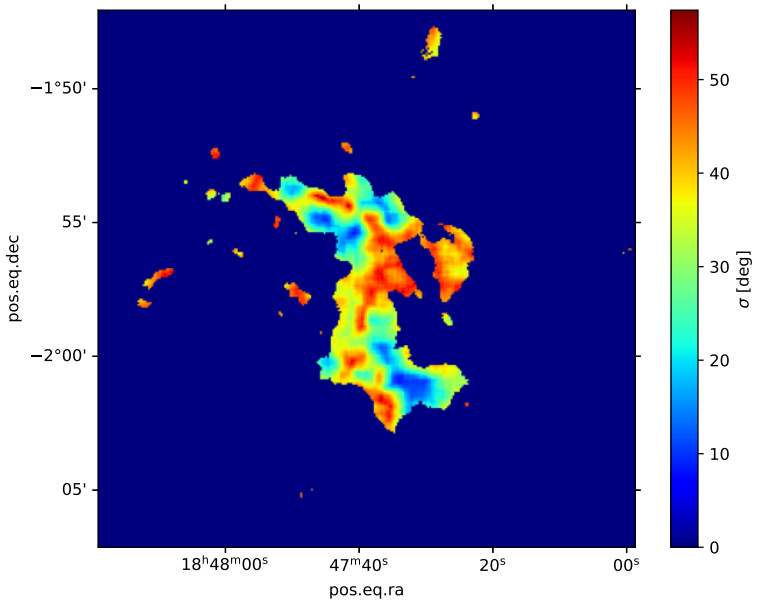

Figure 5.12: Map of polarization angle dispersion across W43 obtained from NIKA2 polarimetry data.

Velocity dispersion map To analyze the velocity structure of the ^{13}CO (2-1) emission line data, we utilized the spectral cube obtained from *HERA* data presented in Carlhoff et al. 2013

[57][1], which consists of intensity measurements as a function of velocity, right ascension (RA), and declination (DEC). The integrated intensity map was obtained by summing the emission across all velocity channels:

$$I_{\rm int}(x,y) = \sum_v T_{\rm mb}(x,y,v)\,, \tag{5.10}$$

where $T_{\rm mb}(x,y,v)$ represents the main beam brightness temperature at spatial coordinates (x,y) and velocity channel v. This map provides a measure of the total emission over the observed velocity range, spanning from 30 to 130 km/s.
For individual spatial pixels, we extracted velocity profiles, plotting the main beam brightness temperature, $T_{\rm mb}$, as a function of velocity, v. These profiles were further analyzed to identify regions where the emission exceeds a predefined threshold $T_{\rm threshold}$. Masking was applied to isolate regions of significant emission, indicated by M:

$$M(x,y,v) = \begin{cases} 1 & \text{if } T_{\rm mb}(x,y,v) > T_{\rm threshold}, \\ 0 & \text{otherwise.} \end{cases} \tag{5.11}$$

The value of $T_{\rm threshold}$ was chosen as 4 times the noise value in each profile, so $4\sigma_T = 6$ K.

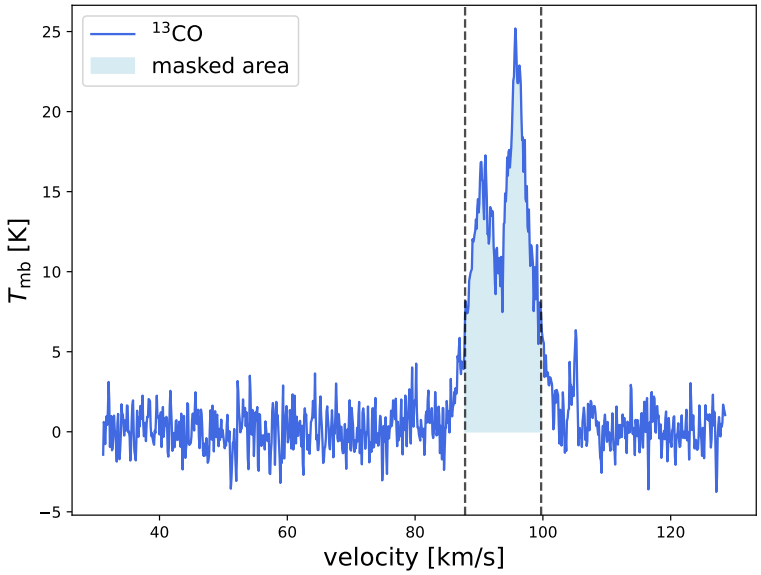

Figure 5.13: Example of one velocity channel line, with the masked area highlighted in light blue.

Using the masked data (as shown in Fig. 5.13), we calculated the velocity dispersion σ_v for each spatial pixel. The velocity centroid was computed as:

$$\langle v\rangle(x,y) = \frac{\sum_v v\, T_{\rm mb}(x,y,v)\, M(x,y,v)}{\sum_v T_{\rm mb}(x,y,v)\, M(x,y,v)}\,. \tag{5.12}$$

The velocity dispersion was then derived as:

$$\sigma_v(x,y) = \sqrt{\frac{\sum_v ((v-\langle v\rangle)(x,y))^2\, T_{\rm mb}(x,y,v)\, M(x,y,v)}{\sum_v T_{\rm mb}(x,y,v)\, M(x,y,v)}}\,, \tag{5.13}$$

and the relative map is shown in Fig. 5.14. In the map, a pattern is visible: this is due to the mosaic structure of the original map. While visually disturbing, this does not impact the

[1]Data available at https://cdsarc.cds.unistra.fr/ftp/J/A+A/560/A24/fits/.

scientific meaning of it. Moreover, after resolution degrading of the map, this small-scale effect will not be significant anymore.

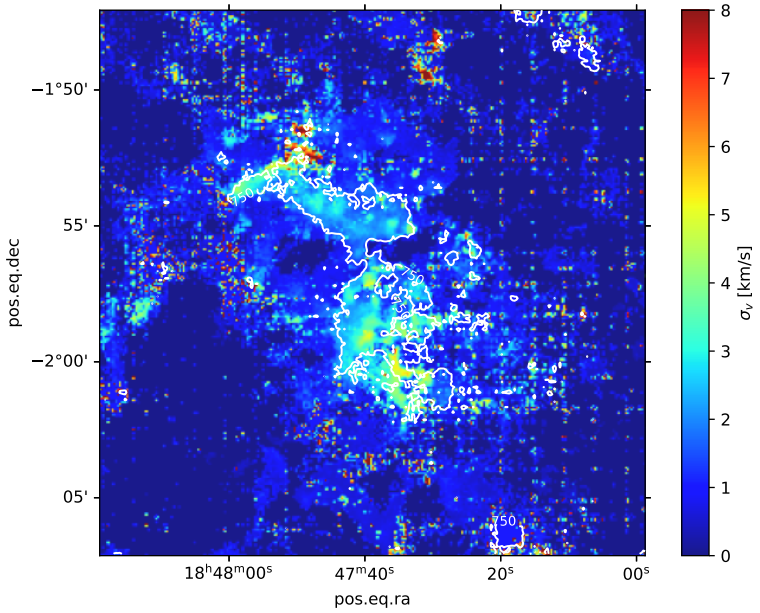

Figure 5.14: Velocity dispersion map of W43 from *HERA* data. In white, we show the contour of the ^{13}CO total intensity map at 750 K.

Mass density map The analysis to reconstruct the mass density map begins from the column density map, taken from Ngueyn-Luong et al. 2013 [218].
From the column density map, however, we need to derive a mass density map, representing the mass of gas per unit volume in [g/cm^{-3}]. This step is needed to apply the DCF method to derive the magnetic field morphology. To do so, a model of the spatial distribution of gas was created. We opted for a bi-modal model, considering the massive clumps and the diffuse region separately. For the dense clumps, we considered a spherical uniform distribution, while for the diffuse a simple constant layer along the line of sight. We assume a radius of ∼1 pc for each clump and a depth of ∼16 pc for the diffuse component. The choice of a 1 pc radius for the clumps is common in the literature and is further supported by direct inspection of the NIKA2 maps: converting the angular size of a NIKA2 pixel to physical units, we find that a typical clump spans approximately six pixels, corresponding to ∼1 pc in radius. For the depth of the diffuse gas, we adopt the common assumption that the elongation in the plane of the sky is comparable to the extension along the line of sight. Considering the diagonal extent of the observed region, this yields a depth of ∼16 pc. Then, we applied a Gaussian filter to smooth the transition at the edge of the two regions. Assuming a constant metallicity, similar to the Sun neighborhood, we can multiply the column density map by the mean molecular weight of H_2 with metals ($\mu = 2.8$) and by the mass of an hydrogen atom in grams ($\mu_H = 1.67{\times}10^{-24}$ g), to finally obtain the mass density map (Fig. 5.15).

B_{POS} map So far, we showed maps in their native resolution to preserve detailed structure, but in order to combine them, we need to ensure consistent resolution among all maps. The NIKA2 maps of Q and U have the typical resolution of 11", and a pixel size of 4"; the *Herschel* map of column density has a resolution of 18" and a pixel size of 4.5"; the HERA map used to then derive the velocity dispersion map has a resolution of 12" and a pixel size of 5.6". Therefore, we needed to degrade NIKA2 and HERA maps to the resolution of the *Herschel*

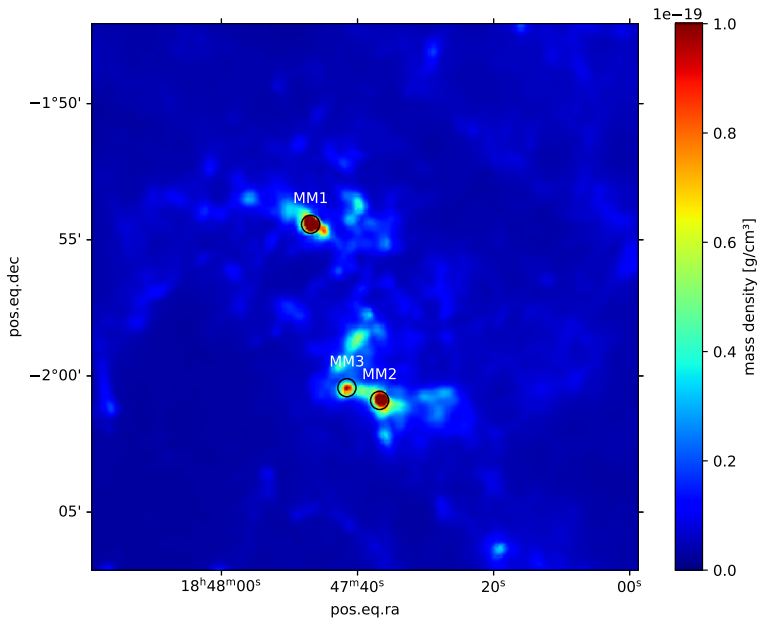

Figure 5.15: Mass density map of W43 built from *Herschel* data. The dashed circles with associated labels identify the three main clumps of W43: MM1, MM2 and MM3.

map, by applying a typical beam convolution.
At this point, the DCF method can be applied following Eq. 5.5, where we chose the factor $\mathcal{F}$ = 0.5. The factor $\mathcal{F}$ accounts for line-of-sight integration effects, projection smoothing, and non-linear perturbations of the magnetic field. This value is commonly used in observational studies and supported by numerical magneto-hydrodynamic (MHD) simulations, which show that the original DCF formulation tends to overestimate the magnetic field strength due to idealized assumptions such as isotropic turbulence, small-angle dispersion, and uniform field geometry. Simulations (Ostriker et al. 2001 [224], Heitsch et al. 2001 [135]) suggest that a value of $\mathcal{F} \sim 0.5$ provides a more accurate estimate of the plane-of-sky magnetic field strength in molecular clouds.
The maps, now all being in the same resolution and NIKA2 reprojected frame, can be directly combined to obtain the final map of the magnetic field intensity on the plane of the sky. The derived map is shown in Fig. 5.16.

Estimation of uncertainties In order to obtain a significant result in terms of the magnetic field intensity, we need to associate an uncertainty map to Fig. 5.16. To do so, we compute individual uncertainty maps for the components used: the velocity dispersion map, the polarization angle dispersion map and the mass density map.
The uncertainty on the velocity dispersion map was estimated using a method based on the noise properties of the spectral cube. First, the root-mean-square (RMS) noise level σ_T was estimated from line-free channels of the ^{13}CO data. For each pixel, the peak intensity $T_{\rm peak}$ was extracted from the spectrum, and the effective number of contributing spectral channels $N_{\rm eff}$ was computed by summing the number of valid channels within the emission mask. We compute the uncertainty by considering only the channels with significant signal in each pixel, as identified by the line mask, to avoid biasing the error estimate with noise-dominated regions. The relative uncertainty on the velocity dispersion, $\delta\sigma_v/\sigma_v$, was then computed analytically as:

$$\frac{\delta\sigma_v}{\sigma_v} = \frac{\sigma_T}{T_{\rm peak}\sqrt{2N_{\rm eff}}}\,, \tag{5.14}$$

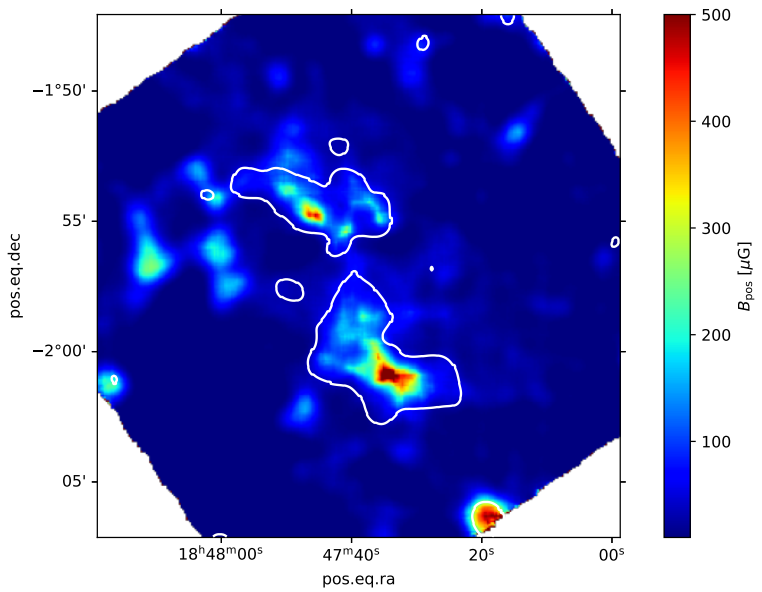

Figure 5.16: Magnetic field intensity derived through the DCF method. The white contour marks a mass density of 5×10^{-20} g cm^{-3}.

assuming Gaussian noise and uncorrelated channel measurements. This relative uncertainty was converted into an absolute uncertainty $\delta\sigma_v$ by multiplying with the velocity dispersion σ_v at each pixel.
The uncertainty on the dispersion of the polarization angle, $\Delta\theta$, was estimated using a Monte Carlo approach. For each "super-pixel" of 10×10 pixels, the same used for the computation of the dispersion itself, we extracted the Stokes parameters Q and U together with their associated uncertainties σ_Q and σ_U, obtained from the variance maps. We then generated $N_{\rm MC} = 1000$ Gaussian realizations of noise, with zero mean and unit variance, and scaled them by σ_Q and σ_U respectively. These noise maps were added to the original Q and U values, producing 1000 perturbed realizations of the super-pixel. For each realization, we computed $\Delta\theta$ using Eq. 5.8. The resulting distribution of 1000 values of $\Delta\theta$ was then used to estimate the uncertainty on the dispersion: the standard deviation of this distribution is adopted as the error on $\Delta\theta$ for the corresponding super-pixel. This procedure ensures that the uncertainties on Q and U are consistently propagated into the final error budget of the polarization angle dispersion.
The uncertainty on the mass density was assumed to be the 40% of the map itself, following the estimates given in Schneider et al. 2022 [277].
Finally, the uncertainty on the plane-of-sky magnetic field intensity, $B_{\rm pos}$, was estimated through standard error propagation from the input quantities in the DCF method. Assuming the input quantities are uncorrelated, the total relative uncertainty on the magnetic field strength was estimated by adding the relative errors in quadrature:

$$\left(\frac{\delta B_{\rm pos}}{B_{\rm pos}}\right)^2 = \left(\frac{\delta\rho}{\rho}\right)^2 + \left(\frac{\delta\sigma_v}{\sigma_v}\right)^2 + \left(\frac{\delta\sigma_\theta}{\sigma_\theta}\right)^2 . \tag{5.15}$$

The absolute uncertainty on $B_{\rm pos}$ was computed as:

$$\delta B_{\rm pos} = B_{\rm pos} \times \sqrt{\left(\frac{\delta B_{\rm pos}}{B_{\rm pos}}\right)^2} . \tag{5.16}$$

This approach provides an uncertainty map for the magnetic field strength that accounts for measurement errors in the input maps and uncertainties inherent in the physical assumptions

(Fig. 5.17).

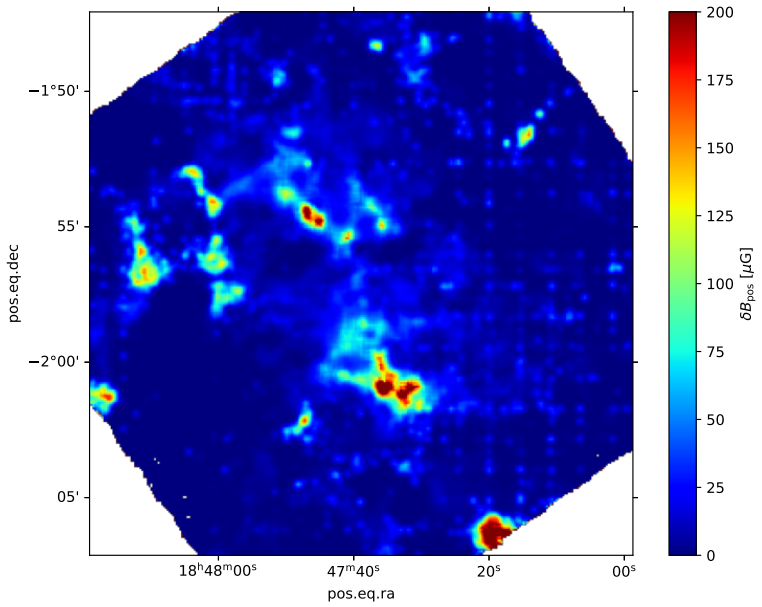

Figure 5.17: Uncertainty associated with the magnetic field strength on the plane of the sky.

5.4.4 Results and interpretation

Thanks to the methodology described in the previous section, we obtained a complete map of the magnetic field projected onto the plane of the sky, together with its associated uncertainty map. We now aim to provide an estimate of the magnetic field strength in the main clumps under analysis (MM1, MM2 and MM3), as well as in the diffuse region. It is important to note that the magnetic field values are not independent within areas corresponding to the kernel over which the polarization angle dispersion was computed. Consequently, within an effective beam of 40″, we obtain a single value for the magnetic field strength and its associated uncertainty. This situation differs from the maps shown in the previous subsections, which were smoothed to improve visualization and to facilitate the identification of the clumps. In fact, the clumps have a typical size of 1 pc, which approximately corresponds to the effective 40″ beam. Therefore, in the following we will report values of the magnetic field strength for the identified clumps, together with their associated uncertainties.

Magnetic field intensity in main clumps The values of the magnetic field intensity on the plane-of-sky for the three main clumps, with their associated uncertainty are:

- MM1: $B_{\rm pos} = (631 \pm 257)\ \mu$G [±41%]
- MM2: $B_{\rm pos} = (753 \pm 334)\ \mu$G [±44%]
- MM3: $B_{\rm pos} = (277 \pm 113)\ \mu$G [±41%]

These values suggest that the magnetic field in the densest parts of the W43 main ridge is relatively strong, ranging from ∼0.3 to 0.8 mG, with comparable fractional uncertainties of around 40%. Such estimates are coherent with the work of Cortes et al. 2019 [78] on ALMA data of MM2 and MM3 as well as with the work of Cortes et al. 2016 [77] on MM1. In the diffuse region, we observe values between 10 and 100 μG, depending on the area taken into account.

This result provides a wealth of information essential for understanding the dynamics of the region. One of the primary objectives of this study was to investigate the physical conditions of the main clumps in W43: MM1, MM2, and MM3. These three dense cores are the key sites where star formation is expected to occur.

Virial analysis To determine whether global collapse is occurring in these regions, a virial analysis was performed by evaluating their virial parameter. A virial analysis examines the balance between kinetic, magnetic, and gravitational energies in a system to assess its stability. In the context of the star-forming region W43, these energy components are compared to determine whether the region is in equilibrium, undergoing collapse, or dispersing. The magnetic energy density is given by:

$$E_B = \frac{B_{\rm pos}^2}{8\pi}\,, \tag{5.17}$$

where $B_{\rm pos}$ is the total magnetic field strength on the plane-of-sky, previously derived.
The turbulent (or kinetic) energy density can be expressed as:

$$E_{\rm turb} = \frac{3}{2}\rho\sigma_v^2\,, \tag{5.18}$$

where ρ is the gas mass density and σ_v is the velocity dispersion obtained from molecular line observations.
The gravitational energy is computed as:

$$E_G = -\frac{3}{5}\frac{GM^2}{R}\,, \tag{5.19}$$

where M is the mass of the cloud and R its characteristic radius. To assess the stability of the clumps in W43, we compare the different energy components, using the following criterion:

$$E_B + E_{\rm turb} \geq |E_G| \quad \Rightarrow \quad \text{stable region,} \tag{5.20}$$
$$E_B + E_{\rm turb} < |E_G| \quad \Rightarrow \quad \text{gravitational collapse.} \tag{5.21}$$

Another way of seeing this involves deriving the virial parameter, α_{vir}, as:

$$\alpha_{vir} = \frac{2(E_{turb} + E_B)}{|E_{grav}|}\,. \tag{5.22}$$

The virial parameter is a dimensionless quantity that evaluates the balance between a gas cloud's gravitational potential energy and internal support mechanisms (e.g., turbulence, thermal pressure). It provides insight into the likelihood of gravitational collapse, depending on its value as follows:

- $\alpha_{\rm vir} \approx 1$: the cloud is in virial equilibrium, with kinetic and magnetic energies balancing gravity;
- $\alpha_{\rm vir} < 1$: the cloud is gravitationally bound and likely to collapse, promoting star formation;
- $\alpha_{\rm vir} > 1$: internal support dominates, preventing collapse.

This parameter helps identify regions prone to collapse and assess the impact of turbulence, thermal pressure, and magnetic fields on cloud stability and star formation. By computing

these energy components for all three main clumps of W43 and by propagating the uncertainties associated, we obtain:

- $\alpha_{vir,MM1} = 0.34 \pm 0.09 \quad [\pm 26.4\%]$
- $\alpha_{vir,MM2} = 0.75 \pm 0.14 \quad [\pm 20.5\%]$
- $\alpha_{vir,MM3} = 0.41 \pm 0.09 \quad [\pm 22.2\%]$

Hence, we can conclude that the clumps are prone to collapse, but there might be a braking action from the magnetic fields. These values are coherent with the knowledge that these regions are forming stars at a relatively high rate. The presence of a strong magnetic field is braking yet not preventing dense clouds to collapse.

5.5 Conclusions and perspectives

We conducted polarimetric observations of the entire W43 star-forming region with NIKA2 at 260 GHz. From the resulting Stokes I, Q, and U maps, we derived both the magnetic field morphology and the map of the polarization angle dispersion. The latter was combined with maps of the velocity dispersion and mass density to apply the Davis-Chandrasekhar-Fermi (DCF) method, ultimately producing a map of the magnetic field strength in the plane of the sky. This represents the first full-scale map of the magnetic field strength across the entire W43 region. From this map, we estimated the mean magnetic field strength within the three main clumps: MM1, MM2, and MM3. With such information, we performed a virial analysis to assess the gravitational stability of the gas. We find that, even accounting for the uncertainties associated with the virial parameters, all three clumps appear to be undergoing global gravitational collapse. This supports the presence of ongoing star formation, despite the opposing influence of relatively strong magnetic fields.
Following the approval of the remaining observing time at IRAM, new data of W43 will be available after the Summer Semester 2025, assuming favorable weather conditions. These new observations will benefit from the upgraded capabilities of NIKA2+, including the newly developed arrays for the 260 GHz focal plane, which feature improved sensitivity (NEFD), at least in total intensity. Building on this work, we aim to pursue three key studies: (i) compare the magnetic field morphology across multiple angular scales, from ALMA (0.5") on dense cores to Planck (5') on diffuse regions, to assess morphological coherence; (ii) analyze the relative orientation between the magnetic field and the column density gradient, to investigate abrupt transitions and possible fragmentation patterns within clumps; and (iii) compare the level of fragmentation from Cortes et al. 2019 [78] to this measure of B_{POS}.

Chapter 6

A novel method for polarization calibration: the COSMOCal project

Contents

6.1 The COSMOCal project framework **146**
6.1.1 Scientific purpose 146
6.1.2 The spatial calibrator 147
6.1.3 Project phases 149
6.2 The Phase 1 adapted 260 GHz prototype **149**
6.2.1 Internal polarization angle calibrator 149
6.2.2 Photogrammetry 150
6.3 Phase 1.1: in-lab proof of concept **151**
6.3.1 Adapted experimental setup 151
6.3.2 Coupling COSMOCal - cryostat 151
6.3.3 Data model and methods 152
6.3.4 Data acquisition strategy 153
6.3.5 Diffraction pattern results 154
6.3.6 KID results 154
6.3.7 Remarks on the in-lab proof-of-concept 158
6.4 Phase 1.2: IRAM 30m test campaign **158**
6.4.1 Optical model 159
6.4.2 Signal model 164
6.4.3 Preliminary detection 164
6.4.4 Pipeline for data reduction: key concepts 166
6.4.5 Radio alignment 168
6.4.6 Photogrammetry and diffraction pattern analyses 168
6.4.7 Polarization measurements 170
6.4.8 Final considerations on the campaign 174
6.5 Perspectives on Phases 2 and 3 . . . . . **175**
6.6 Conclusions **175**

Abstract The COSMOCal project[1] aims to establish a polarized source in space for precise calibration of microwave frequency observations, addressing the critical need for accurate polarization angle measurements with a precision better than 0.1° (see Subsec. 2.6.3). Such calibration is essential to identify signatures of primordial gravitational waves and cosmic birefringence within the CMB polarization. By providing a unified calibration scale, COSMOCal seeks to harmonize data from various observatories, surely ground-based and indirectly space-based, enhancing their scientific capabilities and enabling robust data combination. To demonstrate the feasibility of the project, a prototype instrument operating at 260 GHz was developed and tested at LPSC facility and with the NIKA2 camera at the IRAM 30m telescope. This chapter presents the 260 GHz prototype design and laboratory characterization conducted in February 2024 in LPSC, with the main results on the estimate of the polarization angle. The results of the in-lab proof of concept are published in Ritacco et al. 2024 [268]. Moreover, in this chapter we present the first test campaign conducted at the IRAM 30m telescope in September 2024. The measurement strategy, analysis approach and preliminary results are presented.
My contribution to the COSMOCal project has been substantial both during the in-lab proof of concept phase and the IRAM 30m campaign. I was responsible of the raw data reduction and calibration, the analysis of KID data and the production of results regarding the polarization angle estimate. For the IRAM 30m campaign, in particular, I significantly contributed to the planning and development of the on-site operations, interpretation of preliminary and advanced results. As such, I am one of the two main authors (together with L. Bizzarri) of the IRAM internal report giving a comprehensive description of the test run and its results.
This work will contribute to pave the way for the next steps of the COSMOCal project, involving the realization of a new multi-frequency instrument to be launched on board of a satellite for space-based calibrations of large ground based instruments.

6.1 The COSMOCal project framework

6.1.1 Scientific purpose

A central challenge for future CMB experiments is the unbiased calibration of polarization angles, independent of both the standard cosmological model and Galactic foregrounds. Relying on the microwave sky itself as a reference introduces circularity, motivating the development of an artificial, external calibrator.
Several approaches have been explored, such as ground-based or drone-mounted polarized sources (Nati et al. 2017 [214], Coppi et al. 2022 [72], Cornelison et al. 2022 [76]), or a proposed CubeSat at the L2 Lagrange point dedicated to a single CMB mission (Casas et al. 2021 [59]). While effective for small-aperture telescopes or specific space experiments, these strategies are not suitable for large ground-based observatories. For such instruments, the far field is higher than the Earth atmosphere, which requires deployment in space.
The COSMOCal project addresses this need by placing a polarized calibration source in geostationary orbit. This configuration ensures long-term visibility from both small and large ground-based telescopes, providing a stable far-field reference. COSMOCal will deliver a multi-frequency polarized signal in the 90–300 GHz range, with a polarization angle accuracy better than 0.1°. Such precision is essential for reaching the scientific goals of next-generation CMB polarization measurements.
By establishing a space-based calibrator, COSMOCal will unify calibration scales across observatories of different sizes and platforms, both ground-based and eventually space-based too. For the moment, the targeted ground-based observatories are located in Europe or in Chile:

[1] Project's website: https://sites.google.com/view/cosmocal-website/home-page?authuser=0.

the IRAM 30m telescope, the Sardinia Radio Telescope (SRT) and Simons Observatory's Large Aperture Telescope (LAT). In practice, once these large telescopes are accurately calibrated with COSMOCal, they will transfer this precision to bright astrophysical sources, such as the Crab Nebula. These sources will then serve as universal polarization standards, accessible to all CMB and Galactic astrophysics experiments. In this way, COSMOCal maximizes the scientific return of current and future observatories by enabling robust, cross-experiment data integration.

6.1.2 The spatial calibrator

The chosen location for the COSMOCal calibrator is a geostationary orbit (GEO, Fig. 6.1), as this configuration best meets the requirements of large-aperture ground-based CMB telescopes. A GEO orbit is a circular orbit in the equatorial plane at an altitude of 35786 km, where the orbital period matches the Earth's rotation. As a result, the satellite remains fixed at a constant position in the sky for a ground-based observer. This stability ensures continuous visibility and guarantees that the calibrator lies in the far field of even the largest millimeter telescopes.
Other orbital options present significant drawbacks. A low Earth orbit (LEO) satellite, although easier to launch, crosses the sky rapidly and cannot provide stable calibration for long integration times. An L2 orbit, on the other hand, is well suited for space missions such as LiteBIRD, but places the calibrator far beyond the visibility range of ground-based observatories. By contrast, a geostationary orbit combines accessibility from Earth with long-term stability, making it the optimal choice for COSMOCal to serve as a universal polarization calibrator.

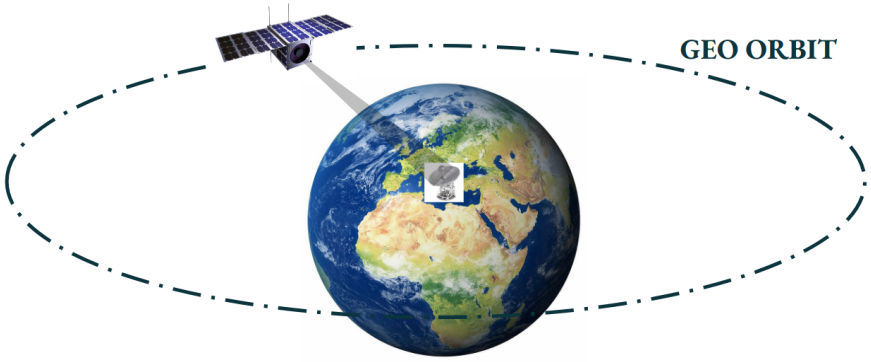

Figure 6.1: Sketch of the geostationary orbit where COSMOCal will be launched during the space phase (Phase 3).

The space calibrator is currently being designed by the collaboration, and it consists of multiple complex systems, combined in the box. In the following paragraphs, all these subsystems, shown in Fig. 6.2, will be detailed. We emphasize that this design is an ongoing work in progress.

mm-source and RF chain The millimeter source consists of a chain of radio-frequency (RF) components, while the optical system consists of various optical elements necessary to obtain an independent measurement of the polarization angle during observations. The millimeter source, assembled at the LERMA institute, is designed to operate at three frequency channels: 90, 150, and 260 GHz. The millimeter source chain employs a 24 times frequency multiplication scheme to emit a Gaussian beam monochromatic signal at each central frequency. The key technologies used in the schematic have been space-qualified to TRL8 (Treuttel et al. 2023 [292]). The chain comprises a dielectric resonator oscillator (DRO) injecting a signal at 11.041 GHz into a W band sextupler (AFM 60-90), a W band power amplifier (E-MPA 66-80), two frequency doublers at 150 and 300 GHz, and two adjustable attenuators securing the interface ports matching and

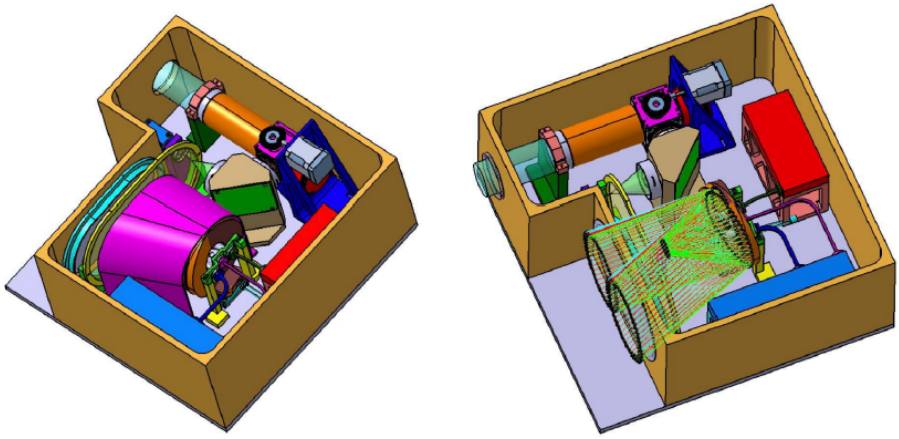

Figure 6.2: Image of the fully assembled box of the COSMOCal spatial instrument, by P. Morfin.

isolation. The output signal is coupled, to free space, with a 20 dB pyramidal horn and monitored with a PM5 power meter through a 10 dB directional coupler located before the feed-horn. The characterization of the coupler at different frequencies has been performed at the IAS (Orsay) institute using a vector network analyzer (VNA). The frequency stability is given by the DRO 1000 generating an output signal at 11.0416 GHz with a power of 21 dBm, easily attenuated, and very stable over a temperature range of 0°C to 50°C. The DRO spectrum is peaked around the central frequency, with a spread of $\sim$ 100 kHz, a phase noise of -97 dBc / Hz at 10 kHz, and a frequency dependence on temperature of 4.4 kHz/°C. This configuration meets the frequency stability requirements.

Optics Given the large distance between the GEO orbit and the ground, controlling the beam divergence is essential in order to limit the illumination footprint to about 300 km on the Earth's surface. To achieve this, the COSMOCal box incorporates a compact telescope with a primary aperture of approximately 12 cm, determined by combining the optical requirements of both the IRAM 30-m telescope and the Simons Observatory LAT. The optical chain is designed to provide an overall transmission of about 50%, corresponding to an effective optical efficiency of 60% when coupled to instruments such as NIKA2 on the IRAM 30 m. The system must allow for an adjustable beam divergence, ranging from about 10° down to 30 arcmin, in order to match the apertures and distances of different ground-based telescopes. The optical design relies on a two-mirror configuration to collimate and direct the radiation, while three microwave sources operate simultaneously along the optical axis to ensure continuous frequency coverage. Polarization purity is maintained to better than 0.05°, which guarantees accurate calibration of ground-based polarimeters.

Pointing system In addition to controlling beam divergence, it is necessary to provide the ability to steer the signal toward different observatories on the ground. For this purpose, the COSMOCal optics include a movable tilting mirror that redirects the collimated beam to selected positions, allowing the source to illuminate multiple telescopes without physically reorienting the payload. This pointing system, combined with the adjustable beam optics, ensures that the GEO-based source can deliver well-characterized, stable, and highly polarized signals to different ground instruments in succession.

6.1.3 Project phases

The COSMOCal project is structured in three main phases. Phase 1 focused on the development of a prototype at 260 GHz, tailored for the IRAM 30m telescope. This stage included both laboratory characterization of the box itself, as well as validation in two cryostat-coupled configurations: in-lab in Grenoble and at the IRAM 30m telescope. The work presented in this chapter is dedicated to this first phase, to which I contributed fully. Phase 2 corresponds to the qualification model: the construction of the final COSMOCal calibrator in its space-ready configuration. Although tested on the ground, this version will already reproduce the conditions of space operation. In this context, an on-going R&D effort at LPSC is dedicated to the design and development of linear polarizers to be integrated into COSMOCal. Phase 3 will then realize the flight model, i.e. the launch of the instrument as a payload in geostationary orbit.
At present, only Phase 1 has been completed, but it has laid the foundations for the next stages. Discussions held earlier this year with CNES have addressed key aspects of a potential satellite mission, and the project could realistically enter CNES Phase A as early as next year. In this perspective, Phase 2 and Phase 3 would ensure the transition from the qualification model to the actual flight model, culminating in the launch of the calibrator in space, foreseen for 2030.

6.2 The Phase 1 adapted 260 GHz prototype

To establish a proof-of-concept and validate the observational strategy that underlies the COSMOCal project, a prototype instrument has been developed at a single frequency to operate within the atmospheric window centered at 260 GHz. With respect to what was described in Subsec. 6.1.2, only one frequency channel was realized. This instrument was designed for a test campaign at the IRAM 30m telescope with the NIKA2 camera. The adapted design of the COSMOCal prototype is shown in Fig. 6.3.

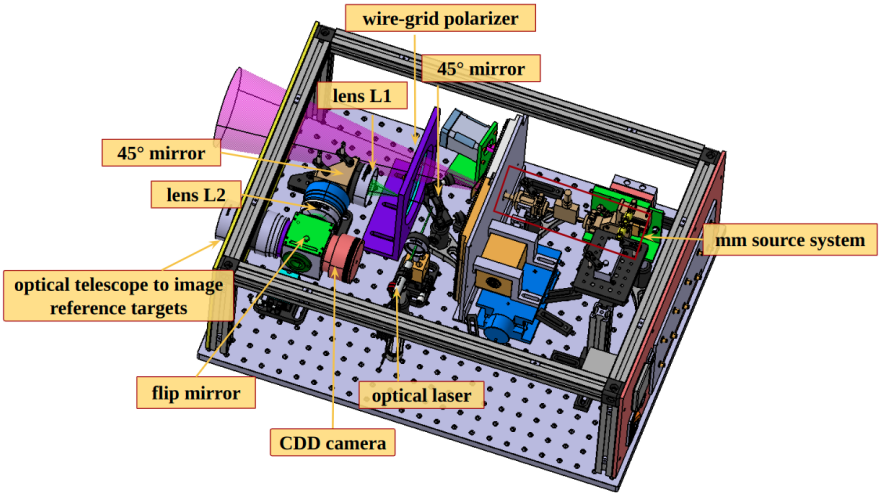

Figure 6.3: Mechanical drawing of the COSMOCal box.

The results on the characterization of the prototype prior to testing are elaborated in greater detail in the first part of Ritacco et al. 2024 [268].

6.2.1 Internal polarization angle calibrator

The COSMOCal optical system is designed to determine the polarization angle of the COSMOCal system with an accuracy of $\Delta\psi < 0.1°$. A polarizing grid (P1) ensures pure polarization of

the millimeter source signal, while an auxiliary optical setup determines its orientation. This setup includes a 520 nm laser, lenses (L1 and L2), a refractor telescope, a CCD camera, and a flip mirror. The laser passes through P1, producing a diffraction pattern captured by the CCD camera. Ground reference images provide updates on relative angles between the camera and the telescope's ENU coordinate system. East–North–Up (ENU) coordinates define a local reference frame centered at an observer's location, with axes pointing east, north, and upward toward the zenith.
The polarization uncertainty ($\sigma_{\rm cal}$) combines contributions from the diffraction pattern orientation and roll angle reconstruction:

$$\sigma_{\rm cal} = \sqrt{\sigma^2_{\rm diffraction} + \sigma^2_{\rm roll}}\,. \tag{6.1}$$

The laser ($\lambda = 520$ nm) produces a diffraction pattern through P1, which is captured as a rotated parabola. Key parameters include the incident angle φ_i (affecting curvature) and the polarization orientation θ (relative to the CCD's x-axis). Pre-processing removes noise below 1.5σ, where $\sigma = \sqrt{S}$ is the Poisson error on the image. Centroids of maxima are identified using a 2D Gaussian fit, and the diffraction pattern is modeled using a rotated parabola with parameters (x_V, y_V), a, and θ. The orientation θ provides the relative polarization angle. Statistical errors dominate the total uncertainty, which meets the requirement of $\Delta\psi < 0.1°$. A typical diffraction pattern image and fit result are shown in Fig. 6.4.

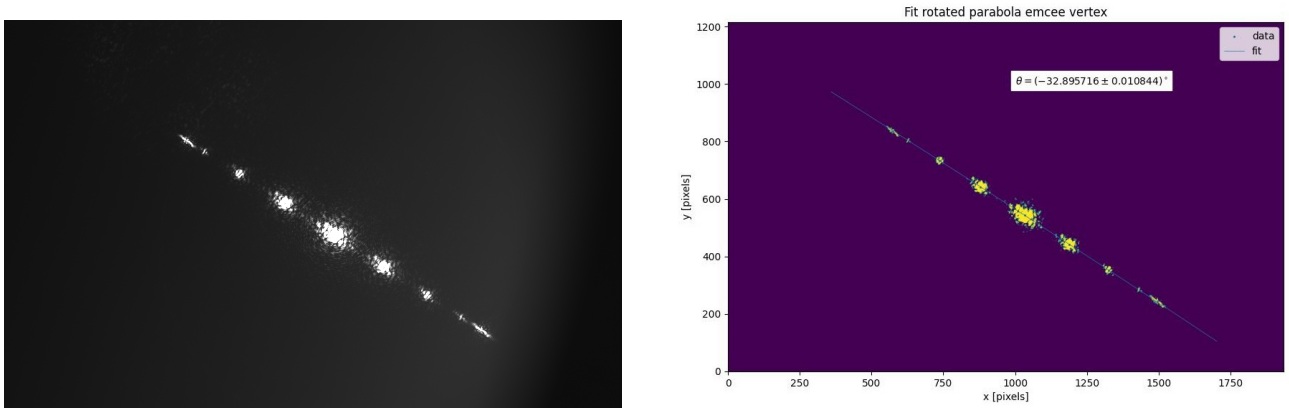

Figure 6.4: Left: typical image of the diffraction pattern acquired by the CCD camera. Right: estimation of the orientation of the polarization in the camera plane. Figures from L. Bizzarri.

6.2.2 Photogrammetry

A method to determine COSMOCal's absolute orientation with respect to the ground is also applied: the photogrammetry maps of geo-referenced targets. Photogrammetry determines the CCD camera's orientation relative to the ENU coordinate system. Landmarks around the IRAM 30m telescope are identified using GPS and refractor telescope measurements. The process yields the three Euler angles (yaw, pitch, roll), with roll directly related to the polarization orientation. This provides an independent estimation of the polarization expected to be measured by NIKA2 detectors. Promising results align with prior studies, as Dunner et al. 2020 [97] and Coppi et al. 2022 [72].

6.3 Phase 1.1: in-lab proof of concept

To validate the COSMOCal prototype before the observing campaign at the IRAM 30m telescope in September 2024, we conducted a dedicated test week using the fully assembled prototype. This testing was carried out alongside an instrument similar to NIKA2, namely the facility installed in the cryogenic lab at LPSC (described in Chap. 4). The primary objectives of these tests were to evaluate the functionality of the COSMOCal prototype and to establish a data analysis framework utilizing KIDs as receivers. This setup provided an ideal test bench for the prototype prior to interfacing with NIKA2. During the one-week session held in February 2024, we successfully demonstrated the capability to measure the polarization angle both through KID data and the diffraction pattern independent analysis.

6.3.1 Adapted experimental setup

The KID array used in the laboratory tests of the COSMOCal mm source is optimized for measurements at 260 GHz. In the current setup, with a source emitting at 260 GHz, an optical low-pass filter (LPF) is installed at the 1 K cryogenic stage to limit the array's bandwidth around this frequency. To improve signal focusing, a 54 mm pupil is placed at the 100 mK stage. The optical system also incorporates several additional focusing elements. At the 4 K stage, an LPF with a cutoff at 11 cm^{-1}, a high-density polyethylene (HDPE) lens, and a field stop with a diameter of 108 mm are included. At the 50 K stage, another LPF with a cutoff at 12 cm^{-1}, coated with an anti-reflection layer, is added, followed by a thermal filter at the 150 K stage. An external HDPE window lens is positioned at the entrance of the cryostat to focus incoming radiation.
A crucial component of this adapted setup is the set of polarizers. In particular, the experimental setup includes three linear polarizers aligned along the same optical axis, each serving distinct purposes. The first polarizer (P1), located within the COSMOCal box, is a critical component of the optical system. P1 can be rotated along the optical axis, with its angle roughly estimated by visual inspection. The second polarizer (P2) is placed at the entrance of the cryostat and can also rotate along the same axis. Its rotation angle is precisely adjustable and can be read from a graduated scale on the mechanical support. Finally, the third polarizer (P3) is positioned in the coldest cryogenic stage, where it splits the signal onto two arrays. As it is part of the cryogenic system, P3 remains fixed during measurements. Its disposition in the cryostat is shown in Chap. 4, Fig. 4.4. A full representation of the described configuration is shown in Fig. 6.5.

6.3.2 Coupling COSMOCal - cryostat

The COSMOCal box includes a mechanical chopper that modulates the emission from the millimeter source. The chopper consists of an aluminum plate that moves vertically, with its modulation frequency adjustable via dedicated software. A layer of absorbing Eccosorb is placed between the source and the chopper. This layer serves two critical functions: it attenuates the source power and absorbs any waves reflected by the chopper back toward the source. This configuration ensures precise modulation of the emission while minimizing unwanted reflections, thereby improving measurement accuracy.
The COSMOCal box was mounted on a tripod and positioned approximately 2 m from the cryostat entrance, at a height of 135 cm. Accurate alignment of the source with respect to the cryostat was a key requirement for reliable data collection. To achieve this, a cross-laser was employed, as illustrated in Fig. 6.6. This alignment method ensures precise positioning, which is essential for the integrity of the measurements.

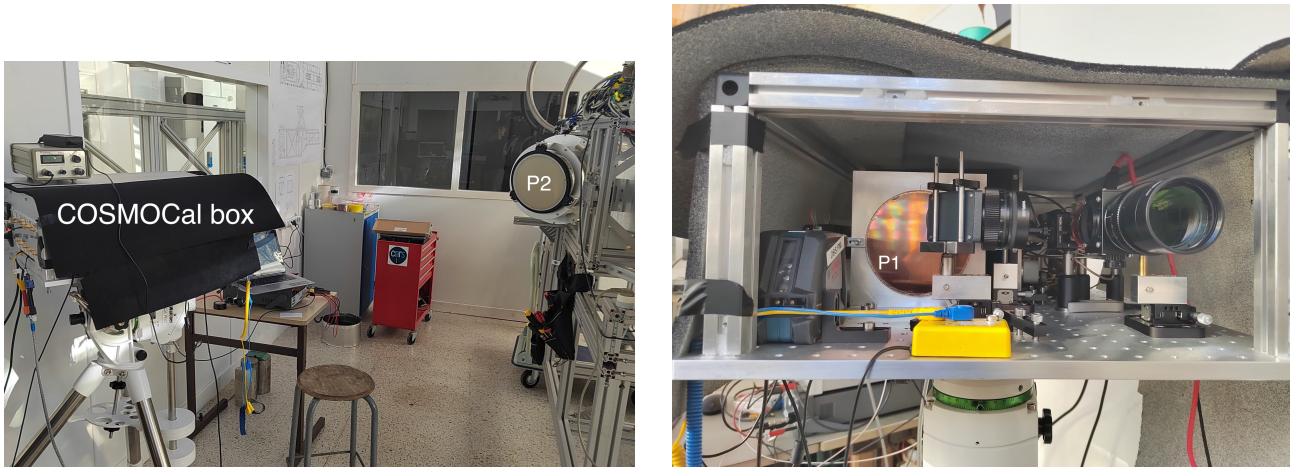

Figure 6.5: Pictures showing the COSMOCal box oriented towards the cryostat with the entrance P2 polarizer (left), and a front view of the COSMOCal box with a tag on P1. The cryogenic polarizer (P3) could not be shown.

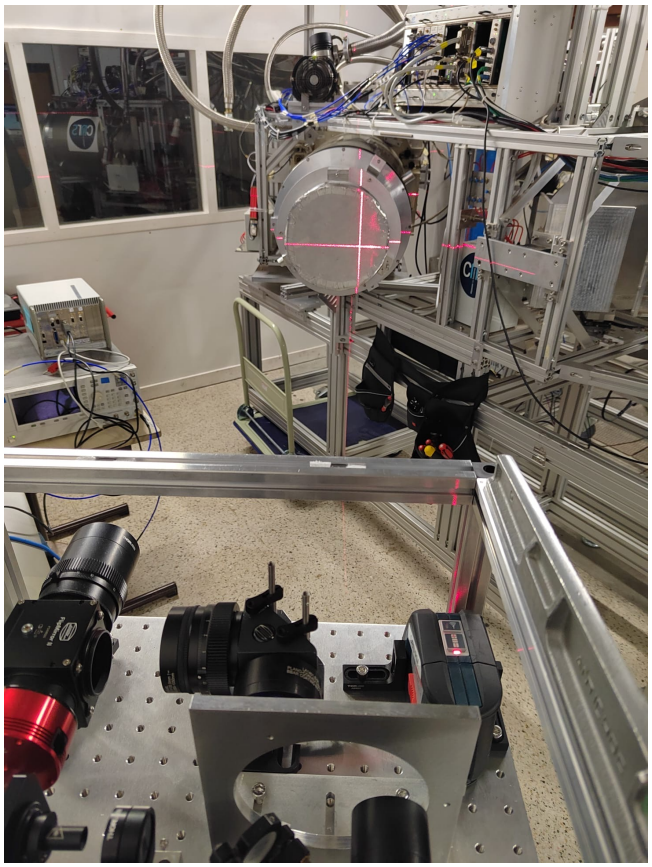

Figure 6.6: Picture shot during the laboratory measurements at the LPSC laboratory. The cross laser displayed on the cryostat window shows the alignment measurements.

6.3.3 Data model and methods

The starting point for understanding these measurements is a data model designed to simulate the experimental conditions expected in the laboratory. To this end, the Stokes and Mueller polarization modeling formalism has been used to compute the theoretical signal expected to be received by the detectors (see Chap. 2, Sec. 2.2). In this preliminary model, the polarizers are assumed to be perfect. In this formalism, a perfect polarizer whose transmission axis makes the angle α with respect to the laboratory reference reads:

$$
\begin{aligned}
M' &= M(-2\alpha)\cdot M_{pol}\cdot M(2\alpha) \\
&= \frac{1}{2}\begin{bmatrix} 1 & \cos 2\alpha & \sin 2\alpha \\ \cos 2\alpha & \cos^2 2\alpha & \cos 2\alpha \sin 2\alpha \\ \sin 2\alpha & \cos 2\alpha \sin 2\alpha & \sin^2 2\alpha \end{bmatrix},
\end{aligned} \tag{6.2}
$$

where M_{pol} is the matrix of an ideal polarizer. In this model, we consider Eq. 6.2 and replace α with: i) ψ to simulate the COSMOCal's polarizer (P1), ii) γ to account for the polarizer (P2) at the entrance of the cryostat and β that refers to the cold splitting wire grid (P3). The final signal reaching the detectors is therefore the result of an input Stokes vector S_{in} multiplied by three Mueller matrices: $S_{model} = P_3(\beta)\cdot P_2(\gamma)\cdot P_1(\psi)\cdot S_{in}$. Considering only the first row in $P_3(\beta)$, that gives the amplitude of the signal detected, we obtain:

$$
\begin{aligned}
S_{\rm model} = \; & 1 + \tfrac{1}{2}\cos 2(\beta-\psi) + \cos 2\gamma(\cos 2\beta + \cos 2\psi) \\
& + \sin 2\gamma(\sin 2\beta + \sin 2\psi) + \tfrac{1}{2}\cos 4\gamma \cos 2(\beta+\psi) \\
& + \tfrac{1}{2}\sin 4\gamma \sin 2(\beta+\psi)\,.
\end{aligned} \tag{6.3}
$$

Due to the mechanical design of the cryostat, β is fixed at 90°, while γ varies between [0,π]. ψ is fixed for each set of measurements. A sample of three different examples is shown in Fig. 6.7.

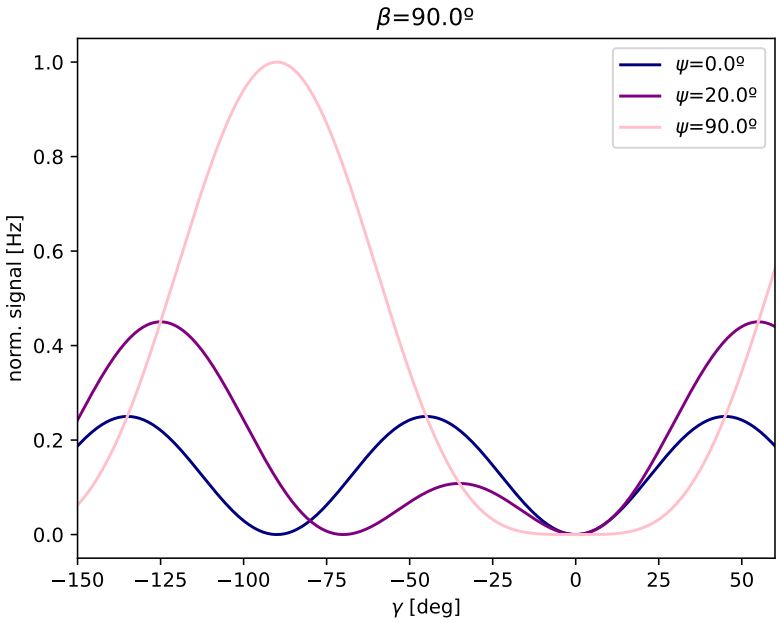

Figure 6.7: Model signal derived through Mueller formalism for three different configurations of the COSMOCal's polarizer (P1), as a function of γ, corresponding to the rotating polarizer (P2).

6.3.4 Data acquisition strategy

Three sets of measurements have been performed, each corresponding to a different angle of the polarizer P1, denoted by $\psi \simeq [0°, 45°, 70°]$, with respect to the vertical position marked on P1 that indicates the output polarization direction. The exact values were determined *a posteriori* through a detailed analysis of the diffraction pattern, as explained in Subsec. 6.3.5. For each fixed value of ψ, we rotated P2, which acts as an analyzer, through a range of 10 different angles, spaced at 20° intervals, spanning from -130° to +50°. The angle of P2 was known with a precision of better than 1°, thanks to the markings on its mechanical mount.

During laboratory testing, we observed that rotating the COSMOCal input polarizer (P1) caused significant changes in the response of the KIDs, due to variations in the polarization signal amplitude. As a result, we had to perform a re-tuning procedure to return the KIDs to their operating resonance frequency after any change in the P1 rotation angle. Lastly, a mechanical chopper modulated the signal at 0.16 Hz before P2, enabling lock-in detection and the rejection of low-frequency electronic noise.

6.3.5 Diffraction pattern results

To accurately determine the COSMOCal output, the polarization angle was independently measured using the diffraction pattern analysis method described in Subsec. 6.2.1. Due to the absence of photogrammetry in the laboratory, a plumb line was employed to measure the camera roll angle, aligning it with a reference. However, this introduced the main source of uncertainty.
The diffraction pattern analysis yielded the following polarization angles for the three positions of P1:

$$\psi_{1,DP} = (351.295 \pm 0.023)^\circ, \quad \psi_{2,DP} = (23.477 \pm 0.041)^\circ, \quad \psi_{3,DP} = (51.662 \pm 0.011)^\circ . \quad (6.4)$$

The roll angle was estimated using an OpenCV algorithm applied to images of millimeter paper aligned with the plumb line, captured by the COSMOCal CCD camera. The roll angle uncertainty was calculated using the inter-quartile range, giving:

$$\varphi_{roll} = (13.062 \pm 0.065)^\circ . \quad (6.5)$$

This roll angle correction was applied to the diffraction pattern results, yielding the final polarization angles reported in Tab. 6.1. Although the uncertainty in the polarization angles is below the required $\Delta\psi < 0.1^\circ$, the primary source of uncertainty stems from the roll angle estimation. This is due to the limited precision in aligning the plumb line with the millimeter paper in the laboratory. Nevertheless, these results demonstrate our ability to independently determine the polarization angle output of the COSMOCal prototype, with further improvements expected during the IRAM 30m test campaign using photogrammetry.

6.3.6 KID results

At the conclusion of the measurement campaign, a comprehensive data set was acquired and analyzed in several stages. Initially, the raw (I, Q) data were converted into a phase timeline, which is proportional to the total optical power reaching the detectors (Chap. 3). Once this streamlined data set was obtained, a more complex noise treatment and data reduction process was applied to yield refined data points suitable for detailed analysis and fitting to the model function.

Raw data treatment Once the phase data were acquired, they were cleaned of glitches and disturbances caused by signal fluctuations induced by the chopper. This was achieved by subtracting the median of the signal for each plateau corresponding to the up and down movements of the chopper. Since the KIDs do not exhibit identical responsiveness and therefore do not record the same signal amplitude, an inter-calibration process was necessary. KID #4 was used as the reference for this calibration. The difference between the raw and inter-calibrated data is shown in Fig. 6.8.

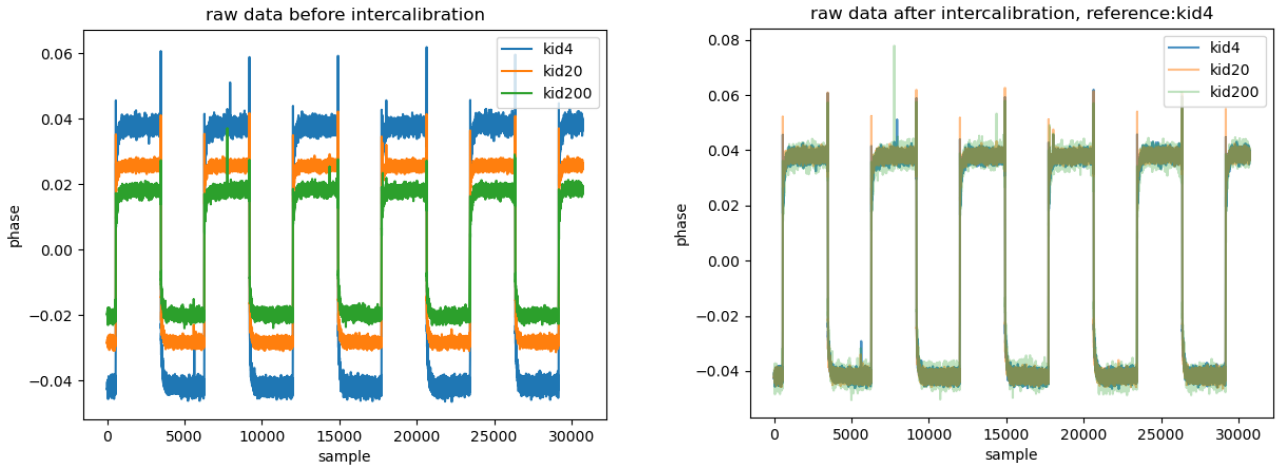

Figure 6.8: Raw phase data for a set of three KIDs (4, 20, 200) before (*left*) and after (*right*) inter-calibration.

The average signal for all up and down blocks was computed from the raw data, yielding a single data point for each time series. This process provided ten data points per KID for each angle of ψ. The next step involved fitting these ten data points to the model function, incorporating minor corrections. The first correction addresses the tilted position of P2 relative to its optical axis, approximately 10°, which helps prevent or significantly reduce reflections. Due to this tilt, the transmitted polarization corresponds to the component projected onto the plane perpendicular to the optical axis. The corrected angle, which replaces $\cos\gamma$ in the model function, was calculated as shown in Eq. 6.6, where τ represents the tilt angle:

$$\cos\gamma_{tilt} = \frac{\cos\gamma \cdot \cos\tau}{\sqrt{\cos\gamma^2 \cdot \cos\tau^2 + \sin\gamma^2}}\,. \tag{6.6}$$

The second correction considered is due to the fact that all polarizers used are not actually ideal, which means that they do not transmit one pure component along the opposite direction of the wires, but some other minor components of the signal are transmitted as well. To apply this correction, the matrix in Eq. 6.2 should be modified, adding the appropriate constants. The corrected version of the Mueller matrix assuming a non-ideal polarizer is shown in Eq. 6.7, where K and q are constants depending on the polarizer's imperfections:

$$M = \begin{bmatrix} K & k\cos 2\alpha & k\sin 2\alpha \\ k\cos 2\alpha & K\cos^2 2\alpha + q\sin^2 2\alpha & (K-q)\cos 2\alpha \sin 2\alpha \\ k\sin 2\alpha & (K-q)\cos 2\alpha \sin 2\alpha & K\sin^2 2\alpha + q\cos^2 2\alpha \end{bmatrix}. \tag{6.7}$$

However, by applying the non-ideal polarizer corrected Mueller matrix, only minor corrections with respect to the original signal intervene, while adding non-negligible complexity to the fitting function, due to multiple constants to be handled. Therefore, the simpler -all ideal polarizers- model, was eventually preferred.
Once the tilt angle correction reported in Eq. 6.6 was included in the model, the data were fitted with the final model function, also adding an overall amplitude in front of it (Eq. 6.8) to account for normalization:

$$S_{tot}(\gamma_{tilt}, \psi) = A \cdot S_{corr}(\gamma_{tilt}, \psi)\,. \tag{6.8}$$

Polarization angle fit The goodness of fit was assessed by calculating the χ^2 values, with the top 20 KIDs exhibiting the lowest χ^2 being selected. A second round of fitting was then per-

formed using only these 20 KIDs, resulting in an initial estimate for the two fitted parameters: the amplitude and the angle ψ. The data points and fitted curves are shown in Fig. 6.9.

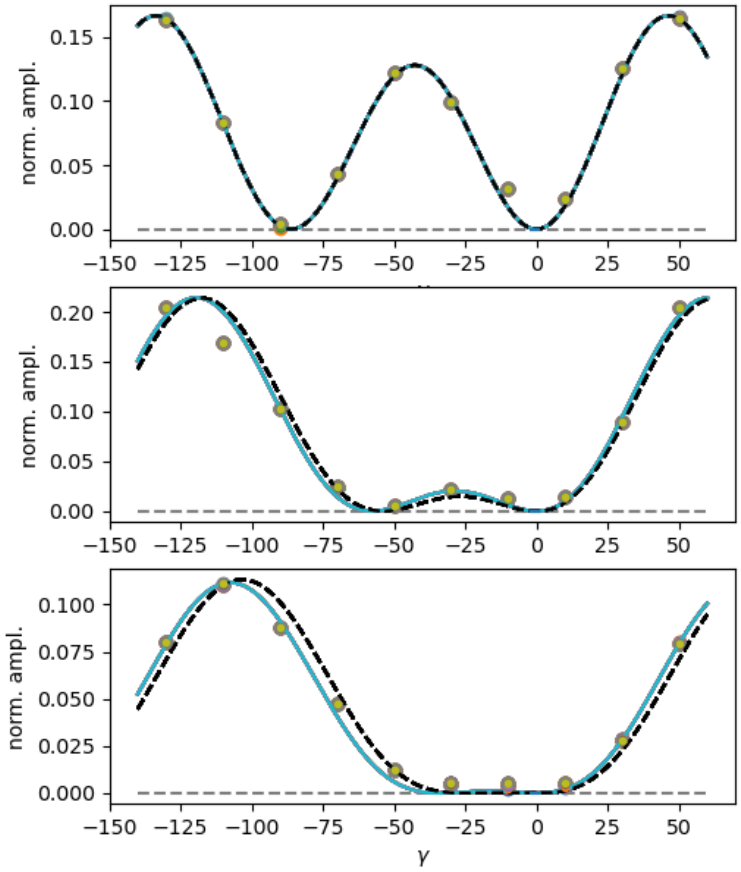

Figure 6.9: For all plots, the green dots actually hide the 19 other best KIDs that were selected and whose data are superposed. The dashed black line is the fit of the data obtained by imposing the ψ angles derived by the diffraction pattern analysis. The blue line is again a superposition of the 20 best fit of the KIDs of the data, this time leaving ψ as a free parameter. The three panels show data for the three sets of measurements, corresponding to $\psi = [0°, 45°, 70°]$.

The fitted estimates of A and ψ are provided in Tab. 6.1.

	A	ψ	ψ_{DP}
set1	0.146 ± 0.002	$(3.8 \pm 0.3)°$	$(4.357 \pm 0.069)°$
set2	0.091 ± 0.002	$(31.9 \pm 0.9)°$	$(36.539 \pm 0.077)°$
set3	0.0334 ± 0.0005	$(55.9 \pm 0.9)°$	$(64.724 \pm 0.066)°$

Table 6.1: Fit results for amplitude A and polarization angle ψ for the three sets of measurements, compared to the values of ψ_{DP} obtained from diffraction pattern analysis.

These results can be directly compared with the angles derived from the diffraction pattern analysis, which are listed in Tab. 6.1. A noticeable difference is evident among these values, with the percentage error being approximately 15% for all cases. The absolute error reaches as high as 9° for the third set of measurements.
The experimental setup, along with the characteristics of the source, imposes certain limitations that may introduce unwanted effects. Specifically, the source power is designed to match the requirements of a telescope configuration, particularly for the IRAM 30m tests. However,

this power exceeds the level that KIDs can tolerate in the laboratory setup due to the near field configuration. In fact, the walls of the room and the instrument itself are not anti-reflection coated, therefore parasitic reflections were anticipated. The most likely source of these reflections is the COSMOCal polarizer P1. The portion of the source radiation that is not transmitted and is instead directed to the cryostat is reflected, and it may bounce around the room before eventually re-entering the cryostat. This reflected component has a phase shift of 90° relative to the transmitted component. This additional component is accounted for in the fitting model. Since this component also passes through the entrance analyzer and the splitter, its form is the same as in Eq. 6.3. Thus, the fitting model becomes:

$$S_{tot} = A \cdot S_{pure}(\gamma, \psi) + B \cdot S_{parasite}(\gamma, \bar{\psi}) \,, \tag{6.9}$$

where $\bar{\psi} = \psi + \phi$, and ϕ is an angular phase between the two components.
Finally, the data were re-fitted to include the new parasitic component, and the values for the four fitted parameters were estimated. The plot of the new fit, incorporating the parasitic components, is shown in Fig. 6.10. The updated fitted parameters are listed in Tab. 6.2. This fit was performed using an *emcee* MCMC to address any potential degeneracies among the fit parameters. Priors were set for the three polarization angles (ψ) as follows: [3,6], [30,40], [55,65] degrees, while the phase angle (ϕ) priors were set to [50,90] degrees for all three cases. Based on the results, it was concluded that the priors do not limit the fitting process, and this choice of priors is supported by the prior knowledge of the fitted polarization angles obtained from the fit without parasitic components.

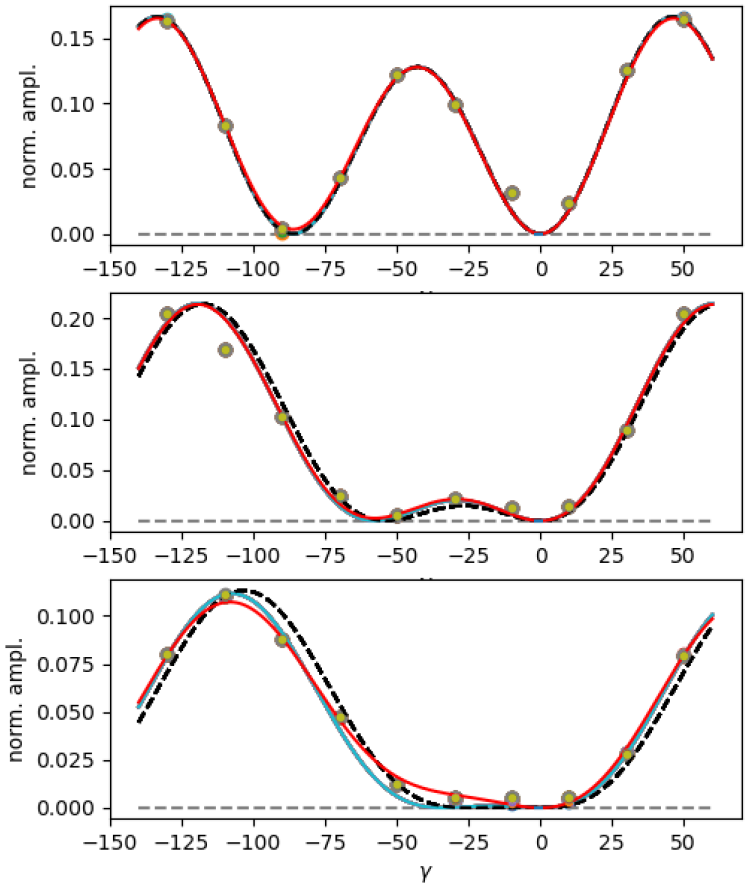

Figure 6.10: Same curves as Fig. 6.9, with the added fit including the parasitic component in red.

ψ_{box}	ψ_{det}	A	B	ϕ
$(4.357 \pm 0.069)^\circ$	$(4.3 \pm 0.7)^\circ$	0.146 ± 0.002	0.0116 ± 0.0001	$(77 \pm 5)^\circ$
$(36.539 \pm 0.077)^\circ$	$(35.6 \pm 0.9)^\circ$	0.069 ± 0.003	0.023 ± 0.005	$(78 \pm 6)^\circ$
$(64.724 \pm 0.066)^\circ$	$(63.8 \pm 0.8)^\circ$	0.027 ± 0.003	0.012 ± 0.004	$(76 \pm 5)^\circ$

Table 6.2: First two columns show the comparison between the COSMOCal independent measurements of the polarization angle (ψ_{box}) and the ones measured through analysis of KIDs data (ψ_{det}). Third, fourth and fifth columns show the results of the MCMC fit.

6.3.7 Remarks on the in-lab proof-of-concept

The final results for the fitted parameters remain unsatisfactory, although the inclusion of a parasitic component clearly plays a significant role in reducing discrepancies between the polarization angle ψ values estimated through different methods. However, a complete understanding of the physical nature of these parasitic signals, which contribute to the pure source signal, is still lacking. The most probable factor is the coupling between the source and the cryostat, as the source was not designed for this kind of environment.
Laboratory tests at LPSC with the fully assembled COSMOCal prototype and a KIDs camera revealed several technical challenges, particularly due to the detection of a stray microwave signal and uncertainties in estimating the camera roll angle. Despite these challenges, rigorous data analysis provided valuable insights. Notably, independent measurements of the roll angle of the COSMOCal polarizer and the signal polarization using the KIDs camera agreed within 2-3% in absolute value. This discrepancy is likely due to limitations in the laboratory setup, which does not effectively cancel reflections. Additionally, the uncertainties in the camera measurements dominate the error budget.
The tests at the IRAM 30m telescope, presented in Sec. 6.4, were expected to yield more precise results, as the receiver cabin at the telescope is more adapted to measure polarized signals with high precision. The primary goal of this campaign was to ensure the fidelity of data collected by the NIKA2 camera regarding the orientation of the COSMOCal polarization signal across the entire optical chain of the telescope. While this initial assessment is crucial for validating assumptions and assessing the current calibration of the NIKA2 polarization system, a comprehensive exploration and mitigation of all systematic effects, including instrumental polarization and optical efficiency, will require deployment of the COSMOCal system in space, in the far field of large telescopes.

6.4 Phase 1.2: IRAM 30m test campaign

The second part of Phase 1 focused on testing the 260 GHz prototype at the interface with a single-dish antenna, aiming to demonstrate the performance and capabilities of the calibrator in these conditions. This configuration provides a balance between controlled experimental setups, as it was the case for the in-lab testing at LPSC, and practical deployment scenarios, so the future space mission.
The purpose of the campaign was to demonstrate the performance and capabilities of the calibrator coupled with a real millimeter telescope. Near-field testing provides a first attempt of characterization of possible systematics in the optical chain between the telescope and the calibrator. The NIKA2 camera (Chap. 5) was selected due to the accurate instrument knowledge available within the COSMOCal collaborators and because of its sensitivity. The IRAM 30m telescope, situated just below Pico Veleta, offers a very good environment for such an experiment. While very close to the telescope, the peak of the mountain just in front of the telescope was convenient for the placement of the COSMOCal instrument, directly facing the

antenna, and ensuring unobstructed signal transmission and reception while minimizing logistical challenges. The COSMOCal calibrator was placed approximately 100 m below the summit, at the University of Granada (UGR) location (Fig. 6.11), previously used by the telescope staff to perform holography tests.

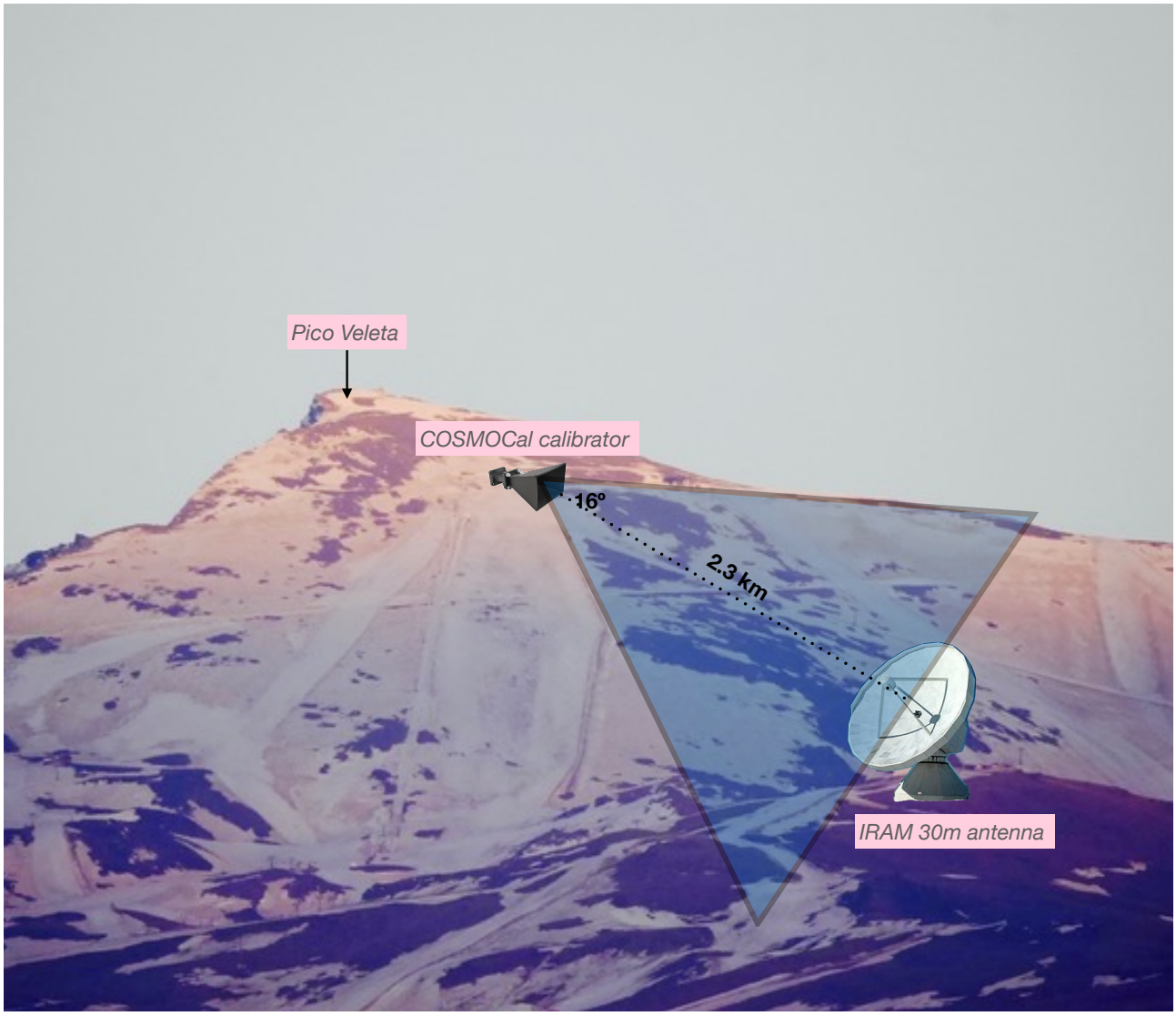

Figure 6.11: Graphic representation of the working environment at the IRAM 30m location, during the test campaign.

Some preliminary work was carried out in preparation for the test campaign at the telescope to develop the analysis code and anticipate any potential issues that could affect the quality of the collected data. As in the in-lab proof of concept, the expected signal was simulated to provide a foundation for subsequent analysis.
The measurement campaign was conducted in three main steps: (i) ensuring the detection of the signal emitted by the COSMOCal source, (ii) aligning the calibrator and the antenna by maximizing the incoming signal, (iii) performing the primary polarization measurements by rotating the COSMOCal polarizer and acquiring fixed track scans.

6.4.1 Optical model

To model the emitted signal of the source and quantify the misalignment effect on the focal plane, we performed optical simulations with Zemax. These simulations were mostly run by

S. Leclercq and A. Catalano. Moreover, in this subsection we present the power estimate we performed to ensure that the source did not saturate NIKA2's KIDs, then comparing with the actual power received.

Simulation setup and results For the simulation, we considered the following elements:

- Source distance: 2.31 km from the telescope (distance from Zayas station to the 30m telescope);
- Gaussian illumination: 16° FHWM, 10° elevation;
- Pointing offsets: 0 m, 1 m, 2 m, 4 m, 12 m, 16 m.

The pointing offsets in azimuth were analyzed to observe how the received energy varies as the telescope points off-source. The results are as follows:

- For the first four offsets (0 m, 1 m, 2 m, 4 m), the optical elements are all illuminated by the source, except for areas in the shadow of the secondary mirror and the quadrupod;
- At a 12 m offset, some detectors no longer see the source because the line source-detector does not intersect the entrance pupil disk;
- At a 16 m offset, only a small fraction of detectors still receives a signal, and beyond this, the source is no longer visible to any NIKA2 detector.

These results are also shown in Fig. 6.12, where we can notice that the misalignment plays a non-negligible role in the energy fraction received by the detectors. In fact, the fraction of received energy (E_{trans}) increases significantly when shadows from the secondary mirror and quadrupod diminish. If we push the simulation further (not shown in figures), we notice that, once there is no shadow, the energy fraction continues to rise gently until a point where more pixels can no longer see the source, resulting in a drop in energy fraction to zero for large offsets. Notably, the energy fractions are slightly higher compared to the uniform illumination case due to the Gaussian illumination's higher central ray density.

Source misalignment and model limitations In the context of the optical simulations, we introduced a deliberate tilt to the source so that the peak of the Gaussian does not align with the telescope's entrance. This adjustment required increasing the size of a fictive surface known as the STOP to ensure that rays from the tilted source reach the entrance pupil. As a result, the energy fraction calculated in the Polarization Pupil Maps is now relative to rays passing through the STOP rather than the 30-meter diameter entrance pupil, leading to smaller calculated fractions compared to when the STOP size matched the entrance pupil.
This model poses limitations as tilting the source by more than 1° surpasses the capability of the simple tools previously used due to the required extensive gridding. Larger tilts create a significant disparity between the STOP size and the array size, demanding a vast number of grid points and more sophisticated tools for energy fraction calculation, which increases computation time substantially.
Despite these challenges, preliminary results align with expectations. When the source is slightly misaligned but the telescope is aimed directly at it, the energy fraction received by the array is slightly higher compared to a perfectly aligned setup. This occurs because the peak of the Gaussian is no longer obscured by the secondary mirror, allowing illumination of part of the detector arrays. As the source becomes more misaligned, the energy fraction passing through the telescope's entrance pupil decreases, but given the large size of the Gaussian

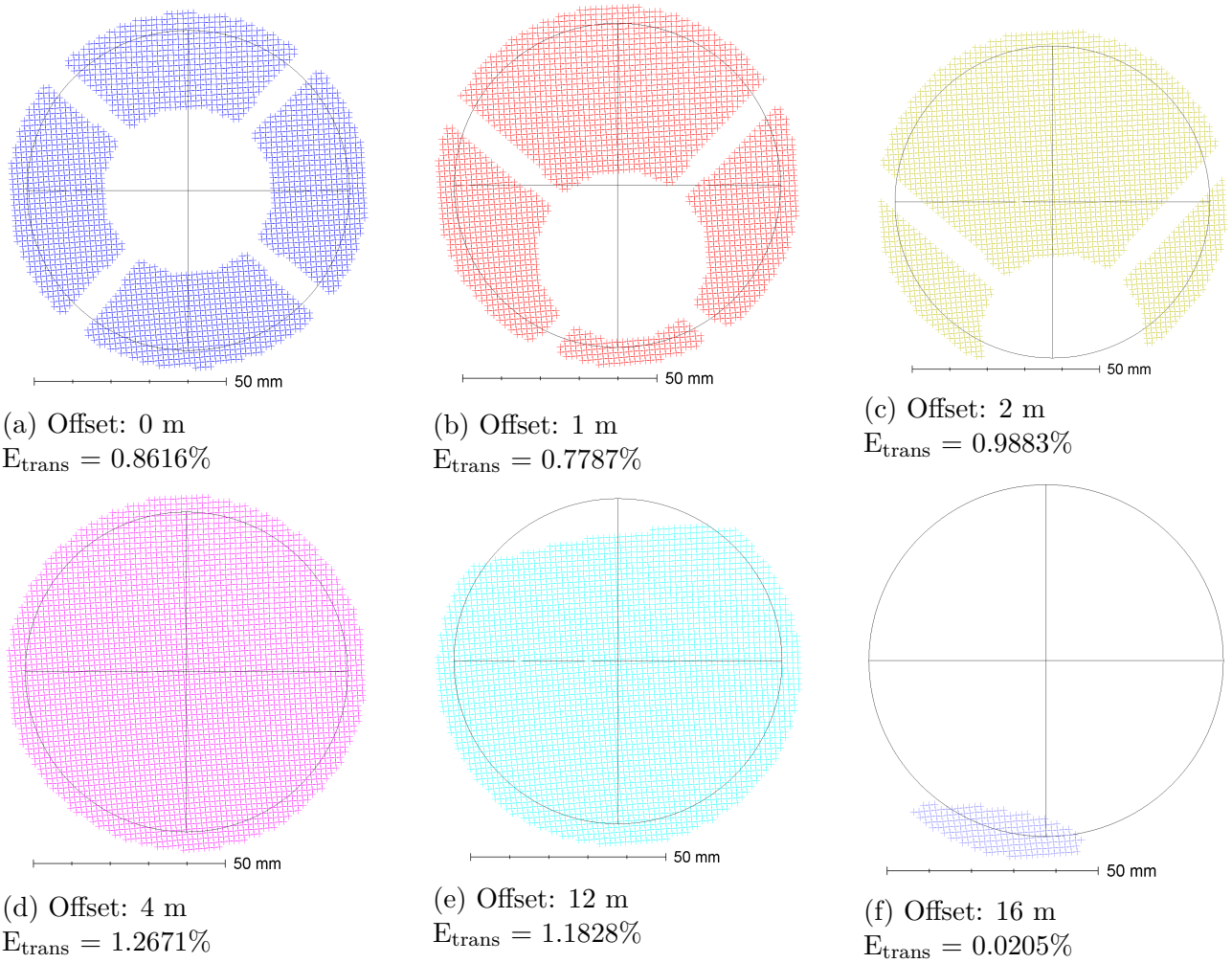

(a) Offset: 0 m
E_{trans} = 0.8616%

(b) Offset: 1 m
E_{trans} = 0.7787%

(c) Offset: 2 m
E_{trans} = 0.9883%

(d) Offset: 4 m
E_{trans} = 1.2671%

(e) Offset: 12 m
E_{trans} = 1.1828%

(f) Offset: 16 m
E_{trans} = 0.0205%

Figure 6.12: Comparison of source signal projection maps for different offsets. Surface transmission values are indicated for each configuration. Zemax simulation by S. Leclercq.

relative to the telescope entrance (649.2 m diameter for the FWHM versus 30 m for the primary mirror), there is considerable margin before significant effects from source misalignment become apparent (see Fig. 6.13).
In Fig. 6.14, we can see the direct representation of this result, meaning the fraction of enclosed energy as a function of the radius from the centroid. The blue curve represents the case of a perfect alignment, while the red one is showing a 1 m misalignment.

Power estimate In order to determine the level of attenuation required to prevent saturation of the KIDs, we first need to estimate the optical power that would be delivered to the focal plane in the current setup. This requires comparing the solid angle of the source illumination with the much smaller solid angle corresponding to the instrument field of view.
The source is placed at a distance of $d = 2300$ m from the 30-m dish and emits with a beam of 16° full width. The corresponding radius of the illuminated spot on the telescope is

$$r_{\mathrm{src}} = d \times \tan\left(\frac{16^\circ}{2}\right) = 2300 \text{ m} \times \tan(8^\circ) \approx 323 \text{ m}\,, \tag{6.10}$$

yielding an illuminated area on the dish of

$$A_{\mathrm{src}} = \pi r_{\mathrm{src}}^2 \approx \pi \times (323 \text{ m})^2\,. \tag{6.11}$$

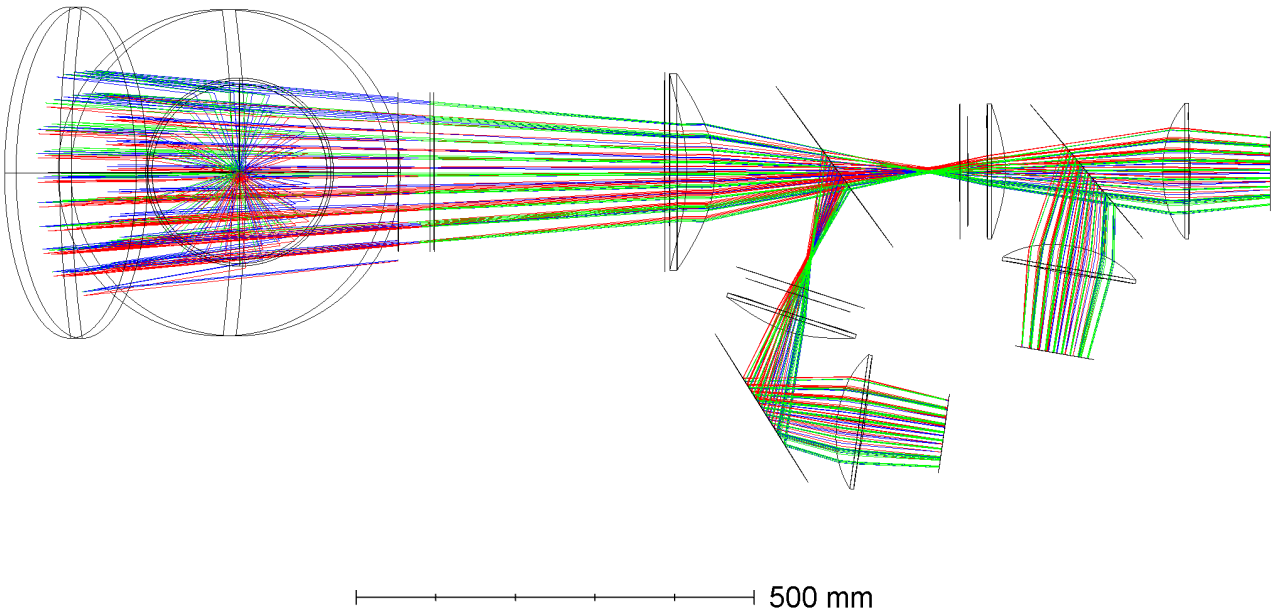

Figure 6.13: Complete ray tracing from the primary mirror to the focal plane. The blue rays correspond to a perfect alignment; the red ones correspond to a 1 m misalignment; the green ones correspond to a 2 m misalignment. Zemax simulation by S. Leclercq.

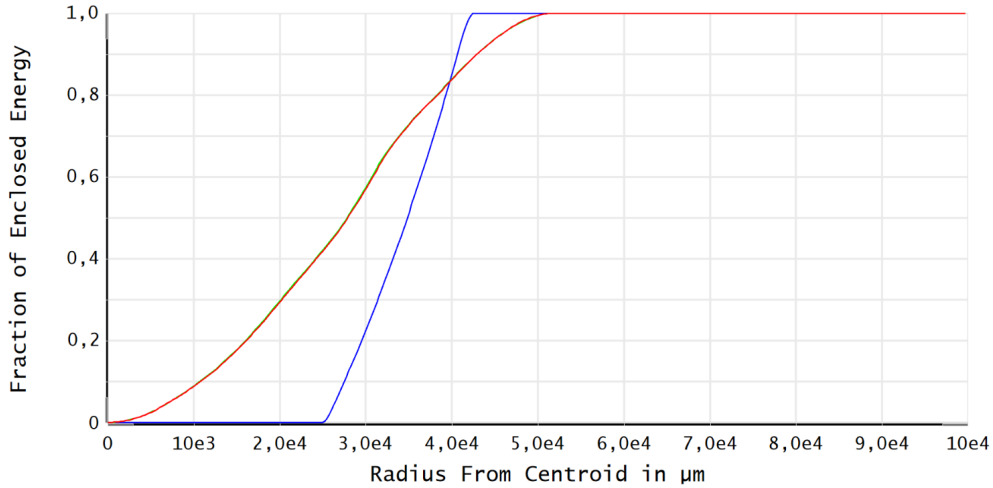

Figure 6.14: Fraction of encircled energy as a function of the radius of the antenna. The blue curve represents the case of a perfect alignment, while the red one is showing a 1 m misalignment. Zemax simulation by S. Leclercq.

By contrast, the instrument field of view corresponds to an angular diameter of 6.5′. At the same distance d, this translates into a projected radius of

$$r_{\mathrm{FoV}} = d \times \tan\left(\frac{6.5'}{2}\right) \approx 2300 \text{ m} \times \tan(0.054^\circ) \approx 2.17 \text{ m}\,, \tag{6.12}$$

and hence an effective area of

$$A_{\mathrm{FoV}} = \pi r_{\mathrm{FoV}}^2 \approx \pi \times (2.17 \text{ m})^2\,. \tag{6.13}$$

The ratio of these two areas defines the dilution factor, i.e. the fraction of the source emission effectively intercepted by the instrument FoV:

$$D = \frac{A_{\rm FoV}}{A_{\rm src}} = \frac{(2.17\ {\rm m})^2}{(323\ {\rm m})^2} \approx 4.5 \times 10^{-5}\,. \tag{6.14}$$

This demonstrates that only a tiny fraction of the source output is collected by the telescope. The Zemax simulation of Fig. 6.15 illustrates this near-field effect: since the illumination is not in plane waves, only rays within the instrument FoV are efficiently directed to the focal plane.

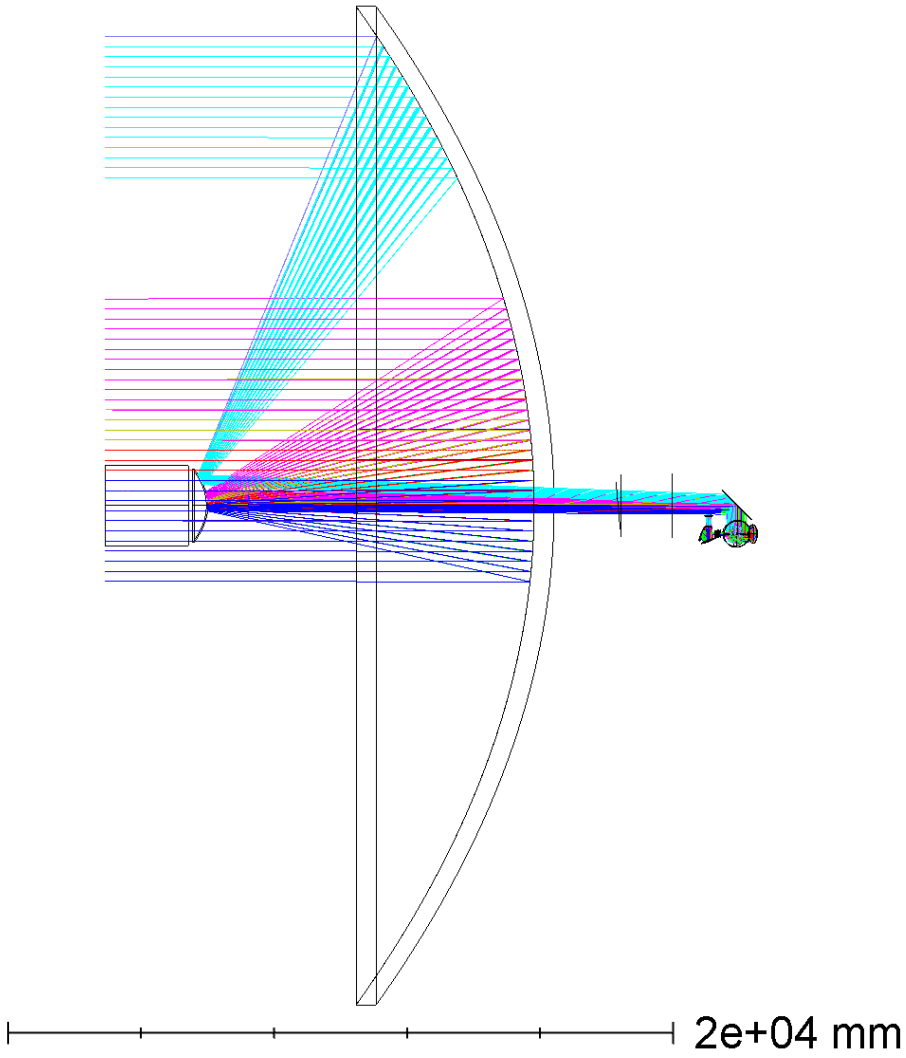

Figure 6.15: Ray tracing from the telescope M1 mirror down to the detector arrays for the six pointing offsets (0 m, 1 m, 2 m, 4 m, 12 m, 16 m), using the same color code of Fig. 6.12. Only the unvignetted rays that reach the detectors plane are displayed, and only for the top half. Zemax simulation by S. Leclercq.

We can now estimate the power received per detector. We consider an attenuated source emission of 0.2 mW, equally split between the two 260 GHz arrays (A1 and A3), while the 2-mm channel receives negligible power. We further assume that the transmission losses can be represented by the optical efficiency of 35% reported in Perotto et al. 2020 [235], multiplied by the dilution factor computed above. The total collected power is then distributed over the ~ 1000 pixels of each array, giving

$$P_{\rm pix} = \frac{P_{\rm emitted} \times D \times \epsilon}{N_{\rm pix}} = \frac{0.2\,{\rm mW} \times 4.5 \times 10^{-5} \times 0.35}{1000} = 3.15\,{\rm pW/pixel}\,, \tag{6.15}$$

where D is the dilution factor, ϵ the optical efficiency, and $N_{\rm pix}$ the number of detectors.

This calculation provides an order-of-magnitude estimate of the optical load on a single KID when observing the source in near-field conditions. It directly proves that this level of loading is compatible with the detector's linear response regime, ensured until a few tens of pW.

6.4.2 Signal model

The expected modulated signal has been simulated by computing the Stokes I parameter from Mueller matrices, while incorporating the appropriate optical elements, as it was done for the Grenoble setup. In this case, three optical components have been modeled and considered in the calculations: the COSMOCal polarizer, with its rotation angle relative to the vertical axis denoted by ψ; the NIKA2 continuously rotating HWP, where the angle of the principal axis relative to the vertical is $\theta = \omega t$, with ω being the rotational frequency of the HWP and t the time; and the NIKA2 cold polarizer, which is responsible for splitting the incoming radiation onto two perpendicular arrays, with the angle between its wires and the vertical represented by β. Thus, by considering an initial Stokes vector of unpolarized light, we can model the outgoing signal as described by:

$$S_{out} = M_{pol\beta} \times M_{HWP} \times M_{pol\psi} \times S_{in}\,, \tag{6.16}$$

where S_{in} = [1,0,0], each of the two Mueller matrices has the form of Eq. 6.17 and the Mueller matrix of the HWP is the one shown in Eq. 6.18:

$$M_{pol} = \begin{bmatrix} 1 & \cos 2\alpha & \sin 2\alpha \\ \cos 2\alpha & \cos^2 2\alpha & \cos 2\alpha \sin 2\alpha \\ \sin 2\alpha & \cos 2\alpha \sin 2\alpha & \sin^2 2\alpha \end{bmatrix}\,, \tag{6.17}$$

$$M_{HWP} = \begin{bmatrix} 1 & 0 & 0 \\ 0 & \cos 4\theta & \sin 4\theta \\ 0 & \sin 4\theta & -\cos 4\theta \end{bmatrix}\,. \tag{6.18}$$

So, by computing the first element of S_{out}, corresponding to the total intensity, we obtain the final out-coming signal of Eq. 6.19:

$$S = 1 + \cos 4\theta \cos(2\beta + 2\psi) + \sin 4\theta \sin(2\beta + 2\psi)\,. \tag{6.19}$$

By using this model function, we can choose proper parameters for the angles and the rotational frequency of the HWP to obtain a simulated representation of the out-coming signal. The signal is also modulated by an electrical chopper, which turns on and off the source at a given frequency. For example, by choosing $\omega_{HWP} = 3$ Hz, $\beta = 0°$, $\psi = 45º$ and $f_{\rm chop} = 1$ Hz, we derive the curve shown in Fig. 6.16.
From this, we can see that the modulation frequency is 4x the rotational frequency of the HWP, as expected.

6.4.3 Preliminary detection

The first preliminary measurement involved activating the millimeter-wave source and verifying the proper response of NIKA2's detectors. A particularly challenging aspect of this phase was the tuning of the detectors. This difficulty arose because the antenna is positioned to face the mountain, causing significant variations in the background across measurements, with additional fluctuations potentially interfering with the signals.
The campaign started by ensuring that the main components where present in the signal,

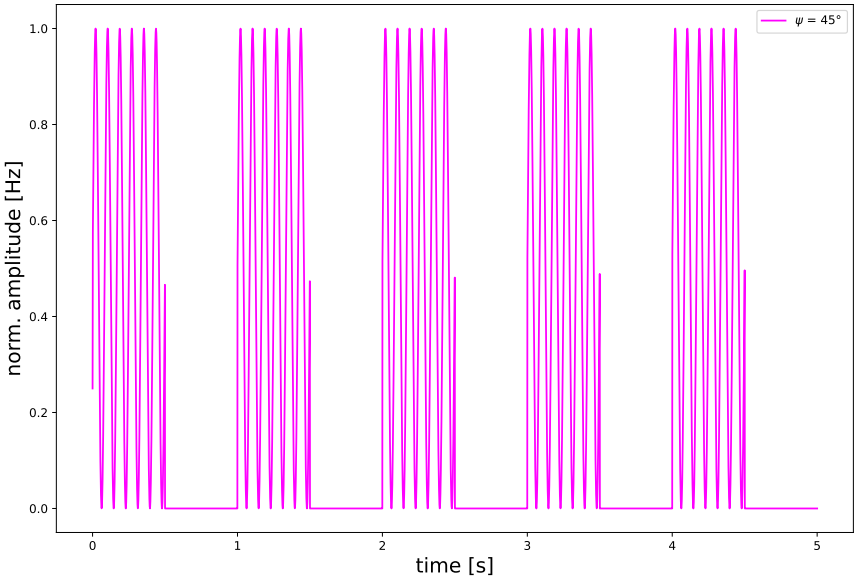

Figure 6.16: Simulated signal for one sample orientation of the orientation angle of the COSMOCal's polarizer, ψ, also considering the contribution of the chopper modulated at 1 Hz.

meaning the chopper, with a power spectrum peaking at the selected modulation frequency and the HWP also peaking at 4x the nominal modulation frequency. We can see in Fig. 6.17 on the left a sample timeline for one KID of NIKA2's A1, while on the right the relative power spectrum is shown. We can notice two patterns in the raw signal: the ON-OFF plateaus due to the chopper modulation and the high-frequency modulation. The latter is due to the Half Wave Plate Synchronous Signal (HWPSS), which will be discussed in Subsec. 6.4.4.

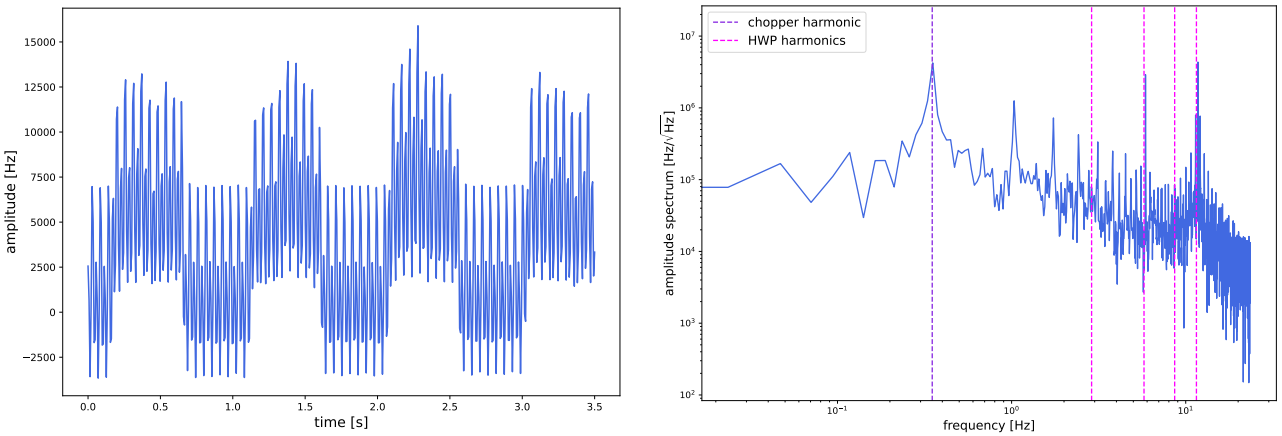

Figure 6.17: Timeline of one sample pixel of A1 (*left*) and relative power spectrum (*right*). The dashed lines in violet the chopper's main harmonic and in pink the 4 first harmonics of the HWP.

This preliminary detected signal already contains a wealth of information. Firstly, we observe a difference in the shape of the timeline compared to the simulated one in Fig. 6.16. It looks like the HWP modulation is not entirely effective, as the signal fails to reach zero even when the chopper is active, and the HWP should theoretically suppress it completely. This depolarization effect could have two origins: an imperfect transmission of the HWP or external factors. The first is one actually understandable, knowing that the HWP is not ideal, but rather has a

transmission efficiency of $\sim 70\%$, as characterized by Pisano et al. 2022 [237]. The second one will be discussed in more detail later on.
The power spectrum on the right plot reveals that the harmonics of both the chopper and the HWP are located at their expected frequencies: 0.35 Hz for the chopper's first harmonic and 12 Hz for the HWP's fourth harmonic. This alignment confirms that the system's key modulation components are functioning as anticipated.

6.4.4 Pipeline for data reduction: key concepts

The next sections will outline the main results of the IRAM campaign, including the preliminary radio alignment and polarization angle estimation. Before diving into the results and their interpretation, it is useful to describe the pipeline used to estimate the Stokes parameters I, Q and U starting from raw KIDs data.
The pipeline described here is a tailored data analysis workflow designed to extract physical parameters, such as intensity and polarization, from observations made with NIKA2. This process begins with the ingestion of raw data, which includes timelines, detector array configurations and hardware positional data, such as the HWP position. A critical aim of the pipeline is to disentangle the polarized and unpolarized components of the incoming radiation.
The first step in the pipeline involves parsing the raw data and assigning positional information to the detectors based on their known geometric arrangement, which is retrieved from a geometry file. The geometry file maps detector names to their coordinates, enabling the association of timeline data with specific detectors. This positional information is crucial for interpreting the spatial structure of the signal across the detector arrays.
A critical component of the pipeline is the synchronization with the HWP. The HWP rotates at a known frequency and modulates the polarization of the incoming radiation. By analyzing synchronization signals, the pipeline identifies rotation periods and determines the phase of the HWP as a function of time. This phase, $\phi_{\rm HWP}$, is essential for extracting polarization information because the HWP introduces a predictable modulation into the signal. The total signal recorded by a detector can be expressed as:

$$S(t) = I + Q\cos(4\phi_{\rm HWP}) + U\sin(4\phi_{\rm HWP})\,, \tag{6.20}$$

where I represents the unpolarized intensity, while Q and U describe the linear polarization state.

In Fig. 6.17, we presented an example of a KID timeline and its power spectrum. The modulation of the chopper is clear with the alternation of high and low plateaus. In addition to this, there is a rapidly oscillating signal. This is the sum of COSMOCal's polarized signal modulated by the HWP and that of the spurious emission of the HWP at all harmonics of its rotation frequency (a well-known component; see e.g. Ritacco et al. 2016 [264]). It must be subtracted from all KID timelines. We do this iteratively to not deteriorate the signal. We perform a first estimation on the full timeline of the reference KID and subtract it (Fig. 6.18). This suppresses most of the effect and enhances the contrast between high and low chopper plateaus. With a Fourier transform, we determine the first harmonic of the chopper (in blue, second plot). This harmonic is positive on high plateaus, when COSMOCal is on, and negative when COSMOCal is obscured by the chopper. This enables us to locate the low plateaus when there is no COSMOCal signal. We restrict to a conservative central interval to prevent from inaccurate plateau determination due to boundary conditions. We then fit the HWPSS on all KIDs and only on low plateaus, and subtract it everywhere. A baseline is determined on low plateaus only and subtracted everywhere to remove potential time drift (e.g. atmosphere). Last, restricting again to a safe central portion of each high plateau, we fit the data to Eq. 6.19

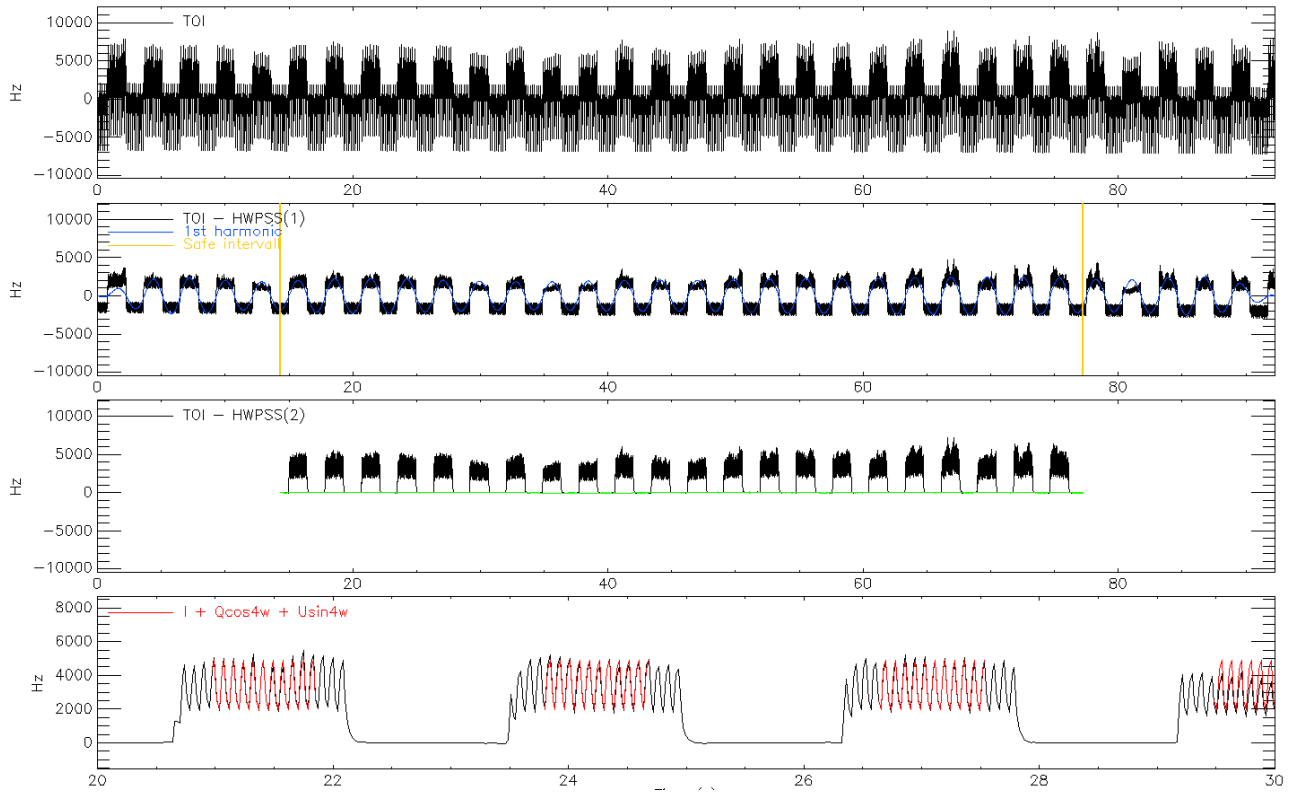

Figure 6.18: Illustration of the different steps of the TOI processing. Top plot: the raw KID timeline is the sum of COSMOCal, HWPSS and noise. Second plot: a first estimate of the HWPSS is subtracted to reveal the chopper modulation. Third plot: the HWPSS is now fit only on low plateaus and subtracted everywhere. Bottom plot: restricting to the safest portion of each high plateau, we fit COSMOCal's signal with Eq. 6.19. Plot by N. Ponthieu through a dedicated IDL pipeline.

and average the derived values of I, Q and U of all plateaus, for each KID independently. The polarized intensity is defined as:

$$I_{pol} = \sqrt{Q^2 + U^2}\,, \tag{6.21}$$

and it relates to the degree of polarization as:

$$p = \frac{I_{pol}}{I_{tot}}\,, \tag{6.22}$$

and the polarization angle is given by:

$$\psi = \frac{1}{2}\arctan\left(U, Q\right)\,, \tag{6.23}$$

where the arctan is defined in $]-\pi, \pi]$. The pipeline processes data from two detector arrays (labeled A1 and A3), which enable the independent assessment of intensity and polarization in different regions of the field of view. By averaging the extracted values across multiple scans, the pipeline improves the signal-to-noise ratio and provides robust measurements of the unpolarized intensity (I_{tot}) and the polarized intensity (I_{pol}).

6.4.5 Radio alignment

Although the coordinates of the UGR location, where the COSMOCal calibrator was placed, were known, ensuring proper alignment between the source's main beam emission line and the antenna was crucial, as highlighted by the simulations of Subsec. 6.4.1.
The initial selected coordinates of the antenna are in AzEl = [116.19º, 10.49º]. From this initial position, the antenna has been slightly tilted in Azimuth and Elevation, taking a fix track scan for each position. The goal was to find the maximum signal in total intensity, so that we could define the offset corrections ensuring optimal alignment. For the set of acquired scans, the polarized intensity has been derived as described in the previous section. First, we only scanned in Azimuth, keeping the Elevation fixed at 0º. Then, once found the optimal Azimuth correction of -5', we scanned in Elevation, finding an optimal offset correction of -14', as shown in Fig. 6.19.

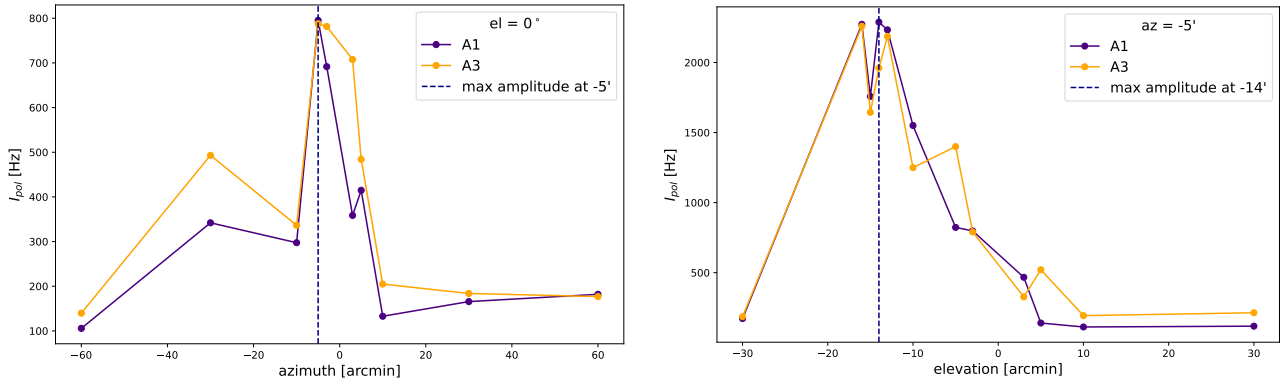

Figure 6.19: *Left*: polarized intensity as a function of the azimuth correction, for a set of offsets between -1º and +1º. The dashed vertical line highlights the Azimuth offset maximizing the signal, i.e. Az_{offset} = -5'. *Right*: polarized intensity as a function of the elevation, with a fixed azimuth offset of -5'. The elevation correction maximizing the signal is -14'.

Finally, we can conclude that the best set of offsets with respect to the initial coordinates is [-5', -14'], which have been subtracted to the initial chosen coordinates, giving a final set of target coordinates [116.10º, 10.25º].

6.4.6 Photogrammetry and diffraction pattern analyses

As it was done for the in-lab proof of concept phase, also for this campaign we relied on two independent referencing systems: the photogrammetry and the diffraction pattern analyses. This part was L. Bizzarri's Master's thesis work and his main responsibility during the IRAM campaign.

Photogrammetry Photogrammetry is a technique that determines the attitude of the COSMOCal calibrator by matching the 2D positions of ground targets in CCD camera images with their measured 3D coordinates in a local ENU reference frame. We already briefly introduced this technique in Subsec. 6.2.2. A total of 14 targets were placed around the antenna, as shown in Fig. 6.20.
The GPS-measured target positions showed a standard deviation of $\sim$ 0.2 m, corresponding to an intrinsic uncertainty on the calibrator attitude of $\sim 5 \times 10^{-3}$ deg. The calibrator GPS position varied by up to $\sim$ 3 m, implying an uncertainty on the attitude reconstruction of $\sim$ 0.05 deg.
Target centroid identification in the CCD camera plane has an uncertainty of $\sim$ 12 cm (from a

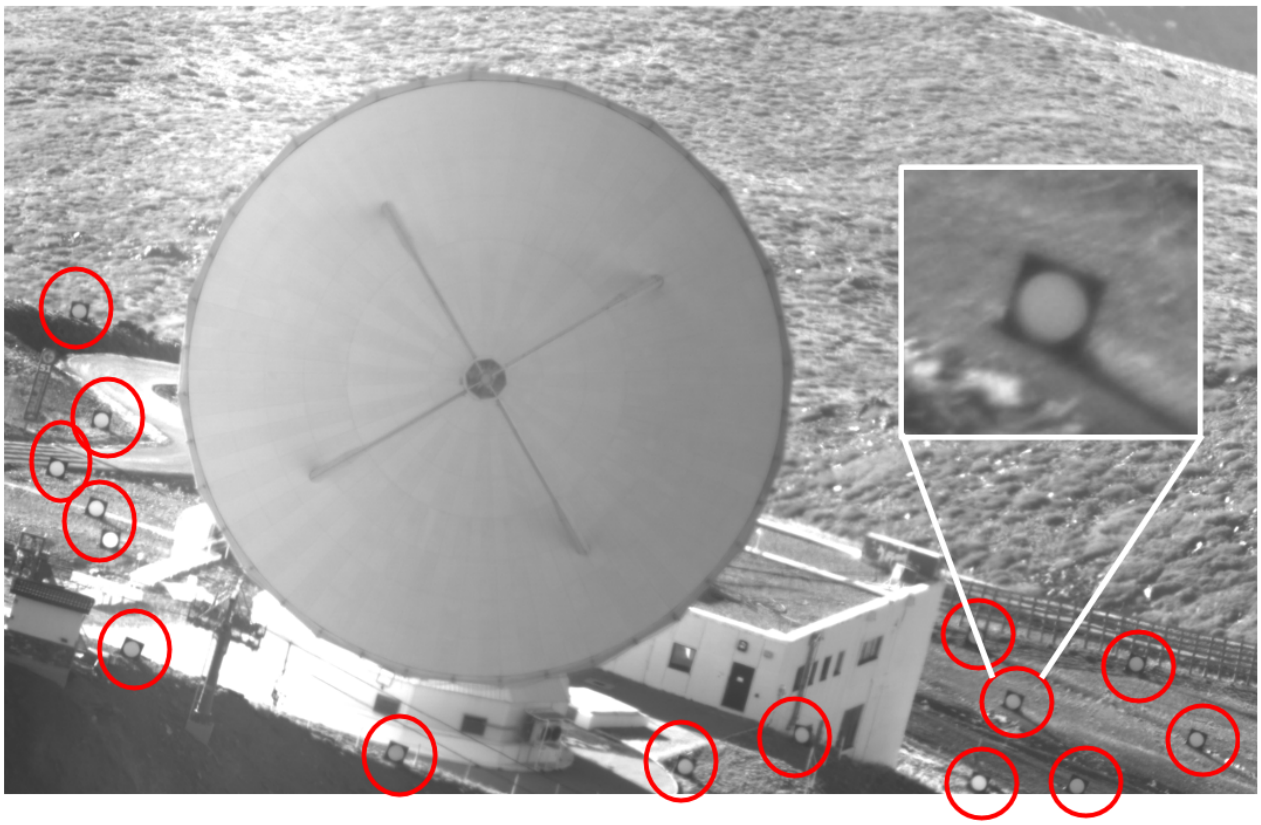

Figure 6.20: Image shot by the COSMOCal on-board camera, showing the targets identification. Realized by L. Bizzarri.

2 pixel spread and 6 cm/pixel resolution), compatible with RTK GPS uncertainties.
Applying the *solvePnP* solution with jackknife resampling, the yaw and pitch angles relative to the telescope line of sight were measured as:

$$\theta_{\text{yaw}} = (-0.1672 \pm 0.0012)^\circ \tag{6.24}$$

$$\theta_{\text{pitch}} = (0.0271 \pm 0.0020)^\circ \,. \tag{6.25}$$

The roll angle of the calibrator, after applying quality cuts (more than 12 targets identified and target 1 included), is:

$$\theta_{\text{roll}} = (-15.1865 \pm 0.0308)^\circ \,. \tag{6.26}$$

The uncertainty is dominated by GPS position measurement limitations.

Diffraction pattern The diffraction pattern analysis yields the orientation of the polarization in the camera plane for each polarizer position. The typical uncertainty on the diffraction pattern orientation for a fixed polarizer angle is:

$$\sigma_\theta \sim 0.01^\circ \,. \tag{6.27}$$

Combining photogrammetry and diffraction pattern analysis allows projection of the polarization orientation from the camera frame to the telescope line of sight, enabling a precise calibration of the polarization angle as seen by NIKA2.

6.4.7 Polarization measurements

Once the alignment was ensured, the main polarization measurements were conducted. This phase consisted in turning the COSMOCal polarizer by an arbitrary angle and acquiring a fix track scan for each orientation of the polarizer. The angles used in the following plots are the COSMOCal angles derived through the diffraction pattern analysis. Moreover, we adopted the AzEl convention for the coordinates, rather than the Nasmyth cabin's.

Malus law First, we want to verify the Malus law in total intensity and in polarized intensity. The Malus law describes the behavior of the intensity of a light beam as a function of the relative orientation with a polarizing filter. In the context of the COSMOCal campaign, this law is crucial for understanding the attenuation of light as it interacts with various polarizing agents in space. The intensity I of the transmitted light is related to the initial intensity I_0 and the angle φ between the light's polarization direction and the axis of the polarizer by the equation:

$$I = I_0 \cos^2(\varphi) \tag{6.28}$$

This relation helps to analyze how light is modified in different environments during the campaign. In Fig. 6.21, Malus law is demonstrated, both for total intensity ($left$) and polarized intensity ($right$), in all cases giving a phase $\varphi = 88.9^{\circ}$, consistent with the expected 90°. An average of the whole array has been taken to trace the data points.

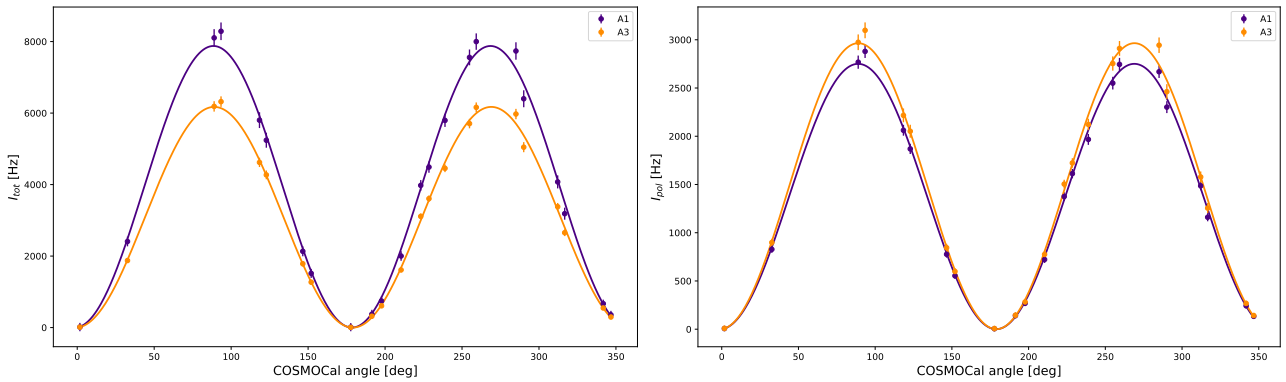

Figure 6.21: *Left*: average total intensity (Stokes I parameter) as a function of the rotational angle of COSMOCal's polarizer. *Right*: average polarized intensity ($\sqrt{Q^2 + U^2}$) again as a function of COSMOCal's polarizer rotation angle.

From these plots, we can see how A3 seems to be receiving less unpolarized intensity with respect to A1, while this effect is absent if we look at the polarized intensity. Moreover, if we compute the ratio between the fitted parameter I_0 for the polarized and unpolarized intensity, we can have an estimate of the polarization degree, as shown in Fig. 6.22.
We notice that the polarization degree is constantly around 40% for A1 and around 50% for A3, hence we witness a depolarization effect on the COSMOCal's signal, which is supposed to show a pure polarization. This could come from the field conditions with which these data were acquired: we are in the near-field, hence we are probably witnessing some reflection effects causing a partial depolarization of light.

Polarized intensity map across the focal plane An essential aspect of this analysis is examining the distribution of polarized intensity (I_{pol}) and polarization angle (ψ) across the focal plane to assess uniformity and response consistency. This evaluation is critical for understanding the performance and reliability of the COSMOCal system. Notably, certain

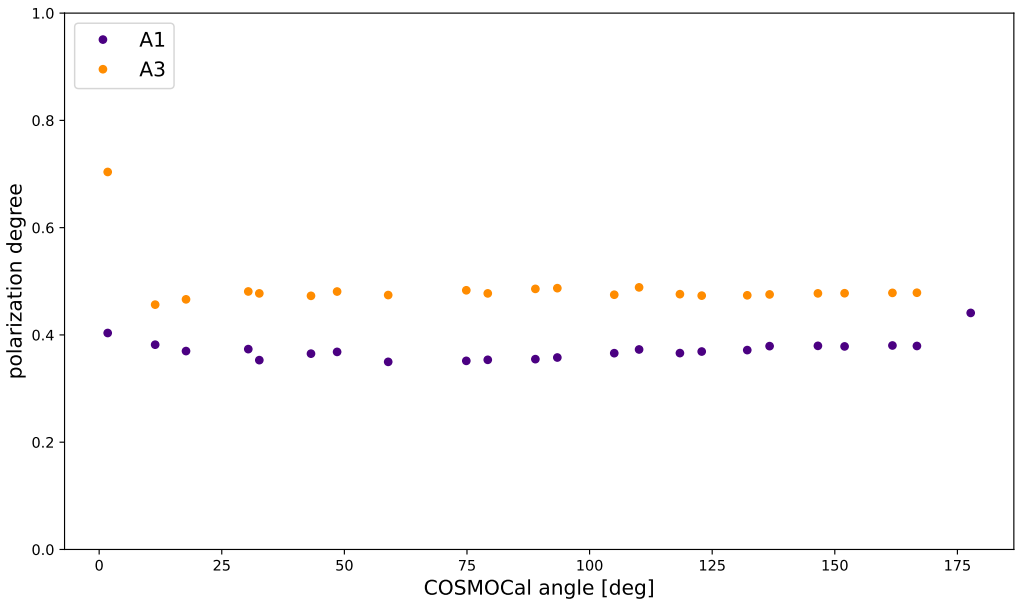

Figure 6.22: Polarization degree on A1 and A3 as a function of the COSMOCal angle.

KIDs within each array were excluded from the analysis due to suboptimal properties, such as high noise levels or other performance deficiencies. These exclusions ensure that the analysis focuses on detectors with reliable and accurate data.
In Fig. 6.23, the projected polarization maps for A1 in the top panel and A3 in the bottom panel are presented, corresponding to a selection of rotation angles of the COSMOCal polarizer: 0º, 45º, 90º, 135º and 180º. The maps illustrate the spatial distribution of polarized intensity across the focal plane, where each point represents a KID's response projected in the Nasmyth coordinate system.
From the visualizations, two key observations can be made. First, the polarization intensity adheres closely to the Malus' law behavior (Fig. 6.21). This confirms that the COSMOCal system responds predictably to changes in the polarization angle. Second, the polarization intensity is relatively homogeneous across the focal plane for both arrays. Such uniformity indicates that the system maintains consistent sensitivity across its detectors, aside from the excluded KIDs.

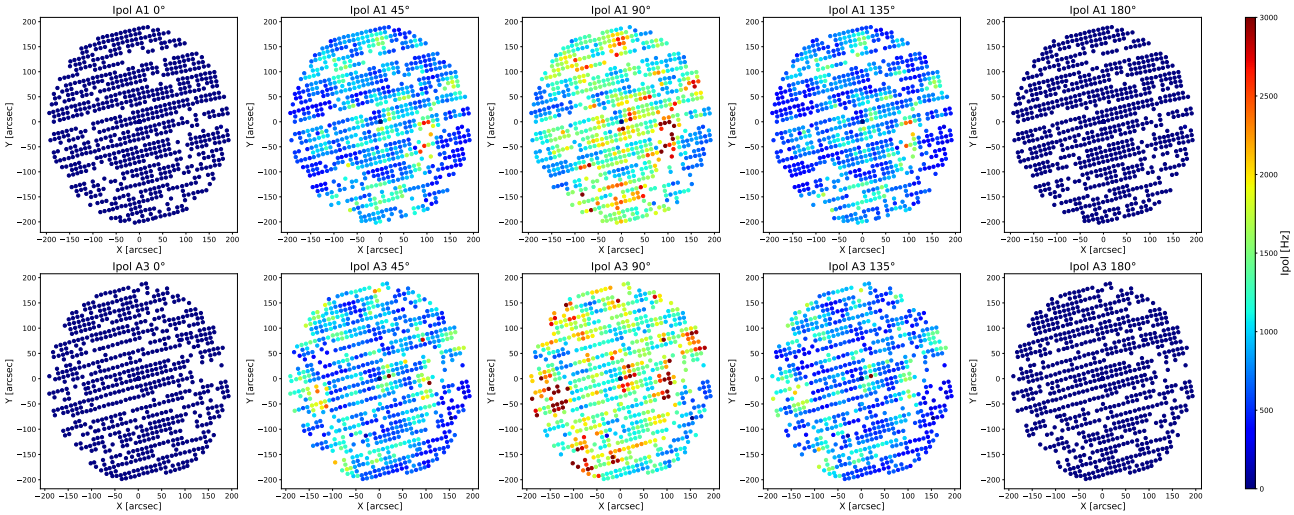

Figure 6.23: Maps of the polarized intensity of A1 (*top*) and A3 (*bottom*), for a sample of rotation angle of the COSMOCal polarizer (0º, 45º, 90º, 135º, 180º).

A similar map can be created for the polarization angle, which is the main targeted variable to characterize the polarization properties of the observed signal. The polarization angle has been computed directly from the Stokes parameters using its standard definition (Eq. 6.23). From the resulting maps (Fig. 6.24), we can observe the complementarity of the polarization angles seen by A1 and A3. This complementarity is expected, as it reflects the change in the polarization angle in accordance with the orientation of the COSMOCal polarizer, which alters the polarization state detected by each array. However, we also notice an unusual effect in the maps: the polarization angle is not uniform across the array, and there is a noticeable gradient in the distribution of the angle.

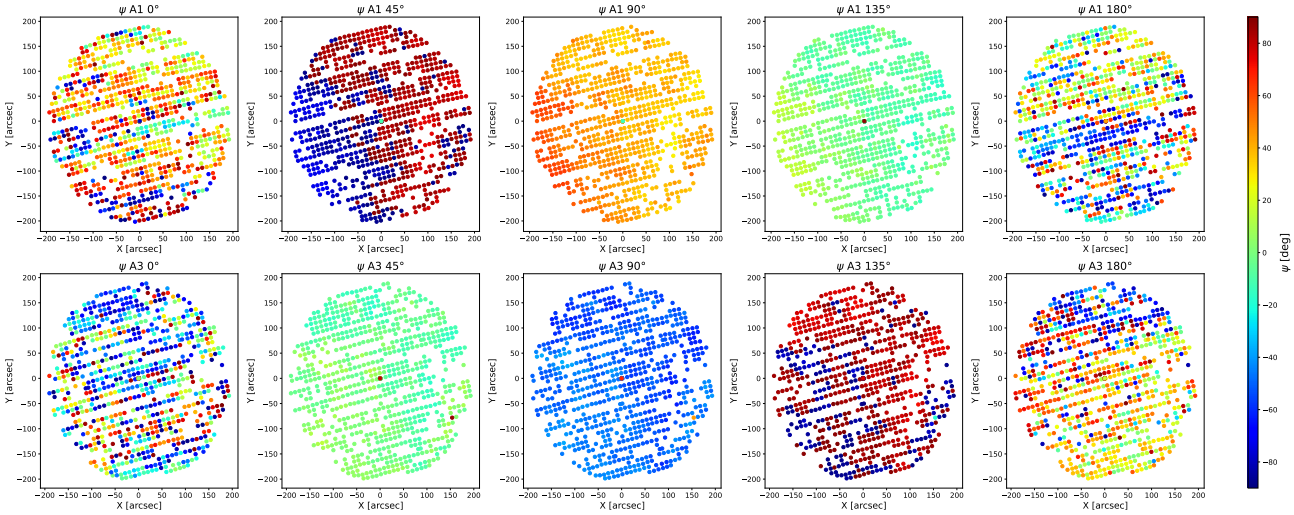

Figure 6.24: Maps of the polarization angle detected by A1 (*top*) and by A3 (*bottom*), for a sample of rotation angles of the COSMOCal polarizer (0º, 45º, 90º, 135º, 180º).

This gradient, particularly evident on A1, suggests the presence of spatial variations in the polarization characteristics, which might be indicative of systematic effects, instrumental artifacts or physical variations in the observed source. One potential explanation for this effect is to be attributed to the dichroic filter inside the NIKA2 cryostat. The dichroic is responsible for splitting the signal between the two channels at 1 and 2 mm. Due to inhomogeneities in its texture and prolonged utilization, the transfer of polarization might not be coherent across the whole focal plane, resulting in the observed gradient effect. Indeed, this effect was already noticed in the work of Perotto et al. [235]. We discussed how the recent NIKA2+ upgrade solved such issue in Chap. 5, Sec. 5.2, Subsec. 5.2.6.

NIKA2 vs COSMOCal polarization angle Despite the presence of this gradient across the focal plane, if we average the estimated polarization angle over all the pixels of each array individually and trace the polarization angles found by NIKA2 as a function of the angles obtained by the COSMOCal's internal reference system, we see in Fig. 6.25 a solid linear correlation. It is important to stress that the slope of these curves has been imposed to -1, in order to constrain all sources of uncertainty on the intercept alone.

Uncertainty on the polarization angle Providing a reliable estimate of the uncertainty on the polarization angle measured by NIKA2 was the main objective of this experimental campaign. Ideally, our goal was to determine the polarization angle with an uncertainty below 0.1°. However, obtaining such a precise and reliable estimate proved to be quite challenging. The Malus law fit, discussed in Subsec. 6.4.7, yields an angle of approximately 89°. It is, however, difficult to assess whether this result is significantly different from 90°—possibly reflecting

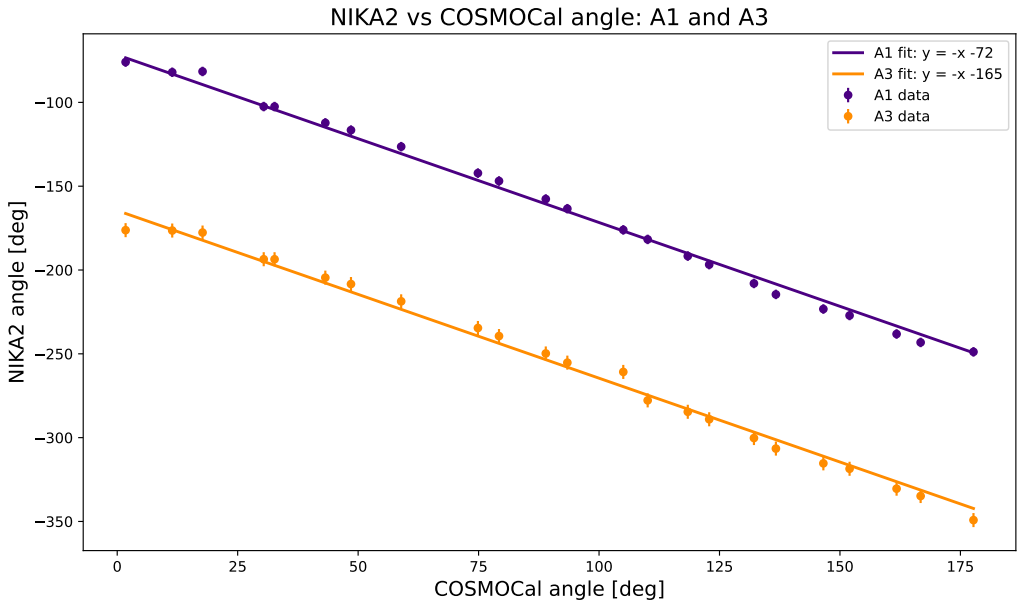

Figure 6.25: Values of the polarization angle ψ detected by NIKA2 as a function of the angles found by the internal independent COSMOCal's system.

a real offset between the assumed and true orientation of the polarizer—or whether it is statistically compatible with 90°. In any case, the result being close to 90° suggests that the rotating polarizer is quite well aligned with the COSMOCal reference direction.
Considering the dispersion of the reconstructed polarization angle across the entire focal plane, as shown in Fig. 6.24, we obtain a standard deviation of around 6°. When plotting the polarization angle ψ per array as a function of the COSMOCal angle (see Fig. 6.25), we observe that the angular difference between arrays A1 and A3 tends toward 93°, rather than the expected 90°. This holds true even when restricting the analysis to the best-performing KIDs and to the central pixels unaffected by the dichroic.
Taking into account the *a posteriori* derived error bars on each measurement, the uncertainty on the median angle for A1 is 0.4°, and for A3 it is 0.6°. This discrepancy suggests that either the statistical uncertainties are underestimated, or there is a residual systematic error affecting the measurement.
We also analyzed a second dataset acquired on 30/09/2024. However, the quality of this dataset was lower, and it did not help in constraining the overall uncertainty.
In the AzEl convention adopted here, the COSMOCal polarization direction should appear either at 0° or 90°, depending on the array. However, for A3, observed in transmission, we measure a deviation of 15° from the expected 180° value of the intercept. Part of this discrepancy can be attributed to an offset of 5.6° previously estimated through quasar observations. After subtracting this correction, a residual offset of about 9° remains unexplained.
Considering all these elements, we estimate a reasonable overall uncertainty on our polarization angle measurement to be approximately ±3°.

COSMOCal calibrator polarization angle measurement To compute the polarization angle of the emitted signal, as seen by the NIKA2 camera, we combine the photogrammetry results with the diffraction pattern ones. In particular, knowing that 1) the diffraction pattern orientation in the camera plane is defined with respect to the x axis, having positive values for counterclockwise rotations and 2) the photogrammetry roll angle is defined positive for counterclockwise rotations with respect to the y axis, we can compute the polarization angle of the signal as seen by NIKA2 as:

$$\psi = \frac{\pi}{2} - \theta_{\text{dp}} + \theta_{\text{roll}} \,. \tag{6.29}$$

According to the method described, the overall uncertainty on the polarization angle independent measurement performed by the COSMOCal calibrator is computed as:

$$\sigma_\psi = \sqrt{\sigma^2_{\text{DP}} + \sigma^2_{\text{roll}}} \,. \tag{6.30}$$

From the results obtained in Subsec. 6.4.6, it is immediate to notice how the uncertainty in Eq. 6.30 will be dominated by the roll angle determination accuracy. Indeed, the typical uncertainty on the polarization angle estimate is of the order of $\sim 0.035°$.
In particular, the obtained estimate of the polarization angle are compatible with the expected ones (according to the manual tilt of the polarizer) within a standard deviation of $\sim 2.6°$. However, this uncertainty is probably dominated by the human error in placing the filter in the correct position, since the graduated scale of the filter holder, thanks to which the manual rotation of the polarizer was quantified, had a resolution of 1°.

6.4.8 Final considerations on the campaign

Calibrator The results from the independent measurement of the polarization angle performed by the COSMOCal calibrator are really promising, however, there is still margin for improvement.
On the photogrammetry side, due to the restricted field of view of the optical refractor telescope on board, the amount of physical space to place the geo-referenced targets was limited. This translates in a looser constraint for the camera-to-world correspondence estimation, resulting in a spreader distribution of results. Therefore, by having a larger field of view of the on-board camera and a larger number of targets, we could definitely increase the accuracy of the attitude determination algorithm. In addition, both for photogrammetry and for the diffraction pattern, it could be useful to acquire videos and not pictures, to increase the statistical sample of acquired data.
Overall, the results obtained during this campaign are validating the reliability of the methods and the solutions proposed to provide an artificial calibrator able to retrieve an independent measurement of the polarization angle within the required accuracy of 0.1°.

Interface with NIKA2 The results obtained in terms of polarization data are quite encouraging, as they demonstrate the coherence of COSMOCal's system from multiple complementary perspectives: the internal reference frame determined by the analysis of the diffraction pattern, the photogrammetry and the analysis of the NIKA2 detectors. Notably, we find the expected 90° difference between the polarization angles determined by A1 and A3, along with a clear linear correlation between COSMOCal's and NIKA2's reconstructed polarization angles. However, the presence of a gradient across the focal plane complicates the determination of the true statistical error, as it is convolved with systematic errors induced by the dichroic. Localized error estimation for different regions of the focal plane could be an avenue for future work to address this challenge. Another limitation arises from the observational conditions we have. Specifically, we are operating in the near field, where reflection effects cannot be neither neglected nor fully controlled. In this setup, we observe an extended source with potential reflections and spurious effects interfering with the measurements. This is a key factor reflecting in the estimation of the polarization degree, only 50%, while it is supposed to be 100%. A reduced efficiency in the transmission by the HWP could not account for such a big reduction in COSMOCal's polarization degree. These combined factors currently prevent us from achieving the targeted precision of 0.1^{o} in the determination of the polarization angle.

These issues, however, are solvable, and efforts are ongoing in this direction. The gradient induced by the dichroic filter is expected to disappear with the replacement of the dichroic, which was carried out during the recent NIKA2+ upgrade in March 2025. This upgrade involved changes to the detector arrays and other optical components, including the problematic dichroic. On the other hand, resolving the near-field condition will require a different experimental setup, potentially with an alternative instrument that allows the COSMOCal calibrator to be positioned farther away, thereby better simulating space-like conditions.

6.5 Perspectives on Phases 2 and 3

Building on the successful completion of Phase 1, COSMOCal is now preparing for its next stages: the Qualification Model (Phase 2) and the Flight Model (Phase 3). Phase 2 will focus on developing the full COSMOCal calibrator in its space configuration, including a multi-frequency polarized source operating in the 90–300 GHz range. Although the instrument will still be tested on the ground, this phase will validate the design in conditions as close as possible to those of a space mission. This includes verification of optical performance, polarization accuracy, and thermal and mechanical stability. Concurrently, ongoing R&D at LPSC on linear polarizers aims to optimize the system for Phase 2 and the eventual space deployment.
Phase 3 corresponds to the Flight Model, i.e. the actual launch of the COSMOCal calibrator into geostationary orbit. To support this ambitious goal, a collaboration with CNES has been established. This partnership provides access to their expertise in space mission design and engineering, enabling the project to leverage existing infrastructure, spacecraft integration knowledge, and operational support. The discussions held earlier this year suggest that COSMOCal could realistically enter CNES Phase A as early as next year, marking a critical step towards an operational space-based calibration system.
These next phases represent both technical and scientific opportunities: they will allow testing and validation of the instrument under near-space conditions, provide access to flight-like data, and strengthen collaborations within the cosmology and space science communities.

6.6 Conclusions

Overall, Phase 1 of the COSMOCal project can be considered a success. The in-lab proof-of-concept campaign conducted at LPSC in Grenoble in February 2024 marked the first light of the COSMOCal millimeter source and its initial detection by a KID array. During this campaign, we completed a full set of measurements, testing three different orientations of the COSMOCal polarizer and determining the polarization angle with an uncertainty better than 1°. Some limitations arose due to reflections of the strong COSMOCal signal within the laboratory environment, which slightly affected certain measurements.
The subsequent IRAM 30m test campaign also yielded valuable results. We successfully executed the full planned observational program, acquiring a substantial dataset that enabled a meaningful analysis of polarization angle reconstruction. Despite applying a detailed and tailored data reduction procedure, the polarization angle could only be determined to within $\sim 3°$. This limitation is primarily due to the NIKA2's dichroic gradient and the near-field configuration, where reflections and other effects alter the polarization state of the emitted light. A significant portion of the campaign was dedicated to ensuring precise alignment between the source and the telescope, which proved non-trivial but provided important practical insights. Overall, the campaign highlighted the inherent challenges of near-field testing and reinforced the scientific rationale for a space-based calibration source.

Chapter 7

LEKIDs for dark matter search: the DANDELION experiment

Contents

7.1 Dark photons as a dark matter candidate **178**
7.1.1 The dark photons physics 179
7.1.2 meV dark photons as a window towards the Early Universe 179
7.1.3 State-of-the-art on dark photon detection 180
7.2 The DANDELION experiment **181**
7.2.1 Experiment baseline 181
7.2.2 The instrumental setup 181
7.2.3 Background and noise mitigation 182
7.2.4 Measurement strategy 183
7.2.5 Signal modeling 184
7.2.6 Expected sensitivities 186
7.3 DANDELION first data run **187**
7.3.1 Raw detected signal 188
7.3.2 Displacement of the signal on the focal plane 189
7.3.3 PCA-based background modeling and signal extraction 189
7.3.4 Exclusion curves on the χ parameter 190
7.4 Conclusions and perspectives **191**

Abstract The cryogenic platform developed at LPSC, originally designed for millimeter-wave polarization studies, has proven to be highly versatile, enabling experimental investigations beyond its initial scope. In particular, the platform was required to be employed by the dark matter team at LPSC to search for dark photons (DPs), a compelling dark matter candidate. This led to my involvement in the DANDELION experiment, a novel dish-antenna setup aimed at detecting DPs with masses around the meV scale.
In DANDELION, standard millimeter photons produced via the kinetic mixing of dark photons on the surface of a spherical mirror are detected by a 400-pixel LEKID array cooled to 150 mK. The mirror is periodically tilted at 1 Hz, shifting the expected signal across the array and enabling continuous background measurement. The signal exhibits two distinct modulations: a spatial modulation, providing a directional signature for unambiguous DP detection, and an intensity modulation, allowing the determination of the DP polarization. For DP masses near the meV, the inflationary production of longitudinal and transverse modes are mutually exclusive, making polarization measurements with DANDELION a potential probe of the inflationary phase of the early Universe.
In this chapter, we introduce dark photons as a current perspective in dark matter searches, present the DANDELION instrumental setup, outline the data acquisition strategy, and describe the analysis of the first 24-hour data run.
My personal contributions focused on the conception and installation of the setup, the supervision of data acquisition during the campaigns, and the initial stages of data processing, including raw data reduction and calibration. The subsequent scientific analysis was carried out by Ilias Ourahou, a PhD student in the Theoretical Physics group at LPSC under the supervision of Daniel Santos. While a detailed description of the physical principles and experimental design is provided in Beaufort et al. 2024 [29], the latest results will be presented in Ourahou et al. 2025 (in preparation).

7.1 Dark photons as a dark matter candidate

The nature of Dark Matter (DM) remains one of the most pressing open questions in modern physics. Observational evidence from galactic rotation curves, gravitational lensing, cosmic microwave background measurements, and large-scale structure formation indicates that DM constitutes approximately 27% of the total energy density of the Universe (Bertone et al. 2005 [38]). Despite its pervasive influence on cosmic structures, the particle nature of DM remains unknown.
Over the past decades, numerous candidates have been proposed, ranging from Weakly Interacting Massive Particles (WIMPs) and axions to sterile neutrinos and other exotic species (Jungman et al. 1996 [157], Marsh 2016 [190]). Experimental searches have employed a variety of strategies, including direct detection, indirect detection through astrophysical signals, and production in particle colliders. While significant effort has focused on WIMPs, the absence of unambiguous signals in increasingly sensitive experiments has motivated the exploration of alternative candidates, including light bosonic particles such as dark photons (Arias et al. 2012 [14]).
Dark photons (DP) are hypothetical gauge bosons associated with a hidden $U(1)$ symmetry that can kinetically mix with ordinary photons, providing a potential avenue for laboratory detection (Pospelov et al. 2008 [259]). Their low mass and weak interactions make them attractive targets for novel direct detection experiments, complementing traditional searches for dark matter and offering new insights into the dark sector.
Direct detection of dark matter (DM) particles generally relies on complementary strategies aimed at probing the broad spectrum of hypothesized DM candidates (Billard et al. 2022 [43]). While the observation of a DM-like signal in a detector would represent a major breakthrough,

conclusively demonstrating that such a signal originates from local DM remains a challenging task, often deferred to future investigations. Directional detection provides a promising solution by designing experiments capable of identifying unmistakable DM signatures that can be clearly distinguished from background noise. This method exploits the correlation between the detected signal and the motion of the detector through the galactic DM halo, enabling a robust identification of true DM events (Spergel et al. 1988 [284], Mayet et al. 2016 [193]).

7.1.1 The dark photons physics

The dark photon is a hypothetical massive spin-1 boson predicted by extensions of the Standard Model (SM) that introduce a new U(1) symmetry under which SM fields are uncharged (Jaeckel et al. 2010 [155], Fabbrichesi et al. 2020 [110]). Various cosmological production mechanisms, both thermal and non-thermal, make the DP a compelling cold DM candidate (Nelson et al. 2011 [215], Graham et al. 2016 [127], Bastero-Gil et al. 2019 [27]). Additionally, the DP serves as an effective vector portal to the dark sector (Alexander et al. 2016 [9]). Being the gauge boson of an Abelian U(1) symmetry, it interacts with the standard photon via kinetic mixing, described by:

$$\mathcal{L} = -\frac{1}{4}F_{\mu\nu}F^{\mu\nu} - \frac{1}{4}X_{\mu\nu}X^{\mu\nu} - \frac{\chi}{2}F_{\mu\nu}X^{\mu\nu} + \frac{1}{2}m_X^2 X_\mu X^\mu + eJ^\mu_{\rm em}A_\mu\,, \tag{7.1}$$

where A_μ and X_μ are the photon and DP fields, $F_{\mu\nu}$ and $X_{\mu\nu}$ their field strengths, J^{em}_μ is the electromagnetic current, χ quantifies the kinetic mixing, m_X is the dark photon mass and e is the electric charge coupling constant.
Experiments have placed constraints on DPs, but for masses near 1 meV, the kinetic mixing parameter remains poorly bounded (Caputo et al. 2021 [55]). A DP mass around 1 meV offers an opportunity to distinguish between production mechanisms, making it an important probe of early Universe physics. Recent efforts aim to improve sensitivity in this range (Redondo et al. 2008 [261], Ehret et al. 2010 [98], Knirck et al. 2018 [166]), with projects like BREAD (BREAD collaboration 2022 [183]) planning significant advancements.

7.1.2 meV dark photons as a window towards the Early Universe

A population of DPs capable of accounting for the DM abundance can be produced through various non-thermal mechanisms, such as gravitational production during Inflation (Graham et al. 2016 [127], Ema et al. 2019 [101], Ahmed et al. 2020 [7], Kolb et al. 2021 [168]), parametric resonance (Bastero-Gil et al. 2019 [27], Agrawal et al. 2020 [5], Co et al. 2019 [68]), dark Higgs dynamics (Sato et al. 2022 [274], Redi et al. 2022 [260]), or cosmic strings from the breaking of the Dark U(1) symmetry (Long et al. 2019 [185], Kitajima et al. 2023 [165]). These mechanisms allow for a meV DP candidate, each with distinct cosmological implications. We focus on inflationary production, comparing longitudinal and transverse DPs.
Inflationary production of longitudinal modes requires $0 < m_X < H_I$, with H_I as the inflationary scale. For instant or fast reheating ($m_X < H_{\rm RH}$), their abundance, normalized to DM today, is (Graham et al. 2016 [127]):

$$\frac{\Omega_L}{\Omega_{\rm DM}} \simeq \sqrt{\frac{m_X}{\rm meV}}\left(\frac{H_I}{2.7\times10^{13}\ {\rm GeV}}\right)^2\,. \tag{7.2}$$

For late reheating ($m_X > H_{\rm RH}$), the abundance depends on the equation of state w (Ema et al. 2019 [101], Ahmed et al. 2020 [7], Kolb et al. 2021 [168]):

$$\frac{\Omega_L}{\Omega_{\rm DM}} \simeq \left(\frac{m_X}{0.33\ {\rm GeV}}\right)^{2w/(1+w)} \left(\frac{H_I}{3.3\times10^{10}\ {\rm GeV}}\right)^2 \left(\frac{2.1\times10^9\ {\rm GeV}}{T_{\rm RH}}\right)^{(3w-1)/(1+w)} . \tag{7.3}$$

This mechanism requires large-scale inflation ($H_I \sim O(10^{13})$ GeV), producing a detectable tensor-to-scalar ratio, $r \sim O(10^{-2})$, constrained by current observations. In contrast, transverse DP production involves tachyonic instability with the coupling $\mathcal{L}_{\rm inf} = -\alpha_V \phi X_{\mu\nu}\tilde{X}^{\mu\nu}/f$, where ϕ is the Inflaton (Bastero-Gil et al. 2019 [27], Bastero-Gil et al. 2022 [28]). The abundance depends on $\xi_{\rm end}$ (controlling tachyonic efficiency) and reheating details:

$$\frac{\Omega_T}{\Omega_{\rm DM}} \simeq 2\times10^{-13} \left(\frac{m}{\rm meV}\right) \left(\frac{H_{\rm end}}{10^{12}\ {\rm GeV}}\right)^{3/2} \left(\frac{10^{-1}}{\epsilon_R}\right)^3 \frac{e^{2\pi\xi_{\rm end}}}{\xi_{\rm end}^3} . \tag{7.4}$$

Efficient production occurs for $\xi_{\rm end} \gtrsim 6$. Transverse modes also source parity-violating GW, peaking at high frequencies (O(MHz)) for $H_{\rm end} \sim O(10^{13})$ GeV (Sorbo et al. 2011 [283], Anber et al. 2012 [11], García-Bellido et al. 2016 [121], Bastero-Gil et al. 2023 [26]). Detectability of this spectrum remains uncertain.

To summarize, longitudinal and transverse production mechanisms are mutually exclusive for a meV DP and correspond to distinct cosmological signatures. Longitudinal production predicts a detectable r, while transverse modes may yield high-frequency GW signals. The DANDELION experiment could determine DP polarization, ruling out one of these mechanisms. However, cosmological evolution may mix polarizations, leading to a random DP background today. A detailed study of polarization conversion lies beyond the scope of this work.

7.1.3 State-of-the-art on dark photon detection

A prominent class of experiments targets dark photon dark matter (DPDM) in the ultra-light mass range ($\sim 10^{-22}$ eV to 1 eV), where the dark photon behaves as a classical, oscillating field. Experiments such as CROWS (CERN Resonator Oscillator Weakly-interacting Sub-eV Particle Search) use resonant microwave cavities to detect dark photons converting into ordinary photons via kinetic mixing. The CROWS setup has placed strong constraints on χ in the μeV to meV range (Betz et al. 2013 [40]).

Laboratory tests of Coulomb's law offer another detection approach. In the presence of a massive hidden photon, electrostatic forces between charges would deviate slightly from the inverse-square law. Cavendish-type experiments, originally designed to test the validity of Coulomb's law with high precision, have been repurposed to set upper limits on χ for very light dark photons with masses below $\sim 10^{-14}$ eV.

A different class of searches focuses on solar dark photons, produced via kinetic mixing in the Sun's interior and subsequently detected on Earth. These so-called helioscope experiments include SHiPS (Solar Hidden Photon Search), which uses a vacuum tube aligned with the Sun to detect photons regenerated from solar dark photons (SHiPS collaboration 2021 [281]). Other solar-related searches such as CAST (Anastassopoulos et al. 2015 [10]) and FUNK (FUNK collaboration 2017 [109]) employ magnetic or optical components to enhance the detection probability, probing dark photons in the $\sim 10^{-5}$ eV range.

Collectively, these experimental efforts cover a wide portion of the dark photon parameter space. While no dark photon signal has yet been observed, increasingly sensitive measurements have allowed experiments to set competitive exclusion limits on the kinetic mixing parameter χ. The diversity of methods (resonant cavities, precision force measurements, and solar flux detection) ensures that the experimental landscape continues to evolve rapidly, probing new regions of parameter space and guiding future searches.

7.2 The DANDELION experiment

DANDELION stands for DArk photoN DirEctionaL detectION. Similar to how the pappus of a dandelion drifts with the wind, DANDELION aims to trace the direction of the dark photon wind, attributed to the Earth's motion through the DM halo. The conversion surface facilitating the transformation of DPs into standard photons is a spherical aluminum mirror.

7.2.1 Experiment baseline

Our experiment introduces a key innovation: the use of a directional detection strategy to identify DPs. This approach, based on the dish antenna concept (Horns et al. 2013 [146]), employs a spherical metallic mirror as a conversion surface to transform DPs into photons. These photons focus on a detector at a distance R from the mirror, corresponding to the mirror's curvature radius. Emissions deviate by an angle $\psi = |p_{||}|/m$, where $p_{||}$ is the DP momentum parallel to the surface, creating a spatial modulation correlated with the detector's motion through the galactic DM halo (Jaeckel et al. 2013 [154]).
The DP-induced photon power at time t and position (x, y) on the detector is given by (Horns et al. 2013 [146]):

$$P(x, y, t; E_\gamma) = \chi^2 \rho_{\rm CDM} \eta(E_\gamma) A_{\rm mirr.} I(x, y, t) \cos^2 \alpha(t)\,, \tag{7.5}$$

where $\rho_{\rm CDM}$ is the local DM density, $\eta(E_\gamma)$ is the photon detection efficiency, $A_{\rm mirr.}$ is the mirror's area, $I(x, y, t)$ is the normalized signal spread, and $\alpha(t)$ is the angle between the DP polarization and the mirror tangent. The working principle just described is represented in Fig. 7.1.

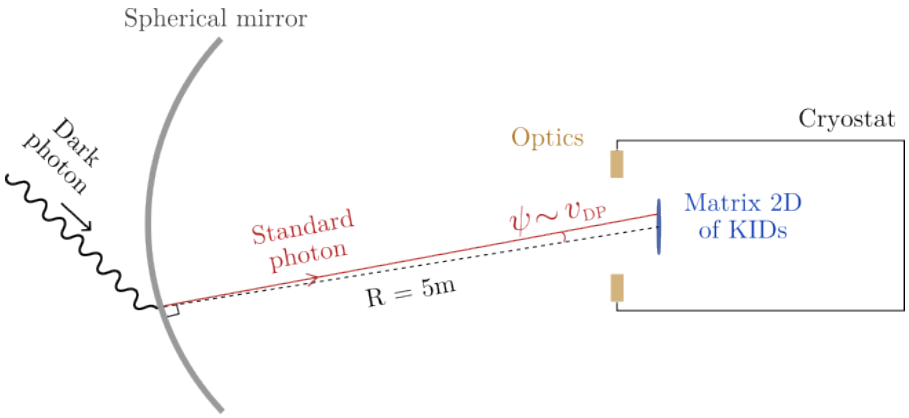

Figure 7.1: Schematics of the working principles of the DANDELION experiment.

7.2.2 The instrumental setup

The setup employs a spherical mirror with a curvature radius of $R = 5$ m and an aperture diameter of $D = 50$ cm. For such a mirror, incident photons parallel to the optical axis converge at $R/2$, as commonly observed in astrophysical measurements, whereas photons emitted perpendicularly to the surface focus at R. This distinction ensures that DP-induced photons and reflected ambient background photons do not converge at the same point. Therefore, the detector is positioned at a distance R from the mirror. The experiment is conducted in LPSC's cryogenic lab in Grenoble, France, at a latitude of 45.1° and a longitude of 5.7°. The mirror faces North-West, tilted at an angle of 48° with respect to the North. These coordinates will be essential in Subsec. 7.2.5 for modeling the directional signal.

The detector comprises a matrix of LEKIDs arranged in a disk of diameter 6.5 cm, consisting of 400 pixels, each measuring 2.8×2.8 mm^2. This array is one of the two whose characterization is described in Chap. 3, Sec. 3.6, while the cryogenic facility is the same used for measurements of Chap. 4. The detection efficiency of the KIDs, $\eta(E_\gamma)$, peaks at 250 GHz (corresponding to 1 meV) and exceeds 50% within the range of 200 to 300 GHz. Optical components optimize the focus on the KIDs. To ensure proper alignment between the detector and the mirror, an optical laser located at the mirror's center, where a hole has been drilled, is used for initial checks. To minimize alignment uncertainties, the mirror is mechanically fixed to the cryostat. The mechanical connection is assured by a solid metallic structure that encapsulates both the cryostat and the mirror. Fig. 7.2 presents a CAD model of the setup on the left and the corresponding real installation in LPSC's cryogenic lab on the right.



Figure 7.2: *Left:* CAD (Computed-Assisted Design) of the experimental setup; the cryostat hosting the detector is tight to the mirror by a mechanical structure. *Right:* top view of the experimental setup installed in the cryogenic laboratory at LPSC, showing the arrangement of the instruments and the configuration of the optical system.

7.2.3 Background and noise mitigation

The primary source of background in the experiment is thermal radiation. This background contribution is minimized by the optics placed in front of the KIDs matrix. Specifically, the input pupil is designed to be smaller than the mirror's aperture at a distance R, as illustrated in Fig. 7.3. The reflected signal from the mirror's surface is maintained at 150 mK, corresponding to the camera's temperature.
To suppress $1/f$ noise, a synchronous modulation technique is employed. The mirror is tilted by 5 mrad at a frequency of 1 Hz around its vertical axis, perpendicular to the mirror's main axis, using a motor. This tilting motion shifts the expected signal spot by 2.5 cm, moving the signal out of the central pixels and focusing it on other pixels of the KIDs matrix. This modulation occurs at a sufficiently high frequency such that the background can be considered constant during each cycle. As a result, the noise for each pixel is continuously measured and subtracted, enabling the extraction of the signal with improved accuracy.
Using Planck's law, the thermal background, arising from emission and reflection, can be calculated for a single pixel of the detector, allowing the determination of the optical NEP. In essence, the NEP represents the lowest power distinguishable from the system's own noise background. In our setup, this background is dominated by thermal emission from the optical system. The total power received by a pixel includes the contribution from the mirror, attenuated by the optical transmission, and the self-emission of the optics, modeled as:

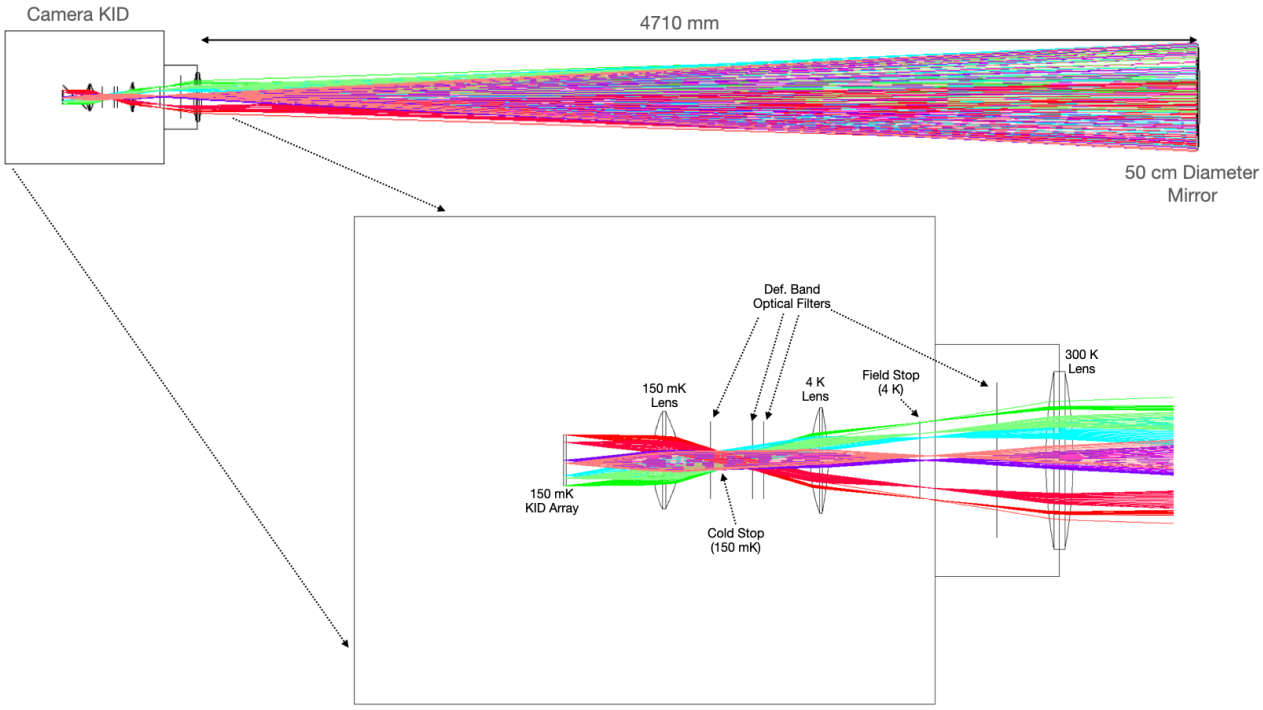

Figure 7.3: DANDELION optical design (Zemax software) with details of the cold optics inside the cryostat. Inverse ray tracing simulation from detectors to the 50 cm diameter mirror. Detector illumination is constrained inside the mirror in order to minimize the thermal loading.

$$P_{\text{total}} = A\Omega \int_{\nu_{\text{min}}}^{\nu_{\text{max}}} \left[\eta(\nu)H(\nu)B(\Delta T + \epsilon_{\text{ALT}}T_{\text{mirror}}, \nu) + (1-\eta(\nu))H(\nu)B(T_{\text{lens}} = 300\text{ K}, \nu)\right] d\nu\,, \tag{7.6}$$

where $A\Omega$ is the throughput, $\eta(\nu)$ the transmission efficiency, $H(\nu)$ the spectral response, $B(T, \nu)$ the Planck function, and ϵ_{ALT} the mirror emissivity. The lens temperature is assumed to be 300 K.
Detector sensitivity is fundamentally limited by statistical fluctuations in this thermal background, known as photon noise. The photon-limited NEP is expressed as:

$$\text{NEP}_{\text{photon}} = \sqrt{2h\Delta\nu\, P_{\text{total}}}\,, \tag{7.7}$$

where h is Planck's constant, and $\Delta\nu$ the bandwidth. Using our thermal and optical model, we compute the photon-limited NEP for both mirror positions:

$$\text{NEP}_{\text{photon},\,m1} = 1.65 \times 10^{-16}\ \text{W}/\sqrt{\text{Hz}} \tag{7.8}$$

$$\text{NEP}_{\text{photon},\,m2} = 1.64 \times 10^{-16}\ \text{W}/\sqrt{\text{Hz}}\,. \tag{7.9}$$

These values establish the baseline sensitivity of our detector in each configuration.

7.2.4 Measurement strategy

Two data sets were collected with this experimental setup, the first in January 2024 and the second in October 2024. The initial acquisition lasted for 24 consecutive hours, while the second covered a full week of continuous operation. Both data sets were obtained using the electronic readout system described in Chap. 4. We present here only the results of the 24-hour

run, as the analysis of the longer data set is still ongoing. A tilting mirror, controlled by a precision motor, was integrated into the setup. The motor initiates the mirror's movement and maintains continuous operation throughout the measurement duration, ensuring a stable and reliable modulation of the optical signal. The KIDs camera is continuously acquiring data in the meantime.

7.2.5 Signal modeling

This section explores the characteristics of the expected signal, including its spatial and intensity modulations, and the design choices for optimizing detection efficiency. Three different features of the signal behavior are analyzed separately: the diffraction produced by the image on the focal plane, the spatial modulation of the signal on the focal plane, meaning its local displacement, and the intensity modulation.

Diffraction Diffraction imposes a key limitation for dish antennas detecting DPs with masses below 100 meV. Using the Huygens-Fresnel principle, the electric field at the KIDs plane, $E(x, y, R)$, is related to the mirror's surface field, $E(x', y', 0)$, by (Goodman 2005 [126]):

$$E(x,y,R) \simeq \frac{e^{-ikR}}{i\lambda R} \int_{\text{mirr.}} dx'dy' E(x',y',0) e^{i\phi(x',y')} \exp\left(-i\frac{k}{2R}[(x-x')^2+(y-y')^2]\right), \quad (7.10)$$

where $k = m/(\hbar c)$ is the wavenumber, and $\phi(x', y')$ accounts for the mirror's geometry. Numerical evaluation shows that the diffraction causes a limited spread, with one-third of the signal contained within 5 pixels and two-thirds within 13 pixels. Fig. 7.4 illustrates the spread on the KID array on the left, and the intensity of the signal projected along the radial component on the right.

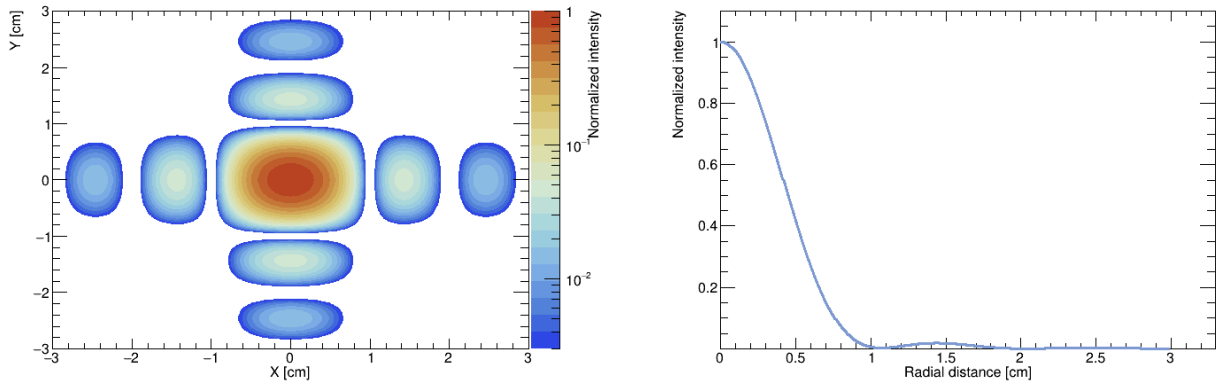

Figure 7.4: The diffraction of the signal at the readout plane in 2D representation (left) and projected along the radial component (right).

This information is crucial from an experimental point of view: in fact, knowing the configuration of the array and its KIDs' distribution, we can adapt the location and distribution of the signal accordingly.

Spatial modulation The spatial displacement of the signal on the focal plane is another key aspect of this kind of measurement. In fact, the spatial modulation of the signal can be seen as the actual directional signature of dark photons. Spatial modulation arises from the angle $\psi = |p_{\parallel}(t)|/m$, determined by the velocity vector of the DP in the mirror frame, $-\vec{v}_{\text{lab}}$, and its

projection on the mirror tangent. Fig. 7.5 demonstrates a simulated modulation over 50 hours, showing:

- Pixel-level shifts in X and Y, spanning 1–2 pixels
- A 24-hour periodicity with 12-hour extrema
- A 2-hour delay between X and Y extrema

The 24-hour periodicity is clearly a consequence of the Earth's rotation along its axis. The 2-hour delay between the X and Y extrema arises from the relative orientation of the experimental setup with respect to the Earth's rotation and the galactic DM wind. As the Earth rotates, the laboratory frame moves relative to the DM halo, causing periodic variations in the DP velocity components along the X and Y directions. The phase difference reflects the alignment of the mirror and its tilt angle, leading to an asymmetric projection of the velocity vector onto the detector plane. This delay is a direct consequence of the experiment's geometric configuration and the interplay between the Earth's motion and the galactic wind. This directional modulation, derived from the hypothetical DM halo, is distinct from any background signal.

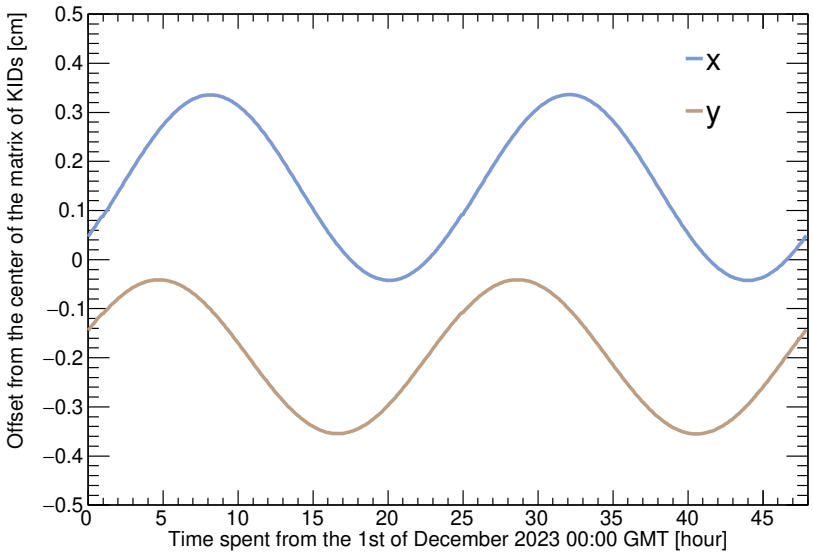

Figure 7.5: The expected spatial modulation for a 50h-long measurement starting on January 2023. Based on the modeling of Bozorgnia et al. 2011 [49].

Intensity modulation The signal intensity modulates as $\cos^2\alpha(t)$, where $\alpha(t)$ is the angle between the DP polarization and the mirror tangent. The time-averaged value, $\langle\cos^2\alpha(t)\rangle_T$, is used for analysis, with detailed motion modeling in Appendix A of Beaufort et al. 2024 [29]. Unlike Caputo et al. 2021 [55], this study adopts the galactic frame for better integration with spatial modulation. Fig. 7.6 compares $\langle\cos^2\alpha(t)\rangle_T$ and $\cos^2\alpha(t)$ for random and fixed DP polarizations: for random polarization, $\langle\cos^2\alpha(t)\rangle_T$ stabilizes at 2/3 for $T > 1$ day; instantaneous $\cos^2\alpha(t)$ shows two maxima and minima daily; fixed polarization scenarios exhibit greater variability in minima.
While intensity modulation provides insight into DP polarization, spatial modulation offers a stronger directional signature. From an experimental point of view, we will mostly focus on the spatial modulation features.

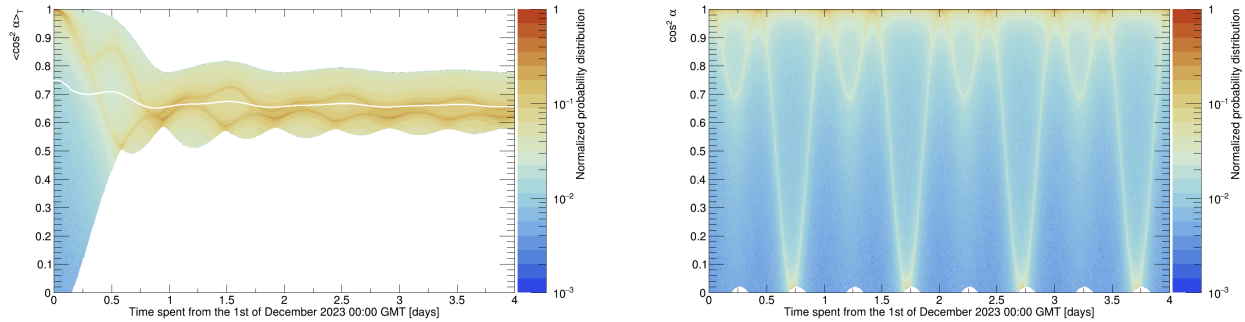

Figure 7.6: Time evolution of the probability distribution for the time-averaged $\langle \cos^2 \alpha(t) \rangle_T$ (left) and $\cos^2 \alpha(t)$ (right), where $\alpha(t)$ is the angle between the DP polarization and the tangent of the mirror. The probability distributions are normalized such that their maxima are equal to unity. The plots are based on 10^5 DP polarizations randomly sampled from an isotropic distribution in the galactic frame. In the left plot, the white curve represents the distribution of the mean value at each time.

7.2.6 Expected sensitivities

We now have all the necessary ingredients to evaluate the DP signal power, adopting a local dark matter density of $\rho_{\rm CDM} = 0.45\,{\rm GeV/cm}^3$ for consistency with other searches (Caputo et al. 2021 [55]). The signal distribution on the focal plane, $I(x, y, t)$, includes both diffraction and spatial modulation, and is normalized to unity at each time step. Its temporal dependence, together with $\cos^2 \alpha(t)$, is computed numerically to account for the motion of the detector through the galactic halo.
For an integration time T, the signal collected on a pixel (i, j) is defined as

$$S_{ij} = \frac{1}{T} \int_0^T dt \int_{\rm pixel} dx\, dy\, P(x, y, t)\,, \tag{7.11}$$

where the spatial integral is restricted to the pixel area. The noise level is assumed uniform and given by the NEP, such that the background after an integration time T is $B_{ij} \approx {\rm NEP}/\sqrt{T}$. A region of interest (ROI) is chosen around the 13 pixels with the highest expected signal. A detection is claimed when the total signal in the ROI exceeds the background by 5σ:

$$\frac{\sum_{i,j} S_{ij}}{\sum_{i,j} B_{ij}} > 5\,. \tag{7.12}$$

Beyond exclusion limits, DANDELION exploits the spatial modulation of the signal for discovery potential. The modulation radius $r(t)$ defines time intervals corresponding to minimum and maximum displacements, allowing the comparison of signals S^{min} and S^{max} in the same pixels. A directional detection requires that both are individually above 5σ and differ significantly:

$$\left| 1 - \frac{S^{max}}{S^{min}} \right| > 5\,. \tag{7.13}$$

If a signal is established, polarization properties can also be probed. In particular, the time evolution of $\langle \cos^2 \alpha(t) \rangle$ over a 6-hour interval provides a discriminator: random polarization yields $\langle \cos^2 \alpha \rangle \simeq 2/3$, whereas fixed polarization produces variations up to a factor of 5. A conservative condition is set by requiring the signal difference between two time bins to exceed twice the background.
The projected sensitivities of DANDELION for a 30-day run are shown in Fig. 7.7. The experiment could improve existing limits around the meV mass scale by more than an order of

magnitude, providing unprecedented discovery potential and enabling polarization discrimination. Compared to Tokyo-2 [166], which lacks directional information, DANDELION explores a significantly larger parameter space.

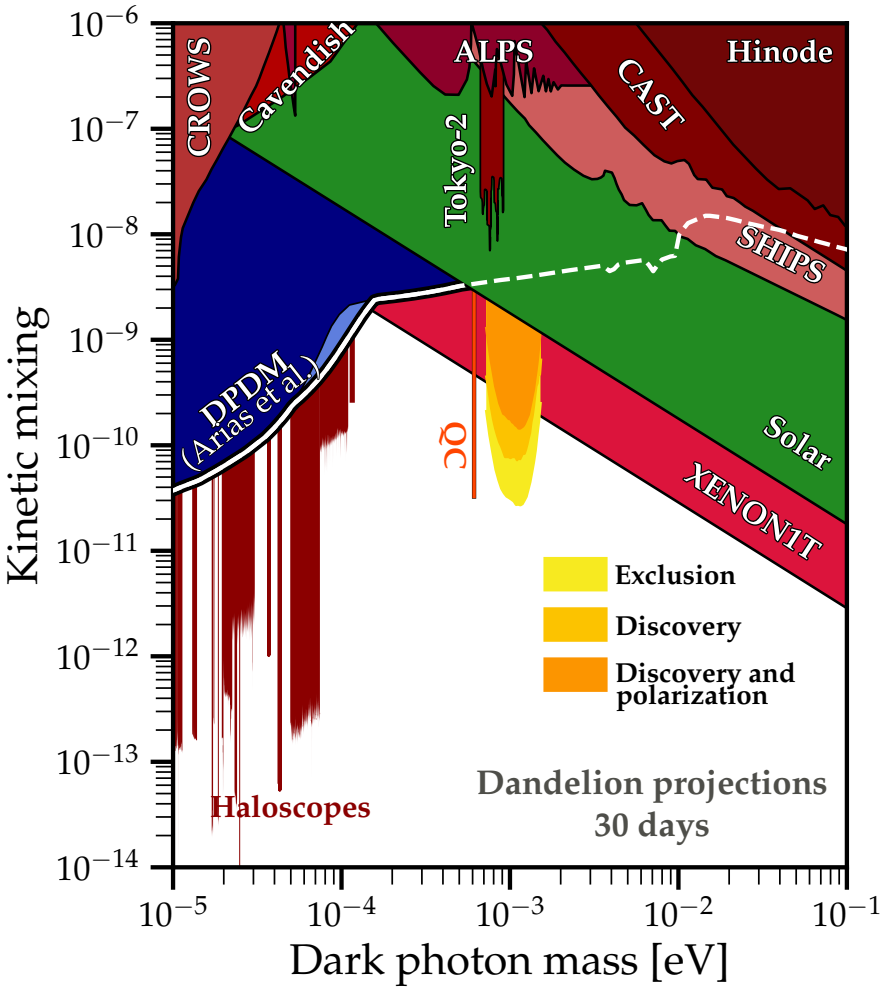

Figure 7.7: The expected sensitivities for the DANDELION prototype running for 30 days. We show the exclusion limits, the discovery potential, and the discovery potential discriminating between the polarization scenarios. Figure adapted from the Github of Ciaran O'Hare (https://github.com/cajohare/AxionLimits).

7.3 DANDELION first data run

The first data acquisition run, conducted over a continuous 24-hour period on January 14, 2024, was highly successful from multiple perspectives. The cryogenic system maintained a stable and precise temperature throughout the operation, ensuring optimal experimental conditions. The data acquisition software operated reliably and consistently for the entire duration, demonstrating robustness even under extended usage, despite not being adapted for such long measurements. The acquired data exhibited the expected signal characteristics, including the correct modulation features, validating the system's performance. Most notably, this data run enabled the establishment of a new constraint on dark photons, significantly advancing their characterization as potential dark matter candidates.

7.3.1 Raw detected signal

Over the 24 hour data run, we collected 148 10-minute long data files, that were subsequently combined to recreate the full length measurements. In Fig. 7.8 we show an example of a segment of calibrated time ordered data. In particular, we show the signal from one single KID, together with the mask indicating the motor's position at each moment.

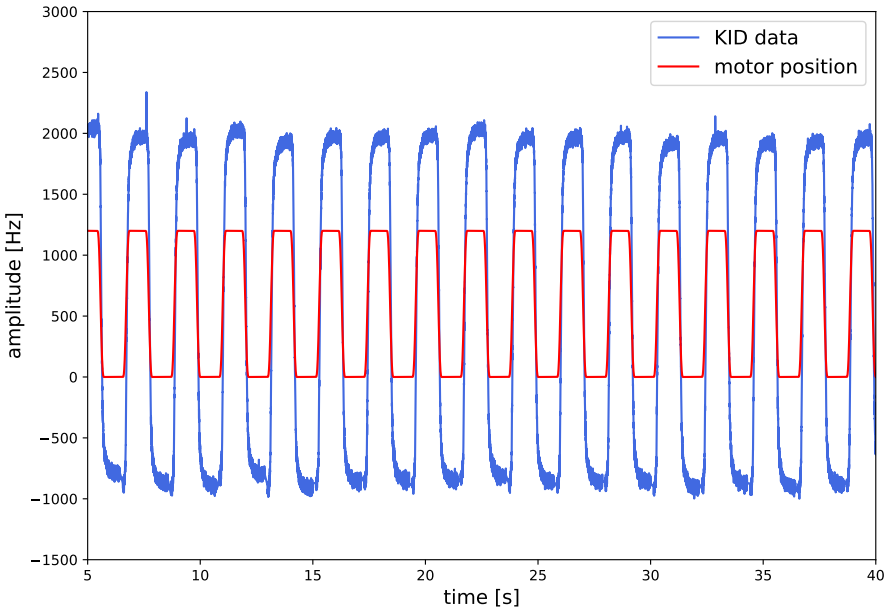

Figure 7.8: Sample segment showing the type of signal we are observing on each KID. In blue we show the KID data, in red the motor's position.

The motor's position is a crucial element for this measurement, since the two positions (up and down in the plot) will be treated separately. We can see the presence of glitches in this timeline, whose nature and characteristics have been explained in Chap. 4, Subsec. 4.4.1. Such glitches have been removed before data treatment, following the same algorithm.
The frequency measurements obtained for each pixel are converted into temperature values by multiplying them by the calibrated pixel response. This response was derived in the same way as described in Chap. 4, Subsec. 4.4.1. The resulting time series for each pixel represents the evolution of the temperature equivalent to the power absorbed by that pixel over the entire observation period.
To analyze the long-term behavior while minimizing the impact of transient noise, such as glitches, we compute the median value from each file, resulting in one data point every 10 minutes. This allows us to track the evolution of the absorbed temperature by the entire array. The measured power originates from various background sources, including thermal emission from the mirror and optical elements, stray light, and other instrumental contributions. Against this background, we aim to detect the target signal: standard photons arising from the conversion of dark photons.
The temperature as a function of time shows a perfectly correlated behavior among KIDs. This comes from a fluctuating thermal background, normally expected by the environmental changes in the room temperature. We accounted and corrected for it by recording the mirror temperature all along the data run and by decorrelating for such function.

7.3.2 Displacement of the signal on the focal plane

To isolate the signal, our analysis strategy relies on the spatial separation of signal and background noise by exploiting the directionality of the signal trajectory. As illustrated in Figs. 7.9, the focal plane is divided into two distinct regions: the background region, composed of KIDs that are never intersected by the expected signal path or are unaffected by the diffraction spot; and the signal region, composed of KIDs that lie along the expected signal trajectory and thus may contain both background and signal contributions.

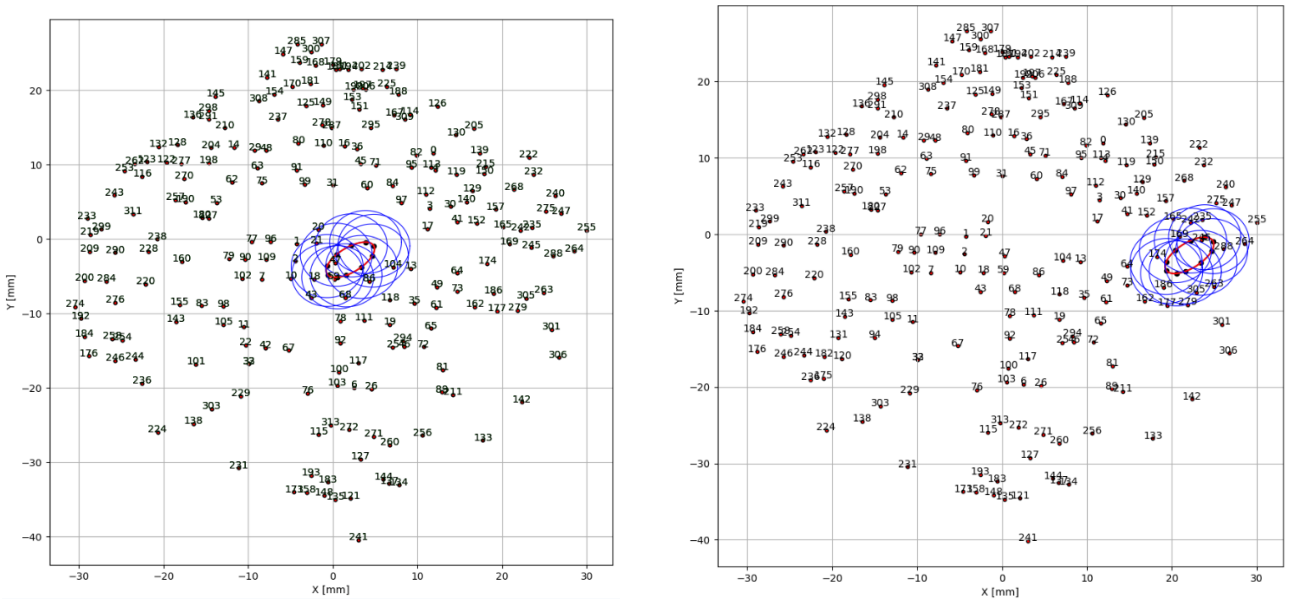

Figure 7.9: Focal plane geometry with labels for each KID and the trajectory of the signal's diffraction spot. The blue ellipses represent each diffraction spot, while the red circle represents the cumulated trajectory. On the left we show the case for the first, central, mirror position; on the right we show the case of the second, tilted, mirror position. Focal plane geometry produced by myself; signal's diffraction spot and trajectory traced by I. Ourahou.

For instance, in the first pointing position, the central pixels are likely to overlap with the signal path, while the remaining pixels are used to characterize the thermal background.
The contributions to the background are manifold and include: thermal emission from the mirror at 300 K; the emissivity of three lenses (operating at 300 K, 4 K, and 150 mK respectively); electronic noise; and stray light. Accurately modeling this background is particularly challenging due to uncertainties in the absorption and emission coefficients of the optical system. These coefficients depend sensitively on the material properties, which themselves are highly temperature-dependent. This temperature dependence makes precise modeling of the background, and the extraction of the faint signal, even more complex.

7.3.3 PCA-based background modeling and signal extraction

To model the correlated background noise, we apply Principal Component Analysis (PCA) to the time series data of pixels in the background region. PCA identifies orthogonal modes of temporal variation (principal components, PC_i) that capture the majority of the background fluctuations. Each KID's noise, $\mathrm{B}_{\mathrm{KID}}$, is then modeled as a linear combination of these components:

$$\mathrm{B}_{\mathrm{KID}} = b_{\mathrm{KID}} + \sum_{i=0}^{12} a_{\mathrm{KID},i} \cdot \mathrm{PC}_i \,. \tag{7.14}$$

This model is extended to the signal region by fitting each KID's temperature time series with an added Gaussian-shaped signal term:

$$T_{\mathrm{KID}}(t) = \sum_{i=0}^{12} a_{\mathrm{KID},i} \cdot \mathrm{PC}_i(t) + b_{\mathrm{KID}} + A_{\mathrm{temp}} \cdot \exp\left(-\frac{(x(t) - x_{\mathrm{KID}})^2 + (y(t) - y_{\mathrm{KID}})^2}{2\sigma^2}\right), \quad (7.15)$$

where A_{temp} is the signal's amplitude, the primary parameter of interest. The number of PCs used (13 for the first mirror position and 14 for the second) is chosen to minimize the uncertainty on A_{temp}.
The fits show good agreement with the data, validating the PCA-based model. No significant signal was detected, and we derive upper limits on the temperature amplitude. For the first mirror position, we obtain $\Delta T_{\text{upper-limit},\,m1} = 2 \cdot \sigma_T = 38$ mK; for the second mirror position we obtain $\Delta T_{\text{upper-limit},\,m2} = 2 \cdot \sigma_T = 34$ mK, where σ_T is the error associate to the amplitude of the signal in K.

7.3.4 Exclusion curves on the χ parameter

The analysis of the data revealed no statistically significant excess above the background fluctuations. In the absence of a detected signal, we proceed to set an upper limit on the physical parameters of the dark photon model. This is achieved in three main steps: first, determining an upper bound on the signal amplitude in temperature units, then converting this temperature constraint into a limit on the power incident on the detector, and finally translating this into a constraint on the kinetic mixing parameter χ.
Using linear regression, we set a 95% confidence upper limit on the temperature amplitude of the signal: $\Delta T < 0.038$ K. To convert this into a power limit, we apply the Stefan-Boltzmann law integrated over the instrument's spectral response $H(\nu)$. The absorbed power is given by:

$$P = A\Omega \int_{\nu_{\min}}^{\nu_{\max}} \eta(\nu) H(\nu) B(\Delta T, \nu)\, d\nu\,. \quad (7.16)$$

In our regime, where $k_B T_{\mathrm{tot}} \gg h\nu$, the Rayleigh-Jeans approximation is valid, allowing us to express the difference in blackbody spectral radiance as $B(T_{\mathrm{background}} + \Delta T, \nu) - B(T_{\mathrm{background}}, \nu)$. This condition holds in particular for the 300 K lens, where the thermal energy is significantly higher than the energy of a 244 GHz photon.
By performing this integral and incorporating the measured spectral bandwidth and temperature limit ΔT_{lim}, we compute the corresponding limit on detectable power. This in turn allows us to constrain the kinetic mixing parameter χ, using the expression:

$$\chi = \sqrt{\frac{P}{\rho_{\mathrm{CDM}} \cdot A_{\mathrm{mirror}} \cdot \frac{2c\eta}{3}}}\,, \quad (7.17)$$

where $\rho_{\mathrm{CDM}} = 0.45$ GeV/cm^3 and assume $\eta(E_\gamma) = 1$ at the maximum of the spectral band (250 GHz). The analysis was conducted independently for two different mirror positions (m1 and m2), producing the following results over the frequency range 150–350 GHz, corresponding to dark photon masses between 0.06 meV and 1.44 meV: for mirror position m1, we obtain $\chi_{m1} = 2.7536 \times 10^{-10}$; for mirror position m2, $\chi_{m2} = 2.6038 \times 10^{-10}$. Combining both measurements statistically yields a tighter constraint: $\chi_{\mathrm{comb}} = 2.2547 \times 10^{-10}$, valid in the dark photon mass range from 0.6 meV to 1.6 meV.
This result, as illustrated in the exclusion curve of Fig. 7.10, represents a new competitive limit in the ongoing search for dark photon dark matter.

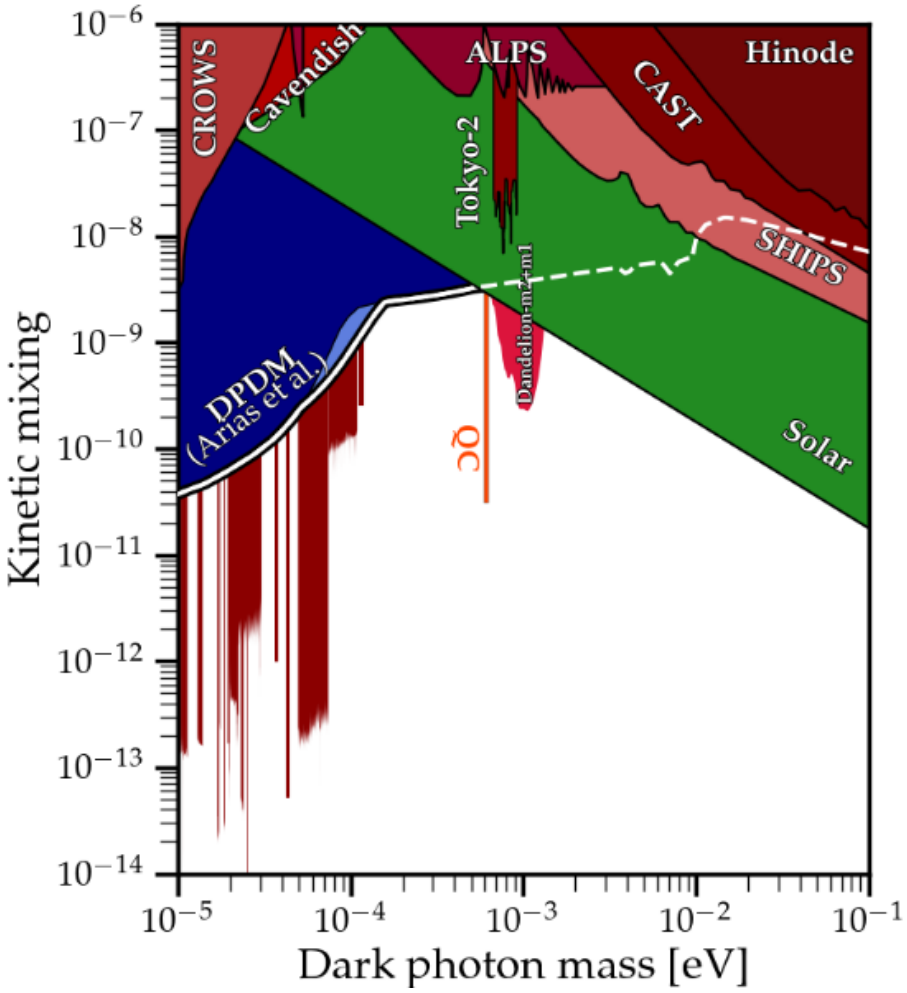

Figure 7.10: Exclusion curve in parameter space kinetic mixing parameter χ vs dark photon mass, after combining the two mirror positions.

7.4 Conclusions and perspectives

The 24-hour data acquisition campaign was successfully completed and marked an important milestone in the search for dark photon dark matter. From an experimental standpoint, the entire system operated reliably and with high stability: the cryogenic setup, the readout electronics, and the data acquisition chain all performed optimally throughout the observation, demonstrating the robustness of the instrument.

I was one of the key contributors to the preparation and execution of this experiment. My work included designing, installing and pre-calibrating the detection setup, ensuring its proper functioning during the acquisition phase, and playing a central role in the handling and processing of the raw data. In particular, I managed a large dataset of approximately 60 GB of raw KID readout data, and performed the reduction pipeline to convert these raw signals into calibrated frequency time streams. I was also actively involved in the discussion and interpretation of the data, contributing to the development and application of decorrelation techniques, as well as to the physical interpretation of the final results.

The first DANDELION data run already enabled us to set new constraints on the kinetic mixing parameter of dark photons. In particular, we were able to establish an upper limit of $\chi_{\text{comb}} = 2.2547 \times 10^{-10}$ in the mass range around 1 meV, contributing a new competitive exclusion limit in this region of parameter space.

Looking ahead, multiple directions are under consideration to improve the sensitivity of the experiment. The first involves extending the integration time. Although a subsequent one-

week-long run was conducted, its scientific outcome was limited by high and unstable noise levels, together with the issues arising from a long data acquisition run with a non-optimized system. In the long term, a longer continuous observation could significantly enhance our sensitivity and allow us to reach the target detection thresholds illustrated in Fig. 7.7.
A second perspective concerns the extension of the accessible dark photon mass range. The current setup is optimized for photons with energies around 1 meV (corresponding to a wavelength of approximately 1.2 mm). By modifying the optical filtering to center the spectral bandwidth around 2 mm, we could target dark photon masses near 2 meV, thereby broadening the scope of the search.
The third perspectives involves the replacement of the 50 cm mirror with a larger one, which would clearly intensify the observed signal. Moreover, we could cool it down to avoid thermal instabilities that contribute significantly to the background variation.

Conclusions and perspectives

The work presented in this thesis is built to span the study of polarization in astrophysics and cosmology from multiple, interconnected perspectives: from the physical foundations and observational challenges, to the development and testing of instrumental solutions, and finally to the application of these tools to both astrophysical sources and fundamental physics searches.
The first part of the manuscript (Chap. 1) laid the astrophysical and cosmological context, providing the theoretical framework necessary to interpret the polarization signals arising from Galactic, extragalactic, and cosmological sources. Building on this foundation, the subsequent discussion of observational strategies and systematic effects (Chap. 2) emphasized the experimental challenges inherent to polarization measurements, including the mitigation of instrumental systematics, the design of modulation and calibration schemes, and the performance requirements of upcoming CMB experiments. This part served as a bridge between theoretical motivations and the instrumental developments described later in the thesis.
The following section explored the technology at the core of several experiments presented here: Kinetic Inductance Detectors (KIDs) and, more specifically, Lumped Element KIDs (LEKIDs) (Chap. 3). After reviewing their working principle and fabrication, I reported on my own experience producing ready-to-use aluminum arrays in a cleanroom environment. These detectors were then implemented in a dedicated experimental setup (Chap. 4), where two orthogonal LEKID arrays were used in combination with a linearly oriented polarizer to split and analyze the incoming beam. Through photometric and polarimetric measurements, we demonstrated that this configuration allows a reconstruction of the polarization angle with an uncertainty below 0.1°, meeting the most stringent requirements for high-precision polarization studies. These results, published in Savorgnano et al. 2025a [276], pave the way for applying this methodology to future high-precision polarization experiments, also by extending the method to other wavelengths, notably at 1 mm, and by testing other simulated sources.
On the more observational side of this thesis, Chap. 5 details the polarimetric campaign on the massive star-forming region W43, conducted with the NIKA2 camera at the IRAM 30m telescope and complemented with *Herschel* and HERA data. These observations were part of an accepted open-time proposal that I led, originally awarded 19 hours of telescope time. Only 6.5 h could be observed during the allocated semester due to weather constraints, prompting a successful resubmission that granted the remaining hours. The second observing run will benefit from the newly upgraded NIKA2+ instrument, offering higher sensitivity and faster scanning speed. From the data obtained so far, we derived magnetic field morphology and strength maps across the cloud and performed a virial analysis of the main clumps (MM1, MM2, MM3). We found virial parameters around 0.4, indicating a global collapse scenario consistent with ongoing star formation. The strong magnetic fields, between 800 and 1800 μG, appear to counteract gravity and regulate the collapse. This work (Savorgnano et al. 2025b, in preparation) could evolve towards a multi-scale analysis, from *Planck* at $1'$ resolution down to ALMA at $30''$.
As highlighted in Chap. 2, and specifically in Sec. 2.6, the matter of calibration is crucial for the current and future generation of CMB polarization experiments. Therefore a complementary effort focused on the development and field testing of a calibration source for ground-based

CMB polarimetry (Chap. 6). After a successful in-lab proof-of-concept, the prototype was deployed at the IRAM 30m telescope and coupled to NIKA2. This campaign revealed both the potential and the challenges of such a calibrator: while the polarization angle of the source could be measured to within 3° of uncertainty, the tests also highlighted the importance of far-field operation and precise alignment to avoid spurious polarization. Parallel analyses, including diffraction pattern modeling and photogrammetry, confirmed the feasibility of the design for future — potentially space-based — implementations, in the context of ongoing collaborations with CNES.

The final part of the thesis (Chap. 7) broadened the scope beyond astrophysical sources to a direct search for a dark matter candidate — dark photons — using the reconfigured cryogenic platform at LPSC, in the context of the DANDELION experiment. Two measurement campaigns were conducted, of 24 hours and 7 days, and demonstrated both the stability of the instrumental setup and the sensitivity to constrain the kinetic mixing parameter, adding a new exclusion limit to the dark photon parameter space. Future improvements could involve longer integration times and the use of arrays optimized for different frequency bands, such as 2 mm.

A key element underlying several of these projects has been the development of a versatile cryogenic and optical platform, initially conceived for the PolarKID project but subsequently adapted for other purposes, such as hosting the DANDELION experiment and the COSMOCal in-lab prototype. This adaptability demonstrates its potential as a long-term infrastructure for testing and validation of novel instrumentation concepts, and as a host for future experiments that may emerge from ongoing collaborations.

Starting from the scientific motivations for the study of astronomical polarization, I addressed the experimental and instrumental challenges it entails, designed and tested new solutions, and carried out the analysis of observational data. In doing so, I sought to highlight the coherence of the link between instrumentation, observation, and data analysis. The versatility of the detectors and instruments developed in Grenoble also gave me the opportunity to take part in other fundamental physics projects, such as a prototype for the detection of a dark matter particle, the dark photon.

Beyond the purely scientific results, the work conducted throughout this thesis helped me building a strong and broad knowledge spanning multiple topics in experimental astrophysics and cosmology. I have greatly enjoyed engaging with these challenges, and my passion for experimental cosmology has grown even stronger. The opportunity to collaborate extensively with the NIKA2 community, which granted me membership in the NIKA2 core team, as well as with the COSMOCal collaboration, has been particularly rewarding.

Conclusions et perspectives

Le travail présenté dans cette thèse est construit pour couvrir l'étude de la polarisation en astrophysique et en cosmologie sous plusieurs angles interconnectés : des fondements physiques et des défis observationnels, au développement et au test de solutions instrumentales, jusqu'à l'application de ces outils à la fois à des sources astrophysiques et à la recherche en physique fondamentale.
La première partie du manuscrit (Chap. 1) a posé le contexte astrophysique et cosmologique, en fournissant le cadre théorique nécessaire pour interpréter les signaux de polarisation provenant de sources galactiques, extragalactiques et cosmologiques. Sur cette base, la discussion ultérieure des stratégies d'observation et des effets systématiques (Chap. 2) a mis en évidence les défis expérimentaux inhérents aux mesures de polarisation, notamment la réduction des effets systématiques instrumentaux, la conception de schémas de modulation et de calibration, ainsi que les exigences de performance des futures expériences CMB. Cette partie a servi de lien entre les motivations théoriques et les développements instrumentaux décrits plus loin dans la thèse.
La section suivante a exploré la technologie au cœur de plusieurs expériences présentées ici : les détecteurs à inductance cinétique (KIDs) et, plus spécifiquement, les KIDs à éléments localisés (LEKIDs) (Chap. 3). Après avoir présenté leur principe de fonctionnement, j'ai rendu compte de mon expérience personnelle dans la production de matrices en aluminium prêtes à l'emploi dans un environnement de salle blanche. Ces détecteurs ont ensuite été mis en œuvre dans un dispositif expérimental dédié (Chap. 4), où deux matrices de LEKIDs orthogonales étaient utilisées en combinaison avec un polariseur linéairement orienté pour séparer et analyser le faisceau incident. Grâce à des mesures photométriques et polarimétriques, nous avons démontré que cette configuration permet de reconstruire l'angle de polarisation avec une incertitude inférieure à 0.1°, répondant ainsi aux exigences les plus strictes pour les études de polarisation de haute précision, notamment la recherche des modes B d'origine primordiale dans la polarisation du CMB. Ces résultats, publiés dans Savorgnano et al. 2025a [276], renforcent l'intérêt d'utiliser des LEKIDs dans des projets d'observation du CMB, y compris à des longueurs d'onde relativement petites comme 1mm.
En transition vers le versant plus observationnel de cette thèse, le Chap. 5 présente la campagne polarimétrique menée avec la caméra NIKA2 au télescope IRAM 30m sur la région massive de formation stellaire W43, complétée par des données de *Herschel* et de HERA. Ces observations faisaient partie d'une proposition de temps ouvert acceptée que j'ai dirigée, initialement allouée pour 19 heures de temps de télescope. Seules 6.5 h ont pu être observées durant le semestre prévu en raison des conditions météorologiques, ce qui a motivé une nouvelle soumission couronnée de succès permettant d'obtenir les heures restantes. La deuxième session bénéficiera du nouvel instrument NIKA2+, offrant une sensibilité accrue et une vitesse de balayage plus rapide. À partir des données obtenues jusqu'à présent, nous avons reconstruit la morphologie et l'intensité du champ magnétique à travers le nuage et réalisé une analyse virielle des principaux amas (MM1, MM2, MM3). Nous avons trouvé des paramètres viriels autour de 0.4, indiquant un scénario d'effondrement global cohérent avec la formation stellaire en cours. Les champs magnétiques intenses, compris entre 800 et 1800 μG, semblent contrebalancer la gravité et réguler l'effondrement. Ce travail (Savorgnano et al. 2025b, en préparation)

pourrait évoluer vers une analyse multi-échelle, entre *Planck* à une résolution de $5'$ et ALMA à $0.5''$.
Compte tenu des exigences accrues en terme de calibration des instruments de mesure du CMB, j'ai consacré un effort important au cas particulier de la calibration de l'orientation absolue d'un instrument. Pour cela, j'ai testé, en laboratoire, puis au télescope de 30m de l'IRAM avec NIKA2, un prototype de source polarisée de référence: COSMOCAL (Chap. 6). Cette campagne a révélé à la fois le potentiel et les défis d'un tel calibrateur : l'angle de polarisation de la source n'a pas pu être mesuré avec une incertitude meilleure que 3°, ce qui a mis en évidence l'importance d'un fonctionnement en champ lointain et d'un alignement précis pour éviter les polarisations parasites. Cependant, ce travail a pu confirmer la faisabilité du concept pour de futures mises en œuvre — potentiellement spatiales — dans le cadre de collaborations en cours avec le CNES.
La dernière partie de la thèse (Chap. 7) a élargi le champ d'étude au-delà des sources astrophysiques vers une recherche directe d'un candidat à la matière noire — les *dark photons* — en utilisant la plateforme cryogénique reconfigurée au LPSC, dans le cadre de l'expérience DANDELION. Deux campagnes de mesures, de 24 heures et de 7 jours, ont démontré à la fois la stabilité du montage instrumental et la sensibilité suffisante pour contraindre le paramètre de mélange cinétique, ajoutant ainsi une nouvelle limite d'exclusion à l'espace des paramètres des *dark photons*. De futures améliorations pourraient inclure des temps d'intégration plus longs et l'utilisation de matrices optimisées pour différentes bandes de fréquences, telles que 2 mm.
Un élément clé commun à plusieurs de ces projets a été le développement d'une plateforme cryogénique et optique polyvalente, initialement conçue pour le projet PolarKID mais ensuite adaptée à d'autres usages, tels que l'hébergement de l'expérience DANDELION et du prototype en laboratoire de COSMOCal. Cette adaptabilité démontre son potentiel en tant qu'infrastructure à long terme pour les tests et validations de nouveaux concepts instrumentaux.
Partant des motivations scientifiques pour l'étude de la polarisation astronomique, j'ai abordé les défis expérimentaux et instrumentaux que pose celle-ci, conçu et testé de nouvelles solutions, et mené l'analyse de données observationnelles. Ce faisant, j'ai cherché à montrer la cohérence du lien entre instrumentation, observation et analyse des données. La versatilité des détecteurs et instruments développés à Grenoble m'a également offert l'opportunité de participer à d'autres projets de physique fondamentale, comme un prototype de détection de particule de matière noire, le dark photon.
Au-delà des résultats purement scientifiques, le travail mené tout au long de cette thèse m'a aidée à construire une solide et large connaissance couvrant de nombreux sujets en astrophysique et en cosmologie expérimentale. J'ai pris un grand plaisir à relever ces défis, et ma passion pour la cosmologie expérimentale en est sortie encore renforcée. La possibilité de collaborer étroitement avec la communauté NIKA2, qui m'a accordé le statut de membre du core team, ainsi qu'avec la collaboration COSMOCal, a été particulièrement enrichissante.

References

[1] R. Adam. "The First Observation of Galaxy Clusters Via the Thermal SZ Effect with Kinetic Inductance Detectors Using the NIKA Camera". In: *SnowCLUSTER 2013, Physics of Galaxy Clusters*. Ed. by Maxim Markevitch. Mar. 2013, 102, p. 102.

[2] R. Adam et al. "The NIKA2 large-field-of-view millimetre continuum camera for the 30 m IRAM telescope". In: *Astronomy & Astrophysics* 609, A115 (Jan. 2018), A115. DOI: 10.1051/0004-6361/201731503. arXiv: 1707.00908 [astro-ph.IM].

[3] P. A. R. Ade et al. "Improved Constraints on Primordial Gravitational Waves using Planck, WMAP, and BICEP/Keck Observations through the 2018 Observing Season". In: *Physical Review Letters* 127.15, 151301 (Oct. 2021), p. 151301. DOI: 10.1103/PhysRevLett.127.151301. arXiv: 2110.00483 [astro-ph.CO].

[4] Peter Ade et al. "The Simons Observatory: science goals and forecasts". In: *Journal of Cosmology and Astroparticle Physics* 2019.2, 056 (Feb. 2019), p. 056. DOI: 10.1088/1475-7516/2019/02/056. arXiv: 1808.07445 [astro-ph.CO].

[5] Prateek Agrawal et al. "Relic abundance of dark photon dark matter". In: *Physics Letters B* 801, 135136 (Feb. 2020), p. 135136. DOI: 10.1016/j.physletb.2019.135136.

[6] I. Agudo et al. "3C 286: a bright, compact, stable, and highly polarized calibrator for millimeter-wavelength observations". In: *Astronomy & Astrophysics* 541, A111 (May 2012), A111. DOI: 10.1051/0004-6361/201218801. arXiv: 1201.2150 [astro-ph.IM].

[7] Aqeel Ahmed, Bohdan Grzadkowski, and Anna Socha. "Gravitational production of vector dark matter". In: *Journal of High Energy Physics* 2020.8, 59 (Aug. 2020), p. 59. DOI: 10.1007/JHEP08(2020)059. arXiv: 2005.01766 [hep-ph].

[8] Randol W. Aikin et al. "Optical performance of the BICEP2 Telescope at the South Pole". In: *Millimeter, Submillimeter, and Far-Infrared Detectors and Instrumentation for Astronomy V*. Ed. by Wayne S. Holland and Jonas Zmuidzinas. Vol. 7741. Society of Photo-Optical Instrumentation Engineers (SPIE) Conference Series. July 2010, 77410V, p. 77410V. DOI: 10.1117/12.857868.

[9] Jim Alexander et al. "Dark Sectors 2016 Workshop: Community Report". In: *arXiv e-prints*, arXiv:1608.08632 (Aug. 2016), arXiv:1608.08632. DOI: 10.48550/arXiv.1608.08632. arXiv: 1608.08632 [hep-ph].

[10] V. Anastassopoulos et al. "Search for chameleons with CAST". In: *Physics Letters B* 749 (Oct. 2015), pp. 172–180. DOI: 10.1016/j.physletb.2015.07.049. arXiv: 1503.04561 [astro-ph.SR].

[11] Mohamed M. Anber and Lorenzo Sorbo. "Non-Gaussianities and chiral gravitational waves in natural steep inflation". In: *Physical Review D* 85.12, 123537 (June 2012), p. 123537. DOI: 10.1103/PhysRevD.85.123537. arXiv: 1203.5849 [astro-ph.CO].

[12] B. G. Andersson, A. Lazarian, and John E. Vaillancourt. "Interstellar Dust Grain Alignment". In: *Annual Review of Astronomy and Astrophysics* 53 (Aug. 2015), pp. 501–539. DOI: 10.1146/annurev-astro-082214-122414.

[13] Ph. André et al. “From filamentary clouds to prestellar cores to the stellar IMF: Initial highlights from the Herschel Gould Belt Survey”. In: *Astronomy & Astrophysics* 518, L102 (July 2010), p. L102. DOI: 10.1051/0004-6361/201014666. arXiv: 1005.2618 [astro-ph.GA].

[14] Paola Arias et al. “WISPy cold dark matter”. In: *Journal of Cosmology and Astroparticle Physics* 2012.6, 013 (June 2012), p. 013. DOI: 10.1088/1475-7516/2012/06/013. arXiv: 1201.5902 [hep-ph].

[15] K. Arnold et al. “The bolometric focal plane array of the POLARBEAR CMB experiment”. In: *Millimeter, Submillimeter, and Far-Infrared Detectors and Instrumentation for Astronomy VI*. Ed. by Wayne S. Holland and Jonas Zmuidzinas. Vol. 8452. Society of Photo-Optical Instrumentation Engineers (SPIE) Conference Series. Sept. 2012, 84521D, p. 84521D. DOI: 10.1117/12.927057. arXiv: 1210.7877 [astro-ph.IM].

[16] D. Arzoumanian et al. “Characterizing interstellar filaments with Herschel in IC 5146”. In: *Astronomy & Astrophysics* 529, L6 (May 2011), p. L6. DOI: 10.1051/0004-6361/201116596. arXiv: 1103.0201 [astro-ph.GA].

[17] J. Aumont et al. “Absolute calibration of the polarisation angle for future CMB B-mode experiments from current and future measurements of the Crab nebula”. In: *mm Universe @ NIKA2 - Observing the mm Universe with the NIKA2 Camera*. Vol. 228. European Physical Journal Web of Conferences. June 2020, 00003, p. 00003. DOI: 10.1051/epjconf/202022800003. arXiv: 1911.03164 [astro-ph.CO].

[18] J. E. Austermann et al. “SPTpol: an instrument for CMB polarization measurements with the South Pole Telescope”. In: *Millimeter, Submillimeter, and Far-Infrared Detectors and Instrumentation for Astronomy VI*. Ed. by Wayne S. Holland and Jonas Zmuidzinas. Vol. 8452. Society of Photo-Optical Instrumentation Engineers (SPIE) Conference Series. Sept. 2012, 84521E, 84521E. DOI: 10.1117/12.927286. arXiv: 1210.4970 [astro-ph.IM].

[19] J. E. Austermann et al. “Millimeter-Wave Polarimeters Using Kinetic Inductance Detectors for TolTEC and Beyond”. In: *Journal of Low Temperature Physics* 193.3-4 (Nov. 2018), pp. 120–127. DOI: 10.1007/s10909-018-1949-5. arXiv: 1803.03280 [astro-ph.IM].

[20] J. W. M. Baars et al. “The IRAM 30-m millimeter radio telescope on Pico Veleta, Spain”. In: *Astronomy & Astrophysics* 175.1-2 (Mar. 1987), pp. 319–326.

[21] J. Bardeen. “Theory of the Meissner Effect in Superconductors”. In: *Physical Review* 97.6 (Mar. 1955), pp. 1724–1725. DOI: 10.1103/PhysRev.97.1724.

[22] J. Bardeen, L. N. Cooper, and J. R. Schrieffer. “Theory of Superconductivity”. In: *Physical Review* 108.5 (Dec. 1957), pp. 1175–1204. DOI: 10.1103/PhysRev.108.1175.

[23] J. J. A. Baselmans et al. “Development of high- Q superconducting resonators for use as kinetic inductance detectors”. In: *Advances in Space Research* 40.5 (Jan. 2007), pp. 708–713. DOI: 10.1016/j.asr.2007.06.041.

[24] J. J. A. Baselmans et al. “Ultra-sensitive THz microwave kinetic inductance detectors for future space telescopes”. In: *Astronomy & Astrophysics* 665, A17 (Sept. 2022), A17. DOI: 10.1051/0004-6361/202243840. arXiv: 2207.08647 [astro-ph.IM].

[25] Jochem Baselmans. “Large Format, Background Limited Arrays of Kinetic Inductance Detectors for Sub-mm Astronomy”. In: *Atacama Large-Aperture Submm/mm Telescope (AtLAST)*. Jan. 2018, 1, p. 1. DOI: 10.5281/zenodo.1158838.

[26] Mar Bastero-Gil and António Torres Manso. "Parity violating gravitational waves at the end of inflation". In: *Journal of Cosmology and Astroparticle Physics* 2023.8, 001 (Aug. 2023), p. 001. DOI: 10.1088/1475-7516/2023/08/001. arXiv: 2209.15572 [gr-qc].

[27] Mar Bastero-Gil et al. "Vector dark matter production at the end of inflation". In: *Journal of Cosmology and Astroparticle Physics* 2019.4, 015 (Apr. 2019), p. 015. DOI: 10.1088/1475-7516/2019/04/015. arXiv: 1810.07208 [hep-ph].

[28] Mar Bastero-Gil et al. "Dark photon dark matter from a rolling inflaton". In: *Journal of Cosmology and Astroparticle Physics* 2022.2, 015 (Feb. 2022), p. 015. DOI: 10.1088/1475-7516/2022/02/015. arXiv: 2103.12145 [hep-ph].

[29] C. Beaufort et al. "Directional detection of meV dark photons with Dandelion". In: *Journal of Cosmology and Astroparticle Physics* 2024.6, 058 (June 2024), p. 058. DOI: 10.1088/1475-7516/2024/06/058. arXiv: 2310.16505 [physics.ins-det].

[30] R. Beck. "Magnetism in the spiral galaxy NGC 6946: magnetic arms, depolarization rings, dynamo modes, and helical fields". In: *Astronomy & Astrophysics* 470.2 (Aug. 2007), pp. 539–556. DOI: 10.1051/0004-6361:20066988. arXiv: 0705.4163 [astro-ph].

[31] R. Beck. "Galactic and extragalactic magnetic fields - a concise review". In: *Astrophysics and Space Sciences Transactions* 5.1 (Oct. 2009), pp. 43–47. DOI: 10.5194/astra-5-43-2009.

[32] R. Beck. "Magnetic Fields in Disks and Halos of Galaxies". In: *EAS Publications Series*. Ed. by Miguel A. de Avillez. Vol. 56. EAS Publications Series. Sept. 2012, pp. 51–59. DOI: 10.1051/eas/1256006.

[33] Rainer Beck. "Magnetic Fields in Galaxies". In: *Space Science Reviews* 166.1-4 (May 2012), pp. 215–230. DOI: 10.1007/s11214-011-9782-z.

[34] T. Beckert, W. J. Duschl, and P. G. Mezger. "Free-free and recombination radiation from massive star-forming regions". In: *Astronomy & Astrophysics* 356 (Apr. 2000), pp. 1149–1156.

[35] C. L. Bennett et al. "Nine-year Wilkinson Microwave Anisotropy Probe (WMAP) Observations: Final Maps and Results". In: *The Astrophysical Journal Supplement Series* 208.2, 20 (Oct. 2013), p. 20. DOI: 10.1088/0067-0049/208/2/20. arXiv: 1212.5225 [astro-ph.CO].

[36] A. Benoît et al. "First detection of polarization of the submillimetre diffuse galactic dust emission by Archeops". In: *Astronomy & Astrophysics* 424 (Sept. 2004), pp. 571–582. DOI: 10.1051/0004-6361:20040042. arXiv: astro-ph/0306222 [astro-ph].

[37] Jose Luis Bernal. "Cosmology on the Edge of Lambda-Cold Dark Matter". PhD thesis. University of Barcelona, Spain, Sept. 2019.

[38] Gianfranco Bertone, Dan Hooper, and Joseph Silk. "Particle dark matter: evidence, candidates and constraints". In: *Physics Reports* 405.5-6 (Jan. 2005), pp. 279–390. DOI: 10.1016/j.physrep.2004.08.031. arXiv: hep-ph/0404175 [hep-ph].

[39] M. Béthermin et al. "The NIKA2 cosmological legacy survey at 2 mm: catalogs, colors, redshift distributions, and implications for deep surveys". In: *arXiv e-prints*, arXiv:2506.22046 (June 2025), arXiv:2506.22046. DOI: 10.48550/arXiv.2506.22046. arXiv: 2506.22046 [astro-ph.GA].

[40] M. Betz et al. "First results of the CERN Resonant Weakly Interacting sub-eV Particle Search (CROWS)". In: *Physical Review D* 88.7, 075014 (Oct. 2013), p. 075014. DOI: 10.1103/PhysRevD.88.075014. arXiv: 1310.8098 [physics.ins-det].

[41] A. Bharti and N. Goyal. *Fundamental of Synchrotron Radiations. In Synchrotron Radiation - Useful and Interesting Applications*. 2019. DOI: 10.5772/intechopen.82202.

[42] BICEP2/Keck Collaboration et al. "Joint Analysis of BICEP2/Keck Array and Planck Data". In: *Physical Review Letters* 114.10, 101301 (Mar. 2015), p. 101301. DOI: 10.1103/PhysRevLett.114.101301. arXiv: 1502.00612 [astro-ph.CO].

[43] Julien Billard et al. "Direct detection of dark matter-APPEC committee report". In: *Reports on Progress in Physics* 85.5, 056201 (May 2022), p. 056201. DOI: 10.1088/1361-6633/ac5754. arXiv: 2104.07634 [hep-ex].

[44] L. Bing et al. "NIKA2 Cosmological Legacy Survey. Survey description and galaxy number counts". In: *Astronomy & Astrophysics* 677, A66 (Sept. 2023), A66. DOI: 10.1051/0004-6361/202346579. arXiv: 2305.07054 [astro-ph.GA].

[45] N. W. Boggess. "The Cosmic Background Explorer (COBE)." In: *Journal of the Royal Astronomical Society of Canada* 86.6 (Dec. 1992), pp. 282–283.

[46] J. R. Bond. "Theory and Observations of the Cosmic Background Radiation". In: *Cosmology and Large Scale Structure*. Ed. by Richard Schaeffer et al. Jan. 1996, p. 469.

[47] J. R. Bond and G. Efstathiou. "Cosmic background radiation anisotropies in universes dominated by nonbaryonic dark matter". In: *The Astrophysical Journal Letters* 285 (Oct. 1984), pp. L45–L48. DOI: 10.1086/184362.

[48] O. Bourrion et al. "NIKEL_AMC: readout electronics for the NIKA2 experiment". In: *Journal of Instrumentation* 11.11 (Nov. 2016), P11001. DOI: 10.1088/1748-0221/11/11/P11001.

[49] Nassim Bozorgnia, Graciela B. Gelmini, and Paolo Gondolo. "Daily modulation due to channeling in direct dark matter crystalline detectors". In: *Physical Review D* 84.2, 023516 (July 2011), p. 023516. DOI: 10.1103/PhysRevD.84.023516. arXiv: 1101.2876 [astro-ph.CO].

[50] Sean Bryan. "Half-wave Plates for the Spider Cosmic Microwave Background Polarimeter". In: *arXiv e-prints*, arXiv:1402.2591 (Feb. 2014), arXiv:1402.2591. DOI: 10.48550/arXiv.1402.2591. arXiv: 1402.2591 [astro-ph.IM].

[51] Immanuel Buder and BICEP Collaboration. "Cosmic Microwave Background Polarization Measurements from Three Years of BICEP Observations". In: *American Astronomical Society Meeting Abstracts*. Vol. 222. American Astronomical Society Meeting Abstracts. June 2013, 103.01, p. 103.01.

[52] B. J. Burn. "On the depolarization of discrete radio sources by Faraday dispersion". In: *Monthly Notices of the Royal Astronomical Society* 133 (Jan. 1966), p. 67. DOI: 10.1093/mnras/133.1.67.

[53] R. S. Bussmann, W. L. Holzapfel, and C. L. Kuo. "Millimeter Wavelength Brightness Fluctuations of the Atmosphere above the South Pole". In: *The Astrophysical Journal* 622.2 (Apr. 2005), pp. 1343–1355. DOI: 10.1086/427935. arXiv: astro-ph/0412031 [astro-ph].

[54] M. Calvo et al. "Improved mm-wave photometry for kinetic inductance detectors". In: *Astronomy & Astrophysics* 551, L12 (Mar. 2013), p. L12. DOI: 10.1051/0004-6361/201219854.

[55] Andrea Caputo et al. "Dark photon limits: A handbook". In: *Physical Review D* 104.9, 095029 (Nov. 2021), p. 095029. DOI: 10.1103/PhysRevD.104.095029. arXiv: 2105.04565 [hep-ph].

[56] J. A. Cardelli, G. C. Clayton, and J. S. Mathis. "The relationship between IR, optical, and UV extinction." In: *Interstellar Dust*. Ed. by Louis J. Allamandola and A. G. G. M. Tielens. Vol. 135. IAU Symposium. Dec. 1989, pp. 5–10.

[57] P. Carlhoff et al. "Large scale IRAM 30 m CO-observations in the giant molecular cloud complex W43". In: *Astronomy & Astrophysics* 560, A24 (Dec. 2013), A24. DOI: 10.1051/0004-6361/201321592. arXiv: 1308.6112 [astro-ph.GA].

[58] Sean M. Carroll, George B. Field, and Roman Jackiw. "Limits on a Lorentz- and parity-violating modification of electrodynamics". In: *Physical Review D* 41.4 (Feb. 1990), pp. 1231–1240. DOI: 10.1103/PhysRevD.41.1231.

[59] Francisco J. Casas et al. "L2-CalSat: A Calibration Satellite for Ultra-Sensitive CMB Polarization Space Missions". In: *Sensors* 21.10 (May 2021), p. 3361. DOI: 10.3390/s21103361.

[60] A. Catalano et al. "Impact of particles on the Planck HFI detectors: Ground-based measurements and physical interpretation". In: *Astronomy & Astrophysics* 569, A88 (Sept. 2014), A88. DOI: 10.1051/0004-6361/201423868. arXiv: 1403.6592 [astro-ph.IM].

[61] A. Catalano et al. "Performance and calibration of the NIKA camera at the IRAM 30 m telescope". In: *Astronomy & Astrophysics* 569, A9 (Sept. 2014), A9. DOI: 10.1051/0004-6361/201423557. arXiv: 1402.0260 [astro-ph.IM].

[62] A. Catalano et al. "Maturity of lumped element kinetic inductance detectors for space-borne instruments in the range between 80 and 180 GHz". In: *Astronomy & Astrophysics* 592, A26 (July 2016), A26. DOI: 10.1051/0004-6361/201527715. arXiv: 1511.02652 [astro-ph.IM].

[63] A. Catalano et al. "Sensitivity of LEKID for space applications between 80 GHz and 600 GHz". In: *Astronomy & Astrophysics* 641, A179 (Sept. 2020), A179. DOI: 10.1051/0004-6361/202038199. arXiv: 2006.14991 [astro-ph.IM].

[64] Anthony Challinor. "CMB anisotropy science: a review". In: *Astrophysics from Antarctica*. Ed. by Michael G. Burton, Xiangqun Cui, and Nicholas F. H. Tothill. Vol. 288. IAU Symposium. Jan. 2013, pp. 42–52. DOI: 10.1017/S1743921312016663. arXiv: 1210.6008 [astro-ph.CO].

[65] S. Chandrasekhar and E. Fermi. "Magnetic Fields in Spiral Arms." In: *The Astrophysical Journal* 118 (July 1953), p. 113. DOI: 10.1086/145731.

[66] Jungyeon Cho and A. Lazarian. "Grain Alignment by Radiation in Dark Clouds and Cores". In: *The Astrophysical Journal* 631.1 (Sept. 2005), pp. 361–370. DOI: 10.1086/432528. arXiv: astro-ph/0505571 [astro-ph].

[67] Ti-Lin Chou, SPT Team, and SPTpol Team. "Improved Measurements of the Temperature and E-Mode Polarization of the CMB from 500 Square Degrees of Multi-Band SPTpol Data". In: *APS April Meeting Abstracts*. Vol. 2022. APS Meeting Abstracts. Apr. 2022, K15.006, K15.006.

[68] Raymond T. Co et al. "Dark photon dark matter produced by axion oscillations". In: *Physical Review D* 99.7, 075002 (Apr. 2019), p. 075002. DOI: 10.1103/PhysRevD.99.075002. arXiv: 1810.07196 [hep-ph].

[69] Fabio Columbro et al. "A polarization modulator unit for the mid- and high-frequency telescopes of the LiteBIRD mission". In: *Space Telescopes and Instrumentation 2020: Optical, Infrared, and Millimeter Wave*. Ed. by Makenzie Lystrup and Marshall D. Perrin. Vol. 11443. Society of Photo-Optical Instrumentation Engineers (SPIE) Conference Series. Dec. 2020, 114436Z, 114436Z. DOI: 10.1117/12.2577818.

[70] A. Comastri, M. Brusa, and R. Gilli. "Relativistic Iron Lines at High Redshifts". In: *Relativistic Astrophysics Legacy and Cosmology - Einstein's Legacy*. Ed. by B. Aschenbach et al. Jan. 2007, p. 202. DOI: 10.1007/978-3-540-74713-0_45. arXiv: astro-ph/0603139 [astro-ph].

[71] CONCERTO Collaboration et al. "A wide field-of-view low-resolution spectrometer at APEX: Instrument design and scientific forecast". In: *Astronomy & Astrophysics* 642, A60 (Oct. 2020), A60. DOI: 10.1051/0004-6361/202038456. arXiv: 2007.14246 [astro-ph.IM].

[72] Gabriele Coppi et al. "PROTOCALC: an artificial calibrator source for CMB telescopes". In: *Millimeter, Submillimeter, and Far-Infrared Detectors and Instrumentation for Astronomy XI*. Ed. by Jonas Zmuidzinas and Jian-Rong Gao. Vol. 12190. Society of Photo-Optical Instrumentation Engineers (SPIE) Conference Series. Aug. 2022, 1219015, p. 1219015. DOI: 10.1117/12.2628312. arXiv: 2207.07595 [astro-ph.IM].

[73] Gabriele Coppi et al. "Calibration of CMB Telescopes with PROTOCALC". In: *Millimeter, Submillimeter, and Far-Infrared Detectors and Instrumentation for Astronomy XII*. Ed. by Jonas Zmuidzinas and Jian-Rong Gao. Vol. 13102. Society of Photo-Optical Instrumentation Engineers (SPIE) Conference Series. Aug. 2024, 1310224, p. 1310224. DOI: 10.1117/12.3015040. arXiv: 2407.13941 [astro-ph.IM].

[74] Gabriele Coppi et al. "PROTOCALC, A W-band polarized calibrator for CMB Telescopes: application to Simons Observatory and CLASS". In: *arXiv e-prints*, arXiv:2502.14473 (Feb. 2025), arXiv:2502.14473. DOI: 10.48550/arXiv.2502.14473. arXiv: 2502.14473 [astro-ph.IM].

[75] J. Cornelison et al. "Polarization calibration of the BICEP3 CMB polarimeter at the South Pole". In: *Millimeter, Submillimeter, and Far-Infrared Detectors and Instrumentation for Astronomy X*. Ed. by Jonas Zmuidzinas and Jian-Rong Gao. Vol. 11453. Society of Photo-Optical Instrumentation Engineers (SPIE) Conference Series. Dec. 2020, 1145327, p. 1145327. DOI: 10.1117/12.2562905. arXiv: 2012.05934 [astro-ph.IM].

[76] J. Cornelison et al. "Improved polarization calibration of the BICEP3 CMB polarimeter at the South Pole". In: *Millimeter, Submillimeter, and Far-Infrared Detectors and Instrumentation for Astronomy XI*. Ed. by Jonas Zmuidzinas and Jian-Rong Gao. Vol. 12190. Society of Photo-Optical Instrumentation Engineers (SPIE) Conference Series. Aug. 2022, 121901X, p. 121901X. DOI: 10.1117/12.2620212. arXiv: 2207.14796 [astro-ph.IM].

[77] Paulo C. Cortes et al. "Interferometric Mapping of Magnetic Fields: The ALMA View of the Massive Star-forming Clump W43-MM1". In: *The Astrophysical Journal Letters* 825.1, L15 (July 2016), p. L15. DOI: 10.3847/2041-8205/825/1/L15. arXiv: 1605.08037 [astro-ph.GA].

[78] Paulo C. Cortes et al. "The Seven Most Massive Clumps in W43-Main as Seen by ALMA: Dynamical Equilibrium and Magnetic Fields". In: *The Astrophysical Journal* 884.1, 48 (Oct. 2019), p. 48. DOI: 10.3847/1538-4357/ab378d. arXiv: 1907.12994 [astro-ph.GA].

[79] Richard M. Crutcher. "Magnetic Fields in Star-Forming Regions". In: *Science with the Atacama Large Millimeter Array (ALMA)*. Oct. 1999, 12, p. 12.

[80] Richard M. Crutcher. "Role of Magnetic Fields in Star Formation". In: *Highlights of Astronomy* 15 (Nov. 2010), pp. 438–439. DOI: 10.1017/S1743921310010173.

[81] Richard M. Crutcher. "Magnetic Fields in Molecular Clouds". In: *Annual Review of Astronomy and Astrophysics* 50 (Sept. 2012), pp. 29–63. DOI: 10.1146/annurev-astro-081811-125514.

[82] Richard M. Crutcher et al. “SCUBA Polarization Measurements of the Magnetic Field Strengths in the L183, L1544, and L43 Prestellar Cores”. In: *The Astrophysical Journal* 600.1 (Jan. 2004), pp. 279–285. DOI: 10.1086/379705. arXiv: astro-ph/0305604 [astro-ph].

[83] Leverett Davis. “The Strength of Interstellar Magnetic Fields”. In: *Physical Review* 81.5 (Mar. 1951), pp. 890–891. DOI: 10.1103/PhysRev.81.890.2.

[84] Peter K. Day et al. “A broadband superconducting detector suitable for use in large arrays”. In: *Nature* 425.6960 (Oct. 2003), pp. 817–821. DOI: 10.1038/nature02037.

[85] J. Delabrouille and J. Kaplan. “Measuring CMB polarization with the Planck HFI”. In: *Astrophysical Polarized Backgrounds*. Ed. by Stefano Cecchini et al. Vol. 609. American Institute of Physics Conference Series. AIP, Mar. 2002, pp. 135–143. DOI: 10.1063/1.1471836. arXiv: astro-ph/0112458 [astro-ph].

[86] F. X. Desert, F. Boulanger, and J. L. Puget. “Interstellar Dust Models for Extinction and Emission”. In: *Astronomy & Astrophysics* 237 (Oct. 1990), p. 215.

[87] P. Diego-Palazuelos et al. “Cosmic Birefringence from the Planck Data Release 4”. In: *Physical Review Letters* 128.9, 091302 (Mar. 2022), p. 091302. DOI: 10.1103/PhysRevLett.128.091302. arXiv: 2201.07682 [astro-ph.CO].

[88] Scott Dodelson, Eduardo Rozo, and Albert Stebbins. “Primordial Gravity Waves and Weak Lensing”. In: *Physical Review Letters* 91.2, 021301 (July 2003), p. 021301. DOI: 10.1103/PhysRevLett.91.021301. arXiv: astro-ph/0301177 [astro-ph].

[89] Jiazheng Dou et al. “Forecasts of effects of beam systematics and deprojection on the third-generation ground-based cosmic microwave background experiment”. In: *Astronomy & Astrophysics* 694, A198 (Feb. 2025), A198. DOI: 10.1051/0004-6361/202452588. arXiv: 2412.20415 [astro-ph.CO].

[90] S. Doyle et al. “Lumped Element Kinetic Inductance Detectors”. In: *Journal of Low Temperature Physics* 151.1-2 (Apr. 2008), pp. 530–536. DOI: 10.1007/s10909-007-9685-2.

[91] Simon Doyle et al. “Optimisation of Lumped Element Kinetic Inductance Detectors for use in ground based mm and sub-mm arrays”. In: *The Thirteenth International Workshop on Low Temperature Detectors - LTD13*. Ed. by Betty Young, Blas Cabrera, and Aaron Miller. Vol. 1185. American Institute of Physics Conference Series. AIP, Dec. 2009, pp. 156–159. DOI: 10.1063/1.3292304.

[92] B. T. Draine and A. Lazarian. “Diffuse Galactic Emission from Spinning Dust Grains”. In: *The Astrophysical Journal Letters* 494.1 (Feb. 1998), pp. L19–L22. DOI: 10.1086/311167. arXiv: astro-ph/9710152 [astro-ph].

[93] B. T. Draine and A. Lazarian. “Electric Dipole Radiation from Spinning Dust Grains”. In: *The Astrophysical Journal* 508.1 (Nov. 1998), pp. 157–179. DOI: 10.1086/306387. arXiv: astro-ph/9802239 [astro-ph].

[94] Bruce T. Draine. *Physics of the Interstellar and Intergalactic Medium*. 2011.

[95] Bruce T. Draine and Aurélien A. Fraisse. “Polarized Far-Infrared and Submillimeter Emission from Interstellar Dust”. In: *The Astrophysical Journal* 696.1 (May 2009), pp. 1–11. DOI: 10.1088/0004-637X/696/1/1. arXiv: 0809.2094 [astro-ph].

[96] Ran Duan and Sunil Golwala. "Readout for kinetic-inductance-detector-based submillimeter radio astronomy". In: *Millimeter, Submillimeter, and Far-Infrared Detectors and Instrumentation for Astronomy X*. Ed. by Jonas Zmuidzinas and Jian-Rong Gao. Vol. 11453. Society of Photo-Optical Instrumentation Engineers (SPIE) Conference Series. Dec. 2020, 114531Z, 114531Z. DOI: 10.1117/12.2576399. arXiv: 2008.11365 [astro-ph.IM].

[97] Rolando Dünner et al. "Millimeter-wave polarization angle calibration using UAV-based sources". In: *Millimeter, Submillimeter, and Far-Infrared Detectors and Instrumentation for Astronomy X*. Ed. by Jonas Zmuidzinas and Jian-Rong Gao. Vol. 11453. Society of Photo-Optical Instrumentation Engineers (SPIE) Conference Series. Dec. 2020, 114532P, 114532P. DOI: 10.1117/12.2561165.

[98] Klaus Ehret et al. "New ALPS results on hidden-sector lightweights". In: *Physics Letters B* 689.4-5 (May 2010), pp. 149–155. DOI: 10.1016/j.physletb.2010.04.066. arXiv: 1004.1313 [hep-ex].

[99] G. Ejlali et al. "Constraining millimeter dust emission in nearby galaxies with NIKA2: The case of NGC2146 and NGC2976". In: *mm Universe 2023 - Observing the Universe at mm Wavelengths*. Vol. 293. European Physical Journal Web of Conferences. June 2024, 00016, p. 00016. DOI: 10.1051/epjconf/202429300016. arXiv: 2310.03428 [astro-ph.GA].

[100] Bruce G. Elmegreen. "Star Formation in a Crossing Time". In: *The Astrophysical Journal* 530.1 (Feb. 2000), pp. 277–281. DOI: 10.1086/308361. arXiv: astro-ph/9911172 [astro-ph].

[101] Yohei Ema, Kazunori Nakayama, and Yong Tang. "Production of purely gravitational dark matter: the case of fermion and vector boson". In: *Journal of High Energy Physics* 2019.7, 60 (July 2019), p. 60. DOI: 10.1007/JHEP07(2019)060. arXiv: 1903.10973 [hep-ph].

[102] A. Endo et al. "Design of an Integrated Filterbank for DESHIMA: On-Chip Submillimeter Imaging Spectrograph Based on Superconducting Resonators". In: *Journal of Low Temperature Physics* 167.3-4 (May 2012), pp. 341–346. DOI: 10.1007/s10909-012-0502-1. arXiv: 1107.3333 [astro-ph.IM].

[103] A. Endo et al. "Development of DESHIMA: a redshift machine based on a superconducting on-chip filterbank". In: *Millimeter, Submillimeter, and Far-Infrared Detectors and Instrumentation for Astronomy VI*. Ed. by Wayne S. Holland and Jonas Zmuidzinas. Vol. 8452. Society of Photo-Optical Instrumentation Engineers (SPIE) Conference Series. Sept. 2012, 84520X, p. 84520X. DOI: 10.1117/12.925637.

[104] H. K. Eriksen et al. "Bayesian foreground analysis with CMB data". In: *New Astronomy Reviews* 50.11-12 (Dec. 2006), pp. 861–867. DOI: 10.1016/j.newar.2006.09.027. arXiv: astro-ph/0604160 [astro-ph].

[105] J. Errard and R. Stompor. "Astrophysical foregrounds and primordial tensor-to-scalar ratio constraints from cosmic microwave background B-mode polarization observations". In: *Physical Review D* 85.8, 083006 (Apr. 2012), p. 083006. DOI: 10.1103/PhysRevD.85.083006. arXiv: 1203.5285 [astro-ph.CO].

[106] J. Errard et al. "Modeling Atmospheric Emission for CMB Ground-based Observations". In: *The Astrophysical Journal* 809.1, 63 (Aug. 2015), p. 63. DOI: 10.1088/0004-637X/809/1/63. arXiv: 1501.07911 [astro-ph.IM].

[107] Johannes R. Eskilt and Eiichiro Komatsu. "Improved constraints on cosmic birefringence from the WMAP and Planck cosmic microwave background polarization data". In: *Physical Review D* 106.6, 063503 (Sept. 2022), p. 063503. DOI: 10.1103/PhysRevD.106.063503. arXiv: 2205.13962 [astro-ph.CO].

[108] T. Essinger-Hileman et al. "Systematic effects from an ambient-temperature, continuously rotating half-wave plate". In: *Review of Scientific Instruments* 87.9, 094503 (Sept. 2016), p. 094503. DOI: 10.1063/1.4962023. arXiv: 1601.05901 [astro-ph.IM].

[109] FUNK Experiment et al. "Search for hidden-photon Dark Matter with FUNK". In: *arXiv e-prints*, arXiv:1711.02961 (Nov. 2017), arXiv:1711.02961. DOI: 10.48550/arXiv.1711.02961. arXiv: 1711.02961 [hep-ex].

[110] Marco Fabbrichesi, Emidio Gabrielli, and Gaia Lanfranchi. "The Dark Photon". In: *arXiv e-prints*, arXiv:2005.01515 (May 2020), arXiv:2005.01515. DOI: 10.48550/arXiv.2005.01515. arXiv: 2005.01515 [hep-ph].

[111] A. Fasano et al. "KISS: a spectrometric imager for millimetre cosmology". In: *mm Universe @ NIKA2 - Observing the mm Universe with the NIKA2 Camera*. Vol. 228. European Physical Journal Web of Conferences. June 2020, 00010, p. 00010. DOI: 10.1051/epjconf/202022800010. arXiv: 1911.04917 [astro-ph.IM].

[112] A. Fasano et al. "Accurate sky signal reconstruction for ground-based spectroscopy with kinetic inductance detectors". In: *Astronomy & Astrophysics* 656, A116 (Dec. 2021), A116. DOI: 10.1051/0004-6361/202141419. arXiv: 2109.03145 [astro-ph.IM].

[113] J. P. Filippini et al. "SPIDER: a balloon-borne CMB polarimeter for large angular scales". In: *Millimeter, Submillimeter, and Far-Infrared Detectors and Instrumentation for Astronomy V*. Ed. by Wayne S. Holland and Jonas Zmuidzinas. Vol. 7741. Society of Photo-Optical Instrumentation Engineers (SPIE) Conference Series. July 2010, 77411N, 77411N. DOI: 10.1117/12.857720. arXiv: 1106.2158 [astro-ph.CO].

[114] Laura M. Fissel et al. "The balloon-borne large-aperture submillimeter telescope for polarimetry: BLAST-Pol". In: *Millimeter, Submillimeter, and Far-Infrared Detectors and Instrumentation for Astronomy V*. Ed. by Wayne S. Holland and Jonas Zmuidzinas. Vol. 7741. Society of Photo-Optical Instrumentation Engineers (SPIE) Conference Series. July 2010, 77410E, 77410E. DOI: 10.1117/12.857601. arXiv: 1007.1390 [astro-ph.IM].

[115] D. J. Fixsen. "The Temperature of the Cosmic Microwave Background". In: *The Astrophysical Journal* 707.2 (Dec. 2009), pp. 916–920. DOI: 10.1088/0004-637X/707/2/916. arXiv: 0911.1955 [astro-ph.CO].

[116] D. J. Fixsen et al. "The Spectrum of the Cosmic Microwave Background Anisotropy from the Combined COBE FIRAS and DMR Observations". In: *The Astrophysical Journal* 486.2 (Sept. 1997), pp. 623–628. DOI: 10.1086/304560. arXiv: astro-ph/9704176 [astro-ph].

[117] A. Fletcher et al. "Magnetic fields and spiral arms in the galaxy M51". In: *Monthly Notices of the Royal Astronomical Society* 412.4 (Apr. 2011), pp. 2396–2416. DOI: 10.1111/j.1365-2966.2010.18065.x. arXiv: 1001.5230 [astro-ph.CO].

[118] Daniel Foreman-Mackey et al. *emcee: The MCMC Hammer*. Astrophysics Source Code Library, record ascl:1303.002. Mar. 2013.

[119] A. Friedmann. "Über die Krümmung des Raumes". In: *Zeitschrift fur Physik* 10 (Jan. 1922), pp. 377–386. DOI: 10.1007/BF01332580.

[120] A. Friedmann. "Über die Möglichkeit einer Welt mit konstanter negativer Krümmung des Raumes". In: *Zeitschrift fur Physik* 21.1 (Dec. 1924), pp. 326–332. DOI: 10.1007/BF01328280.

[121] Juan García-Bellido, Marco Peloso, and Caner Unal. "Gravitational waves at interferometer scales and primordial black holes in axion inflation". In: *Journal of Cosmology and Astroparticle Physics* 2016.12, 031 (Dec. 2016), p. 031. DOI: 10.1088/1475-7516/2016/12/031. arXiv: 1610.03763 [astro-ph.CO].

[122] T. Ghigna et al. "The LiteBIRD mission to explore cosmic inflation". In: *Space Telescopes and Instrumentation 2024: Optical, Infrared, and Millimeter Wave*. Ed. by Laura E. Coyle, Shuji Matsuura, and Marshall D. Perrin. Vol. 13092. Society of Photo-Optical Instrumentation Engineers (SPIE) Conference Series. Aug. 2024, 1309228, p. 1309228. DOI: 10.1117/12.3021377.

[123] S. Giardiello et al. "The Simons Observatory: impact of bandpass, polarization angle and calibration uncertainties on small-scale power spectrum analysis". In: *Journal of Cosmology and Astroparticle Physics* 2024.9, 008 (Sept. 2024), p. 008. DOI: 10.1088/1475-7516/2024/09/008. arXiv: 2403.05242 [astro-ph.CO].

[124] Josep M. Girart et al. "Magnetic Fields in the Formation of Massive Stars". In: *Science* 324.5933 (June 2009), p. 1408. DOI: 10.1126/science.1171807.

[125] B. Gold et al. "Five-Year Wilkinson Microwave Anisotropy Probe Observations: Galactic Foreground Emission". In: *The Astrophysical Journal Supplement Series* 180.2 (Feb. 2009), pp. 265–282. DOI: 10.1088/0067-0049/180/2/265. arXiv: 0803.0715 [astro-ph].

[126] Joseph W. Goodman. *Introduction to Fourier optics*. 2005.

[127] Peter W. Graham, Jeremy Mardon, and Surjeet Rajendran. "Vector dark matter from inflationary fluctuations". In: *Physical Review D* 93.10, 103520 (May 2016), p. 103520. DOI: 10.1103/PhysRevD.93.103520. arXiv: 1504.02102 [hep-ph].

[128] Alan H. Guth. "Inflationary universe: A possible solution to the horizon and flatness problems". In: *Physical Review D* 23.2 (Jan. 1981), pp. 347–356. DOI: 10.1103/PhysRevD.23.347.

[129] J. L. Han. "Magnetic Fields in Our Galaxy: How much do we know? III. Progress in the Last Decade". In: *Chinese Journal of Astronomy and Astrophysics Supplement* 6.S2 (Dec. 2006), pp. 211–217. DOI: 10.48550/arXiv.astro-ph/0603512. arXiv: astro-ph/0603512 [astro-ph].

[130] Diego Harari and Pierre Sikivie. "Effects of a Nambu-Goldstone boson on the polarization of radio galaxies and the cosmic microwave background". In: *Physics Letters B* 289.1-2 (Sept. 1992), pp. 67–72. DOI: 10.1016/0370-2693(92)91363-E.

[131] Kathleen Harrington et al. "Variable-delay polarization modulators for the CLASS telescopes". In: *Millimeter, Submillimeter, and Far-Infrared Detectors and Instrumentation for Astronomy IX*. Ed. by Jonas Zmuidzinas and Jian-Rong Gao. Vol. 10708. Society of Photo-Optical Instrumentation Engineers (SPIE) Conference Series. July 2018, 107082M, p. 107082M. DOI: 10.1117/12.2313614. arXiv: 1807.03807 [astro-ph.IM].

[132] Kathleen Harrington et al. "Two Year Cosmology Large Angular Scale Surveyor (CLASS) Observations: Long Timescale Stability Achieved with a Front-end Variable-delay Polarization Modulator at 40 GHz". In: *The Astrophysical Journal* 922.2, 212 (Dec. 2021), p. 212. DOI: 10.3847/1538-4357/ac2235. arXiv: 2101.00034 [astro-ph.IM].

[133] S. W. Hawking and G. W. Gibbons. "Quantum Aspects of Accretion onto Black Holes in the Early Universe". In: *Gravitational Radiation and Gravitational Collapse*. Ed. by C. Dewitt-Morette. Vol. 64. IAU Symposium. Jan. 1974, p. 185.

[134] Carl Heiles. "9286 Stars: An Agglomeration of Stellar Polarization Catalogs". In: *The Astronomical Journal* 119.2 (Feb. 2000), pp. 923–927. DOI: 10.1086/301236. arXiv: astro-ph/9910303 [astro-ph].

[135] Fabian Heitsch, Mordecai-Mark Mac Low, and Ralf S. Klessen. "Gravitational Collapse in Turbulent Molecular Clouds. II. Magnetohydrodynamical Turbulence". In: *The Astrophysical Journal* 547.1 (Jan. 2001), pp. 280–291. DOI: 10.1086/318335. arXiv: astro-ph/0009227 [astro-ph].

[136] Phillip Helbig. "The flatness problem and the age of the Universe". In: *Monthly Notices of the Royal Astronomical Society* 495.4 (July 2020), pp. 3571–3575. DOI: 10.1093/mnras/staa1082.

[137] S. W. Henderson et al. "Advanced ACTPol Cryogenic Detector Arrays and Readout". In: *Journal of Low Temperature Physics* 184.3-4 (Aug. 2016), pp. 772–779. DOI: 10.1007/s10909-016-1575-z.

[138] M. Hennemann et al. "The spine of the swan: a Herschel study of the DR21 ridge and filaments in Cygnus X". In: *Astronomy & Astrophysics* 543, L3 (July 2012), p. L3. DOI: 10.1051/0004-6361/201219429. arXiv: 1206.1243 [astro-ph.GA].

[139] Roger H. Hildebrand. "Magnetic fields and stardust". In: *Quarterly Journal of the Royal Astronomical Society* 29 (Sept. 1988), pp. 327–351.

[140] Charles A. Hill et al. "Design and development of an ambient-temperature continuously-rotating achromatic half-wave plate for CMB polarization modulation on the POLARBEAR-2 experiment". In: *Millimeter, Submillimeter, and Far-Infrared Detectors and Instrumentation for Astronomy VIII*. Ed. by Wayne S. Holland and Jonas Zmuidzinas. Vol. 9914. Society of Photo-Optical Instrumentation Engineers (SPIE) Conference Series. July 2016, 99142U, 99142U. DOI: 10.1117/12.2232280. arXiv: 1607.07399 [astro-ph.IM].

[141] G. Hinshaw et al. "Nine-year Wilkinson Microwave Anisotropy Probe (WMAP) Observations: Cosmological Parameter Results". In: *The Astrophysical Journal Supplement Series* 208.2, 19 (Oct. 2013), p. 19. DOI: 10.1088/0067-0049/208/2/19. arXiv: 1212.5226 [astro-ph.CO].

[142] J. Hlavacek-Larrondo et al. "Extreme AGN feedback in the MAssive Cluster Survey: a detailed study of X-ray cavities at z>0.3". In: *Monthly Notices of the Royal Astronomical Society* 421.2 (Apr. 2012), pp. 1360–1384. DOI: 10.1111/j.1365-2966.2011.20405.x. arXiv: 1110.0489 [astro-ph.CO].

[143] Thiem Hoang, B. T. Draine, and A. Lazarian. "Improving the Model of Emission from Spinning Dust: Effects of Grain Wobbling and Transient Spin-up". In: *The Astrophysical Journal* 715.2 (June 2010), pp. 1462–1485. DOI: 10.1088/0004-637X/715/2/1462. arXiv: 1003.2638 [astro-ph.GA].

[144] Thuong D. Hoang et al. "Testbed preparation of a small prototype polarization modulator for LiteBIRD Low-Frequency Telescope". In: *Millimeter, Submillimeter, and Far-Infrared Detectors and Instrumentation for Astronomy XI*. Ed. by Jonas Zmuidzinas and Jian-Rong Gao. Vol. 12190. Society of Photo-Optical Instrumentation Engineers (SPIE) Conference Series. Aug. 2022, 121902O, 121902O. DOI: 10.1117/12.2630653. arXiv: 2208.03673 [astro-ph.IM].

[145] Shunsuke Honda et al. "On-site performance of GroundBIRD, a CMB polarization telescope for large angular scale observations". In: *Ground-based and Airborne Telescopes VIII*. Ed. by Heather K. Marshall, Jason Spyromilio, and Tomonori Usuda. Vol. 11445. Society of Photo-Optical Instrumentation Engineers (SPIE) Conference Series. Dec. 2020, 114457Q, 114457Q. DOI: 10.1117/12.2560918.

[146] Dieter Horns et al. “Searching for WISPy cold dark matter with a dish antenna”. In: *Journal of Cosmology and Astroparticle Physics* 2013.4, 016 (Apr. 2013), p. 016. DOI: 10.1088/1475-7516/2013/04/016. arXiv: 1212.2970 [hep-ph].

[147] Martin Houde et al. “Characterizing Magnetized Turbulence in M51”. In: *The Astrophysical Journal* 766.1, 49 (Mar. 2013), p. 49. DOI: 10.1088/0004-637X/766/1/49. arXiv: 1301.7508 [astro-ph.GA].

[148] Wayne Hu and Scott Dodelson. “Cosmic Microwave Background Anisotropies”. In: *Annual Review of Astronomy and Astrophysics* 40 (Jan. 2002), pp. 171–216. DOI: 10.1146/annurev.astro.40.060401.093926. arXiv: astro-ph/0110414 [astro-ph].

[149] Wayne Hu, Naoshi Sugiyama, and Joseph Silk. “The physics of microwave background anisotropies”. In: *Nature* 386.6620 (Mar. 1997), pp. 37–43. DOI: 10.1038/386037a0. arXiv: astro-ph/9504057 [astro-ph].

[150] Kevin Huffenberger et al. “Measuring Planck Beams with Planets”. In: *American Astronomical Society Meeting Abstracts #216*. Vol. 216. American Astronomical Society Meeting Abstracts. May 2010, 318.01, p. 318.01.

[151] Charles L. H. Hull and Qizhou Zhang. “Interferometric observations of magnetic fields in forming stars”. In: *Frontiers in Astronomy and Space Sciences* 6, 3 (Mar. 2019), p. 3. DOI: 10.3389/fspas.2019.00003. arXiv: 1903.03177 [astro-ph.SR].

[152] Charles L. H. Hull et al. “TADPOL: A 1.3 mm Survey of Dust Polarization in Star-forming Cores and Regions”. In: *The Astrophysical Journal Supplement Series* 213.1, 13 (July 2014), p. 13. DOI: 10.1088/0067-0049/213/1/13. arXiv: 1310.6653 [astro-ph.SR].

[153] K. D. Irwin and G. C. Hilton. “Transition-Edge Sensors”. In: *Cryogenic Particle Detection*. Ed. by Christian Enss. Vol. 99. 2005, p. 63. DOI: 10.1007/10933596_3.

[154] Joerg Jaeckel and Javier Redondo. “An antenna for directional detection of WISPy dark matter”. In: *Journal of Cosmology and Astroparticle Physics* 2013.11, 016 (Nov. 2013), p. 016. DOI: 10.1088/1475-7516/2013/11/016. arXiv: 1307.7181 [hep-ph].

[155] Joerg Jaeckel and Andreas Ringwald. “The Low-Energy Frontier of Particle Physics”. In: *Annual Review of Nuclear and Particle Science* 60 (Nov. 2010), pp. 405–437. DOI: 10.1146/annurev.nucl.012809.104433. arXiv: 1002.0329 [hep-ph].

[156] Svetlana G. Jorstad et al. “Polarimetric Observations of 15 Active Galactic Nuclei at High Frequencies: Jet Kinematics from Bimonthly Monitoring with the Very Long Baseline Array”. In: *The Astronomical Journal* 130.4 (Oct. 2005), pp. 1418–1465. DOI: 10.1086/444593. arXiv: astro-ph/0502501 [astro-ph].

[157] G. Jungman, M. Kamionkowski, and K. Griest. “Supersymmetric dark matter”. In: *Physics Reports* 267 (Mar. 1996), pp. 195–373. DOI: 10.1016/0370-1573(95)00058-5. arXiv: hep-ph/9506380 [hep-ph].

[158] N. Kaiser. “Small-angle anisotropy of the microwave background radiation in the adiabatic theory”. In: *Monthly Notices of the Royal Astronomical Society* 202 (Mar. 1983), pp. 1169–1180. DOI: 10.1093/mnras/202.4.1169.

[159] Marc Kamionkowski, Arthur Kosowsky, and Albert Stebbins. “Statistics of cosmic microwave background polarization”. In: *Physical Review D* 55.12 (June 1997), pp. 7368–7388. DOI: 10.1103/PhysRevD.55.7368. arXiv: astro-ph/9611125 [astro-ph].

[160] Marc Kamionkowski and Ely D. Kovetz. "The Quest for B Modes from Inflationary Gravitational Waves". In: *Annual Review of Astronomy and Astrophysics* 54 (Sept. 2016), pp. 227–269. DOI: 10.1146/annurev-astro-081915-023433. arXiv: 1510.06042 [astro-ph.CO].

[161] K. S. Karkare et al. "SPT-SLIM: A Line Intensity Mapping Pathfinder for the South Pole Telescope". In: *Journal of Low Temperature Physics* 209.5-6 (Dec. 2022), pp. 758–765. DOI: 10.1007/s10909-022-02702-2. arXiv: 2111.04631 [astro-ph.IM].

[162] J. P. Kaufman et al. "Self-calibration of BICEP1 three-year data and constraints on astrophysical polarization rotation". In: *Physical Review D* 89.6, 062006 (Mar. 2014), p. 062006. DOI: 10.1103/PhysRevD.89.062006. arXiv: 1312.7877 [astro-ph.IM].

[163] Brian G. Keating, Meir Shimon, and Amit P. S. Yadav. "Self-calibration of Cosmic Microwave Background Polarization Experiments". In: *The Astrophysical Journal Letters* 762.2, L23 (Jan. 2013), p. L23. DOI: 10.1088/2041-8205/762/2/L23. arXiv: 1211.5734 [astro-ph.CO].

[164] R. C. Kennicutt Jr. et al., eds. *Galaxies: Interactions and Induced Star Formation*. Jan. 1998.

[165] Naoya Kitajima and Kazunori Nakayama. "Dark photon dark matter from cosmic strings and gravitational wave background". In: *Journal of High Energy Physics* 2023.8, 68 (Aug. 2023), p. 68. DOI: 10.1007/JHEP08(2023)068. arXiv: 2212.13573 [hep-ph].

[166] Stefan Knirck et al. "First results from a hidden photon dark matter search in the meV sector using a plane-parabolic mirror system". In: *Journal of Cosmology and Astroparticle Physics* 2018.11, 031 (Nov. 2018), p. 031. DOI: 10.1088/1475-7516/2018/11/031. arXiv: 1806.05120 [hep-ex].

[167] A. Kogut et al. "Three-Year Wilkinson Microwave Anisotropy Probe (WMAP) Observations: Foreground Polarization". In: *The Astrophysical Journal* 665.1 (Aug. 2007), pp. 355–362. DOI: 10.1086/519754. arXiv: 0704.3991 [astro-ph].

[168] Edward W. Kolb and Andrew J. Long. "Completely dark photons from gravitational particle production during the inflationary era". In: *Journal of High Energy Physics* 2021.3, 283 (Mar. 2021), p. 283. DOI: 10.1007/JHEP03(2021)283. arXiv: 2009.03828 [astro-ph.CO].

[169] Edward W. Kolb and Michael S. Turner. *The early universe*. Vol. 69. 1990.

[170] Eiichiro Komatsu. "New physics from the polarized light of the cosmic microwave background". In: *Nature Reviews Physics* 4.7 (July 2022), pp. 452–469. DOI: 10.1038/s42254-022-00452-4. arXiv: 2202.13919 [astro-ph.CO].

[171] S. W. Kosowski. "A new theory of distant star brightness built upon the theoretical finding of a distant source acceleration effect." In: *Physics Essays* 9.2 (Jan. 1996), pp. 189–204. DOI: 10.4006/1.3029226.

[172] A. Kosowsky. "Cosmic microwave background polarization." In: *Annals of Physics* 246.1 (Feb. 1996), pp. 49–85. DOI: 10.1006/aphy.1996.0020. arXiv: astro-ph/9501045 [astro-ph].

[173] Julian H. Krolik. *Active galactic nuclei : from the central black hole to the galactic environment*. 1999.

[174] S. Kurtz et al. "Ultracompact HII Regions: A Molecular Point of View". In: *American Astronomical Society Meeting Abstracts #184*. Vol. 184. American Astronomical Society Meeting Abstracts. May 1994, 30.13, p. 30.13.

[175] Brian C. Lacki and Todd A. Thompson. "The Physics of the Far-infrared-Radio Correlation. II. Synchrotron Emission as a Star Formation Tracer in High-redshift Galaxies". In: *The Astrophysical Journal* 717.1 (July 2010), pp. 196–208. DOI: 10.1088/0004-637X/717/1/196. arXiv: 0910.0478 [astro-ph.CO].

[176] Bahia Si Lakhal and Ameur Guezmir. "The Horizon Problem". In: *Journal of Physics Conference Series*. Vol. 1269. Journal of Physics Conference Series. IOP, July 2019, 012017, p. 012017. DOI: 10.1088/1742-6596/1269/1/012017.

[177] Oliver P. Lay and Nils W. Halverson. "The Impact of Atmospheric Fluctuations on Degree-Scale Imaging of the Cosmic Microwave Background". In: *The Astrophysical Journal* 543.2 (Nov. 2000), pp. 787–798. DOI: 10.1086/317115. arXiv: astro-ph/9905369 [astro-ph].

[178] A. Lazarian and Thiem Hoang. "Subsonic Mechanical Alignment of Irregular Grains". In: *The Astrophysical Journal Letters* 669.2 (Nov. 2007), pp. L77–L80. DOI: 10.1086/523849. arXiv: 0707.3805 [astro-ph].

[179] A. Lazarian et al. "Reconnection in Turbulent Astrophysical Fluids". In: *8th International Conference of Numerical Modeling of Space Plasma Flows (ASTRONUM 2013)*. Ed. by N. V. Pogorelov, E. Audit, and G. P. Zank. Vol. 488. Astronomical Society of the Pacific Conference Series. Sept. 2014, p. 23. DOI: 10.48550/arXiv.1408.3134. arXiv: 1408.3134 [astro-ph.SR].

[180] Valentin J. M. Le Gouellec et al. "New Insights on the Accretion Properties of Class 0 Protostars from 2 μm Spectroscopy". In: *The Astrophysical Journal* 966.1, 91 (May 2024), p. 91. DOI: 10.3847/1538-4357/ad2935. arXiv: 2401.16532 [astro-ph.SR].

[181] K. Lee et al. "GroundBIRD: A CMB Polarization Experiment with MKID Arrays". In: *Journal of Low Temperature Physics* 200.5-6 (Aug. 2020), pp. 384–391. DOI: 10.1007/s10909-020-02511-5. arXiv: 2011.07705 [astro-ph.IM].

[182] LiteBIRD Collaboration et al. "Probing cosmic inflation with the LiteBIRD cosmic microwave background polarization survey". In: *Progress of Theoretical and Experimental Physics* 2023.4, 042F01 (Apr. 2023), 042F01. DOI: 10.1093/ptep/ptac150. arXiv: 2202.02773 [astro-ph.IM].

[183] Jesse Liu et al. "Broadband Solenoidal Haloscope for Terahertz Axion Detection". In: *Physical Review Letters* 128.13, 131801 (Apr. 2022), p. 131801. DOI: 10.1103/PhysRevLett.128.131801. arXiv: 2111.12103 [physics.ins-det].

[184] L. Liu. "The monopole problem and the primordial black hole problem in the inflationary universe." In: *Chinese Physics Letters* 4.3 (Jan. 1987), pp. 136–138. DOI: 10.1088/0256-307X/4/3/011.

[185] Andrew J. Long and Lian-Tao Wang. "Dark photon dark matter from a network of cosmic strings". In: *Physical Review D* 99.6, 063529 (Mar. 2019), p. 063529. DOI: 10.1103/PhysRevD.99.063529. arXiv: 1901.03312 [hep-ph].

[186] Thibaut Louis et al. "The Atacama Cosmology Telescope: DR6 Power Spectra, Likelihoods and ΛCDM Parameters". In: *arXiv e-prints*, arXiv:2503.14452 (Mar. 2025), arXiv:2503.14452. DOI: 10.48550/arXiv.2503.14452. arXiv: 2503.14452 [astro-ph.CO].

[187] N. Macellari et al. "Galactic foreground contributions to the 5-year Wilkinson Microwave Anisotropy Probe maps". In: *Monthly Notices of the Royal Astronomical Society* 418.2 (Dec. 2011), pp. 888–905. DOI: 10.1111/j.1365-2966.2011.19542.x. arXiv: 1108.0205 [astro-ph.GA].

[188] J. F. Macías-Pérez et al. "KISS: Instrument Description and Performance". In: *Publications of the Astronomical Society of the Pacific* 136.11, 114505 (Nov. 2024), p. 114505. DOI: 10.1088/1538-3873/ad8189. arXiv: 2409.20272 [astro-ph.IM].

[189] G. Marsden et al. "The Balloon-borne Large-Aperture Submillimeter Telescope for polarization: BLAST-pol". In: *Millimeter and Submillimeter Detectors and Instrumentation for Astronomy IV*. Ed. by William D. Duncan et al. Vol. 7020. Society of Photo-Optical Instrumentation Engineers (SPIE) Conference Series. July 2008, 702002, p. 702002. DOI: 10.1117/12.788413. arXiv: 0805.4420 [astro-ph].

[190] David J. E. Marsh. "Axion cosmology". In: *Physics Reports* 643 (July 2016), pp. 1–79. DOI: 10.1016/j.physrep.2016.06.005.

[191] J. C. Mather et al. "Measurement of the Cosmic Microwave Background Spectrum by the COBE FIRAS Instrument". In: *The Astrophysical Journal* 420 (Jan. 1994), p. 439. DOI: 10.1086/173574.

[192] L. D. Matthews and Kenneth Wood. "Modeling the Interstellar Medium of Low Surface Brightness Galaxies: Constraining Internal Extinction, Disk Color Gradients, and Intrinsic Rotation Curve Shapes". In: *The Astrophysical Journal* 548.1 (Feb. 2001), pp. 150–171. DOI: 10.1086/318687. arXiv: astro-ph/0010033 [astro-ph].

[193] F. Mayet et al. "A review of the discovery reach of directional Dark Matter detection". In: *Physics Reports* 627 (Apr. 2016), pp. 1–49. DOI: 10.1016/j.physrep.2016.02.007. arXiv: 1602.03781 [astro-ph.CO].

[194] Benjamin A. Mazin. "Superconducting Materials for Microwave Kinetic Inductance Detectors". In: *arXiv e-prints*, arXiv:2004.14576 (Apr. 2020), arXiv:2004.14576. DOI: 10.48550/arXiv.2004.14576. arXiv: 2004.14576 [astro-ph.IM].

[195] Christopher F. McKee and Eve C. Ostriker. "Theory of Star Formation". In: *Annual Review of Astronomy and Astrophysics* 45.1 (Sept. 2007), pp. 565–687. DOI: 10.1146/annurev.astro.45.051806.110602. arXiv: 0707.3514 [astro-ph].

[196] Fulvio Melia. "The Friedmann-Lemaître-Robertson-Walker metric". In: *Modern Physics Letters A* 37.3, 2250016 (Jan. 2022), p. 2250016. DOI: 10.1142/S021773232250016X.

[197] C. Meny et al. "Far-infrared to millimeter astrophysical dust emission. I. A model based on physical properties of amorphous solids". In: *Astronomy & Astrophysics* 468.1 (June 2007), pp. 171–188. DOI: 10.1051/0004-6361:20065771. arXiv: astro-ph/0701226 [astro-ph].

[198] Yuto Minami and Eiichiro Komatsu. "Simultaneous determination of the cosmic birefringence and miscalibrated polarization angles II: Including cross-frequency spectra". In: *Progress of Theoretical and Experimental Physics* 2020.10, 103E02 (Oct. 2020), 103E02. DOI: 10.1093/ptep/ptaa130. arXiv: 2006.15982 [astro-ph.CO].

[199] Kayla Mitchell, Darcy Barron, and Polarbear Collaboration. "Measuring Cosmic Microwave Background Polarization with POLARBEAR". In: *The 35th Annual New Mexico Symposium*. Ed. by A. D. Kapinska. Feb. 2020, p. 9.

[200] S. Molinari et al. "Hi-GAL: The Herschel Infrared Galactic Plane Survey". In: *Publications of the Astronomical Society of the Pacific* 122.889 (Mar. 2010), p. 314. DOI: 10.1086/651314. arXiv: 1001.2106 [astro-ph.GA].

[201] A. Monfardini et al. "Kinetic Inductance Detectors development for mm-wave Astronomy". In: *EAS Publications Series*. Ed. by P. Kern. Vol. 37. EAS Publications Series. Jan. 2009, pp. 95–99. DOI: 10.1051/eas/0937011.

[202] A. Monfardini et al. "NIKA: A millimeter-wave kinetic inductance camera". In: *Astronomy & Astrophysics* 521, A29 (Oct. 2010), A29. DOI: 10.1051/0004-6361/201014727. arXiv: 1004.2209 [astro-ph.IM].

[203] A. Monfardini et al. "A Dual-band Millimeter-wave Kinetic Inductance Camera for the IRAM 30 m Telescope". In: *The Astrophysical Journal Supplement Series* 194.2, 24 (June 2011), p. 24. DOI: 10.1088/0067-0049/194/2/24. arXiv: 1102.0870 [astro-ph.IM].

[204] Alessandro Monfardini et al. "Lumped element kinetic inductance detectors for space applications". In: *Millimeter, Submillimeter, and Far-Infrared Detectors and Instrumentation for Astronomy VIII*. Ed. by Wayne S. Holland and Jonas Zmuidzinas. Vol. 9914. Society of Photo-Optical Instrumentation Engineers (SPIE) Conference Series. July 2016, 99140N, 99140N. DOI: 10.1117/12.2231758. arXiv: 1606.00719 [astro-ph.IM].

[205] F. Motte et al. "The unexpectedly large proportion of high-mass star-forming cores in a Galactic mini-starburst". In: *Nature Astronomy* 2 (Apr. 2018), pp. 478–482. DOI: 10.1038/s41550-018-0452-x. arXiv: 1804.02392 [astro-ph.GA].

[206] Telemachos Ch. Mouschovias and Glenn E. Ciolek. "Magnetic Fields and Star Formation: A Theory Reaching Adulthood". In: *The Origin of Stars and Planetary Systems*. Ed. by Charles J. Lada and Nikolaos D. Kylafis. Vol. 540. NATO Advanced Study Institute (ASI) Series C. Jan. 1999, p. 305.

[207] A. Moyer-Anin et al. "Toward the first cosmological results of the NIKA2 Sunyaev-Zeldovich Large Program: The SZ-Mass scaling relation". In: *arXiv e-prints*, arXiv:2409.00977 (Sept. 2024), arXiv:2409.00977. DOI: 10.48550/arXiv.2409.00977. arXiv: 2409.00977 [astro-ph.CO].

[208] M. Muñoz-Echeverría et al. "Galaxy cluster mass bias from projected mass maps. THE THREE HUNDRED-NIKA2 LPSZ twin samples". In: *Astronomy & Astrophysics* 682, A124 (Feb. 2024), A124. DOI: 10.1051/0004-6361/202346986. arXiv: 2305.14862 [astro-ph.CO].

[209] V. F. Mukhanov and G. V. Chibisov. "Quantum fluctuations and a nonsingular universe". In: *Soviet Journal of Experimental and Theoretical Physics Letters* 33 (May 1981), p. 532.

[210] Sigurd Naess et al. "The Atacama Cosmology Telescope: arcminute-resolution maps of 18 000 square degrees of the microwave sky from ACT 2008-2018 data combined with Planck". In: *Journal of Cosmology and Astroparticle Physics* 2020.12, 046 (Dec. 2020), p. 046. DOI: 10.1088/1475-7516/2020/12/046. arXiv: 2007.07290 [astro-ph.IM].

[211] Sigurd Naess et al. "The Atacama Cosmology Telescope: DR6 Maps". In: *arXiv e-prints*, arXiv:2503.14451 (Mar. 2025), arXiv:2503.14451. DOI: 10.48550/arXiv.2503.14451. arXiv: 2503.14451 [astro-ph.CO].

[212] T. Nagasaki et al. "GroundBIRD: Observation of CMB Polarization with a Rapid Scanning and MKIDs". In: *Journal of Low Temperature Physics* 193.5-6 (Dec. 2018), pp. 1066–1074. DOI: 10.1007/s10909-018-2077-y.

[213] Hiromasa Nakatsuka, Toshiya Namikawa, and Eiichiro Komatsu. "Is cosmic birefringence due to dark energy or dark matter? A tomographic approach". In: *Physical Review D* 105.12, 123509 (June 2022), p. 123509. DOI: 10.1103/PhysRevD.105.123509. arXiv: 2203.08560 [astro-ph.CO].

[214] Federico Nati et al. "POLOCALC: A Novel Method to Measure the Absolute Polarization Orientation of the Cosmic Microwave Background". In: *Journal of Astronomical Instrumentation* 6.2, 1740008 (June 2017), p. 1740008. DOI: 10.1142/S2251171717400086. arXiv: 1704.02704 [astro-ph.IM].

[215] Ann E. Nelson and Jakub Scholtz. "Dark light, dark matter, and the misalignment mechanism". In: *Physical Review D* 84.10, 103501 (Nov. 2011), p. 103501. DOI: 10.1103/PhysRevD.84.103501. arXiv: 1105.2812 [hep-ph].

[216] Hagai Netzer. *The Physics and Evolution of Active Galactic Nuclei*. 2013.

[217] Q. Nguyen Luong et al. "W43: the closest molecular complex of the Galactic bar?" In: *Astronomy & Astrophysics* 529, A41 (May 2011), A41. DOI: 10.1051/0004-6361/201016271. arXiv: 1102.3460 [astro-ph.SR].

[218] Q. Nguyen-Lu'o'ng et al. "Low-velocity Shocks Traced by Extended SiO Emission along the W43 Ridges: Witnessing the Formation of Young Massive Clusters". In: *The Astrophysical Journal* 775.2, 88 (Oct. 2013), p. 88. DOI: 10.1088/0004-637X/775/2/88. arXiv: 1306.0547 [astro-ph.GA].

[219] Q. Nguyen-Luong et al. "NIKA2 observations of dust grain evolution from star-forming filament to T-Tauri disk: Preliminary results from NIKA2 observations of the Taurus B211/B213 filament". In: *mm Universe 2023 - Observing the Universe at mm Wavelengths*. Vol. 293. European Physical Journal Web of Conferences. June 2024, 00035, p. 00035. DOI: 10.1051/epjconf/202429300035. arXiv: 2310.16526 [astro-ph.SR].

[220] Satoshi Nozawa, Naoki Itoh, and Yasuharu Kohyama. "Relativistic Thermal Bremsstrahlung Gaunt Factor for the Intracluster Plasma. II. Heavy Elements". In: *arXiv e-prints*, astro-ph/9804204 (Apr. 1998), astro–ph/9804204. DOI: 10.48550/arXiv.astro-ph/9804204. arXiv: astro-ph/9804204 [astro-ph].

[221] S. Oguri et al. "GroundBIRD: Observing Cosmic Microwave Polarization at Large Angular Scale with Kinetic Inductance Detectors and High-Speed Rotating Telescope". In: *Journal of Low Temperature Physics* 184.3-4 (Aug. 2016), pp. 786–792. DOI: 10.1007/s10909-015-1420-9.

[222] Shugo Oguri et al. "GroundBIRD: observations of CMB polarization with fast scan modulation and MKIDs". In: *Ground-based and Airborne Telescopes VI*. Ed. by Helen J. Hall, Roberto Gilmozzi, and Heather K. Marshall. Vol. 9906. Society of Photo-Optical Instrumentation Engineers (SPIE) Conference Series. July 2016, 99063L, p. 99063L. DOI: 10.1117/12.2231672.

[223] A. Omont et al. "A 1.2 mm MAMBO/IRAM-30 m survey of dust emission from the highest redshift PSS quasars". In: *Astronomy & Astrophysics* 374 (Aug. 2001), pp. 371–381. DOI: 10.1051/0004-6361:20010721. arXiv: astro-ph/0107005 [astro-ph].

[224] Eve C. Ostriker, James M. Stone, and Charles F. Gammie. "Density, Velocity, and Magnetic Field Structure in Turbulent Molecular Cloud Models". In: *The Astrophysical Journal* 546.2 (Jan. 2001), pp. 980–1005. DOI: 10.1086/318290. arXiv: astro-ph/0008454 [astro-ph].

[225] S. Padin et al. "South Pole Telescope optics". In: *Applied Optics* 47.24 (Aug. 2008), pp. 4418–4428. DOI: 10.1364/AO.47.004418.

[226] A. Paiella et al. "Kinetic Inductance Detectors and readout electronics for the OLIMPO experiment". In: *Journal of Physics Conference Series*. Vol. 1182. Journal of Physics Conference Series. IOP, Feb. 2019, 012005, p. 012005. DOI: 10.1088/1742-6596/1182/1/012005. arXiv: 1904.01890 [astro-ph.IM].

[227] Scott Paine. *The am atmospheric model*. Version 12.2. July 2022. DOI: 10.5281/zenodo.6774378.

[228] A. Paliwal et al. "Exploiting high-resolution NIKA2 data to study the intracluster medium and dynamical state of ACT-CL J0240.0+0116". In: *Astronomy & Astrophysics* 698, A2 (June 2025), A2. DOI: 10.1051/0004-6361/202452597. arXiv: 2410.11668 [astro-ph.CO].

[229] P. Palmeirim et al. "Herschel view of the Taurus B211/3 filament and striations: evidence of filamentary growth?" In: *Astronomy & Astrophysics* 550, A38 (Feb. 2013), A38. DOI: 10.1051/0004-6361/201220500. arXiv: 1211.6360 [astro-ph.SR].

[230] Juan R. Pardo. "ATM, the reference atmospheric radiative transfer model for ALMA". In: *ALMA Development Workshop*. June 2019, 36, p. 36. DOI: 10.5281/zenodo.3240379.

[231] P. J. E. Peebles. "Recombination of the Primeval Plasma". In: *The Astrophysical Journal* 153 (July 1968), p. 1. DOI: 10.1086/149628.

[232] P. J. E. Peebles. *Principles of Physical Cosmology*. 1993. DOI: 10.1515/9780691206721.

[233] A. A. Penzias and R. W. Wilson. "A Measurement of Excess Antenna Temperature at 4080 Mc/s." In: *The Astrophysical Journal* 142 (July 1965), pp. 419–421. DOI: 10.1086/148307.

[234] A. Pereyra and A. M. Magalhães. "Polarimetry toward the Musca Dark Cloud. I. The Catalog". In: *The Astrophysical Journal* 603.2 (Mar. 2004), pp. 584–594. DOI: 10.1086/381702.

[235] L. Perotto et al. "Calibration and performance of the NIKA2 camera at the IRAM 30-m Telescope". In: *Astronomy & Astrophysics* 637, A71 (May 2020), A71. DOI: 10.1051/0004-6361/201936220. arXiv: 1910.02038 [astro-ph.IM].

[236] T. Pillai et al. "Magnetic Fields in High-mass Infrared Dark Clouds". In: *The Astrophysical Journal* 799.1, 74 (Jan. 2015), p. 74. DOI: 10.1088/0004-637X/799/1/74. arXiv: 1410.7390 [astro-ph.GA].

[237] G. Pisano et al. "Development and application of metamaterial-based half-wave plates for the NIKA and NIKA2 polarimeters". In: *Astronomy & Astrophysics* 658, A24 (Feb. 2022), A24. DOI: 10.1051/0004-6361/202038643. arXiv: 2006.12081 [astro-ph.IM].

[238] Planck Collaboration et al. "Planck 2013 results. XII. Diffuse component separation". In: *Astronomy & Astrophysics* 571, A12 (Nov. 2014), A12. DOI: 10.1051/0004-6361/201321580. arXiv: 1303.5072 [astro-ph.CO].

[239] Planck Collaboration et al. "Planck 2013 results. XVI. Cosmological parameters". In: *Astronomy & Astrophysics* 571, A16 (Nov. 2014), A16. DOI: 10.1051/0004-6361/201321591. arXiv: 1303.5076 [astro-ph.CO].

[240] Planck Collaboration et al. "Planck 2013 results. XXII. Constraints on inflation". In: *Astronomy & Astrophysics* 571, A22 (Nov. 2014), A22. DOI: 10.1051/0004-6361/201321569. arXiv: 1303.5082 [astro-ph.CO].

[241] Planck Collaboration et al. "Planck intermediate results. XXI. Comparison of polarized thermal emission from Galactic dust at 353 GHz with interstellar polarization in the visible". In: *Astronomy & Astrophysics* 576, A106 (Apr. 2015), A106. DOI: 10.1051/0004-6361/201424087. arXiv: 1405.0873 [astro-ph.GA].

[242] Planck Collaboration et al. "Planck 2015 results. X. Diffuse component separation: Foreground maps". In: *Astronomy & Astrophysics* 594, A10 (Sept. 2016), A10. DOI: 10.1051/0004-6361/201525967. arXiv: 1502.01588 [astro-ph.CO].

[243] Planck Collaboration et al. "Planck 2015 results. XIX. Constraints on primordial magnetic fields". In: *Astronomy & Astrophysics* 594, A19 (Sept. 2016), A19. DOI: 10.1051/0004-6361/201525821. arXiv: 1502.01594 [astro-ph.CO].

[244] Planck Collaboration et al. "Planck 2015 results. XXV. Diffuse low-frequency Galactic foregrounds". In: *Astronomy & Astrophysics* 594, A25 (Sept. 2016), A25. DOI: 10.1051/0004-6361/201526803. arXiv: 1506.06660 [astro-ph.GA].

[245] Planck Collaboration et al. "Planck intermediate results. XLVI. Reduction of large-scale systematic effects in HFI polarization maps and estimation of the reionization optical depth". In: *Astronomy & Astrophysics* 596, A107 (Dec. 2016), A107. DOI: 10.1051/0004-6361/201628890. arXiv: 1605.02985 [astro-ph.CO].

[246] Planck Collaboration et al. "Planck 2018 results. I. Overview and the cosmological legacy of Planck". In: *Astronomy & Astrophysics* 641, A1 (Sept. 2020), A1. DOI: 10.1051/0004-6361/201833880. arXiv: 1807.06205 [astro-ph.CO].

[247] Planck Collaboration et al. "Planck 2018 results. III. High Frequency Instrument data processing and frequency maps". In: *Astronomy & Astrophysics* 641, A3 (Sept. 2020), A3. DOI: 10.1051/0004-6361/201832909. arXiv: 1807.06207 [astro-ph.CO].

[248] Planck Collaboration et al. "Planck 2018 results. IV. Diffuse component separation". In: *Astronomy & Astrophysics* 641, A4 (Sept. 2020), A4. DOI: 10.1051/0004-6361/201833881. arXiv: 1807.06208 [astro-ph.CO].

[249] Planck Collaboration et al. "Planck 2018 results. IV. Diffuse component separation". In: *Astronomy & Astrophysics* 641, A4 (Sept. 2020), A4. DOI: 10.1051/0004-6361/201833881. arXiv: 1807.06208 [astro-ph.CO].

[250] Planck Collaboration et al. "Planck 2018 results. V. CMB power spectra and likelihoods". In: *Astronomy & Astrophysics* 641, A5 (Sept. 2020), A5. DOI: 10.1051/0004-6361/201936386. arXiv: 1907.12875 [astro-ph.CO].

[251] Planck Collaboration et al. "Planck 2018 results. VI. Cosmological parameters". In: *Astronomy & Astrophysics* 641, A6 (Sept. 2020), A6. DOI: 10.1051/0004-6361/201833910. arXiv: 1807.06209 [astro-ph.CO].

[252] Planck Collaboration et al. "Planck 2018 results. VII. Isotropy and statistics of the CMB". In: *Astronomy & Astrophysics* 641, A7 (Sept. 2020), A7. DOI: 10.1051/0004-6361/201935201. arXiv: 1906.02552 [astro-ph.CO].

[253] Planck Collaboration et al. "Planck 2018 results. X. Constraints on inflation". In: *Astronomy & Astrophysics* 641, A10 (Sept. 2020), A10. DOI: 10.1051/0004-6361/201833887. arXiv: 1807.06211 [astro-ph.CO].

[254] Planck Collaboration et al. "Planck 2018 results. XI. Polarized dust foregrounds". In: *Astronomy & Astrophysics* 641, A11 (Sept. 2020), A11. DOI: 10.1051/0004-6361/201832618. arXiv: 1801.04945 [astro-ph.GA].

[255] Planck Collaboration et al. "Planck 2018 results. XII. Galactic astrophysics using polarized dust emission". In: *Astronomy & Astrophysics* 641, A12 (Sept. 2020), A12. DOI: 10.1051/0004-6361/201833885. arXiv: 1807.06212 [astro-ph.GA].

[256] Levon Pogosian and Alex Zucca. "Searching for primordial magnetic fields with CMB B-modes". In: *Classical and Quantum Gravity* 35.12, 124004 (June 2018), p. 124004. DOI: 10.1088/1361-6382/aac398. arXiv: 1801.08936 [astro-ph.CO].

[257] Levon Edward Pogosian. "Formation and interactions of topological defects and their role in cosmology". PhD thesis. Case Western Reserve University, Ohio, July 2001.

[258] C. M. Posada et al. "Fabrication of large dual-polarized multichroic TES bolometer arrays for CMB measurements with the SPT-3G camera". In: *Superconductor Science Technology* 28.9, 094002 (Sept. 2015), p. 094002. DOI: 10.1088/0953-2048/28/9/094002.

[259] Maxim Pospelov, Adam Ritz, and Mikhail Voloshin. "Bosonic super-WIMPs as keV-scale dark matter". In: *Physical Review D* 78.11, 115012 (Dec. 2008), p. 115012. DOI: 10.1103/PhysRevD.78.115012. arXiv: 0807.3279 [hep-ph].

[260] Michele Redi and Andrea Tesi. "Dark photon Dark Matter without Stueckelberg mass". In: *Journal of High Energy Physics* 2022.10, 167 (Oct. 2022), p. 167. DOI: 10.1007/JHEP10(2022)167. arXiv: 2204.14274 [hep-ph].

[261] Javier Redondo. "Helioscope bounds on hidden sector photons". In: *Journal of Cosmology and Astroparticle Physics* 2008.7, 008 (July 2008), p. 008. DOI: 10.1088/1475-7516/2008/07/008. arXiv: 0801.1527 [hep-ph].

[262] Mathieu Remazeilles, Jacques Delabrouille, and Jean-François Cardoso. "Foreground component separation with generalized Internal Linear Combination". In: *Monthly Notices of the Royal Astronomical Society* 418.1 (Nov. 2011), pp. 467–476. DOI: 10.1111/j.1365-2966.2011.19497.x. arXiv: 1103.1166 [astro-ph.CO].

[263] Adam G. Riess et al. "A Comprehensive Measurement of the Local Value of the Hubble Constant with 1 km s^{-1} Mpc^{-1} Uncertainty from the Hubble Space Telescope and the SH0ES Team". In: *The Astrophysical Journal Letters* 934.1, L7 (July 2022), p. L7. DOI: 10.3847/2041-8213/ac5c5b. arXiv: 2112.04510 [astro-ph.CO].

[264] A. Ritacco et al. "First Polarised Light with the NIKA Camera". In: *Journal of Low Temperature Physics* 184.3-4 (Aug. 2016), pp. 724–732. DOI: 10.1007/s10909-015-1340-8. arXiv: 1508.00747 [astro-ph.IM].

[265] A. Ritacco et al. "Polarimetry at millimeter wavelengths with the NIKA camera: calibration and performance". In: *Astronomy & Astrophysics* 599, A34 (Mar. 2017), A34. DOI: 10.1051/0004-6361/201629666. arXiv: 1609.02042 [astro-ph.IM].

[266] A. Ritacco et al. "NIKA 150 GHz polarization observations of the Crab nebula and its spectral energy distribution". In: *Astronomy & Astrophysics* 616, A35 (Aug. 2018), A35. DOI: 10.1051/0004-6361/201731551. arXiv: 1804.09581 [astro-ph.CO].

[267] A. Ritacco et al. "NIKA 150 GHz polarization observations of the Crab nebula and its spectral energy distribution (Corrigendum)". In: *Astronomy & Astrophysics* 664, C1 (Aug. 2022), p. C1. DOI: 10.1051/0004-6361/201731551e.

[268] A. Ritacco et al. "Absolute Reference for Microwave Polarization Experiments. The COSMOCal Project and its Proof of Concept". In: *Publications of the Astronomical Society of the Pacific* 136.11, 115001 (Nov. 2024), p. 115001. DOI: 10.1088/1538-3873/ad8aed. arXiv: 2405.12135 [astro-ph.CO].

[269] M. Roesch et al. "Development of Lumped Element Kinetic Inductance Detectors for NIKA". In: *arXiv e-prints*, arXiv:1212.4585 (Dec. 2012), arXiv:1212.4585. DOI: 10.48550/arXiv.1212.4585. arXiv: 1212.4585 [astro-ph.IM].

[270] C. Rosset et al. "Planck pre-launch status: High Frequency Instrument polarization calibration". In: *Astronomy & Astrophysics* 520, A13 (Sept. 2010), A13. DOI: 10.1051/0004-6361/200913054. arXiv: 1004.2595 [astro-ph.CO].

[271] George B. Rybicki and Alan P. Lightman. *Radiative processes in astrophysics*. 1979.

[272] R. K. Sachs and A. M. Wolfe. "Perturbations of a Cosmological Model and Angular Variations of the Microwave Background". In: *The Astrophysical Journal* 147 (Jan. 1967), p. 73. DOI: 10.1086/148982.

[273] Yuki Sakurai et al. “Design and development of a polarization modulator unit based on a continuous rotating half-wave plate for LiteBIRD”. In: *Millimeter, Submillimeter, and Far-Infrared Detectors and Instrumentation for Astronomy IX*. Ed. by Jonas Zmuidzinas and Jian-Rong Gao. Vol. 10708. Society of Photo-Optical Instrumentation Engineers (SPIE) Conference Series. July 2018, 107080E, 107080E. DOI: 10.1117/12.2312391.

[274] Takanori Sato, Fuminobu Takahashi, and Masaki Yamada. “Gravitational production of dark photon dark matter with mass generated by the Higgs mechanism”. In: *Journal of Cosmology and Astroparticle Physics* 2022.8, 022 (Aug. 2022), p. 022. DOI: 10.1088/1475-7516/2022/08/022. arXiv: 2204.11896 [hep-ph].

[275] Giorgio Savini, Giampaolo Pisano, and Peter A. R. Ade. “Achromatic half-wave plate for submillimeter instruments in cosmic microwave background astronomy: modeling and simulation”. In: *Applied Optics* 45.35 (Dec. 2006), pp. 8907–8915. DOI: 10.1364/AO.45.008907.

[276] Sofia Savorgnano et al. “High-precision polarization measurements with Lumped Element Kinetic Inductance Detectors”. In: *arXiv e-prints*, arXiv:2506.23983 (June 2025), arXiv:2506.23983. DOI: 10.48550/arXiv.2506.23983. arXiv: 2506.23983 [astro-ph.IM].

[277] N. Schneider et al. “Understanding star formation in molecular clouds. IV. Column density PDFs from quiescent to massive molecular clouds”. In: *Astronomy & Astrophysics* 666, A165 (Oct. 2022), A165. DOI: 10.1051/0004-6361/202039610. arXiv: 2207.14604 [astro-ph.GA].

[278] Uroš Seljak. “Measuring Polarization in the Cosmic Microwave Background”. In: *The Astrophysical Journal* 482.1 (June 1997), pp. 6–16. DOI: 10.1086/304123. arXiv: astro-ph/9608131 [astro-ph].

[279] Uroš Seljak and Matias Zaldarriaga. “Signature of Gravity Waves in the Polarization of the Microwave Background”. In: *Physical Review Letters* 78.11 (Mar. 1997), pp. 2054–2057. DOI: 10.1103/PhysRevLett.78.2054. arXiv: astro-ph/9609169 [astro-ph].

[280] Meir Shimon et al. “CMB polarization systematics due to beam asymmetry: Impact on inflationary science”. In: *Physical Review D* 77.8, 083003 (Apr. 2008), p. 083003. DOI: 10.1103/PhysRevD.77.083003. arXiv: 0709.1513 [astro-ph].

[281] SHiP Collaboration et al. “Sensitivity of the SHiP experiment to dark photons decaying to a pair of charged particles”. In: *European Physical Journal C* 81.5, 451 (May 2021), p. 451. DOI: 10.1140/epjc/s10052-021-09224-3. arXiv: 2011.05115 [hep-ex].

[282] J. D. Soler et al. “An Imprint of Molecular Cloud Magnetization in the Morphology of the Dust Polarized Emission”. In: *The Astrophysical Journal* 774.2, 128 (Sept. 2013), p. 128. DOI: 10.1088/0004-637X/774/2/128. arXiv: 1303.1830 [astro-ph.GA].

[283] Lorenzo Sorbo. “Parity violation in the Cosmic Microwave Background from a pseudoscalar inflaton”. In: *Journal of Cosmology and Astroparticle Physics* 2011.6, 003 (June 2011), p. 003. DOI: 10.1088/1475-7516/2011/06/003. arXiv: 1101.1525 [astro-ph.CO].

[284] David N. Spergel. “Motion of the Earth and the detection of weakly interacting massive particles”. In: *Physical Review D* 37.6 (Mar. 1988), pp. 1353–1355. DOI: 10.1103/PhysRevD.37.1353.

[285] S. L. Stever et al. “Simulations of systematic effects arising from cosmic rays in the LiteBIRD space telescope, and effects on the measurements of CMB B-modes”. In: *Journal of Cosmology and Astroparticle Physics* 2021.9, 013 (Sept. 2021), p. 013. DOI: 10.1088/1475-7516/2021/09/013. arXiv: 2107.00473 [astro-ph.IM].

[286] R. A. Sunyaev and Ia. B. Zeldovich. "Microwave background radiation as a probe of the contemporary structure and history of the universe". In: *Annual Review of Astronomy and Astrophysics* 18 (Jan. 1980), pp. 537–560. DOI: 10.1146/annurev.aa.18.090180.002541.

[287] R. A. Sunyaev and Ya. B. Zeldovich. "Small-Scale Fluctuations of Relic Radiation". In: *Astrophysics and Space Science* 7.1 (Apr. 1970), pp. 3–19. DOI: 10.1007/BF00653471.

[288] J. C. Tan et al. "Massive Star Formation". In: *Protostars and Planets VI*. Ed. by Henrik Beuther et al. Jan. 2014, pp. 149–172. DOI: 10.2458/azu_uapress_9780816531240-ch007. arXiv: 1402.0919 [astro-ph.GA].

[289] Max Tegmark, Angélica de Oliveira-Costa, and Andrew J. Hamilton. "High resolution foreground cleaned CMB map from WMAP". In: *Physical Review D* 68.12, 123523 (Dec. 2003), p. 123523. DOI: 10.1103/PhysRevD.68.123523. arXiv: astro-ph/0302496 [astro-ph].

[290] Daniel B. Thomas, Nialh McCallum, and Michael L. Brown. "Controlling systematics in ground-based CMB surveys with partial boresight rotation". In: *Monthly Notices of the Royal Astronomical Society* 491.2 (Jan. 2020), pp. 1960–1969. DOI: 10.1093/mnras/stz2607. arXiv: 1905.12647 [astro-ph.CO].

[291] Michael Tinkham and Victor Emery. "Introduction to Superconductivity". In: *Physics Today* 49.10 (Jan. 1996), p. 74. DOI: 10.1063/1.2807811.

[292] Jeanne Treuttel et al. "1200 GHz High Spectral Resolution Receiver Front-End of Submillimeter Wave Instrument for JUpiter ICy Moon Explorer: Part I - RF Performance Optimization for Cryogenic Operation". In: *IEEE Transactions on Terahertz Science and Technology* 13.4 (July 2023), pp. 324–336. DOI: 10.1109/TTHZ.2023.3263623.

[293] M. Tristram et al. "Planck constraints on the tensor-to-scalar ratio". In: *Astronomy & Astrophysics* 647, A128 (Mar. 2021), A128. DOI: 10.1051/0004-6361/202039585. arXiv: 2010.01139 [astro-ph.CO].

[294] M. Tristram et al. "Cosmological parameters derived from the final Planck data release (PR4)". In: *Astronomy & Astrophysics* 682, A37 (Feb. 2024), A37. DOI: 10.1051/0004-6361/202348015. arXiv: 2309.10034 [astro-ph.CO].

[295] C. Megan Urry and Paolo Padovani. "Unified Schemes for Radio-Loud Active Galactic Nuclei". In: *Publications of the Astronomical Society of the Pacific* 107 (Sept. 1995), p. 803. DOI: 10.1086/133630. arXiv: astro-ph/9506063 [astro-ph].

[296] Jordan Wheeler et al. "SuperSpec, The On-Chip Spectrometer: Improved NEP and Antenna Performance". In: *Journal of Low Temperature Physics* 193.3-4 (Nov. 2018), pp. 408–414. DOI: 10.1007/s10909-018-1926-z.

[297] D. C. B. Whittet, ed. *Dust in the galactic environment*. Jan. 2003.

[298] K. Yamada et al. "The Simons Observatory: Cryogenic half wave plate rotation mechanism for the small aperture telescopes". In: *Review of Scientific Instruments* 95.2, 024504 (Feb. 2024), p. 024504. DOI: 10.1063/5.0178066. arXiv: 2309.14803 [astro-ph.IM].

[299] K. Yamada et al. "Erratum: "The Simons Observatory: Cryogenic half wave plate rotation mechanism for the small aperture telescopes" [Rev. Sci. Instrum. 95, 024504 (2024)]". In: *Review of Scientific Instruments* 96.1, 019901 (Jan. 2025), p. 019901. DOI: 10.1063/5.0252360.

[300] Matias Zaldarriaga. "Polarization of the microwave background in reionized models". In: *Physical Review D* 55.4 (Feb. 1997), pp. 1822–1829. DOI: 10.1103/PhysRevD.55.1822. arXiv: astro-ph/9608050 [astro-ph].

[301] Matias Zaldarriaga. "The Polarization of the Cosmic Microwave Background". In: *Measuring and Modeling the Universe*. Ed. by Wendy L. Freedman. Jan. 2004, p. 309. DOI: 10.48550/arXiv.astro-ph/0305272. arXiv: astro-ph/0305272 [astro-ph].

[302] Matias Zaldarriaga and Uroš Seljak. "All-sky analysis of polarization in the microwave background". In: *Physical Review D* 55.4 (Feb. 1997), pp. 1830–1840. DOI: 10.1103/PhysRevD.55.1830. arXiv: astro-ph/9609170 [astro-ph].

[303] Hans Zinnecker and Harold W. Yorke. "Toward Understanding Massive Star Formation". In: *Annual Review of Astronomy and Astrophysics* 45.1 (Sept. 2007), pp. 481–563. DOI: 10.1146/annurev.astro.44.051905.092549. arXiv: 0707.1279 [astro-ph].

[304] Jonas Zmuidzinas and Paul L. Richards. "Superconducting detectors and mixers for millimeter and submillimeter astrophysics". In: *IEEE Proceedings* 92.10 (Oct. 2004), pp. 1597–161.

[305] Jonas Zmuidzinas et al. "Multiplexable Kinetic Inductance Detectors". In: *Far-IR, Submm & MM Detector Technology Workshop*. Jan. 2002, 82, p. 82.

Abstract

This thesis focuses on experimental and observational advancements in millimeter-wave polarimetry using Lumped Element Kinetic Inductance Detectors (LEKIDs). A fully equipped facility was developed to assess the polarization performance of LEKIDs in a filled array configuration. The system achieved high-precision measurements, demonstrating a 6' accuracy in the reconstruction of the polarization angle, meeting the stringent requirements for next-generation Cosmic Microwave Background (CMB) experiments. The thesis also presents an observational study of the high-mass star-forming region W43, using data from the NIKA2 camera at the IRAM 30m telescope. A dedicated observing campaign was conducted, delivering high-quality maps of polarized dust emission. From these, a full reconstruction of the magnetic field morphology and intensity across the W43 region was obtained. A virial analysis showed that the densest clumps are in a state of global collapse, confirming their capacity to sustain high-mass star formation. Complementary developments include the design and in-lab validation of COSMOCal, a 260 GHz polarized source aimed at calibrating the absolute polarization angle. The system was successfully coupled to cryogenic receivers and validated with LEKIDs, paving the way for more robust calibration strategies in future polarimetry experiments. Finally, the versatility of LEKIDs was demonstrated in the context of dark matter searches. The Dandelion experiment aims to detect meV dark photons as dark matter candidates. Two data runs were conducted, leading to new exclusion limits of dark photons as dark matter candidates. Together, these efforts confirm the potential of LEKIDs for precision cosmology, bridging detector development, instrumental calibration, and astrophysical observations.

Résumé

Cette thèse porte sur les avancées expérimentales et observationnelles en polarimétrie dans le domaine des ondes millimétriques, en utilisant des détecteurs à inductance cinétique à éléments localisés (LEKIDs). Une installation complète a été développée pour évaluer les performances en polarisation des LEKIDs dans une configuration de plan focal rempli. Le système a permis d'obtenir des mesures de haute précision, atteignant une exactitude de 6' dans la reconstruction de l'angle de polarisation — répondant ainsi aux exigences des futures expériences sur le fond diffus cosmologique (CMB). La thèse présente également une étude observationnelle de la région de formation d'étoiles massives W43, à partir de données obtenues avec la caméra NIKA2 installée sur le télescope de 30m de l'IRAM. Une campagne d'observation dédiée a été menée, produisant des cartes de l'émission polarisée de la poussière. Cela a permis de reconstruire entièrement la morphologie et l'intensité du champ magnétique dans la région W43. Une analyse virielle a montré que les cœurs les plus denses sont en état de collapse global, confirmant leur aptitude à soutenir la formation d'étoiles massives. Des développements complémentaires incluent la conception et la validation en laboratoire de COSMOCal, une source polarisée à 260 GHz destinée à calibrer l'angle de polarisation absolu. Le système a été couplé avec succès à des récepteurs cryogéniques et validé avec des LEKIDs, ouvrant la voie à des stratégies de calibration plus robustes pour les futures expériences de polarimétrie. Enfin, la polyvalence des LEKIDs a été démontrée dans le cadre de la recherche sur la matière noire. L'expérience Dandelion vise à détecter des photons noirs dans la gamme des meV comme candidats à la matière noire. Deux campagnes de mesures ont été menées, conduisant à de nouvelles limites d'exclusion pour les photons noirs en tant que candidats à la matière noire. Ces travaux confirment le potentiel des LEKIDs pour la Cosmologie de précision, en reliant le développement instrumental, la calibration expérimentale et les observations astrophysiques.